UNIVERSITY OF LATVIA
INSTITUTE OF ATOMIC PHYSICS AND SPECTROSCOPY

Inga Saknite

OPTICAL NON-INVASIVE ESTIMATION AND MAPPING OF SKIN BILIRUBIN, HEMOGLOBIN AND WATER

DOCTORAL THESIS

in Medical Physics

Supervisor:
professor *Dr. habil. phys.* **Janis Spigulis**

RIGA, 2015

ABSTRACT

Methods for *in vivo* estimation and mapping of skin parameters have been developed and validated experimentally and clinically. In the visible spectral range (400–700 nm), new approaches for estimation and mapping of skin bilirubin and hemoglobin content and distribution changes over time in bruises by hyperspectral imaging and RGB imaging have been experimentally validated. A new approach for erythema index estimation by RGB imaging has been proposed and clinically validated; 500 measurements on 50 *rosacea* patients were analyzed and compared with clinician's visual assessment, as well as with a commonly used point-measurement device.

In the near-infrared spectral range (900–1700 nm), a method for *in vivo* determination of skin hydration changes over time after application of a moisturizing cream by reflectance spectroscopy has been developed and experimentally validated. Near-infrared imaging has been applied to distinguish skin regions with increased moisture. Additionally, a new method for follow-up of cream penetration in skin by laser-induced autofluorescence measurements has been proposed and experimentally tested.

The main results have been presented at 18 international conferences and 7 papers cited in the *Scopus* database.

Keywords: hyperspectral imaging, RGB imaging, skin chromophore mapping, erythema index, near-infrared spectroscopy, near-infrared imaging, bilirubin, hemoglobin, water.

ANOTĀCIJA

Darbā izstrādātas un eksperimentāli/klīniski aprobētas metodes *in vivo* ādas parametru novērtēšanai un kartēšanai. Redzamās gaismas spektra diapazonā (400–700 nm) eksperimentāli aprobētas jaunas metodes ādas bilirubīna un hemoglobīna noteikšanai un kartēšanai, kā arī noteikts šo vielu sadalījums ādas hematomās, pielietojot hiperspektrālās un RGB attēlošanas metodes. Izstrādāta un klīniski aprobēta jauna metode eritēmas indeksa izvērtēšanai, pielietojot RGB attēlošanas metodi. 50 rozācijas pacientiem tika veikti 500 mērījumi, un iegūtie rezultāti analizēti un salīdzināti ar sertificēta dermatologa vizuālo izvērtējumu, kā arī ar komerciālu punkta mērījumu ierīci.

Pielietojot atstarotās gaismas spektroskopiju tuvajā infrasarkanā spektra diapazonā (900–1700 nm), izstrādāta un eksperimentāli aprobēta metode *in vivo* ādas mitruma izmaiņu izvērtēšanai dinamikā pēc mitrinošu krēmu lietošanas. Tuvā infrasarkanā spektra attēlošanas metode tika pielietota, lai izšķirtu ādas reģionus ar paaugstinātu mitrumu. Pielietojot lāzera ierosinātas ādas autofluorescences metodi, tika izstrādāta un eksperimentāli novērtēta jauna metode, lai izvērtētu krēmu iespiešanos ādā.

Darba rezultāti prezentēti 18 starptautiskās konferencēs un 7 zinātniskās publikācijās, kas citētas *Scopus* datubāzē.

Atslēgvārdi: hiperspektrālās attēlošanas metode, RGB attēlošanas metode, ādas hromoforu kartēšana, eritēmas indekss, tuvā infrasarkanā diapazona spektroskopija, tuvā infrasarkanā diapazona attēlošana, bilirubīns, hemoglobīns, ūdens.

TABLE OF CONTENTS

ACRONYMS

A	absorbance
ΔA	parameter representing difference in absorption
$\boldsymbol{Bili}$	bilirubin
c	concentration
CEA	Clinician's Erythema Assessment
CMOS	complementary metal-oxide semiconductor
$\boldsymbol{DOHb}$	deoxyhemoglobin
$\boldsymbol{EI}$	erythema index
g	anisotropy factor
$\boldsymbol{H_2O}$	water
$\boldsymbol{Hb}$	total hemoglobin (oxyhemoglobin and deoxyhemoglobin)
$\boldsymbol{i}$	electric current
$\boldsymbol{I}$	light intensity
$\boldsymbol{l}$	distance that light travels in a medium (e.g. skin tissue)
LED	light-emitting diode
$\boldsymbol{Mel}$	melanin
NIR	near-infrared
$\boldsymbol{OD}$	optical density
$\boldsymbol{OHb}$	oxyhemoglobin
R	reflectance
RGB	color representation by red (R), green (G) and blue (B) components
$\boldsymbol{\varepsilon}$	molar extinction coefficient
$\boldsymbol{\lambda}$	wavelength
$\boldsymbol{\mu_a}$	absorption coefficient
$\boldsymbol{\mu_s}$	scattering coefficient

INTRODUCTION

Skin tissue optics is an interdisciplinary field that combines knowledge and understanding of Physics, Engineering, Physiology, Data Science and other fields. For many decades researchers have been trying to understand the manner in which light interacts with tissue, what information can be obtained from this interaction, as well as how light can be used as a treatment therapy for different skin disorders.

Visual assessment of human skin has been used in medicine for many centuries. General condition and appearance of skin is often the first sign of serious health problems. A clinician's visual assessment is usually an observation of skin color, also its roughness and other parameters. Optical methods offer a non-subjective assessment compared to visual assessment by a clinician. With spectroscopic tools now available, it is possible to assess skin condition by quantitative measures, access information from deeper layers of skin not visible to the naked eye, and distinguish between small changes of skin color that are not distinguishable to the unaided eye.

Optical methods offer tools for non-invasive assessment of skin condition for different applications such as diagnostics (neonatal jaundice, *rosacea* severity), forensic medicine (age of a bruise) and the cosmetics industry (how well cosmetic lotions absorb in skin). That optical methods are so widely used is due to their being noninvasive when using visible and near-infrared light sources. Despite many advantages, these potentially perspective methods are not that widely studied, especially those related to skin bilirubin and water. Although there are patents and scientific publications available, there are still quite a lot of unknowns and problems to be solved for those optical methods to become real and reliable applications.

In this doctoral thesis, methods for diffuse reflectance imaging of skin in the visible and near-infrared spectral ranges covering the wavelengths 400–1700 nm are developed and experimentally and clinically tested. In the visible spectral range (400–760 nm), water absorption in upper layers of skin is low compared to other chromophores that are present and that affect the color of skin: hemoglobin, melanin and bilirubin. In the near-infrared spectral range (760–1700 nm) water is the main absorbing matter that greatly affects the diffuse reflectance spectra of skin. This spectral range has a potential for non-invasive determination of skin hydration. However, there is no commonly used methodology or complete understanding as to how to do it properly.

This doctoral thesis covers several different studies carried out to fulfil **the aim of this thesis**: development and experimental validation of optical methods for noninvasive estimation and monitoring of skin parameters in an extended spectral range of 400–1700 nm.

Tasks of this thesis:

Development and experimental/clinical validation of methodologies for:

1. Estimation of skin bilirubin and hemoglobin relative concentration and distribution changes in bruises by hyperspectral imaging and RGB imaging;
2. Estimation of skin hydration by near-infrared reflectance spectroscopy;
3. Water distribution mapping in skin by near-infrared imaging;
4. Assessment of facial skin erythema by RGB imaging;
5. Laser-induced autofluorescence technique for follow-up of cream penetration in skin.

Three main **methods** used for experimental and clinical measurements:

- Reflectance spectroscopy – acquisition of single-spot reflectance spectrum of skin by a spectrometer (visible and near-infrared or near-infrared only);
- Spectral imaging – acquisition of images at different spectral bands (hyperspectral imaging) or red, green and blue spectral bands (RGB imaging);
- Autofluorescence spectroscopy – acquisition of single-spot skin autofluorescence spectrum after illumination with a laser.

This thesis is structured in the following way: Chapter 1 gives a summary of skin tissue optics, including fundamental properties of light, skin chromophores, optical properties of skin, model used for light interaction with tissue and optical methods used for obtaining information about skin; Chapters 2 to 4 consist of literature overview, experimental results and main conclusions on the **three main topics** of this thesis:

1. Estimation of skin bilirubin and hemoglobin relative concentration and distribution changes in bruises over time by hyperspectral and RGB imaging, including the development of skin bilirubin and hemoglobin phantoms, as well as a short study on other skin lesions [Chapter 2];
2. Assessment of facial skin erythema (the redness of skin) by analyzing hemoglobin and melanin absorption parameters in skin by RGB imaging [Chapter 3];
3. Estimation of skin hydration (relative water content in skin) by near-infrared reflectance spectroscopy and imaging, as well as the development of a proof-of concept technique for follow-up of cream penetration in skin by laser-induced autofluorescence technique [Chapter 4];

The work summarized in this thesis was primarily done during years 2012 to 2015 at the Biophotonics Laboratory, Institute of Atomic Physics and Spectroscopy. Some previous studies done during Bachelor (2008 to 2010) and Master (2010 to 2012) studies have been included as well.

This work has mainly been financially supported by the following projects:

- European Social Fund project "Innovative technologies for acquisition and processing of biomedical images" (2013 to 2015).
- European Regional Development Fund project "New optical technologies for complex non-contact skin diagnostics" (2012 to 2013);

The author of this thesis received the following grants and scholarships that allowed participating at international conferences: SPIE Officer Travel grant (participation at "Optics & Photonics" in San Diego, USA, August 2012); SPIE Student Author Travel grant (participation at "Photonics West" in San Francisco, USA, February 2013); OSA Foundation Student Travel grant (participation at "Biomedical Optics" in Miami, USA, April 2014); SPIE Student Author Travel grant (participation at "Photonics West" in San Francisco, USA, February 2015) and OSA Foundation Student Travel grant (participation at "Frontiers in Optics and Laser Science" in San Jose, USA, October 2015). The author has also had the opportunity to participate in the following summer schools: Biophotonics Summer school in Shannon, Ireland (summer of 2010), and Summer school of Physics in Ljubljana, Slovenia (summer of 2011).

The doctoral thesis consists of 157 pages, an introduction, 4 chapters, a summary, 8 appendices, 61 figures and 107 cited references.

A summary of this doctoral thesis is available in Latvian and English.

CHAPTER 1

SKIN TISSUE OPTICS

In this chapter, fundamental properties of skin anatomy/physiology and light interaction with skin tissues are described. They are crucial for understanding skin tissue optics and for being able to use spectroscopic and imaging tools for medical applications.

1.1 LIGHT INTERACTION WITH TISSUES

Light is the visible part of electromagnetic spectrum in the wavelength range of approximately 400–760 nm. There is ultraviolet spectrum to the shorter wavelengths (10–400 nm) and infrared spectrum to the longer wavelengths (700 nm – 1 mm) that is divided in three main ranges: near-infrared (700 nm – 2,5 μm), mid-wavelength infrared (2,5–25 μm), and far-infrared (25 μm – 1 mm) [1].

Classical electromagnetism considers light as waves – propagating oscillations of electric and magnetic fields. Light can be emitted and absorbed in little bursts called photons. In macroscopic world, beams of light have so many photons that light can be considered as a ray of particles that reflects, refracts and disperses [2, 3].

In tissue optics, light geometrical and quantum properties are both of importance. When light comes in contact with tissue surface, some part is reflected off the surface (around 4–7% in the spectral range 250–3000 nm) [4]. Some part continues its way inside the tissue where it can be reflected, refracted, transmitted, scattered or absorbed, and by multiple processes some part of it can reach and cross the surface of the tissue again (Fig. 1).

Human tissues are optically inhomogeneous media with a refractive index higher than the refractive index of air which is the reason of the partial reflection at the tissue-air interface. In the ultraviolet (<400 nm) and infrared (>2 μm) spectral ranges light is easily absorbed, scattering is low and radiation doesn't penetrate deep in the tissue. In the visible and near-infrared spectral ranges scattering can be much higher than absorption, allowing radiation to penetrate deeper (a couple of hundred micrometers at 450 nm and up to

3 millimeters at 1700 nm, depending on type of tissue). However, due to high water absorption in skin, near-infrared radiation typically cannot penetrate more than 1 mm [5, 6].

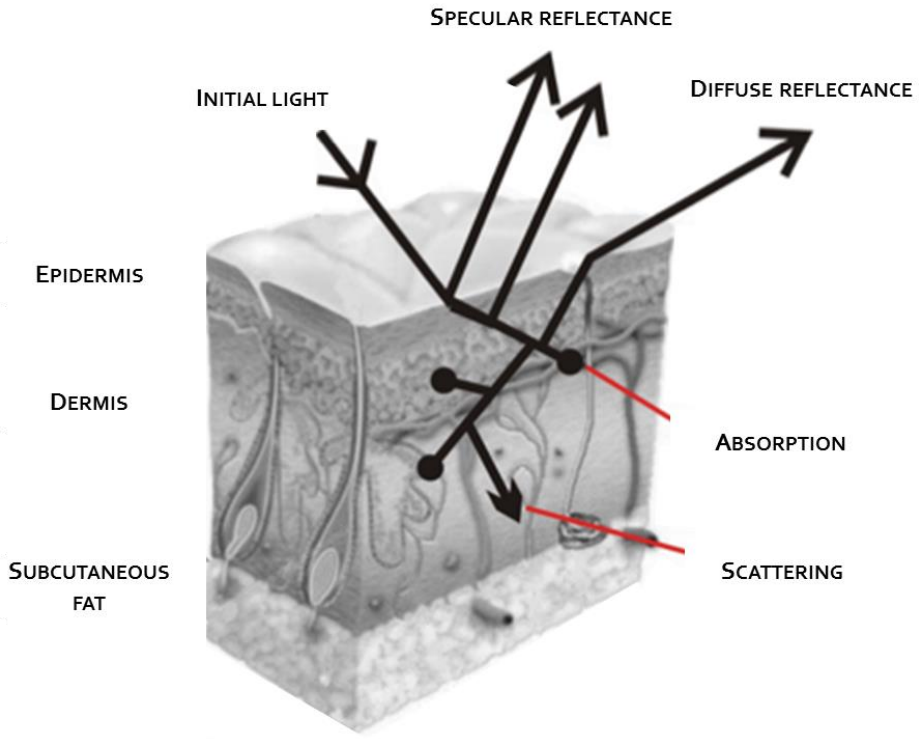

Fig. 1. A schematic of light interaction with tissue [7].

Scattering occurs due to change in refractive index. The dominant scattering in human tissue is Mie scattering which describes scattering from particles with size similar or larger to the wavelength of light that reaches them and which is forward directed. Skin chromophore molecules (hemoglobin, bilirubin, melanin, water), around the size of a couple of nanometers, as well as mitochondria and other sub-cellular biological structures are Rayleigh scatterers [5, 7].

When light gets scattered, it changes its direction by an angle θ and travels a distance between two scattering events that is called the scattering mean free path $x_s = 1/\mu_s$, where $\mu_s = \rho_s \cdot \sigma_s \, [cm^{-1}]$ is the scattering coefficient which describes a medium that contains many scattering particles with an effective cross-sectional area $\sigma_s \, [cm^2]$ at a concentration expressed as volume density $\rho_s \, [cm^3]$. Light in human tissue can get scattered multiple times, thus an anisotropy factor g is introduced as $g = 1 \, / \, \overline{cos\theta}$, where $\overline{cos\theta}$ is the mean cosine of the scattering angles [8, 9]. Typical anisotropy factor values in the visible spectral range in human skin are: $g = 0{,}75$ in subcutaneous fat layer of skin, $g = 0{,}86$ in *stratum corneum*, $g = 0{,}90$ in the upper layers of dermis and $g = 0{,}95$ in the lower layers of dermis where the

blood net is located [8, 10]. Scattering in human tissue is mostly caused by cells and their structures, lipids, water and collagen.

Absorption can occur when the energy of a photon matches the energy difference between two energy levels of a molecule. The reason why we see colors is due to selective absorption, meaning that a medium (consisting of molecules) absorbs some visible light wavelengths more than others. In the near-infrared spectral range vibrational transitions affect which wavelengths are absorbed more than others. Absorption can be expressed by absorption coefficient $\mu_a = \rho_a \cdot \sigma_a \, [cm^{-1}]$, where $\rho_a \, [cm^{-3}]$ is a volume density or concentration of many chromophores and $\sigma_a \, [cm^2]$ is the effective cross-sectional area [5, 7, 11].

Due to absorption of different chromophores, light intensity is attenuated when traveling in the tissue. Theoretical description of this process can be very complex; however, simplified models can be applied. One of the most commonly used is Beer-Lambert-Bouguer's law that states that the initial light intensity I_0 decreases exponentially after traveling a distance l through a medium of concentration c and molar extinction coefficient ε_λ:

$$I = I_0 e^{-\varepsilon_\lambda \cdot c \cdot l} \tag{1}$$

Molar extinction coefficient ε_λ is a measure of how strongly a medium attenuates light, and it is wavelength dependent. The SI unit of ε_λ is [$\frac{m^2}{mol}$] but a commonly used unit is [$cm^{-1} \cdot \left(\frac{mol}{L}\right)^{-1}$] [13]. Then concentration has to be expressed in units [$\frac{mol}{L}$], and the expression $\varepsilon_\lambda \cdot c$ has the unit [cm^{-1}] which essentially describes the absorption coefficient μ_a and Beer-Lambert-Bouguer's law can be also expressed as:

$$I = I_0 e^{-\mu_a \cdot l} \tag{2}$$

Optical density (OD) describing absorption can be introduced by modifying the Beer-Lambert-Bouguer's law:

$$OD = ln\frac{I_0}{I} = \varepsilon_\lambda \cdot c \cdot l = \mu_a \cdot l \tag{3}$$

If there is more than one chromophore present, the total absorption can be expressed as superposition of absorption of all chromophores:

$$OD_{total} = ln\frac{I_0}{I} = \sum_i \varepsilon_i \cdot c_i \cdot l_i \tag{4}$$

1.2 OPTICAL METHODS AND INSTRUMENTS

1.2.1 Reflectance spectroscopy

Reflectance spectroscopy is a simple tool for analyzing the reflected (or absorbed) optical radiation from a sample. The key elements of a reflectance spectroscopy setup are a spectrometer, a light source and optical fiber probes. It is important to select a light source that covers the whole spectrum of interest and is bright enough to suppress the background noise [14].

The basic working principle of a spectrometer is as follows: incoming light is directed towards a diffraction grating and essentially to a single photodetector that converts the signal to light intensity value. By rotating the grating, light intensity is obtained as a function of wavelength. Nowadays, mostly fixed-grating spectrometers are used. Instead of a single photodetector, charged coupled device (CCD) [15] and linear detector arrays are used. Each pixel across the CCD represents a portion of the spectrum, thus simultaneously allowing to obtain the whole spectrum.

An important characterization of a spectrometer is the material used for detection of incoming optical radiation as it determines the spectral range in which the spectrometer operates. The upper wavelength limit that can be detected by the spectrometer can be calculated by the following expression: $\lambda_{max} = \frac{hc}{E_{gap}}$, where h is Plank's constant and c is the speed of light. E_{gap} is the bandgap energy between the valence band and the conduction band, equivalent to the energy (expressed in electron volts) required for an outer shell electron to become a mobile charge carrier and to be able to move freely within the material [16].

For visible and near-infrared spectral ranges (400–1100 nm) silicon-based photodetector arrays are the most commonly used as the bandgap energy of silicon is $1{,}11\ eV$ and thus the upper wavelength limit $\lambda_{max,Si} = 1117{,}11$ nm [17].

For near-infrared spectral range (900–1700 nm) indium gallium arsenide (*InGaAs*) are the most commonly used detectors. *InGaAs* is an alloy created by mixing *InAs* ($E_{gap} = 0{,}36\ eV$) and *GaAs* ($E_{gap} = 1{,}43\ eV$) and the bandgap energy can be chosen between those two values depending on the ratio of *In* and *Ga* in the mixture. However, due to different factors, most of the ratios of *In* and *Ga* are not easily manufactured, thus the most commonly fabricated is the one with *In* and *Ga* ratio of 0,53 to 0,47, respectively [18], with $E_{gap} = 0{,}73\ eV$ and $\lambda_{max} = 1{,}7\ \mu m$. It is possible to fabricate an *InGaAs* detector with sensitivity up to $\lambda_{max} = 2{,}5\ \mu m$ (*In* and *Ga* ratio of 0,80 to 0,20), however the dark current and noise are considerably higher, and spectrometers working in this range need cooling [19].

InGaAs detector sensitivity is temperature dependent – with lower temperatures the sensitivity curve moves to shorter wavelengths ($\sim 75\ nm/K$) and the maximum quantum efficiency decreases with $\sim 0{,}1\ \%/K$, where K is temperature in Kelvins [20].

Other available infrared detectors include mercury cadmium telluride (*HgCdTe*) with spectral sensitivity at 1–18 μm (operating temperature –223°C to –23°C) and indium antimonide (*InSb*) with spectral sensitivity at around 7 μm (operating temperature –193°C) [21].

The most important characteristics of spectrometers are: photosensitivity (ratio of the generated photocurrent and light power [A/W]) which can also be expressed with quantum efficiency (percentage of photons hitting the detector's photoreactive surface that produce charge carriers), dark current, response time, noise equivalent power NEP (the minimum irradiant signal power to generate a signal to noise ratio of 1 in an integration time of 0,5s [$W/\sqrt{Hz}$]) and the lowest detectable power $D^* = 1/NEP$ [22]. A comparison of detectivity of the most commonly used detectors in the visible and near-infrared spectral range is shown in Fig. 2.

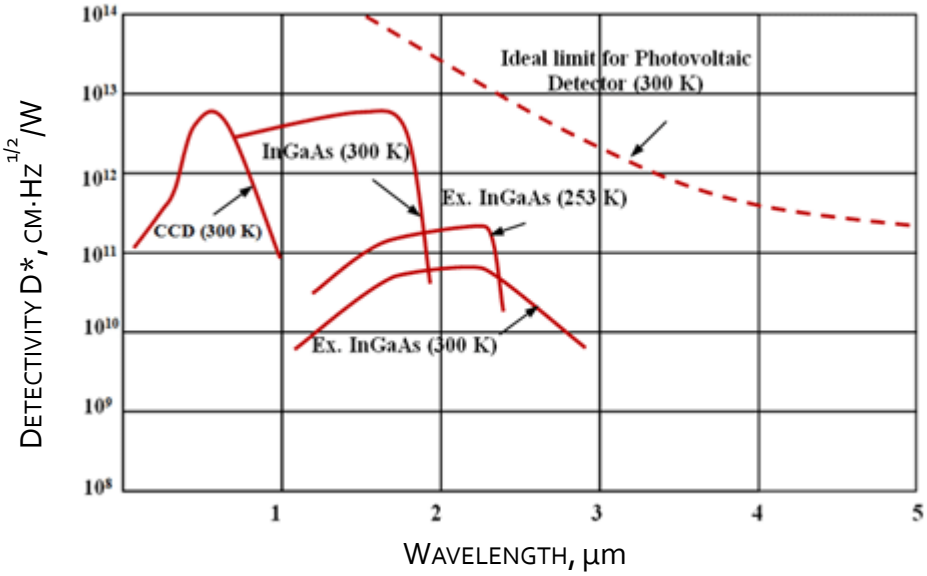

Fig. 2. Comparison of detectivity of the most commonly used detectors [23].

1.2.2 Hyperspectral imaging

Hyperspectral imaging is a technique for acquiring images at adjacent, partially overlapping spectral bands which can be achieved e.g. by the use of optical filters. By a hyperspectral imaging device, a three-dimensional image cube can be created where two are spatial dimensions and the third one is spectral dimension, thus it is possible to acquire spectrum at each image pixel.

There are four common types of hyperspectral imaging devices. Whiskbroom devices take a spectrum at one pixel at a time and scan the whole area of interest in this fashion (Fig. 3a). Pushbroom technology means that a slit of an object is imaged at a time by a two-dimensional camera, where one dimension is spatial information and the second dimension is spectral which is being achieved by a prism (Fig. 3b). The third type is Staring technique that acquires an image at a specific spectral band by use of an optical filter, and spatial dimension is then added by acquiring images by use of different filters (filter wheels containing fixed bandpass filters, linear variable filters, variable interference filters and tunable filters) (Fig. 3c). The fourth type is Snapshot technique (also known as single-shot) that is supposed to record spatial and spectral information on an area detector with single exposure, although the spatial and spectral resolutions are limited as the total number of voxels cannot exceed the total number of pixels on the CCD camera (Fig. 3d) [24, 25].

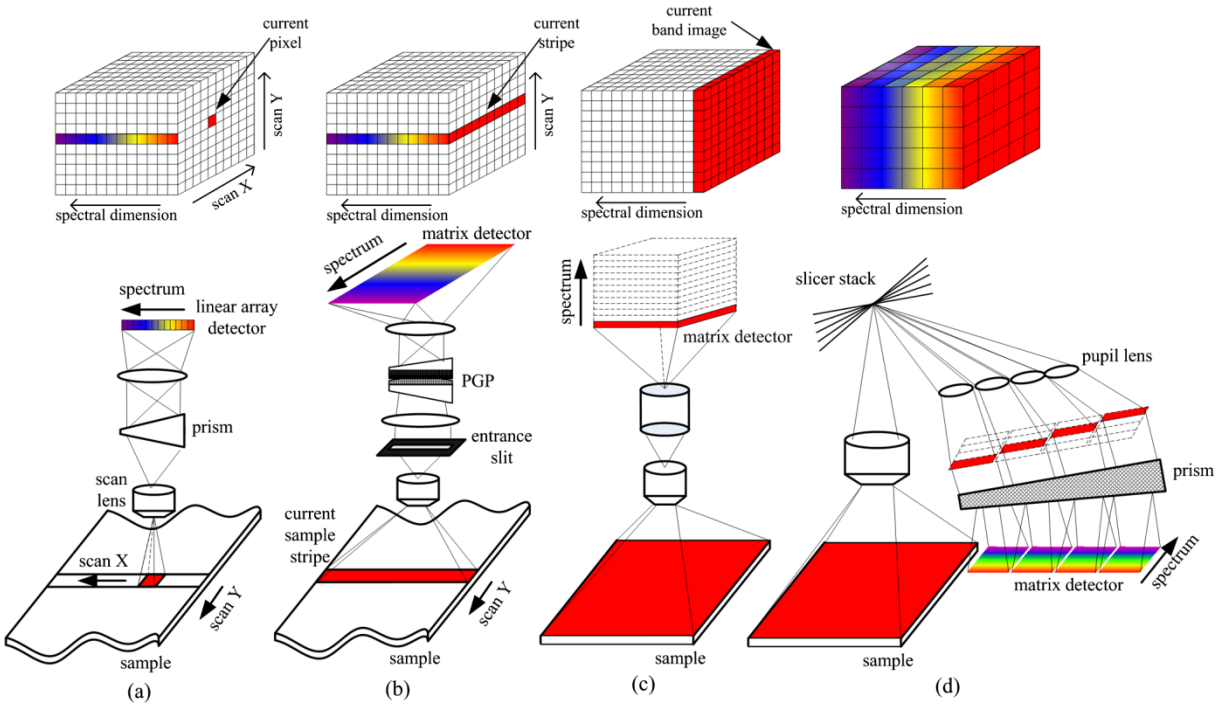

Fig. 3. Typical methods for spectral imaging: a) Whiskbroom, b) Pushbroom, c) Staring and d) Snapshot [25].

RGB imaging is the simplest modality of hyperspectral imaging. An image is acquired at three partially overlapping spectral bands (red, blue and green) simultaneously. The most commonly used sensor for acquiring RGB images is a CMOS sensor that has a color filter matrix on top of the sensor, and each pixel only receives the primary color (red, blue or green) component – the other color components are calculated during image processing by analyzing the neighboring pixel color components as each pixel has a different color filter (Fig. 4) [26, 27].

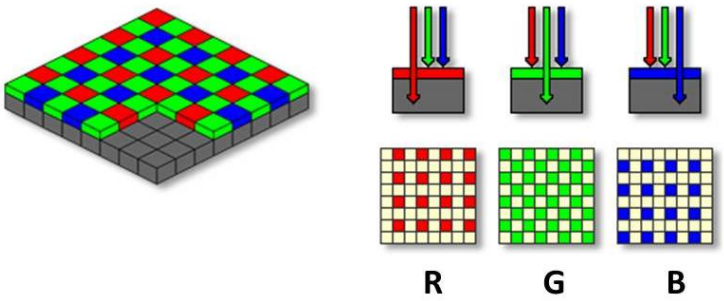

Fig. 4. RGB sensor color filter working principle [27].

1.2.3 Skin autofluorescence spectroscopy

Fluorescence is a type of photoluminescence, the emission of light resulting from absorption of photons, with a typical lifetime of nanoseconds. When a molecule absorbs a photon, it acquires energy which excites it to a higher energy level. Fluorescence occurs when the molecule emits light and the energy of the molecule decreases to a lower state. The energy of the emitted photon is lower (the wavelength is longer), due to some energy being lost in the process [28, 29].

Autofluorescence is the ability of some biological substances to possess intrinsic fluorescence. This term is used to distinguish the intrinsic fluorescence from the fluorescence by exogenous fluorescent markers. The most important fluorophores in skin tissues and cells are: amino acids, NADH and FAD, porphyrins and lipopigments that can be excited by ultraviolet light and observed in the visible spectral range (Fig. 5) [28–31].

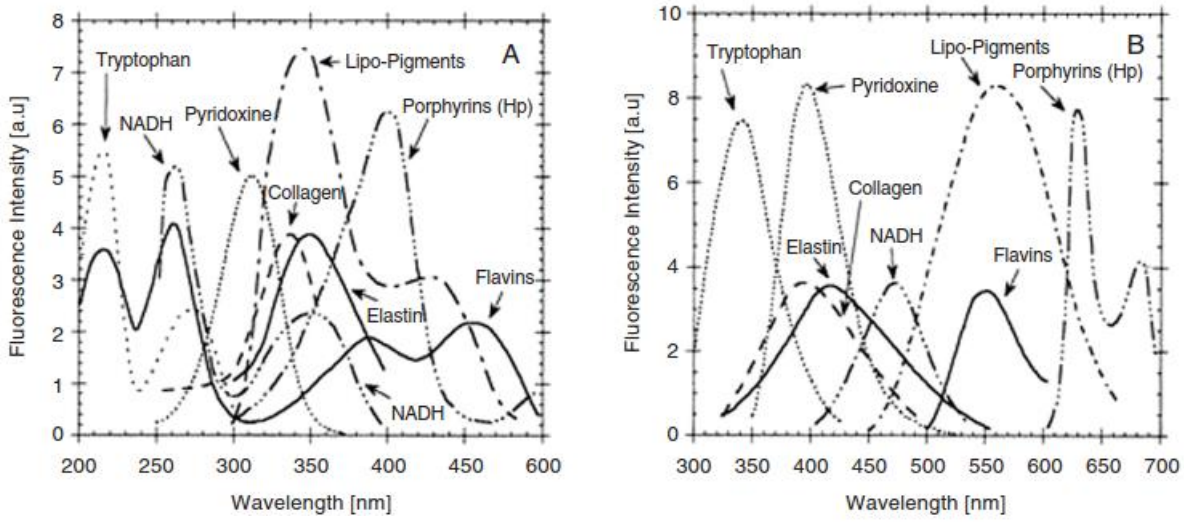

Fig. 5. Excitation (A) and emission (B) spectra of the principal endogenous fluorophores [28].

1.3 SKIN PHYSIOLOGY AND SKIN CHROMOPHORES

Human skin is the outer layer of human body that guards the underlying tissues, muscles and organs, regulates the body temperature, controls evaporation and helps prevent water loss [32]. Three main layers are epidermis (including *stratum corneum*), dermis and subcutaneous fat (Fig. 6), although sublayers are often considered as well [11, 33].

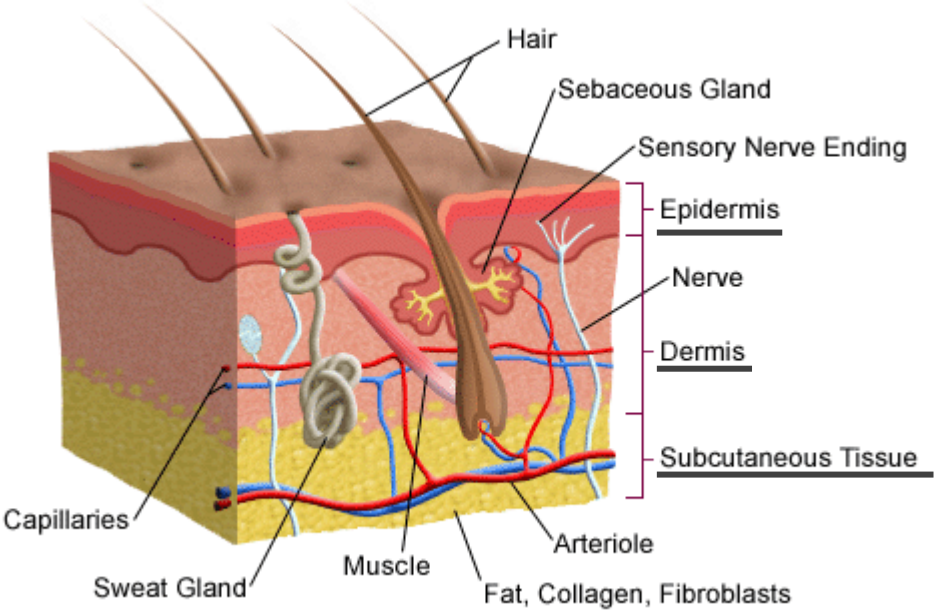

Fig. 6. Three layers of skin and light interaction with tissue [34].

The thin outermost epidermis (typically $40-125\,\mu m$ thick) consists 95% of epithelial cells called keratinocytes, and these cells continually migrate outward toward the surface flattening, dying and cementing together in the process to form a thin and tough outer layer called the *stratum corneum* (typically $7-40\,\mu m$ thick). The remaining 5% of epidermis are mostly melanocytes [33, 35–37].

Epidermis consists of 5 sublayers (Fig. 7), the outer of which, *stratum corneum*, is the main barrier that protects the body from dehydration, as well as from other molecules (e.g. irritants) entering into the skin. *Stratum lucidum* or the clear layer is only found in very thick epidermis (palms, soles) and is located between *stratum corneum* and *stratum granulosum* [38]. Skin has its own natural moisturizing mechanism that keeps it moist. *Stratum granulosum* is the second outer layer of epidermis, and it is where the most important transformations in the formation of *stratum corneum* barrier occur. At the *stratum granulosum* keratinocytes are transformed into corneocytes that are the building blocks of *stratum corneum*. In this process, natural body lipids are released, and they are the main barrier that protects water passing out through the *stratum corneum*. On most body sites,

stratum corneum consists of 12 to 16 cell layers, but it can vary from 9 cell layers at eyelids to more than 50 cell layers at soles [38].

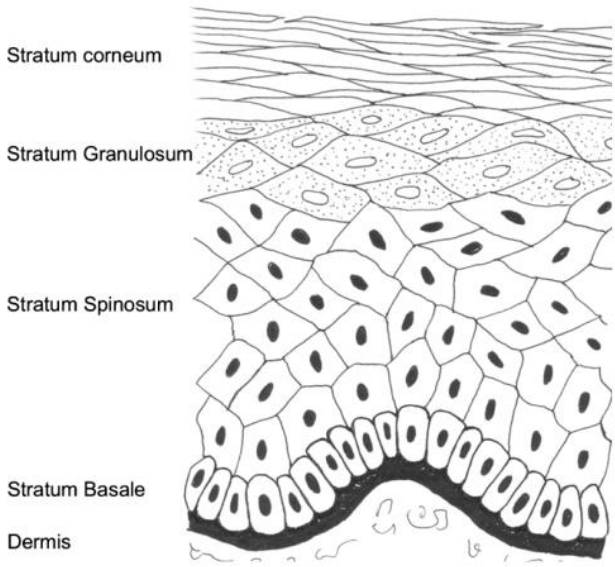

Fig. 7. The five layers of epidermis [38].

The dermis is much thicker than the epidermis, the thickness varying from 1 mm on eyelids to 5 mm on thighs, palms and soles. It has fewer cells and mostly consists of connective tissue, blood vessels, lymphatics, nerve endings, elastic and collagen fibers, hair follicles, sweat glands and macrophages. Proteins and polysaccharides form macromolecules which attract and preserve water [33, 39].

The deepest layer, called subcutaneous fat, mainly consists of fatty tissue that acts as an insulator and a shock absorber. It can be up to 8 mm thick [33, 40, 41].

Skin reflectance is influenced by concentration and depth of chromophores, mainly melanin and hemoglobin in the visible range and water and lipids in the near-infrared spectral range. Both absorption and scattering of different skin structures and chromophores affect skin reflectance measurements.

In the visible spectral range, hemoglobin, melanin and bilirubin are the main chromophores affecting reflectance spectrum of skin. Absorption spectra of these chromophores can be expressed as molar extinction coefficient values ε $[cm^{-1} \cdot (\frac{mol}{L})^{-1}]$ at each wavelength (Fig. 8). These values have been experimentally obtained and are available in literature [42].

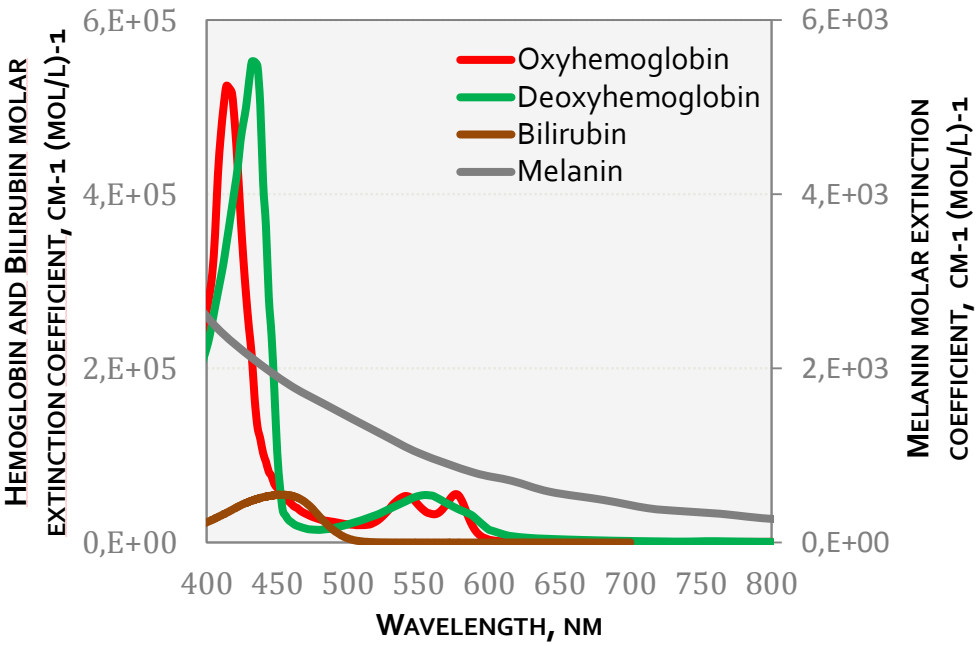

Fig. 8. Molar extinction coefficients of oxy- and deoxyhemoglobin, bilirubin and melanin in the visible and near-infrared spectral range [42].

Melanin is mostly responsible for the darkness of skin, and Fitzpatrick's scale is often used to distinguish skin types from type I (ivory white skin, easily sunburns) to type VI (dark brown skin, never burns) [43]. Melanin is produced by melanocytes which are mainly located in the deepest epidermis sublayer (the basal layer). Vesicles called melanosomes release melanin and transport it via dendrites to adjacent keratinocytes. The amount, shape and size of melanosomes are genetic: Caucasian melanosomes typically contain more melanin granules but less total melanin, compared to Negroid melanosomes, however, Negroid melanosomes are larger. Melanin in healthy skin is only located in the epidermis [44, 45].

Hemoglobin is located in blood vessels of dermis and subcutaneous fat layer. Hemoglobin transports oxygen from lungs to tissues throughout the whole human body, collects CO_2 and brings it to the lungs. There are four heme groups within each hemoglobin molecule, and each heme consists of a porphyrine ring with a central iron atom (Fe^{2+}). Hemoglobin with bound oxygen is called oxyhemoglobin (HbO_2), and it shows a bright red color. Hemoglobin without bound oxygen is called deoxyhemoglobin (Hb), and it shows a dark red, even bluish color [39, 45, 46]. Oxyhemoglobin and deoxyhemoglobin have slightly different absorption spectra in the visible and near-infrared spectral ranges: oxyhemoglobin exhibits absorption maxima at 548 nm and 576 nm, while deoxyhemoglobin shows maximum at 550 nm. Both chromophores also show a very high absorption in the 400–450 nm spectral range with absorption peaks at 410 nm (oxyhemoglobin) and at 430 nm (deoxyhemoglobin) (Fig. 8) [42].

There are other forms of hemoglobin which are mostly present in tissue in very low concentrations, thus are typically not taken into account when doing skin reflectance measurements. Methemoglobin (in normal cases ~1% of total hemoglobin) is chocolate brown in color and it can be formed if hemoglobin is exposed to oxidative stress (for example, by heating), thus the iron atom in the heme group gets oxidized (Fe^{3+}) [47, 48]. Other forms of hemoglobin are: sulfhemoglobin (less than 1% of total hemoglobin) and carboxyhemoglobin (typically less than 1.5% of total hemoglobin, may increase to 9% in smokers) [49, 50].

Bilirubin is the breakdown product of hemoglobin with an absorption maximum at 460 nm (Fig. 8), giving it a yellowish color. Heme oxygenase is a biochemical process that splits a heme ring to form biliverdin, a greenish skin chromophore which subsequently is converted to bilirubin by another biochemical process called biliverdin reductase (Fig. 9). Due to high biliverdin reductase activity in human skin, biliverdin is very quickly converted to bilirubin. Normally, the highest activity of heme oxygenase is in the spleen where erythrocytes are destroyed [45, 51, 52].

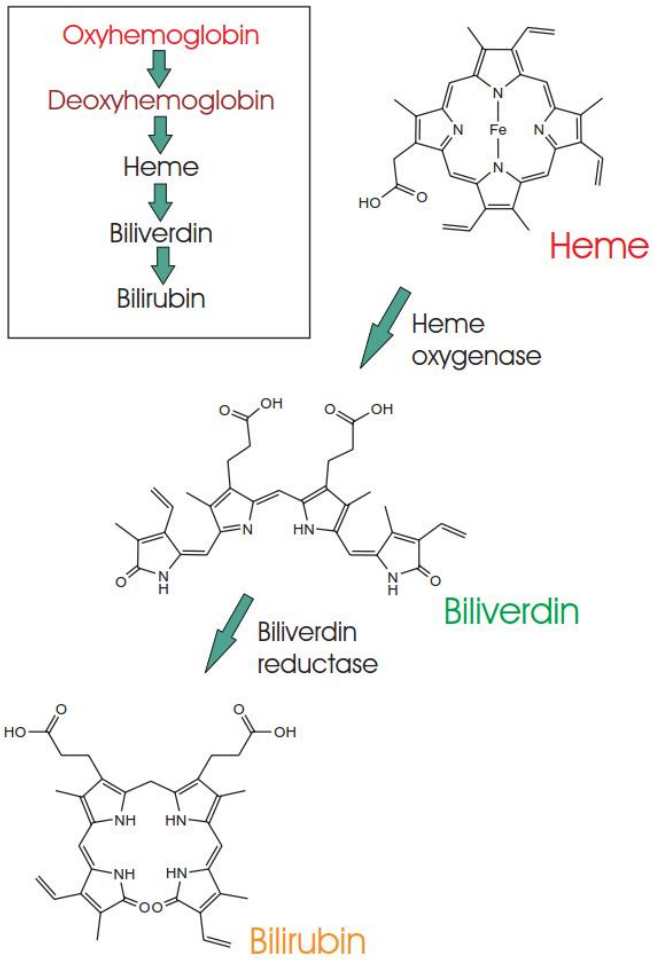

Fig. 9. Biochemical processes of heme breakdown and the production of biliverdin and bilirubin [45].

There is little bilirubin concentration in blood plasma ($c < 17\ \mu mol/L$) in healthy skin but its concentration increases ($> 30\ \mu mol/L$) if a person suffers from jaundice, also called hyperbilirubinemia (increased bilirubin concentration in blood plasma) [53]. Newborns can suffer from increased levels of bilirubin just after birth due to a high hemoglobin turnover and their bodies not being able to get rid of all the bilirubin as quickly as needed. This occurs in approximately 60% of term infants and 80% of preterm infants [54]. If untreated, serious brain damage and even death can occur, thus early diagnostics is crucial. Treatment is usually light therapy, but in severe cases even blood transfusion [55–57].

Typically, bilirubin concentration in skin also increases during bruise development when at first there is an increase in hemoglobin due to destruction of small capillaries and afterwards an increase in bilirubin which is the breakdown product of hemoglobin [45].

Water molecule consists of two hydrogen and one oxygen atom (H_2O) that are bonded with polar covalent bonds. Water highly absorbs a wide range of the electromagnetic radiation but it has a narrow window of transparency in the visible spectrum as there is no physical mechanism that could produce transitions in the spectral range of 400–700 nm – it is too energetic for vibrational transitions and the energies are too low to cause electronic transitions. In the infrared spectral range ($\sim 1 - 10$ μm) absorption occurs due to intramolecular vibrational transitions of the water molecule. The fundamental vibrations of a water molecule are shown in Fig. 10: the O–H symmetric stretching vibrations ν_1 give rise to the absorption maximum at 3.05 μm, the O-H assymetric stretching vibrations ν_3 give rise to the absorption maximum at 2.87 μm and the O-H bend ν_2 give rise to the absorption maximum at 6.08 μm. Combinations of these vibrations are observed in the near-infrared spectrum, for example, the 980 nm absorption maximum is due to the combination band $a \cdot \nu_1 + b \cdot \nu_3$ ($a + b = 3$), the 1200 nm absorption maximum is due to the combination band $a \cdot \nu_1 + \nu_2 + b \cdot \nu_3$ ($a + b = 2$) and the 1470 nm absorption maximum is due to the combination band $a \cdot \nu_1 + b \cdot \nu_3$ ($a + b = 2$) [58–60].

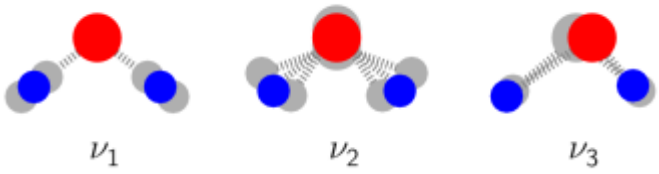

Fig. 10. The fundamental vibrations of water molecule (symmetric stretch, bend asymmetric stretch) [61].

Up to 60% of the human adult body is water, including skin where water content changes at different layers of skin. Very little water content is in the upper layers of skin, including *stratum corneum*, and its content increases with deeper layers to up to around volume fraction of 65% in the lower dermis [11]. Examples of water volume fraction depth profiles of the *stratum corneum*, calculated from *in vivo* Raman measurements are shown in Fig. 11 [62].

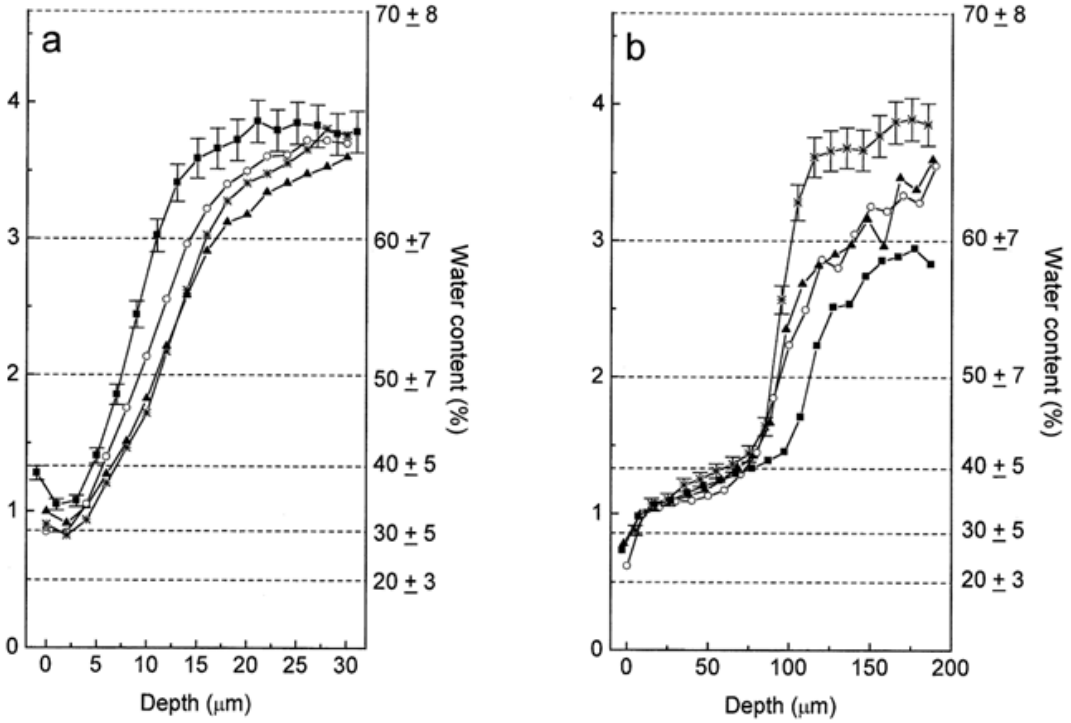

Fig. 11. *In vivo* water volume fraction profiles of the *stratum corneum* by Raman measurements of the volar aspect of forearm (a) and of the thenar (b) [62].

Absorption coefficient [$\frac{1}{cm}$] values are used to represent absorption spectrum of water in the near-infrared spectral range (Fig. 12) [63]. Water has distinct absorption maxima at 980 nm, 1200 nm and 1450 nm. An even higher absorption is at 1920 nm, not shown in Fig. 12.

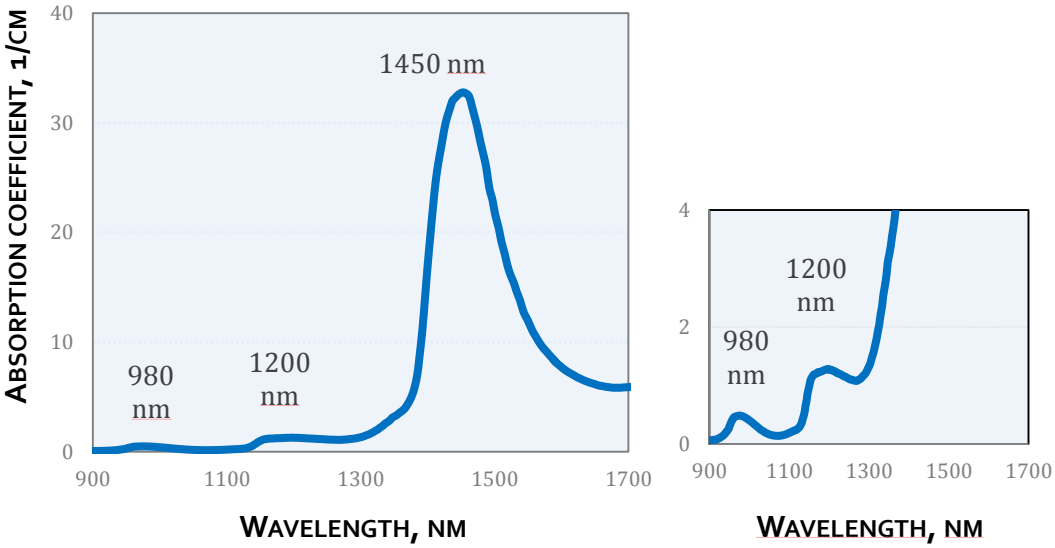

Fig. 12. Absorption spectrum of water in the near-infrared spectral range [63].

CHAPTER 2

HYPERSPECTRAL AND RGB IMAGING FOR MAPPING OF SKIN BILIRUBIN AND HEMOGLOBIN

The first part of this chapter gives an overview of work done by other groups to estimate relative concentration and distribution of skin bilirubin and hemoglobin, with the main focus on how they change over time in bruises. This topic is of particular interest for three main purposes: easy, reliable, fast and noncontact monitoring of bilirubin in neonates (for early detection and monitoring of neonatal jaundice), reliable determination of the age of bruises that is important in forensic science and diagnostics and monitoring of diabetes. There are two main groups who have done research in this field: University of Trondheim in Norway (Lise L. Randeberg) [45, 64–70] and Amsterdam Medical Centre in the Netherlands (Barbara Stam) [71–73].

The second part of this chapter describes the methodology and techniques used for estimation and mapping of skin bilirubin in bruises that the author has performed based on previous work done by other groups. The experimental part consists of two main methods: hyperspectral and RGB imaging to estimate skin bilirubin and hemoglobin relative concentration and distribution changes in bruises over time. This work has been published in papers V, VI and VII and presented at conferences C2, C11, C12, C13, C14, C15, C17 and C18.

The third part describes the development of skin phantoms to mimic skin bilirubin, hemoglobin and melanin absorption in skin. Hyperspectral imaging was used to analyze the data. Skin phantoms are useful for understanding how the concentration and depth of different chromophores change the diffuse reflectance spectrum of skin. This work has been published in papers III and XI and presented at conferences C6 and C16.

The fourth part of this chapter describes a study on skin lesions by diffuse reflectance and fluorescence spectroscopy which was also done by hyperspectral imaging method. The aim of this study was to compare diffuse reflectance and fluorescence imaging of typical and atypical skin lesions to see if it is possible to distinguish between both, which could be a

useful application for early diagnostics of potentially malignant skin lesions. This work has been published in paper II and presented at conferences C7 and C8.

2.1 LITERATURE OVERVIEW

Transcutaneous bilirubinometry for noninvasive determination of skin bilirubin in neonates was first introduced in 1980 by using a bilirubinometer, developed by *Minolta* which used a two-filter design to measure "the yellow color of skin" [74]. Since then other commercial devices have become available, e.g. *ColorMate TLc BiliTest System* [75] which requires an initial measurement shortly after birth, *BiliCheck* (by *SpectRx*) [76] which requires five replicate measurements at one site and is based on reflectance analysis at multiple wavelengths, and *Jaundice Meter* (by *Minolta/Hill-Rom Air-Shields*) which is based on two-wavelength analysis. A study done to compare *BiliCheck* and *Jaundice Meter JM-102* concluded that the variability of the *BiliCheck* system is less than that of the *Jaundice Meter*, and that *BiliCheck* system is not affected by skin color which means that a multi-wavelength analysis gives significantly better results for skin bilirubin estimation [77]. At the same time, another study shows good correlation between *Jaundice Meter JM-102* obtained results and invasive blood sample results in dark-skinned neonates [78].

A study on *in vivo* spectroscopy of jaundiced newborn skin done by Randeberg *et. al.* shows possibilities for determination of transcutaneous bilirubin index (*TcB*) by using reflectance spectroscopy where *TcB* was calculated by algorithms based on diffusion theory. Fig. 13 shows differences in spectrum of non-jaundiced and jaundiced newborn skin. As could be expected, the main differences are in the spectral range 450–500 nm where there is an absorption maximum (460 nm) of bilirubin: there are lower reflectance values in this spectral range for jaundiced than for non-jaundiced skin. Results showed good correlation ($r = 0.81, p < 0{,}05$) between *TcB* values and total serum bilirubin (*SBr*) values that were acquired from heel stick blood samples [65].

A diffusion model for skin is one of the mathematical and physical models used to understand how light interacts with tissue and to acquire skin parameters based on mathematical modeling. In tissue optics, the dual nature of light is of great importance. The theory used for describing light as particles is Radiative Transport theory, and the most common models used are: diffusion theory, Adding-Doubling [79], Kubelka-Munk [5] and Monte Carlo [33]. Maxwell's equations with proper boundary conditions have to be applied to describe light as a wave, and the most common models applied for this purpose are: Finite difference time domain and Pseudo spectral time domain. In Radiative Transport theory

energy conservation and transport are considered rather than electric and magnetic fields from Maxwell's equations [80].

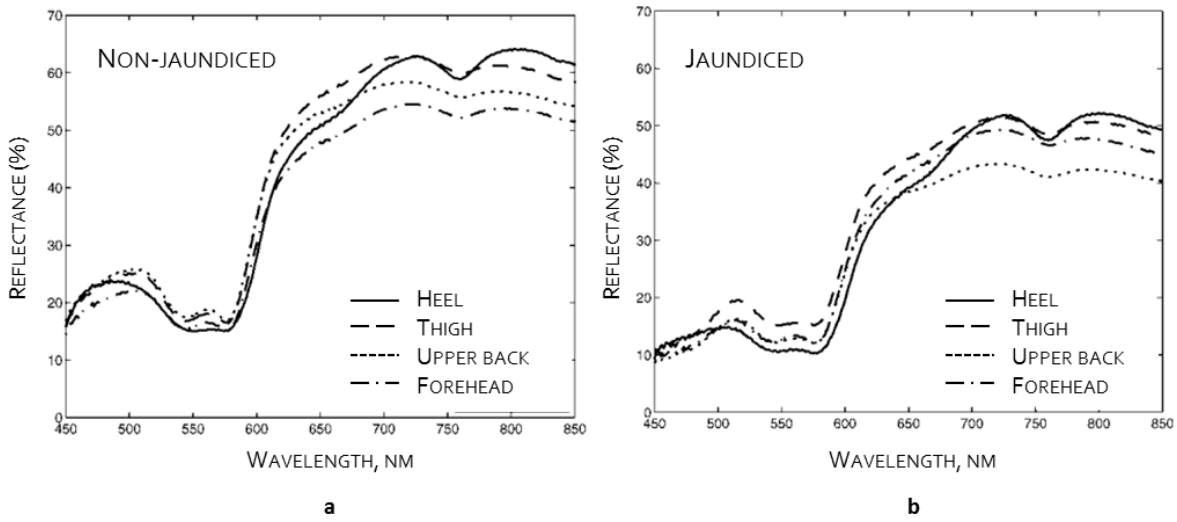

Fig. 13. Reflectance spectrum of nonjaundiced (a) and jaundiced (b) newborn skin [65].

Diffusion model for skin was developed by Svaasand *et. al.* [81] which is based on Boltzmann transport equation. One of the approximate solutions to Boltzmann transport equation when scattering in tissue is much stronger than absorption is the diffusion approximation [45].

Diffusion model has also been used to study possibilities for noninvasive determination of the age of a bruise by analyzing reflectance spectra of bruised and normal skin. A schematic of chemical and physiological processes happening after a trauma to skin surface is presented in Fig. 14a. A bruise is caused by a trauma to skin surface which leads to bleeding from small vessels in tissue. An inflammatory reaction is the primary response from tissue followed by recruitment of neutrophils and macrophages that demolish erythrocytes and free hemoglobin molecules. This causes the heme oxygenase system to break down the hemoglobin and produce hemosiderin and bilirubin which causes bruises to look yellow. Study done by Randeberg *et. al.* consisted of measuring skin thickness and measuring the diffuse skin reflectance of normal and bruised skin. By using a simplified diffuse approximation for blood distribution, transport of hemoglobin in dermis and transport and generation of bilirubin in dermis, normalized average densities of hemoglobin and bilirubin development over time can be acquired (Fig. 14b). By comparing experimentally obtained diffuse reflectance spectrum to the modeled one, it was possible to determine the age of a bruise [67–69].

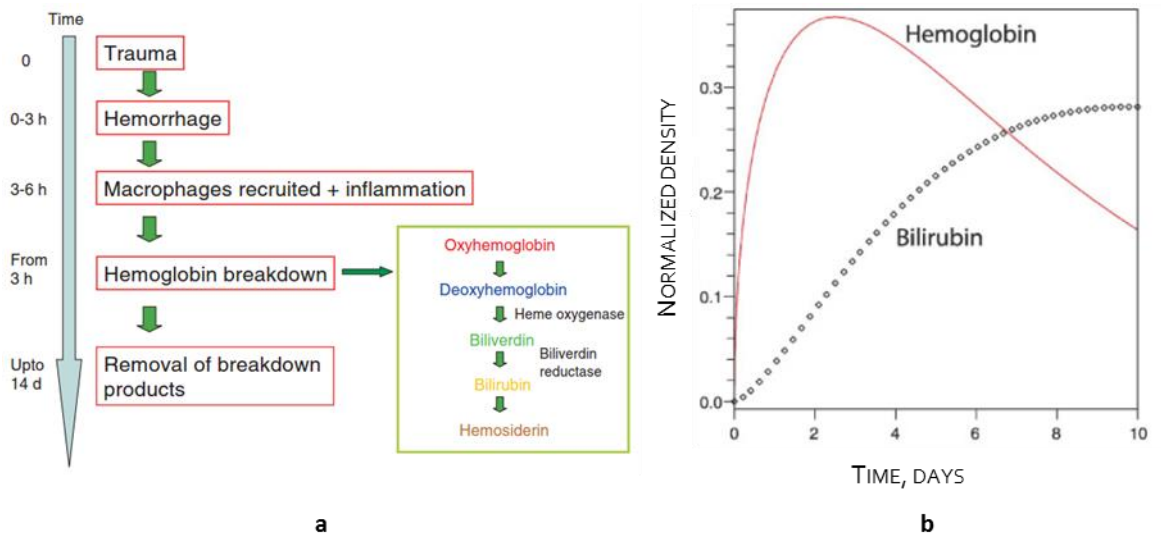

Fig. 14. a) Schematic of chemical/physiological processes of trauma development; b) Modeled bilirubin and hemoglobin normalized density changes over time after the injury [67].

Study on hyperspectral imaging of bruised skin was also done by Randeberg *et. al.* in the spectral range of 400–1000 nm and in the spectral range of 900–1700 nm. The chromophores taken into account were oxy- and deoxyhemoglobin, melanin and also water in the near-infrared spectral range. The melanin index was calculated from the reflectance values at 645 nm, 650 nm, 655 nm, 695 nm, 700 nm and 705 nm. The blood content, represented by erythema index, was calculated from the measured reflectance values at 510 nm, 542 nm, 560 nm, 576 nm and 610 nm. Bilirubin relative concentration was calculated as the gradient of the reflectance spectrum in the spectral region of 460–480 nm where there is a sharp decrease in absorption. The near-infrared hyperspectral images identified wavelengths for separation between bruises and blood vessels: 958 nm and 1584 nm, respectively (Fig. 15) [64].

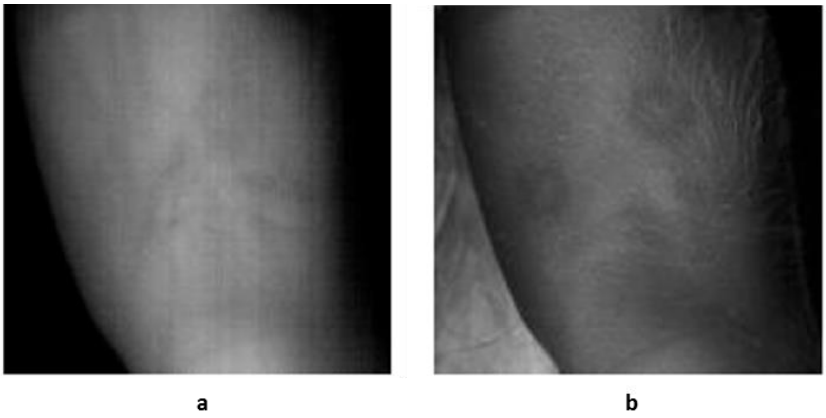

Fig. 15. Near-infrared images of a bruise (66 hours after injury) at 958 nm (a) and 1584 nm (b) [64].

Stam *et. al.* has continued this work even further by expanding the previous one-dimensional analytical diffusion model to a three-dimensional numerical model, including

Michaelis-Menten enzyme kinetics [82] to describe the conversion of hemoglobin to bilirubin, as well as by adding diffusion of both hemoglobin and bilirubin in all directions. A three-layer (top layer of dermis, bottom layer of dermis and subcutaneous layer) skin model consisting of 100x100 compartments was used (Fig. 16). A pool of hemoglobin is located in the subcutaneous layer (Fig. 16b) and converted into bilirubin via Michaelis-Menten kinetics. Both chromophores can flow inside the layers and between the layers. This approach allowed modeling the temporal and spatial changes in hemoglobin and bilirubin concentrations during the development of a bruise (Fig. 17) [73].

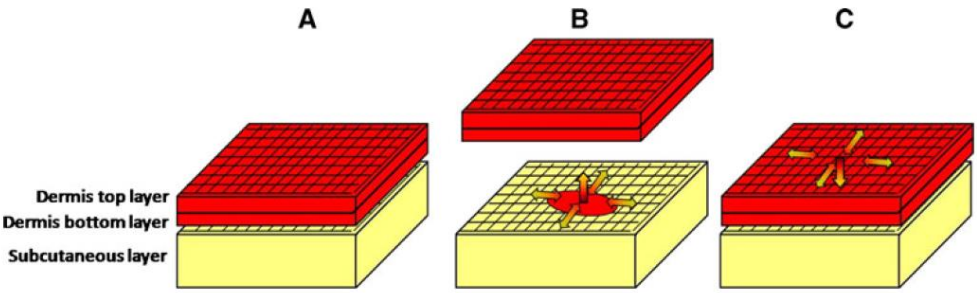

Fig. 16. Skin model consisting of three skin layers and 100x100 compartments [73].

Very important tissue specific input parameters that are crucial for determination of the age of a bruise are: diffusivity of hemoglobin, concentration of the enzyme that converts hemoglobin to bilirubin, and the relaxation time of bilirubin. It was also concluded that these tissue specific parameter values are comparable between bruises measured on the same anatomical position, thus allowing to reduce the measurement frequency needed for determining the age of a bruise [71].

Although several analytical models have been developed for determination of bilirubin relative concentration in skin and determination of the age of a bruise, there is a need for more simple and accessible tools that do not require as much computational power and possibly could be done with a simple RGB camera, for example, a smartphone camera. Also, the methodology for analyzing hyperspectral images of bruises can be further improved.

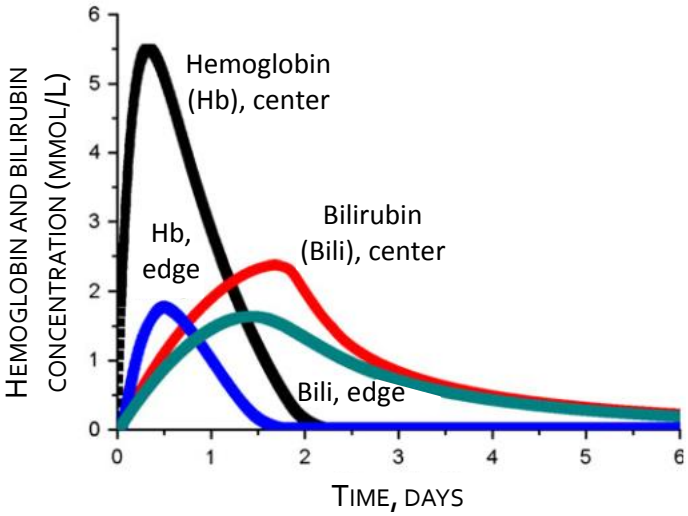

Fig. 17. Modeled kinetics of bilirubin and hemoglobin development over time in the center of a bruise and at the edge (8 mm from center) of a bruise [73].

2.2 BRUISE DEVELOPMENT OVER TIME: HYPERSPECTRAL IMAGING STUDIES

2.2.1 First approach

In this work, study on hemoglobin and bilirubin distribution and concentration changes over time in bruises was initially done by a hyperspectral imaging setup in the spectral range 450–750 nm consisting of a hyperspectral imaging system *CRi Nuance 2.4* [83], self-designed circularly distributed 24 warm-white LED light source, a linear polarizer in front of the light source to eliminate specular reflectance [84] and a PC with *Nuance* software that acquired the Optical Density (*OD*) values by use of a white paper reference to obtain initial light source intensity values $I_0(\lambda)$ (Equation 3) (Fig. 18).

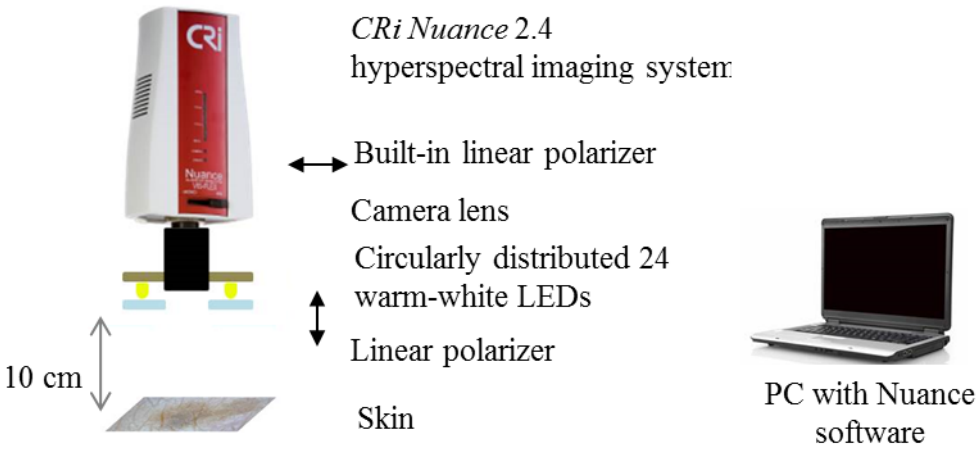

Fig. 18. Experimental setup for hypserspectral imaging of skin.

The chosen skin model considered absorption by four skin chromophores: oxyhemoglobin (OHb), deoxyhemoglobin ($DOHb$), melanin (Mel) and bilirubin ($Bili$):

$$OD_\lambda = \varepsilon_{OHb} \cdot C_{OHb} + \varepsilon_{DOHb} \cdot C_{DOHb} + \varepsilon_{Mel} \cdot C_{Mel} + \varepsilon_{Bili} \cdot C_{Bili} \quad (5)$$

where $C_{OHb}, C_{DOHb}, C_{Mel}$ and C_{Bili} represent relative concentration values of the respective chromophore that are also dependent on the distance that light of a specific wavelength travels in the tissue $C = c \cdot l$. As OD and ε values are wavelength dependent, a system of linear equations has to be solved in order to acquire the relative concentration values which can easily be represented by multiplication of matrices:

$$\begin{pmatrix} \varepsilon_{OH,450} & \varepsilon_{DOH,450} & \varepsilon_{Mel,450} & \varepsilon_{Bil,450} \\ \vdots & \vdots & \vdots & \vdots \\ \varepsilon_{OH,750} & \varepsilon_{DOH,750} & \varepsilon_{Mel,750} & \varepsilon_{Bil,750} \end{pmatrix} \cdot \begin{pmatrix} C_{OH} \\ C_{DOH} \\ C_{Mel} \\ C_{Bil} \end{pmatrix} = \begin{pmatrix} OD_{450} \\ \vdots \\ \vdots \\ OD_{750} \end{pmatrix} \quad (6)$$

Software *Matlab* was used for image processing and analysis, and as a result all four chromophore relative concentrations at each image pixel were obtained, thus producing chromophore relative concentration maps that give a sense of how the chromophores are distributed in a bruise. The relative concentration value was calculated as the average value from a region of interest. This method also allowed obtaining negative concentration values.

Results and discussion

A study of 20 bruises and their development over time (51 measurements in total) was performed in the spectral range 450–750 nm by using an algorithm based on least-squares regression analysis (Eq. 6), and results of relative concentrations of bilirubin in normal skin and bruised skin are summarized in Fig. 19, including comparison between skin types II and III. It is possible to distinguish between normal skin and bruised skin for both skin types, although some relative bilirubin concentration values overlap for skin type II.

An example of a bruise development over time (female, 22 years old, skin type II, bruise on a thigh) is shown in Fig. 20. This was a particularly dark bruise and the main changes are attributed to melanin, although no literature data suggests that melanin should change during the development of a bruise. It can be concluded that this simple approach does not allow mapping of melanin and could possibly influence hemoglobin and bilirubin relative concentration estimations as well.

An improved model needs to be developed that allows a more reliable estimation of bilirubin, hemoglobin and also melanin.

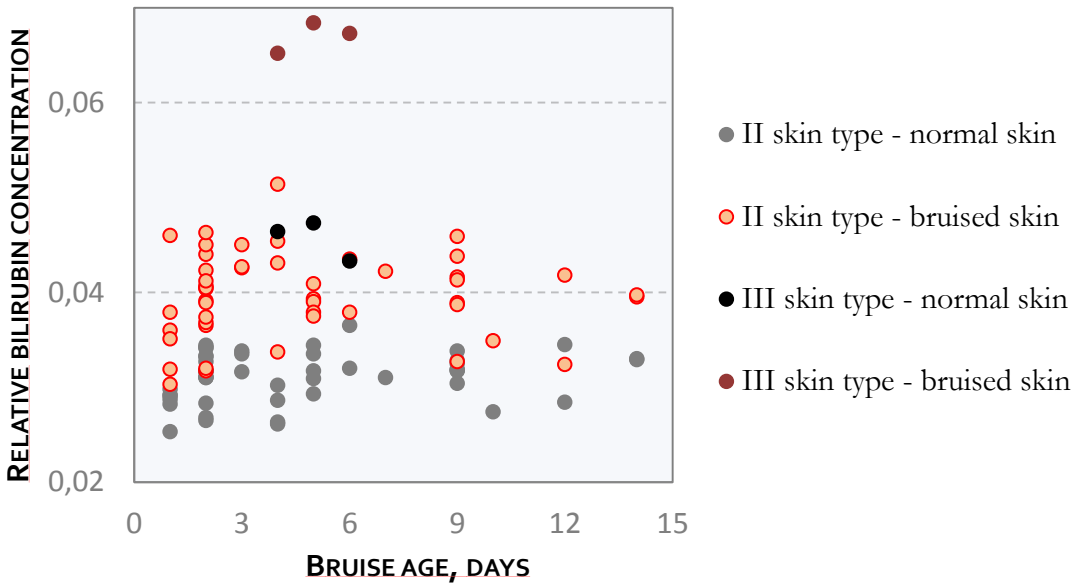

Fig. 19. 51 measurement bilirubin relative concentration values depending on the age of a bruise and skin type (II or III).

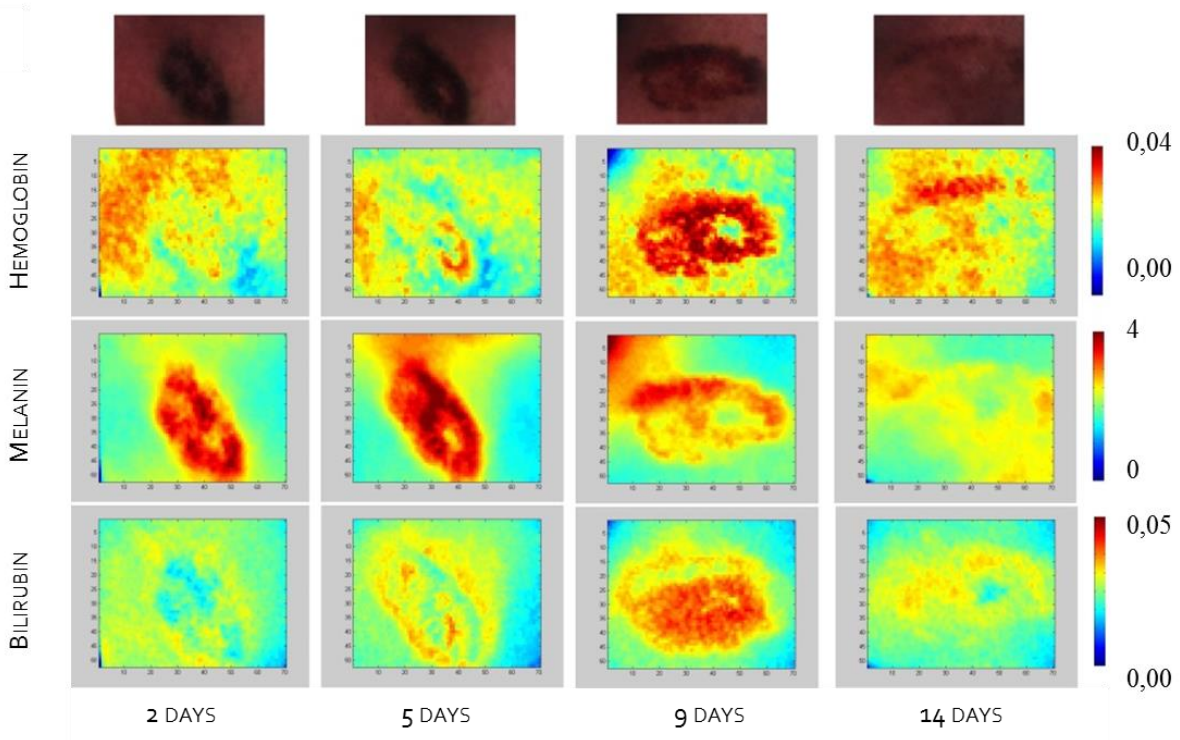

Fig. 20. Example of chromophore relative concentration and distribution maps during bruise development over time.

2.2.2 Advanced approach

Another experimental study on skin bilirubin, hemoglobin and melanin estimation and mapping in bruises was later performed to further develop the previous method. For this study, a similar experimental setup was used as shown in Fig. 18, except the light source was circularly distributed halogen lamps instead of warm-white LEDs. A halogen lamp light source was chosen as it provides a better and more evenly distributed illumination.

A two-step algorithm was proposed for estimation and mapping of skin chromophore relative concentrations. A schematic of the algorithm is shown in Fig. 21. As temporal measurements of the same bruise were taken, at first, image alignment of all temporal images was done by using image registration algorithms. Then, an area of normal skin region was chosen and normal skin OD values were acquired and saved. Afterwards, only the region of a bruise is cropped for further analysis, and algorithm is divided in two parts: for bilirubin estimation and mapping and for oxyhemoglobin, deoxyhemoglobin and melanin estimation and mapping. This is done because both bilirubin and hemoglobin have absorption maxima in the spectral range of 450–500 nm and hemoglobin absorption is almost 10 times higher.

For bilirubin estimation, only spectral images of 450–650 nm (with spectral resolution 10 nm) were used. OD values were first divided by normal skin $OD_{normal\ skin}$ values to reduce hemoglobin and melanin effect in total absorption. A least-squares regression analysis was then performed to calculate relative bilirubin concentration values for each image pixel and a bilirubin relative concentration map was obtained by:

$$OD_\lambda = \varepsilon_{Bili} \cdot C_{Bili} + Offset \tag{7}$$

where $Offset$ is a parameter allowed to change and is not attributed to any chromophore by the algorithm.

The second step of the algorithm was to calculate oxyhemoglobin, deoxyhemoglobin and melanin relative concentration values by using spectral images of 500–700 nm (spectral resolution 10 nm). A least-squares regression analysis was then performed to calculate relative concentrations of these three chromophores for each image pixel by:

$$OD_\lambda = \varepsilon_{OHb} \cdot C_{OHb} + \varepsilon_{DOHb} \cdot C_{DOHb} + \varepsilon_{Mel} \cdot C_{Mel} + Offset \tag{8}$$

After acquiring relative concentration maps of all four chromophores, the mean value of each chromophore at each temporal measurement was calculated to analyze how it changes over time for each bruise.

This method allowed only positive relative concentration values.

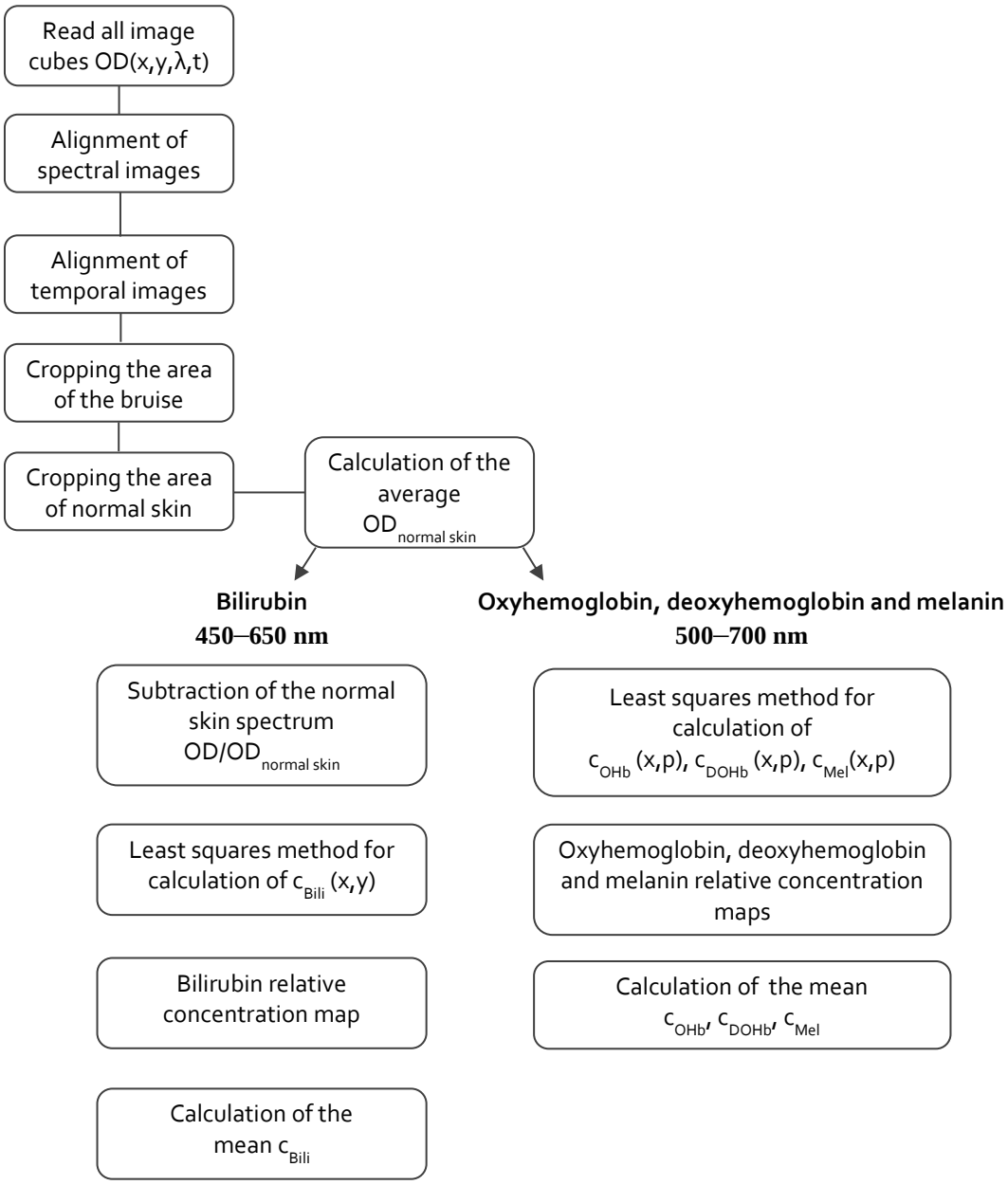

Fig. 21. A schematic of two-step algorithm for estimation and mapping of skin bilirubin, hemoglobin and melanin.

Results and discussion

This algorithm was experimentally tested by analyzing 5 bruise development over time. Bruises were created by a paintball gun (firing speed ~45 m/s, 2 meters between the gun and the skin surface, the bullet was a 3D printed plastic ball 2 cm in diameter). These bruises were created on two female volunteers (female, 25 and 26 years old, skin type II), location on thighs and a hip, by a written consent. Examples of oxyhemoglobin, deoxyhemoglobin and bilirubin relative concentration changes over time for two bruises of a female volunteer (26 years old, skin type II, bruise on a hip (Fig. 22) and on a thigh (Fig. 23)) and for one bruise of a female volunteer (25 years old, skin type II, bruise on a thigh (Fig. 24)) are shown.

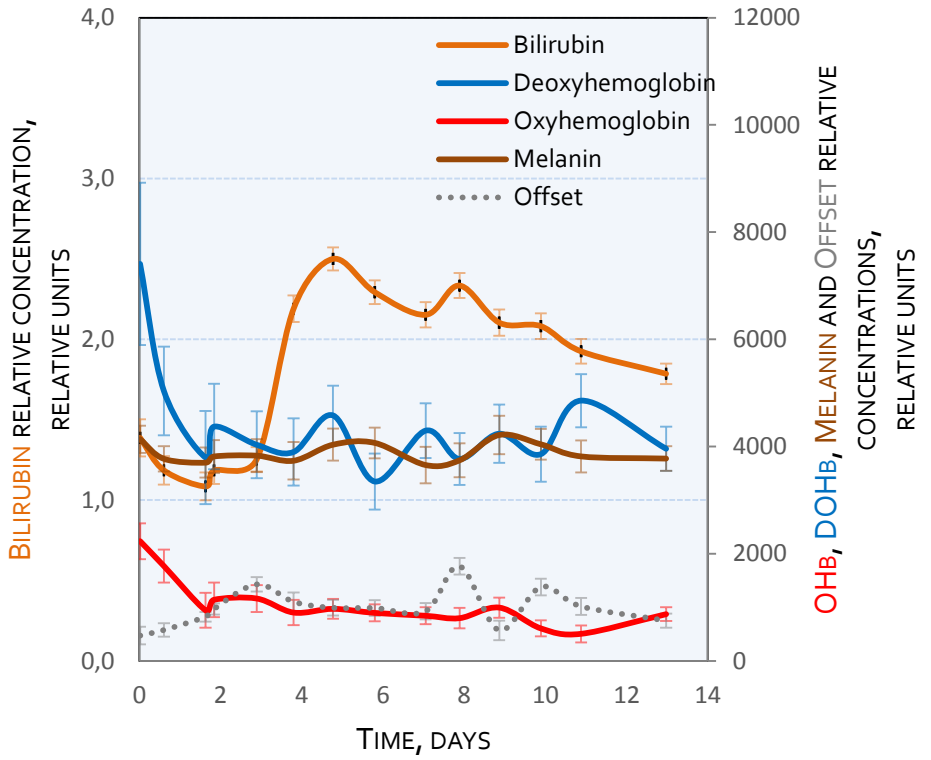

Fig. 22. Chromophore relative concentration changes over time in a bruise (female, 26 years old, skin type II, bruise on a hip).

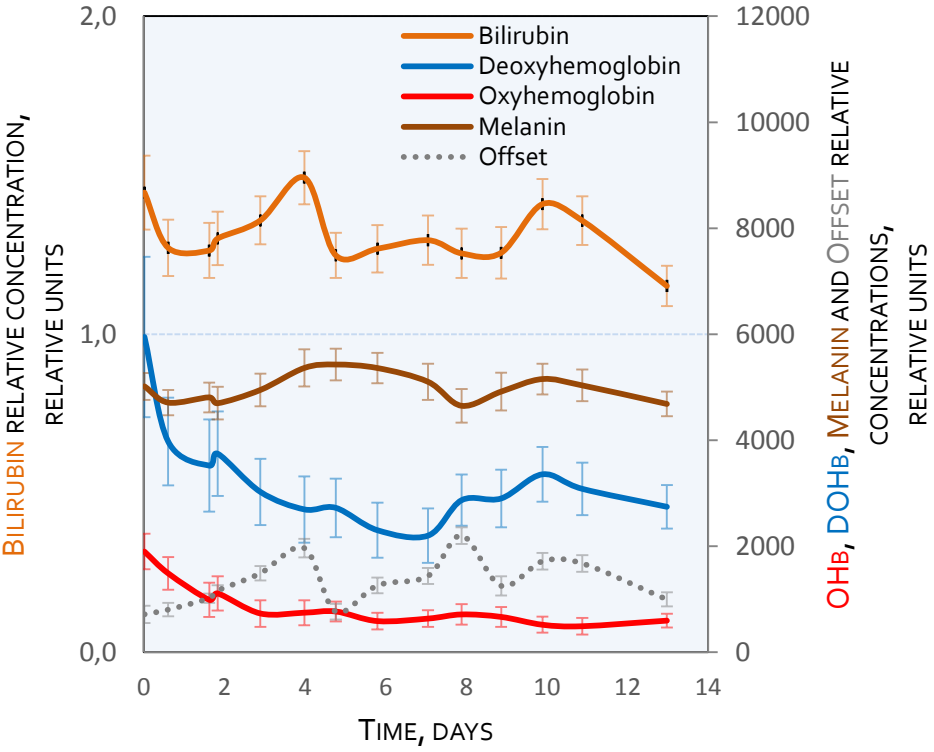

Fig. 23. Chromophore relative concentration changes over time in a bruise (female, 26 years old, skin type II, bruise on a thigh).

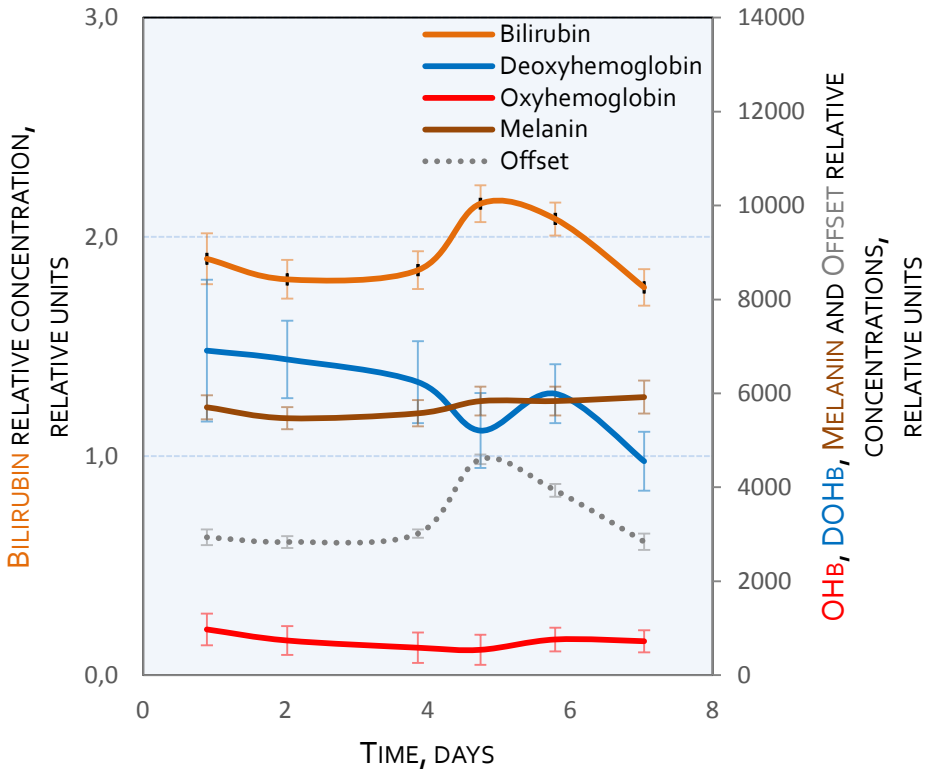

Fig. 24. Chromophore relative concentration changes over time in a bruise (female, 25 years old, skin type II, bruise on a thigh).

The maximum bilirubin concentration during the bruise development for all 5 bruises was reached at day 4–6: for one volunteer at day 4–5 (3 bruises), for the other volunteer at day 5–6 (2 bruises). Both oxyhemoglobin and deoxyhemoglobin relative concentrations decrease during the first days of bruise development as was expected, and melanin concentration stays quite constant throughout the whole measurement time which is an improvement from the first algorithm by which melanin content also changed in bruises over time.

2.3 BRUISE DEVELOPMENT STUDIES BY RGB IMAGING

A simplified approach was tested for skin bilirubin and hemoglobin mapping in bruises by RGB imaging. A self-made RGB imaging device, developed at the Institute of Atomic Physics and spectroscopy, consisted of a CMOS sensor color camera (*iDS UI-1246LE-C-GL*, IDS Imaging Development Systems, Germany, 1.3 megapixel resolution), eight circularly distributed RGB LEDs and two linear polarizers, one in front of the camera and the other one, placed orthogonally to the first one, in front of the light sources to eliminate specular reflection of skin (Fig. 25b) [85]. A spacer was used to keep a constant 3 cm distance between the LEDs and skin area of interest. All LEDs were switched on during the measurement.

Fig. 25a represents that the blue spectral band of the CMOS sensor camera should give information about hemoglobin and bilirubin absorption (besides, hemoglobin absorption in this spectral range is around 10 times higher than that of bilirubin), the green spectral band should contain information about hemoglobin (both oxy- and deoxy-) absorption, and the red spectral band should not contain information about absorption of any of these chromophores. However, these are rough estimations as there is an inter-band cross-talk, for example, the green band could contain some information about bilirubin absorption (the blue band) as well. This effect wasn't calculated but roughly estimated to give relative error less than 10%.

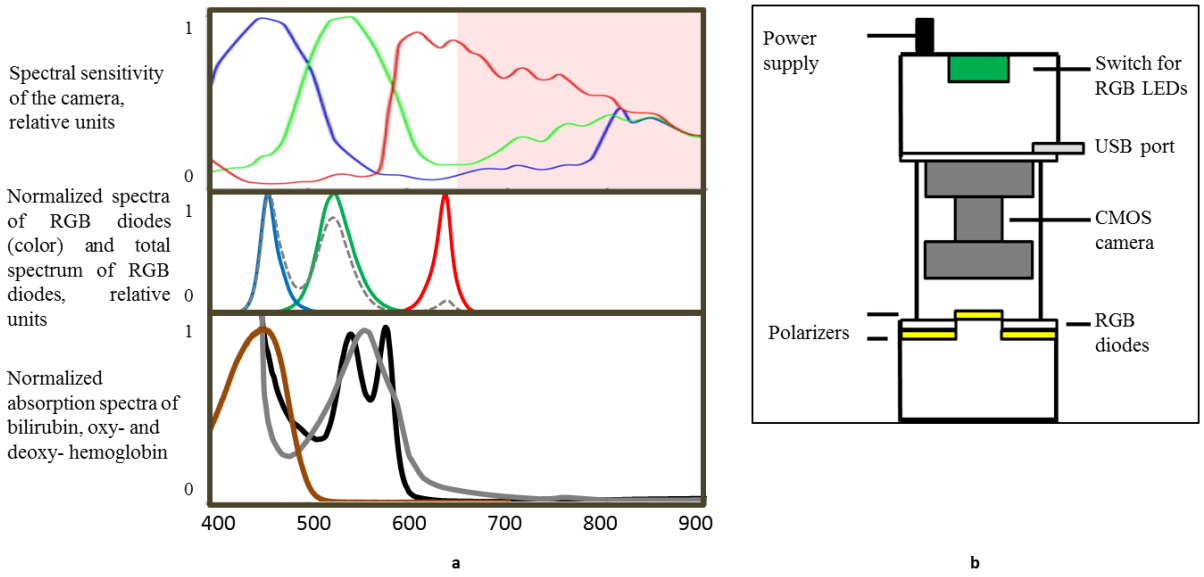

Fig. 25. a) Comparison of spectral sensitivity of the RGB camera (top), spectra of RGB LEDs (middle) and bilirubin and hemoglobin absorption spectra (bottom), b) A schematic of the RGB imaging device.

Each acquired image was separated into three images: reflectance image in the blue band $I(B)$, reflectance image in the green band $I(G)$ and reflectance image in the red band $I(R)$. Hemoglobin relative concentration can be approximated as absorption difference ΔOD between green and red spectral bands and OD can be expressed by Eq. 3 as:

$$c_{Hb} = OD(G) - OD(R) = ln\frac{I_0(G)}{I(G)} - ln\frac{I_0(R)}{I(R)} \approx \frac{I(R)}{I(G)} \quad (9)$$

The constant $ln\frac{I_0(G)}{I_0(R)}$ and natural logarithm can be neglected as only relative hemoglobin concentration values are further analyzed. The approximately equal sign in Eq. 9 is used to show that the important parameter here is the relation between the two signals. In this study, only the relation (not the logarithm of the relation) was further used, as only relative parameter values are observed.

Similarly, hemoglobin and bilirubin (Fig. 25a) relative concentration can be expressed by comparing absorption difference ΔOD between blue and red spectral bands and using similar assumptions as previously:

$$c_{Hb+Bili} = OD(B) - OD(R) \approx \frac{I(R)}{I(B)} \tag{10}$$

To estimate relative bilirubin concentration, Eq. 9 can be subtracted from Eq. 10:

$$c_{Bili} = c_{Hb+Bili} - c_{Hb} \tag{11}$$

By using Eq. 9 and Eq. 11 on each pixel of the image, relative bilirubin and hemoglobin concentration maps can be created. To quantitatively compare how bilirubin and hemoglobin relative concentrations change over time in bruises, threshold concentration values were empirically chosen ($c_{Bili\_Thr} = 0.75$ [relative units] and ($c_{Hb\_Thr} = 0.15$ [relative units]). A new hemoglobin p_{Hb} and bilirubin parameter p_{Bili} was proposed and expressed as the count of pixels of the respective relative concentration map (of either bilirubin or hemoglobin) that have higher or the same relative concentration value than the respective (hemoglobin or bilirubin) threshold value.

Results and discussion

Experimental results show that the simple methodology for mapping of bilirubin and hemoglobin by RGB imaging can be used to monitor development of both chromophores over time. An example is shown in Fig. 26.

Experimental study on 22 bruises of 17 volunteers was performed, and a histogram of the days of the maximum bilirubin parameter value is shown in Fig. 27. The maximum bilirubin parameter value is mostly during days 3 to 7 and some during days 10 to 12.

RGB imaging technique adequately represents bruise development over time and is a cheaper and simpler alternative to hyperspectral imaging.

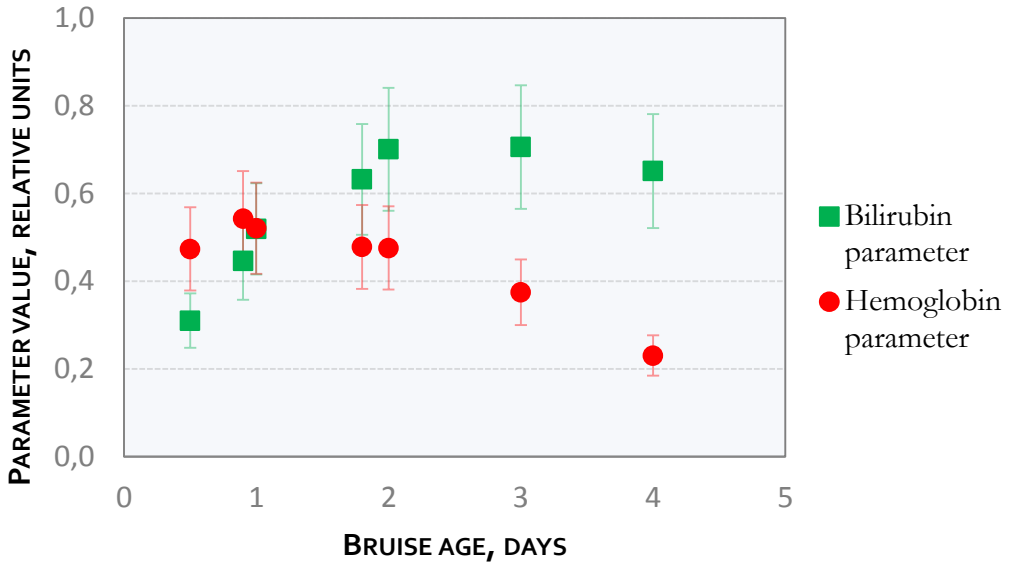

Fig. 26. Example of bilirubin and hemoglobin parameter changes over time in a bruise.

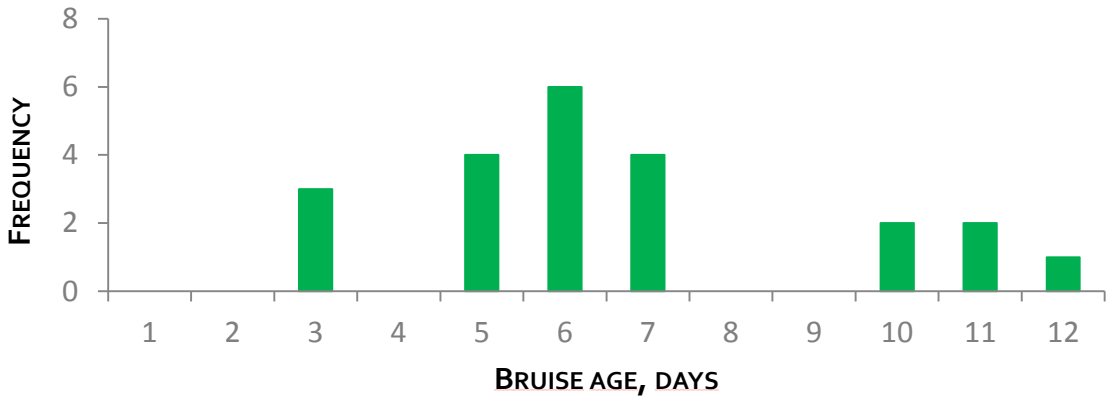

Fig. 27. Histogram of the days of the maximum bilirubin parameter value of all 22 bruises.

2.4 MIMICKING OF CHROMOPHORE ABSORPTION IN SKIN PHANTOMS

To better understand what information can be obtained during reflectance spectroscopy and imaging measurements of skin, a study on skin phantoms was performed. The purpose of including skin phantom studies is to explore a way for possibilities to obtain absolute chromophore concentration values rather than relative, although this study is just a beginning.

Experimental setup comprising hyperspectral imaging system *CRi Nuance 2.4*, circularly distributed halogen lamp light source, a linear polarizer in front of the light source and a PC was used for measurements in order to acquire image cubes with OD values. The distance between the sample and the camera was 17 cm. *Nuance* software tool *Spectral*

Library was used to acquire the average absorption (OD value) spectrum from a region of interest of the sample.

The scattering medium of the phantoms was fibrin matrix which is a protein involved in the clotting of blood (fibrin matrices are used in surgical procedures to prevent blood loss). Fibrin matrix can be prepared by mixing 0.47 ml blood plasma (47% of the solution), 0.4 ml 0.9% sodium chloride (40% of the solution), 0.8 µl tranexamic acid (0.8 mg/ml), and 89.4 µl calcium gluconate (8.94 mg/ml). To polymerize the solution, it was held in a cell incubator (temperature 37°C, CO_2 concentration 5%) for one hour. To mimic skin hemoglobin, bilirubin and melanin, absorbers of different concentrations and at different depths from the surface were added: red blood cells (concentrations 0.2 to 42.4 mg/ml), synthesized bilirubin (concentrations 0.01 to 2.00 mg/ml) and nigrosin (concentrations 1.5 to 312.8 µg/ml).

Skin phantoms were developed as layered structures: bottom layer with fibrin matrix (volume 0.3 ml, corresponding thickness 0.16 cm), middle part with the absorbing molecules, and upper layer with fibrin matrix (volume 0.3 ml, corresponding thickness 0.16 cm) for different concentration measurements. For different depth measurements, the upper fibrin matrix layer ranged from 0.05 cm to 0.64 cm. In total, 24 different concentration measurements were done for each absorber (Fig. 28) and 12 different depth measurements were done for each absorber.

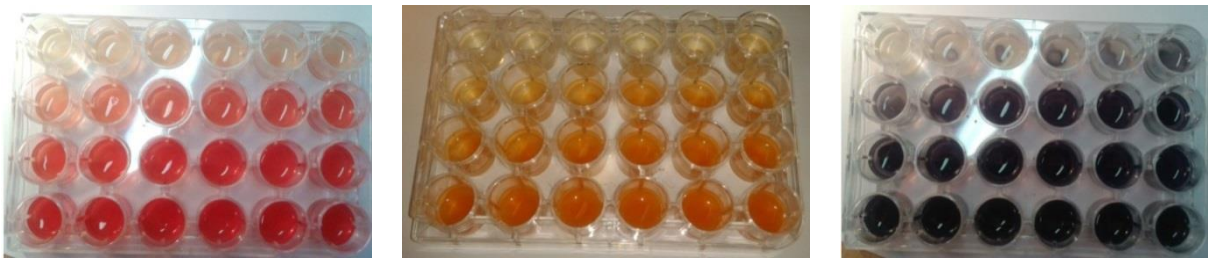

a b c

Fig. 28. Developed phantoms with different concentrations of red blood cells (a), synthesized bilirubin (b) and nigrosin (c).

Results and discussion

With the developed phantom, it was possible to mimic the diffuse reflectance spectrum of skin. Absorption spectra of the fibrin matrix phantom and all three absorbers mimicking skin hemoglobin, bilirubin and melanin are shown in Fig. 29. To analyze how the concentration (Fig. 30) and depth (Fig. 31) of the absorbing substance change the absorption of the phantom, the maximum absorption value in the spectral range 450–950 nm was taken:

for the erythrocyte phantom, at 550 nm, for the synthesized bilirubin phantom, at 470 nm, and for the nigrosin phantom at 450 nm.

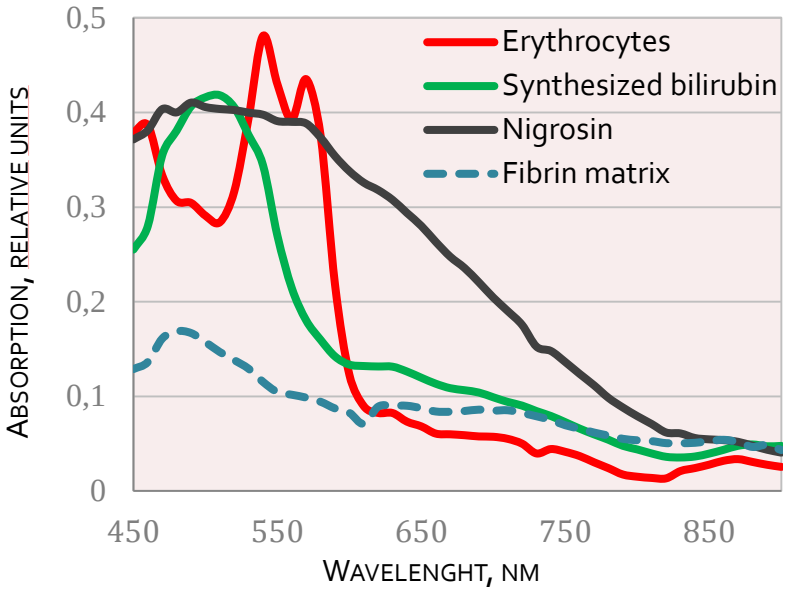

Fig. 29. Absorption spectra of the skin mimicking fibrin matrix phantom and three substances mimicking skin hemoglobin, bilirubin and melanin.

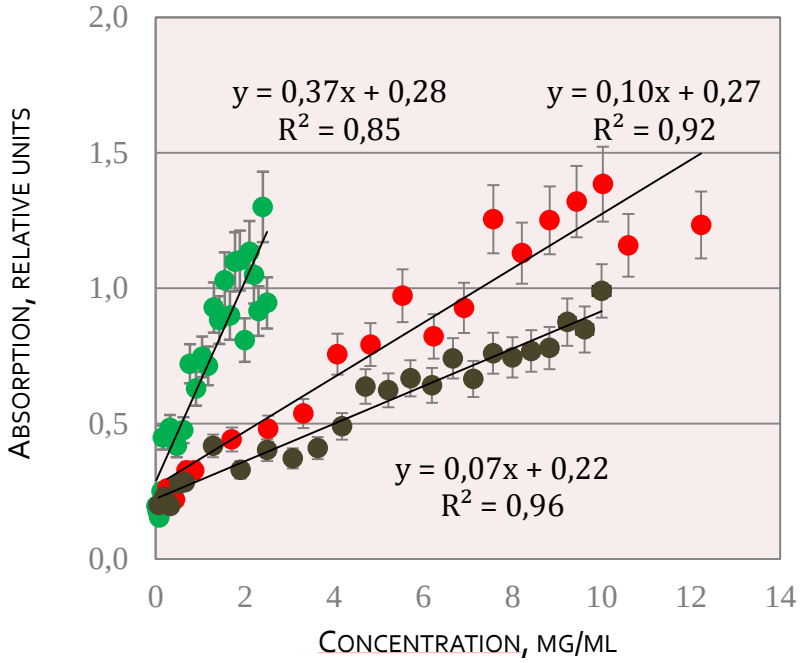

Fig. 30. Absorption dependence on the concentration of the skin chromophore mimicking substances: synthesized bilirubin (green dots), erythrocytes (red dots) and nigrosin (dark dots).

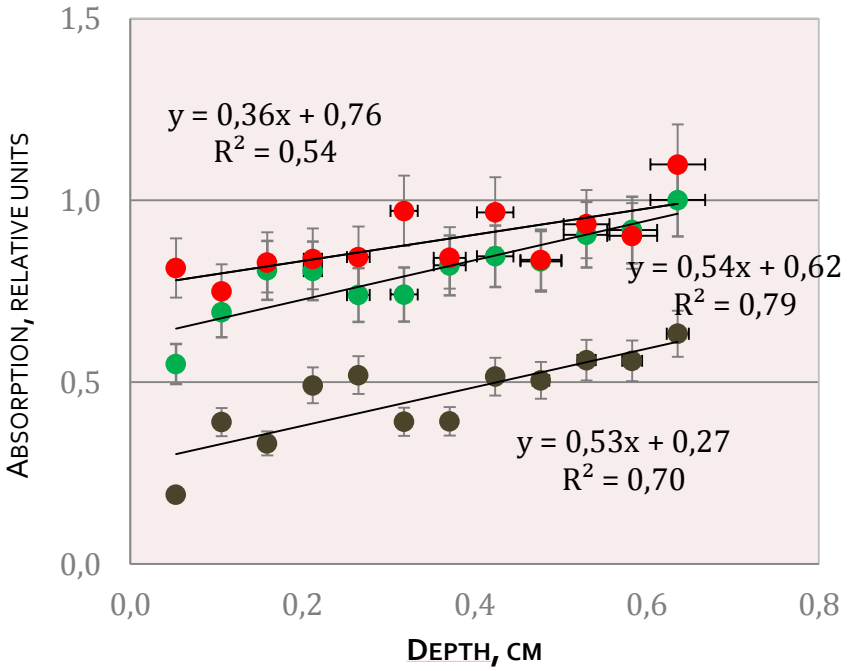

Fig. 31. Absorption dependence on the depth of the skin chromophore mimicking substances: synthesized bilirubin (green dots), erythrocytes (red dots) and nigrosine (dark dots).

As can be seen in Fig. 30, absorption and concentration dependence can be approximated by a linear function for all three phantoms, and for each of the phantoms the dependence is different: absorption increases the most rapidly by increase in concentration for synthesized bilirubin, more slowly for erythrocytes and even more slowly for nigrosin. As can be seen in Fig. 31, absorption dependence on the depth of the substance can also be approximated by a linear function, and for all three phantoms the fashion by which absorption increases with increased depth is similar.

Generally, much more data are needed for possibilities to estimate absolute or close to absolute values of chromophore concentration in skin. However, these results give a sense of how different chromophores in a different manner influence the absorption spectrum of the phantom.

2.5 PARALLEL DIFFUSE REFLECTANCE AND FLUORESCENCE MEASUREMENTS OF SKIN LESIONS

Hyperspectral imaging setup consisting of hyperspectral imaging system *CRi's Nuance 2.4*, light source of LED ring light, diffuser in front of the light source, as well as a computer with *Nuance* software was used for image acquisition in the spectral range of 450–950 nm. The light source was developed as a ring light consisting of LEDs to cover the

spectral range of 450–950 nm for diffuse reflectance mode: warm white, 770 nm, 830 nm and 890 nm. Spectra of used LEDs are shown in Fig. 32. Diffuser in front of the light source was used to achieve a uniform illumination of the skin area of interest.

The light source comprised an inner circle of violet (405 nm) illumination LEDs for skin autofluorescence excitation imaging. No diffuser was used in front of ultraviolet LEDs.

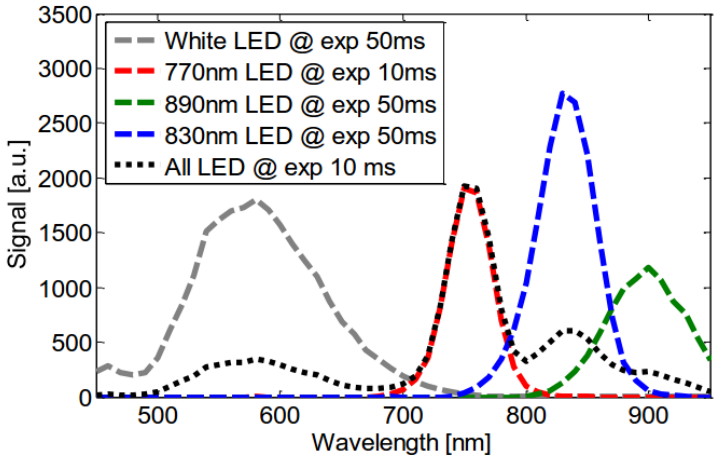

Fig. 32. Spectra of illumination LEDs for diffuse reflectance mode at different exposure times.

For diffuse reflectance imaging mode, various exposure times (from 7…500 ms) were used for each wavelength in the spectral range of 450–950 nm due to spectrally different illumination intensity and system sensitivity. Images were acquired with a spectral step of 10 nm at wavelengths in the spectral range of 450–950 nm. Maximum pixel resolution was used.

For fluorescence mode, a constant exposure time of 200 ms was used to acquire images in the spectral range of 450–950 nm with a spectral step of 10 nm. Reduced pixel resolution was used by combining 4 pixels in 1 pixel.

As the image acquisition process took approximately 30–40 seconds for diffuse reflectance mode and 20–30 seconds for fluorescence mode, motion artefacts are unavoidable. Thus, image registration was performed for each image cube. Simple stickers were applied to the skin area around the lesion in order to improve the image registration performance. Image segmentation was used to distinguish the lesion from normal skin. For diffuse reflectance imaging mode OD values were obtained. For fluorescence mode, reflectance values were obtained.

Image segmentation was done to separate normal skin and lesion regions for both modalities (diffuse reflectance and fluorescence). Afterwards, the average optical density value at each wavelength of all segmented area pixels (for each segment separately) was

calculated to estimate the average absorption (optical density) spectrum of the segmented area. The same was done for fluorescence modality – the average reflected intensity spectrum was estimated.

To see possibilities for distinguishing between atypical and benign nevi by both modalities, variation (standard deviation) of optical density values at each wavelength was calculated for diffuse reflectance images and also variation of fluorescence intensity values at each wavelength was calculated in case of fluorescence images. A t-test (*Matlab* built-in function *ttest2*) was then performed to analyze if there is a statistical difference between benign nevi and atypical nevi for each of the modalities separately.

A pilot study was performed on 75 volunteers with 90 pigmented lesions in total. Two dermatologists were involved to determine whether the lesion is benign nevus or atypical that could potentially become malignant.

Although this study mainly focused on nevi, results on vascular lesions (e.g. hemangioma) in comparison with pigmented ones are of interest in frame of this thesis.

Results and discussion

An example of a hemangioma and a benign nevus is shown in Fig. 33. Comparison of the average optical density values (by diffuse reflectance mode) of normal skin, nevus and hemangioma is shown in the graph above and comparison of the average autofluorescence intensity values (by fluorescence mode) of normal skin, nevus and hemangioma is shown in the graph below.

When looking at diffuse reflectance spectra of hemangioma and benign nevus (Fig. 33), it is easy to see that the average spectrum of hemangioma shows the characteristic absorption maxima of hemoglobin at around 540 nm and 580 nm, comparing to the average reflectance spectrum of benign nevus and normal skin. When looking at autofluorescence spectra of all three different regions, normal skin has the highest autofluorescence intensity values, compared to nevus and hemangioma. Very low fluorescence intensity values in the spectral range 450–600 nm could be related to high hemoglobin absorption in this spectral range in case of hemangioma.

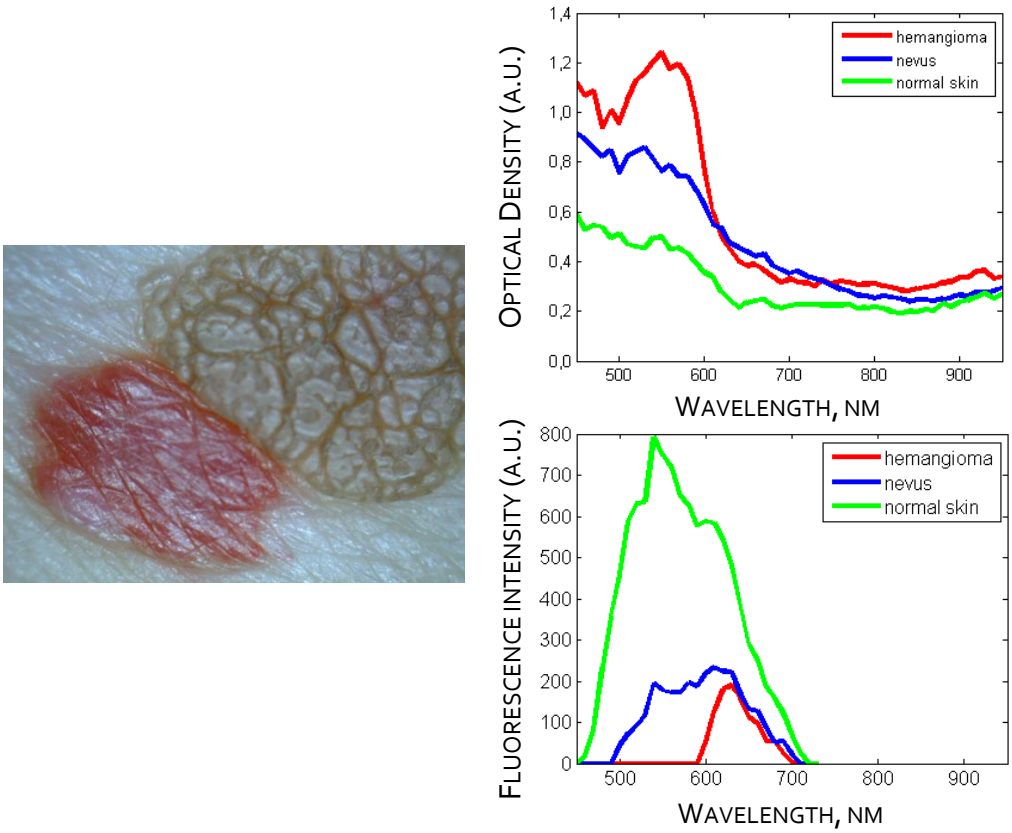

Fig. 33. RGB image of hemangioma and benign nevus (to the left) and comparison of the average optical density values by diffuse reflectance mode (on top) and the average fluorescence intensity valudes by fluorescence mode (on bottom) of normal skin, hemangioma and benign nevus.

For the current study, 47 pigmented lesions, 26 atypical and 21 benign nevi, were further analyzed. For diffuse reflectance modality, an example of optical density values of benign and atypical nevi at each wavelength is shown (Fig. 34a) and an example of optical density variation (standard deviation) values of benign and atypical nevi at each wavelength is shown (Fig. 34b).

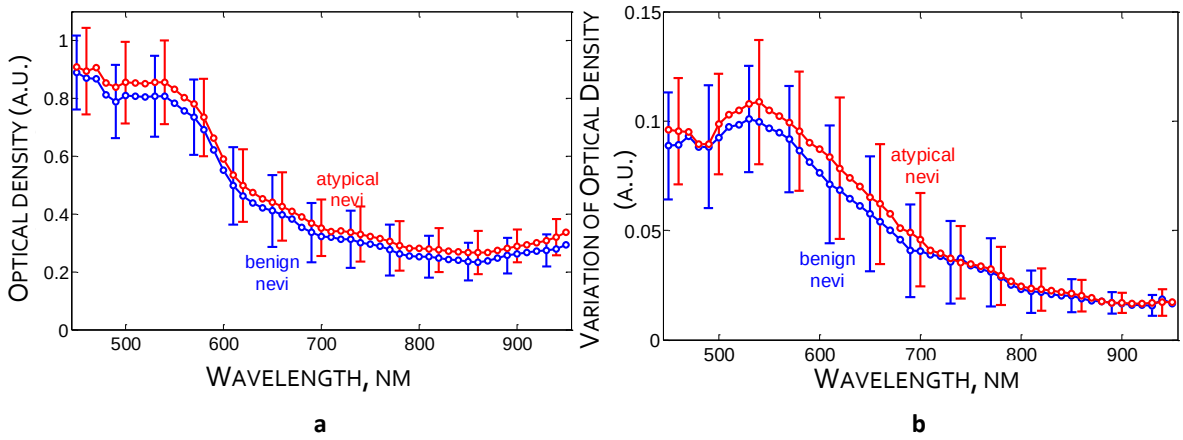

Fig. 34. Optical density (a) and variation of optical density (b) spectra comparison between benign and atypical nevi for diffuse reflectance modality.

For fluorescence modality, an example of fluorescence intensity values of benign and atypical nevi at each wavelength is shown (Fig. 35a) and an example of fluorescence intensity variation (standard deviation) values of benign and atypical nevi at each wavelength is shown (Fig. 35b).

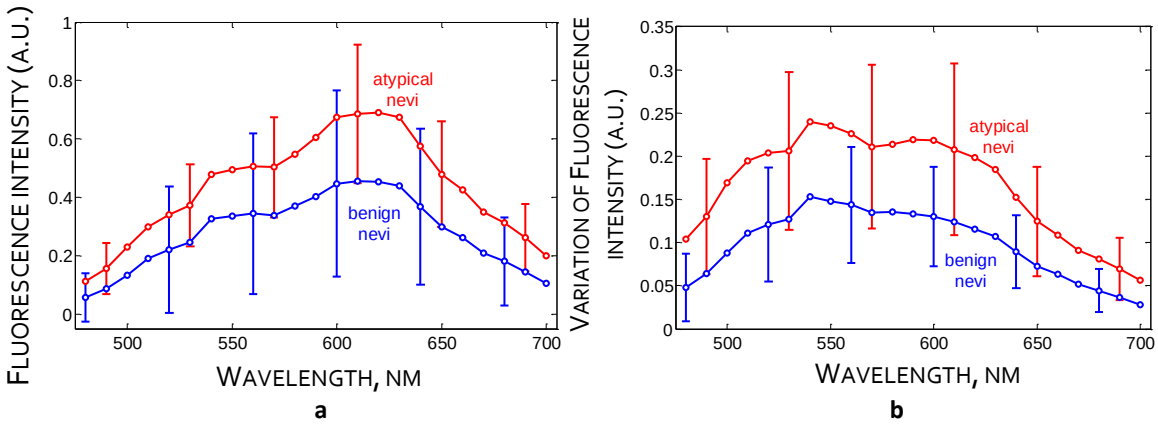

Fig. 35. Fluorescence intensity (a) and variation of fluorescence intensity (b) spectra comparison between benign and atypical nevi for fluorescence modality.

By doing a t-test for possibilities to distinguish between benign and atypical nevi, it was concluded that it is not possible to find statistical significance between both lesion types for diffuse reflectance modality; however, it was possible to find statistical significance between both lesion types for fluorescence modality. By plotting a correlation graph of variation of fluorescence intensity and fluorescence intensity (Fig. 36), it is possible to see some distinguishability between both lesion types.

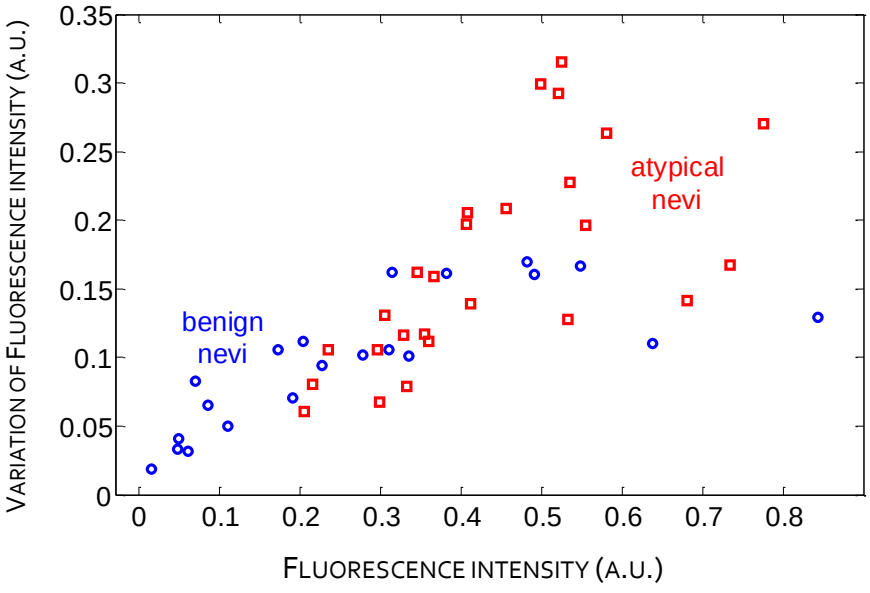

Fig. 36. Correlation graph of variation of fluorescence intensity and fluorescence intensity values for 47 pigmented lesions.

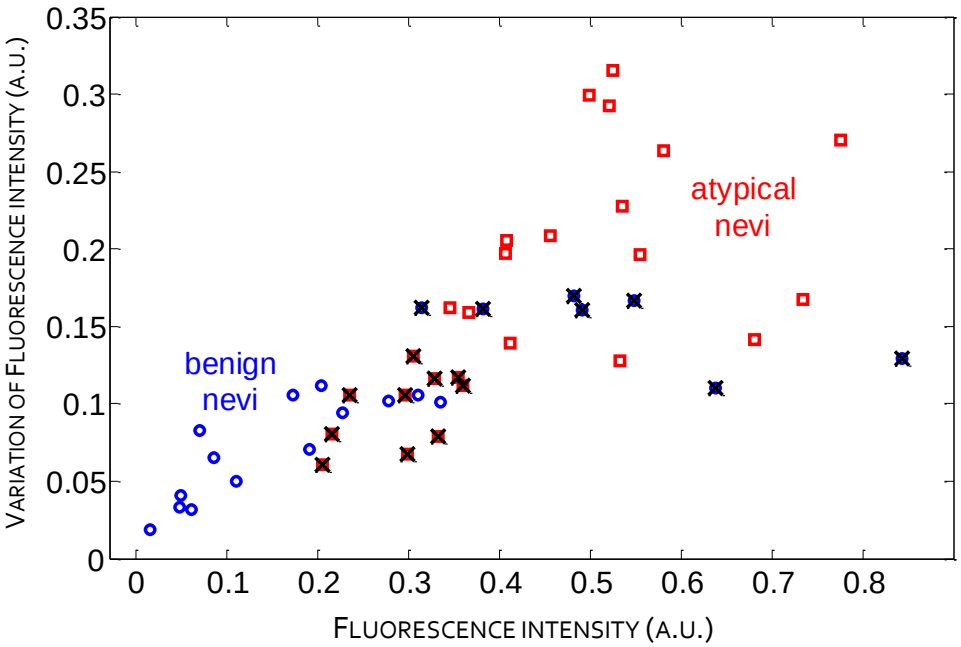

Fig. 37. Correlation graph of variation of fluorescence intensity and fluorescence intensity values for 47 pigmented lesions.

If not taking into account some of the results that are possibly incorrectly classified (Fig. 37), it was possible to achieve 62% sensitivity and 67% specificity for classification between both lesion types.

Fluorescence modality shows a potential in distinguishing between benign and atypical nevi, although more data and statistical analysis is needed. Diffuse reflectance modality does not show significant difference between both lesions; that might also be due to the fact that for this experimental setup polarizers were not used to eliminate the specular reflection of skin and also due to patient's movement artefacts that did not allow to perfectly align spectral images of the same measurement even with image registration algorithms.

CHAPTER 3

RGB IMAGING FOR ESTIMATION OF SKIN ERYTHEMA

This chapter describes a study done in collaboration with dermatologists in order to find better and more reliable ways to estimate erythema severity for *rosacea* patients. RGB imaging method was used to test its possible applications for erythema index estimation. The results were also compared to the visual assessment of three dermatologists and to the results acquired by a commercial point-measurement device *Mexameter*.

The first part of this chapter gives a short introduction on skin erythema and *rosacea*, as well as an overview of different erythema index estimation algorithms already used and available in literature.

In the second part of this chapter, new erythema index estimation is proposed and experimentally tested.

The third part of this chapter describes the clinical study and results.

Results of this study are published in paper X, submitted to be published in paper VIII and presented at the conferences C1, C3, C4 and C9.

3.1 LITERATURE OVERVIEW

Rosacea is a chronic inflammatory skin disease that involves flushing, transient or persistent erythema, visible blood vessels (*telangiectasias*), as well as papules and pustules on central convexities of the facial skin (cheeks, chin, nose, and central forehead) [86]. These are considered the primary features of *rosacea*. It is one of the most common conditions that dermatologists treat with a prevalence of 2–22% in Europe [87]. Pathophysiology of *rosacea* is not fully understood and involves dysregulation of several systems, including innate immunity and neurovascular mechanisms, and the cause of *rosacea* is still being discussed [88, 89]. Its severity is usually determined clinically by visual assessment of primary features of *rosacea*, including erythema. Recently, a reliable Clinician's Erythema Assessment (CEA) grading scale has been introduced that ranges from 0 (clear skin, no erythema) to 4 (severe erythema) [90]. Other methods include spectroscopic devices (e.g., *Mexameter*®,

Chromameter®, *DermaSpectrometer*®), computer analysis of a digital photograph, lesion counts of papules and pustules, assessment of secondary signs and symptoms (burning, stinging, itching), and other [88].

Spectroscopic techniques for erythema assessment are mainly based on comparison of diffuse reflected intensities at different spectral bands – mostly green and red, due to high hemoglobin absorption in the green spectral region and very low absorption in the red (Fig. 8). Erythema index can then be calculated as:

$$EI_{RG} = log\frac{I(R)}{I(G)} \approx \frac{I(R)}{I(G)} \tag{12}$$

where $I(R)$ is reflected intensity of the red light and $I(G)$ is the reflected intensity of the green light [91]. For RGB imaging purposes, logarithm in the formula can be neglected, as only relative values are further used. Although there is even higher hemoglobin absorption in the blue spectral region, it is not commonly used due to lower mean penetration depth in skin (less than 300 μm compared to approximately 500-700 μm for the green light) [6].

Several studies use the spectral imaging for erythema index estimation. Polarization multispectral dermoscope has been developed for *in vivo* imaging of skin lesions by using linearly polarized illumination at wavelengths of 470 nm, 530 nm and 625 nm. Blood contrast parameter was calculated as the difference in green and red polarized light illumination images:

$$EI_{BC} = \frac{Green90 - Red90}{Green90 + Red90} = \frac{I(G) - I(R)}{I(G) + I(R)} \tag{13}$$

where $Green90$ and $Red90$ are images at polarized green and red, respectively, illumination [92].

Noncontact monitoring of vascular lesion phototherapy efficiency has been demonstrated by an experimental RGB imaging system, and melanin-corrected erythema index was calculated as

$$EI_{BRG} = OD(G) - \frac{OD(B) + OD(R)}{2} \approx \frac{\sqrt{I(B) \cdot I(R)}}{I(G)} \tag{14}$$

where $OD(R)$, $OD(G)$ and $OD(B)$ are optical density values representing absorption at the red, green and blue spectral channels and are expressed by Eq. 3, and $I(R)$, $I(G)$ and $I(B)$ are the reflected intensity values as detected in the red, green and blue spectral channels of image sensor. A new parameter representing the contrast of erythema index (CEI) has been introduced as a measure of erythema index deviation throughout the image area:

$$CEI = \frac{EI_{std}}{EI_{mean}} \tag{15}$$

where EI_{std} is the standard deviation of erythema index and EI_{mean} is the mean value of EI at the region of interest [93].

Most devices for erythema estimation use point measurement systems, acquiring reflected intensity value from a small skin spot of some millimeters in diameter. In particular, *Mexameter*® is a commercially available device that comprises 16 circularly arranged LEDs emitting at wavelengths 568 nm, 660 nm and 880 nm, and a photodetector that measures intensity of the light reflected by skin area of 5 mm in diameter. Erythema index is calculated from reflected light intensities at 568 nm and 660 nm, based on Eq. 12. Other commonly used devices are *Chromameter*® and *DermaSpectrometer*® [88, 94].

Point-measurement devices may not be reliable in some cases, for example, when the chosen measurement point is a blood capillary that leads to a much more increased erythema index value than the rest of the skin region of interest. Thus, the development of a more reliable technique and methodology would be important.

3.2 METHODOLOGY AND A NEW ERYTHEMA INDEX ESTIMATION

The experimental RGB imaging prototype, developed at the Biophotonics laboratory, Institute of Atomic Physics and Spectroscopy, with provisional brand name *SkImager* is a handheld wireless, battery-powered device that comprises a 3 Mpix CMOS sensor color camera (*Micron* MT9T031, quantum efficiency shown in Fig. 38a) [95] surrounded by a ring-shaped LED illuminator emitting white, blue (460 nm), green (530 nm) and red (665 nm) spectral bands (Fig. 38b), linear polarizers in front of the LEDs and the camera, oriented orthogonally to each other (in order to suppress the specular reflection [96]), an on-chip microcomputer, a touchscreen and an SD memory card [97]. A changeable nozzle keeps the distance between skin surface and the detector constant at 50 mm, as well as eliminates outside light to reach the detector. Skin area of 30 mm in diameter can be evaluated. Illumination LEDs are evenly distributed in a circle (four LEDs of each type: white, red, green, blue), and each type of LEDs is sequentially switched on for approximately 1 second while an RGB image is taken, thus the total measurement time is approximately 5 seconds.

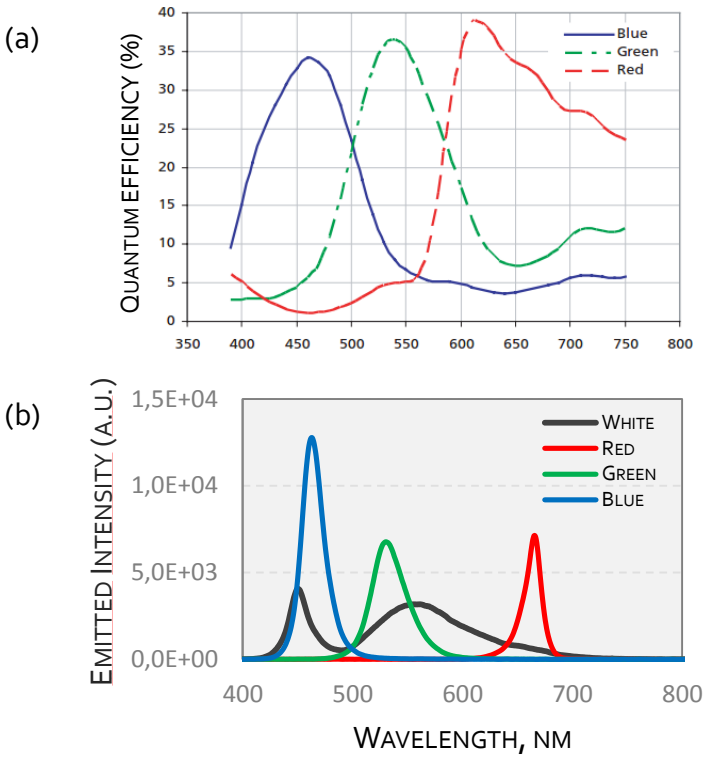

Fig. 38. a) Quantum efficiency of the CMOS sensor used in *SkImager* [95] and b) Spectra of *SkImager* LEDs.

SkImager acquires three spectral images (red, green, and blue) at each illumination (white, red, green, and blue). Each spectral image represents three roughly separated spectral regions: 600–700 nm (red), 500–600 nm (green), and 400–500 nm (blue) (Fig. 38a) [95]. Only one spectral image for each illumination was further used (red spectral image for red illumination, green spectral image for green illumination, and blue spectral image for blue illumination), as there is a much lower signal in the other spectral bands that do not provide much information about absorption in the particular wavelength range. Thus three separate images for each measurement are further used, and each pixel has a reflected intensity value at red, green and blue illumination: $I_i(R)$, $I_i(G)$ and $I_i(B)$, respectively.

For erythema severity estimation, a new erythema index parameter was introduced. Hemoglobin absorption can be related to difference between the red and the green spectral images [91]; however, melanin absorption in the upper skin layers should also be considered [85, 93]. The melanin-corrected erythema index EI_{BRG} (Eq. 14) considers that all three spectral images are used. A new empirical erythema index estimation method with using only two adjacent spectral band images is introduced. The erythema index can be estimated as absorption in green spectral band, melanin absorption can be estimated as difference in absorption between blue and green spectral bands, and thus melanin-corrected erythema index can then be estimated as:

$$\mathrm{EI_{BG}} = \mathrm{OD(G)} - [\mathrm{OD(B)} - \mathrm{OD(G)}] \tag{16}$$

By using Eq. 3, Eq. 16 can then be expressed by using reflected light intensities as:

$$\mathrm{EI_{BG}} = \log\left[\frac{[I_0(G)]^2}{I_0(B)} \cdot \frac{I(B)}{[I(G)]^2}\right] \approx \frac{I(B)}{[I(G)]^2} \tag{17}$$

as the first multiplier in the formula is a constant for all measurements. The approximately equal sign in Eq. 17 is used to show that the important parameter here is the relation between the two signals. In this study, only the relation (not the logarithm of the relation) was further used, as only relative parameter values are observed. Further a multiplier of 100 is used for better data representation:

$$\mathrm{EI_{BG}} = 100 \cdot \frac{I(B)}{[I(G)]^2} \tag{18}$$

Erythema index for each measurement is calculated as the mean erythema index value of all pixels of the skin area of interest.

It was expected that visibly seen blood vessels (and other regions with an increased redness) would result in increased erythema index values, compared to normal skin. Thus an example measurement was chosen to test which erythema index calculation gives the best contrast between areas of an increased redness and normal skin (Fig. 39). For this purpose, erythema index values were normalized for each erythema index distribution map. Three regions of interest (ROI) were selected in the erythema index distribution maps to calculate average erythema index value for normal skin (black ROI line in the Fig. 39 White image), blood vessel (red ROI line) and pigmentation (blue ROI line). Results are shown in Table 1.

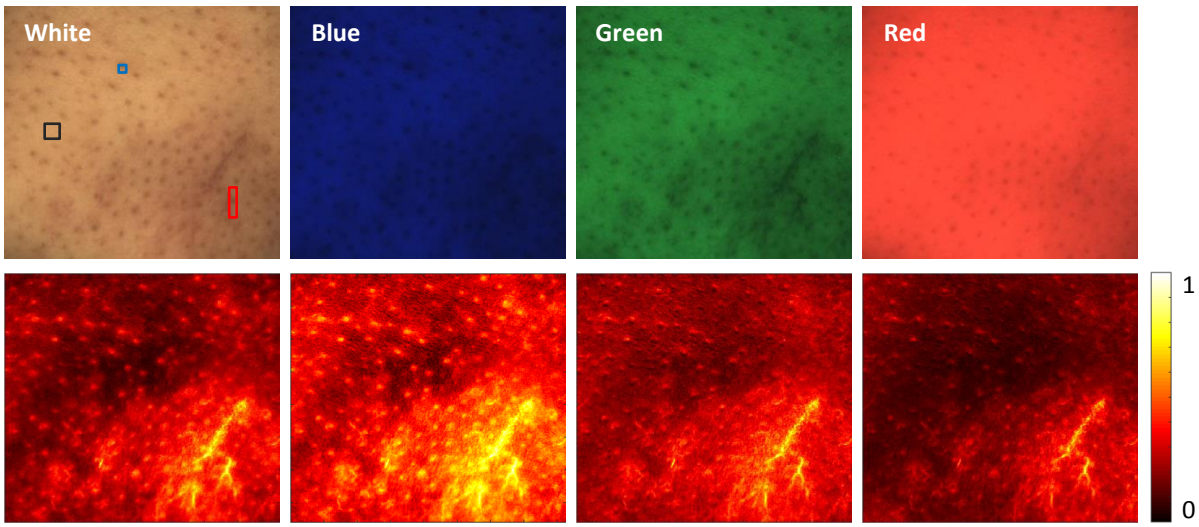

$$EI_{RG} = \frac{I(R)}{I(G)} \qquad EI_{BC} = \frac{I(G) - I(R)}{I(G) + I(R)} \qquad EI_{BRG} = \frac{\sqrt{I(B) \cdot I(R)}}{I(G)} \qquad \mathrm{EI_{BG}} = 100 \cdot \frac{I(B)}{[I(G)]^2}$$

Fig. 39. Example of white light, blue, green and red illumination images of a nose (on top) and different erythema index distribution maps (bottom).

Table 1. Comparison of contrast between different erythema index parameters

	Normal skin	**Blood vessels**	**Pigmentation**	**Contrast of Blood vessels and Normal skin**	**Contrast of Pigmentation and Normal skin**
EI_{RG}	0.11 ± 0.01	0.91 ± 0.05	0.61 ± 0.12	8.64 ± 0.43	5.81 ± 0.70
EI_{BC}	0.18 ± 0.02	0.95 ± 0.03	0.75 ± 0.10	5.15 ± 0.16	4.04 ± 0.41
EI_{BRG}	0.17 ± 0.02	0.90 ± 0.05	0.58 ± 0.13	5.40 ± 0.31	3.44 ± 0.45
EI_{BG}	0.09 ± 0.01	0.89 ± 0.06	0.48 ± 0.13	10.29 ± 0.67	5.53 ± 0.72

The best contrast between an increased erythema (blood vessels) and normal skin were achieved by using the EI_{BG} estimation algorithm. In case of contrast between pigmentation and normal skin, it is better to have less contrast which could be interpreted as subtraction of melanin absorption in the epidermis, and for this purpose the EI_{BRG} estimation parameter seems to work better.

3.3 RESULTS OF THE CLINICAL STUDY

50 female *rosacea* patients (ages 25 to 59) with dermatologists' estimated CEA index of mostly 2 and 3 participated in the study. The study protocol was approved by an ethics committee and each patient gave a written approval. They were separated into two groups: 27 patients were in a control group and 23 patients were in a treatment group. The treatment group patients were using a cream that is supposed to decrease the severity of

erythema on facial skin while the control group patients were using a simple moisturizing cream. Both groups were using the creams daily for a month without doing any other treatments on facial skin. Five parts of facial skin were measured for each patient (central forehead, right cheek, left cheek, right part of nose and left part of nose). For each facial part three data sets were obtained: CEA, *Mexameter* erythema index values (EI_M), and *SkImager* erythema index values (EI_{BG}). Two temporal measurements for each patient were acquired: before treatment and 1 month after the treatment. Before each measurement, patient relaxed for at least 15 minutes in order to avoid other factors affecting their skin color (such as cold outside temperature, fast walking, etc.). None of the people involved (patients, doctors, researchers) knew which patient is in which group before the results had been analyzed.

The obtained results are presented in two parts: comparison of results of all three data sets (CEA, *Mexameter* and *SkImager*) for 500 measurements (50 patients, two temporal measurements 1 month apart, 5 facial regions) and comparison of two patient groups (control and treatment) to find out whether it is possible to see any improvement for the treatment group by each of the data sets.

All 500 measurements were divided in four groups, depending on the corresponding CEA value of each measurement, and histograms of all those four groups show the correlation of CEA and EI_{BG} values, acquired by *SkImager* (Fig. 40a), and correlation of CEA and EI_M values, acquired by *Mexameter* (Fig. 40b). The mean EI_{BG} value and the mean EI_Mvalue for each of the four groups (the corresponding CEA values) was then calculated, and correlation graphs between CEA and the mean EI_{BG} (Fig. 41a) and between CEA and mean EI_M(Fig. 41b) are shown.

Mean values of EI_{BG} show a very good ($R^2 = 0.99$) linear correlation with the CEA values. In case of *Mexameter*, the correlation is not as good. Fig. 40b shows that erythema index values do not make distinctive groups that would match the CEA values, indicating that the dermatologists' subjective view is different from the quantitative estimation by an optical device.

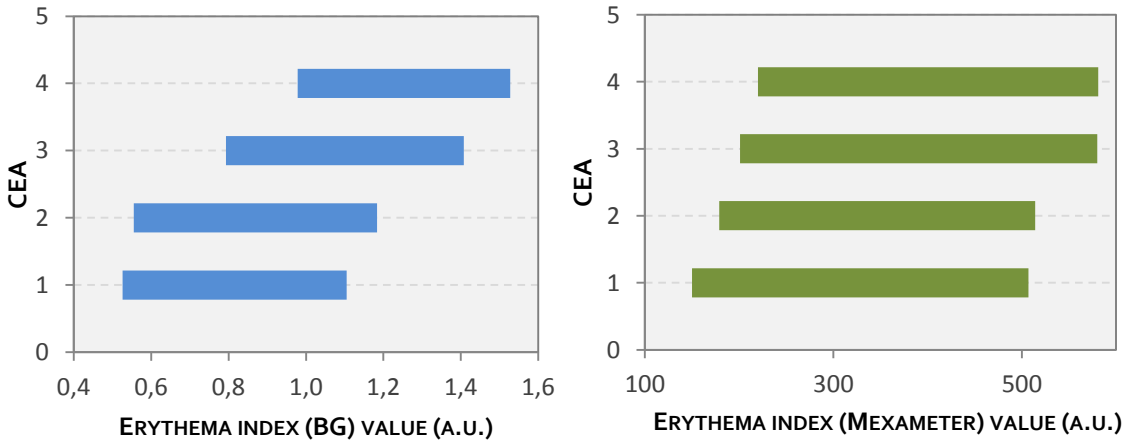

Fig. 40. Histograms of (a) all $\boldsymbol{EI_{BG}}$ values for each corresponding CEA value; (b) all $\boldsymbol{EI_{M}}$ values for each corresponding CEA value.

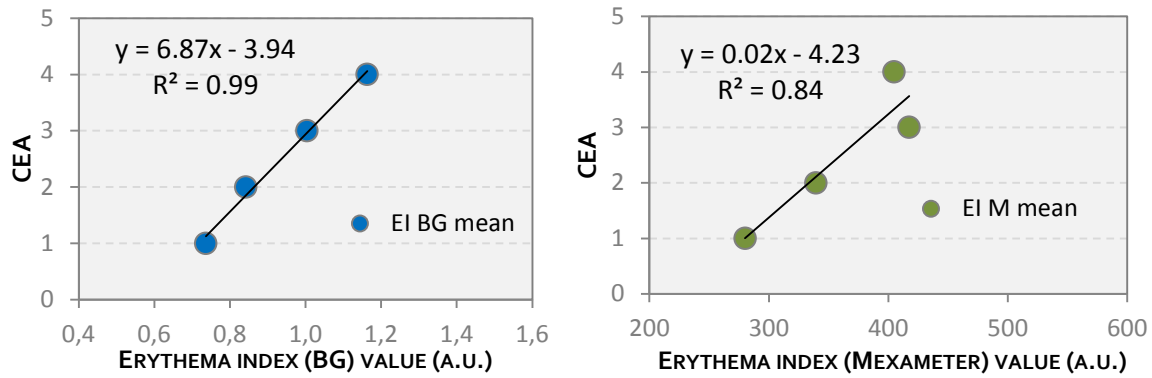

Fig. 41. Correlation graphs of (a) CEA and the mean value of $\boldsymbol{EI_{BG}}$ for each corresponding CEA value; (b) CEA and the mean value of $\boldsymbol{EI_{M}}$ for each corresponding CEA value.

Two temporal measurements were taken for all 50 patients at the beginning of the study and 1 month after: 27 patients in a control group were using a simple moisturizing cream and 23 patients in a treatment group were using a *rosacea* treatment cream. CEA, Mexameter (EI_M) and Skimager (EI_{BG}) data were used to see if there was any improvement (less erythema) after 1 month. For each patient, average value of all five facial measurements was calculated and further analyzed. Percentage of patients with improvement, no matter how great, out of total patients in one group, 23 or 27, was calculated and results are shown in Fig. 42.

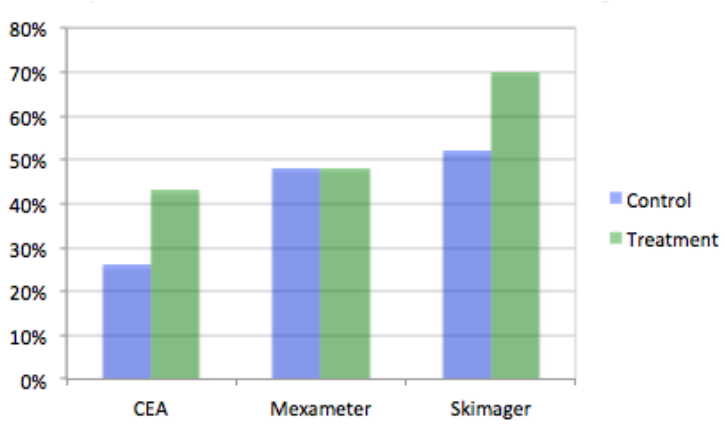

Fig. 42. Percentage of patients with improvement (out of total number of patients in one group) – comparison between CEA, *Mexameter* and *SkImager* results.

In the case of CEA results, for 29 patients (out of 50) there was no change in CEA value (17 in control group and 12 in treatment group); for the rest of patients, there was a higher percentage of patients with improvement for the treatment group than for the control group. *Mexameter* values showed no difference in improvement for both groups. *SkImager* results showed that 52% of patients in the control group had an improvement and 70% of patients in the treatment group had an improvement in their results.

3.4 CONCLUSIONS AND DISCUSSION

This study shows a comparison between different erythema index estimation calculations and proposes a new algorithm using only the blue and green spectral images; the new algorithm shows a better contrast for erythema estimation than other algorithms. The lowest contrast between pigmentation (increased melanin content) and normal skin regions was achieved by using a previously developed erythema index estimation EI_{BRG}.

Output data of two optical devices used for erythema index estimation, a single-spot measurement device *Mexameter* and an RGB imaging device *SkImager*, are compared to dermatologists' assessment (CEA values). The mean EI_{BG} (of all EI_{BG} values with the same CEA value) was calculated, and comparison of the mean EI_{BG} and CEA shows a very good correlation ($R^2 = 99\%$). The same was done with the results of the single-spot measurement device *Mexameter*; however, the correlation of the mean EI_M and CEA is not as good ($R^2 = 84\%$).

When comparing patients in two groups (control and treatment), it is easier to distinguish between both groups by using *SkImager* results as they show also small changes in erythema, compared to the dermatologists' estimation, and also they actually show more improvement for treatment group than for control group. Although it is unclear whether the

rosacea treatment cream actually improves the results (there is no ground truth method to test it), it was expected that there should have been more improvement than for the control group. Regarding the 50% improvement for the control group, it could be explained with the placebo effect (patients might have thought that they were using a treatment cream) or with the fact that the moisturizing cream also improved their skin.

This study shows that single-spot measurements might not be very reliable when compared to the RGB imaging. RGB imaging shows a much better correlation with dermatologists' estimation and shows more reliable results. A new erythema index estimation algorithm was proposed, and it demonstrates a better contrast between blood vessel and normal skin regions than other algorithms.

CHAPTER 4

REFLECTANCE SPECTROSCOPY AND IMAGING FOR ESTIMATION OF WATER IN SKIN

This chapter shows experimental work done in the near-infrared spectral range of 900–1700 nm by reflectance spectroscopy and imaging in order to find possibilities for estimation of water content in skin (skin hydration), especially after application of moisturizing creams.

The first part of this chapter gives a literature overview of research done in the field of near-infrared spectroscopy and its applications for estimation of water content in skin.

The second part describes the first experimental setup and results: single-point measurements done by near-infrared LEDs and photodetectors, published in paper IV and presented at conferences C10 and C11.

The third part describes the experimental setup and the most recent experimental results on possibilities to determine *in vivo* water content in skin by reflectance spectroscopy and imaging in the spectral range 900–1700 nm, published in paper I, submitted to be published in paper IX and presented at conference C5 and at the Biophotonics Summer School in Ven, Sweden, in June 2015.

4.1 LITERATURE OVERVIEW

Near-infrared spectroscopy offers tools to distinguish between different water volume fractions in skin as water has distinct absorption peaks in the near-infrared spectral range. Thus, near-infrared spectroscopy is considered to have a potential to be informative for cosmetics and health industry to determine how dry the skin is, in other words, determine skin moisture level.

There is a huge variety of different moisturizers, lotions and other products that supposedly reduce skin dryness. However, it is not clear how much effect these products actually cause in short and long term. Currently, commercially available devices (e.g. *Corneometer*, *Skicon*, *Nova*, etc.) used for the determination of skin moisture level are based

on electrical properties of skin (conductance, capacitance). Studies show good correlation between results acquired by different commercially available devices [98]. However, these techniques are indirect as the given result is related not only to the level of skin moisture but also the surface state (contact impedance between the skin and the electrode can vary depending on skin roughness) and the thickness of *stratum corneum* (SC) that varies between different body parts [99]. Thus, skin moisture determination by analyzing electrical properties of skin is considered unreliable and there is a need to develop new techniques and methodologies to increase reliability. Optical methods in the near-infrared spectral range show a potential to do that.

Previous studies on near-infrared reflectance spectroscopy as a technology for determination of *in vivo* skin moisture level can be found since the 1990s. In 1993, Martin suggested a method to quantitate water on a relative basis to distinguish free, bulk and bound water which can mainly be done by using wavelengths in the spectral range 1800–2000 nm, as well as additionally using scattering off the skin surface as a measure of skin smoothness [100].

In 2005, Suh *et. al.* presented work on doing *in vitro* skin moisture measurements on hairless mouse, as well as *in vivo* skin moisture measurements on human inner arm by Fourier Transform NIR spectrometer in the spectral range 1100–2500 nm. They used partial least squares regression to develop a calibration model by comparing near-infrared reflectance spectroscopy results to the conventional capacitance method (device *Corneometer*). *In vitro* measurements of a hairless mouse skin, soaked in water for one hour, are shown in Fig. 43: absorption spectra were acquired right after, 4, 9, 21 and 24 hours after the skin was soaked, and it can be seen that the absorption decreases considerably in 24 hours and the most changes are observed at the water absorption peak at 1920 nm [101].

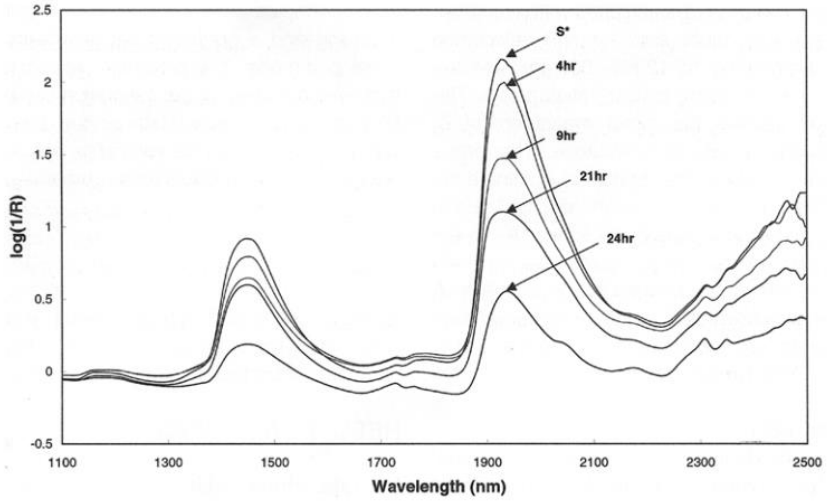

Fig. 43. *In* vitro near-infrared absorption spectra of a hairless mouse skin after it has been soaked in water for 1 hour, by using a Fourier Transform NIR spectrometer [101].

In vivo near-infrared absorption spectra of human skin were collected from 2 persons by using Fourier Transform NIR spectrometer, and results are shown in Fig. 44 [101].

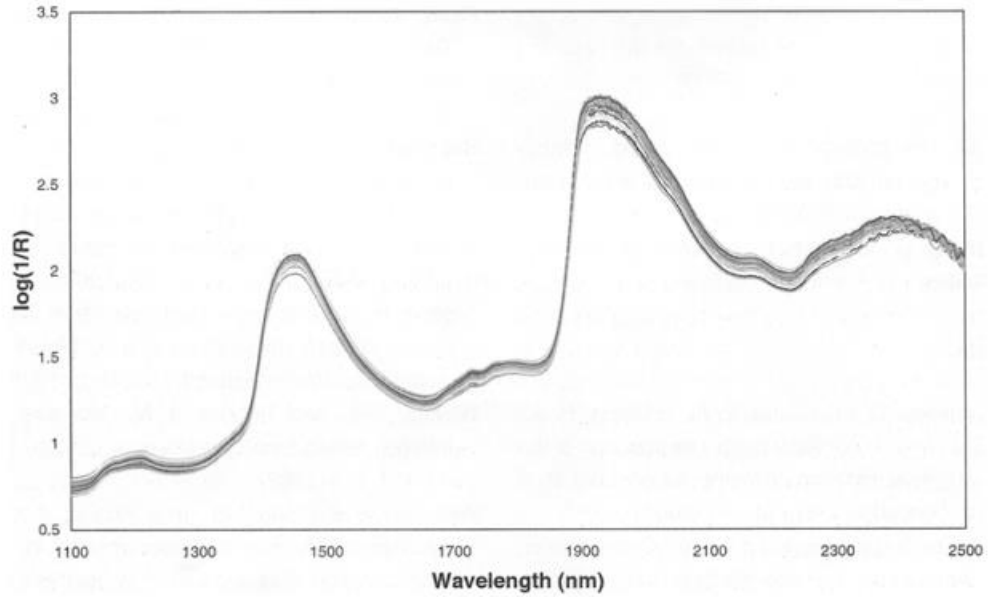

Fig. 44. *In* vivo near-infrared absorption spectra of human skin by using a Fourier Transform NIR spectrometer [101].

In 2006, Iwasaki *et. al.* introduced a NIR spectral imaging system consisting of an indium gallium arsenide (*InGaAs)* NIR camera, halogen bulb light source and optical filters (1060 nm and 1450 nm) to differentiate skin where a moisturizer has been applied. Fig. 45 shows absorbance image differences (subtracting image at 1060 nm from image at 1450 nm) just after application of a moisturizer and 5 hours later, additionally two different moisturizers are compared (lotion and rich cream) [102].

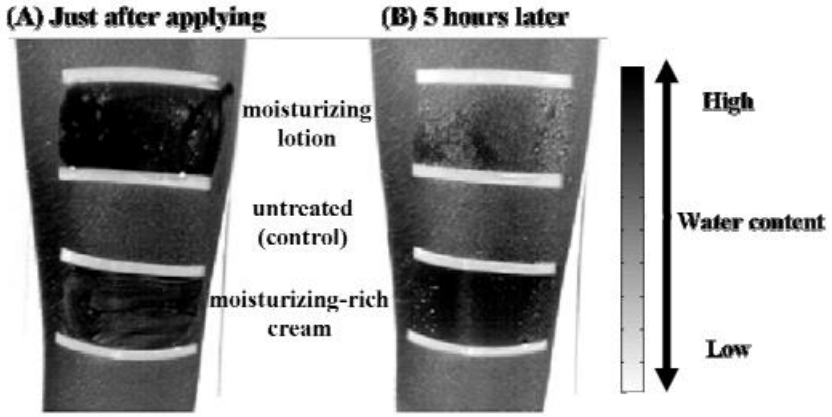

Fig. 45. Absorbance image difference A) just after application of a moisturizer and B) 5 hours after application of a moisturizer [102].

In 2011, Egawa *et. al.* suggested an imaging system for analysis of both water and oil content in facial skin by using a sensitive *InGaAs* NIR camera in the spectral range 1100–2200 nm which was also able to acquire images of skin at 1920 nm which is the strongest water band in this spectral range. They suggest that at 1920 nm it is possible to detect even small changes in water content in skin. Fig. 46 shows how water content, which in this case was attributed to a false color image brightness, changes over time after application of different lotions: it can be seen that there is an increase in water content just after the application of a cream and water content decreases 5 minutes later, although it stays higher than before the application of a cream for at least 90 minutes. Fig. 47 shows false color images of a region on skin where a moisturizer that also consists of oil and lipids was applied. The authors suggest that they were able to see water and oil relative content changes [103].

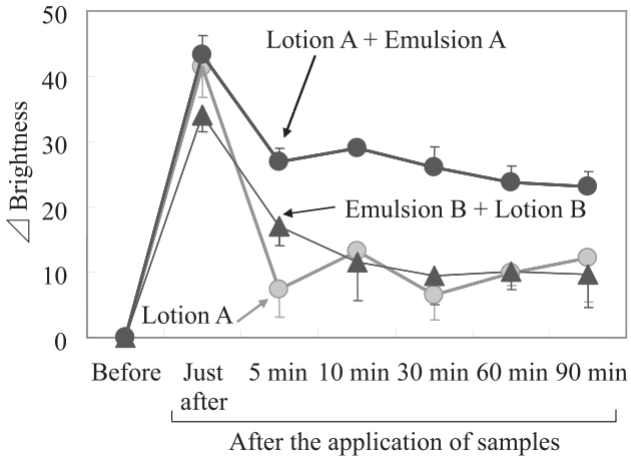

Fig. 46. Change in water content (expressed as false color image brightness) before and up to 90 minutes after application of a moisturizer/emulsion [103].

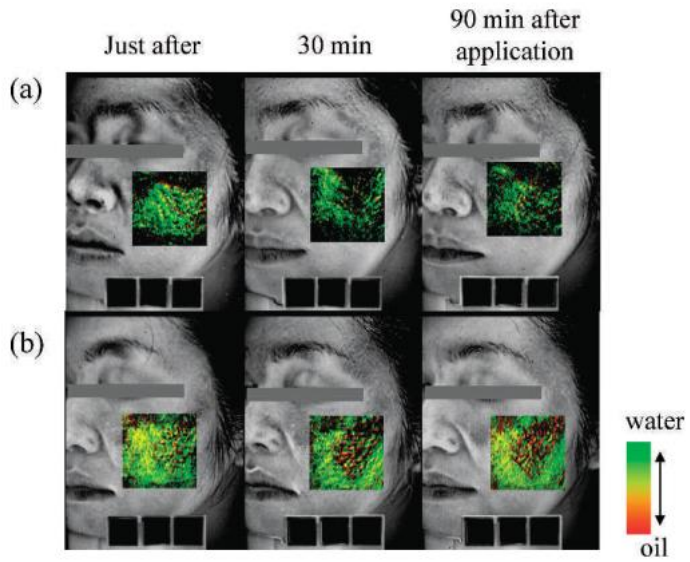

Fig. 47. False color images of water and oil content on facial skin after application of different emulsions (a and b) [103].

Although studies show that with a near-infrared detector with sensitivity up to 2.5 μm it is possible to distinguish even small changes in skin hydration, these types of *InGaAs* detectors are much more expensive and inaccessible than detectors up to 1.7 μm sensitivity. In the spectral range up to 1.7 μm there are also water absorption maxima that could possibly be used for determination of skin hydration, thus this spectral range should be explored further.

4.2 PHANTOM MEASUREMENTS BY DUAL-BAND PHOTODIODES AND LEDS

This chapter presents methodology for experimental work done in the near-infrared spectral range of 900–1700 nm by reflectance spectroscopy and imaging in order to find possibilities for estimation of water content in skin (skin hydration), especially after application of different creams and lotions. It started with a study on the possibilities of detecting skin hydration by using far-end of conventional silicon photo-detectors (sensitivity up to 1100 nm, including the water absorption maximum at 980 nm); however, those studies did not show high sensitivity and it was concluded that near-infrared detectors were needed to explore possibilities for determination of skin hydration.

First study in the near-infrared spectral range above 1100 nm was done with a simple single-point measurement setup by use of near-infrared photodiodes and LEDs. Experimental setup consisted of two illumination LEDs of wavelengths 1200 nm (*Thorlabs*, 2.5mW T-1 3/4) and 1450 nm (*Thorlabs*, 2.0 mW T-1 3/4), dual-band photodiode for detection (*Thorlabs* Dual Sandwich Detector *DSD2*), oscilloscope (*Tektronix MSO4054B*) for signal acquisition from the photodiode, as well as a sample of water in a Petri plate under which a white paper sheet was located. The illumination LEDs were operated by a power source ($i = 20\,mA$), each of them separately. The photodiode was operated by a power source ($i = 10\,mA$). Distance between the diodes (both, illumination and photodiode) and the bottom of the Petri plate with water sample was kept constant (1 cm) for all measurements. The illumination diode and the photodiode were located next to each other (Fig. 48).

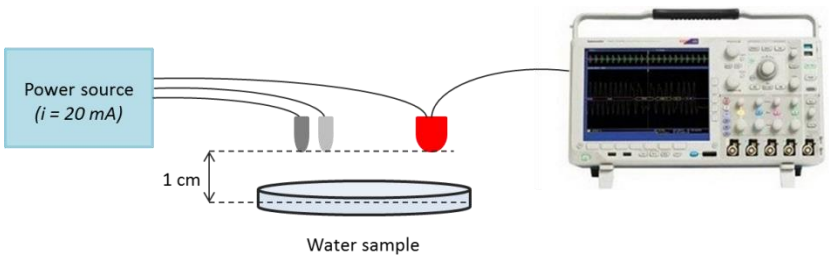

Fig. 48. Experimental setup of water content measurements by LEDs and a photodiode in the near-infrared spectral range.

Measurements were taken separately for each of the illumination LED. When LED was switched on, the RMS (root mean square) value was registered from the oscilloscope. The measurements were taken in dark in order to lower the noise level. At first, a reference value was registered by using the above described experimental setup with an empty Petri plate (without water in it) in order to register incident light. Afterwards, water was filled in the Petri plate with a depth level of 1 mm. After that, measurements were done after adding 1 mm of water level each time. The registered signal by oscilloscope is a value in millivolts (mV). As it is linearly dependent on photons reaching the photodiode, this registered value is assumed to be equivalent to reflected intensity value [relative units]. A relative water absorption parameter can be expressed as optical density value from Beer-Lambert-Bouguer's law by:

$$A_{water} = \frac{I_{ref}}{I_k} \tag{19}$$

where I_k represents each measurement by oscilloscope when there is an amount of water in the Petri plate.

For comparison of absorption parameter when illuminating the sample with both different LEDs (1200 nm and 1450 nm), a parameter representing absorption difference between both wavelength illuminations was introduced:

$$\Delta A = A_{1450} - A_{1200} \tag{20}$$

Results and discussion

Results show that at 1450 nm LED illumination water absorption parameter is higher than at 1200 nm illumination as was expected. The error of the measurement is the standard deviation of RMS signal, registered by the oscilloscope (Table 2).

Table 2. Comparison of relative absorption parameter values by illumination of each of the LEDs.

Illumination LED	$\mathbf{I_{ref}}$, [rel.units]	$\mathbf{I_k}$ (depth 1 mm), [rel.units]	$\mathbf{A_{water}}$, [rel.units]
1450 nm	39.4 ± 0.5	9.2 ± 0.5	4.3 ± 1.0
1200 nm	51.5 ± 0.5	44.7 ± 0.5	1.2 ± 1.0

In Fig. 49, the correlation between absorption parameter A and the water depth level in a Petri plate is presented when illumination the sample with a 1200 nm LED (Fig. 49a) and

when illuminating it with a 1450 nm LED (Fig. 49b). The relative absorption parameter ΔA increases with an increased water depth level (water volume fraction) as expected. When illuminating with 1450 nm LED, with water level higher than 0.3 cm, the reflected intensity value dropped to 0 and absorption parameter could not be estimated. This probably means that all light was absorbed by an increased level of water, thus no light was reflected and detected by the photodiode.

In Fig. 50, the difference parameter ΔA depending on the water depth level is shown. As expected, absorption difference between 1450 nm and 1200 nm spectral bands increases with increased water depth level as the water volume fraction and thus absorption have increased.

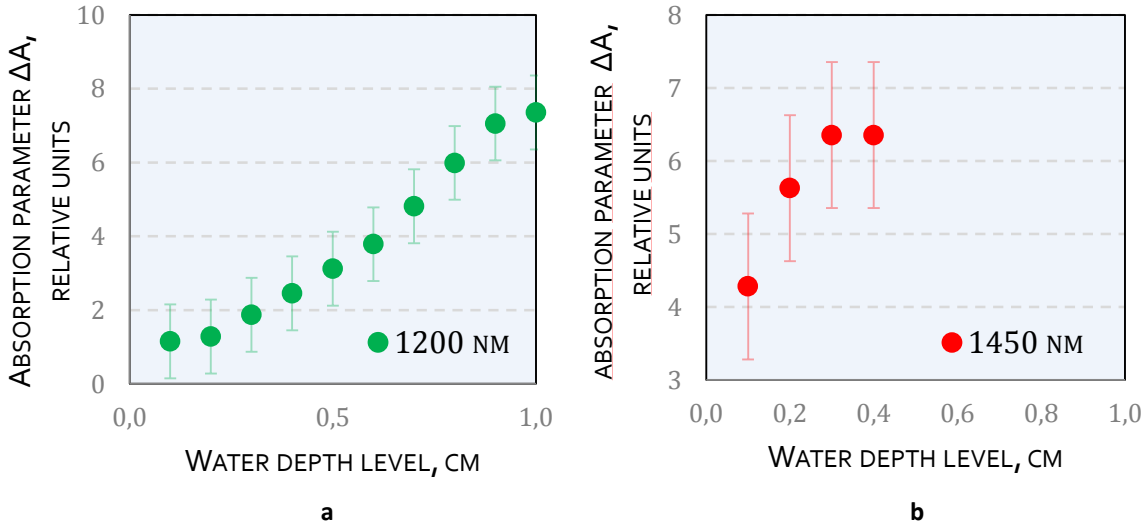

Fig. 49. Relative absorption parameter depending on the water depth level in the Petri plate at 1200 nm LED illumination (a) and 1450 nm illumination (b).

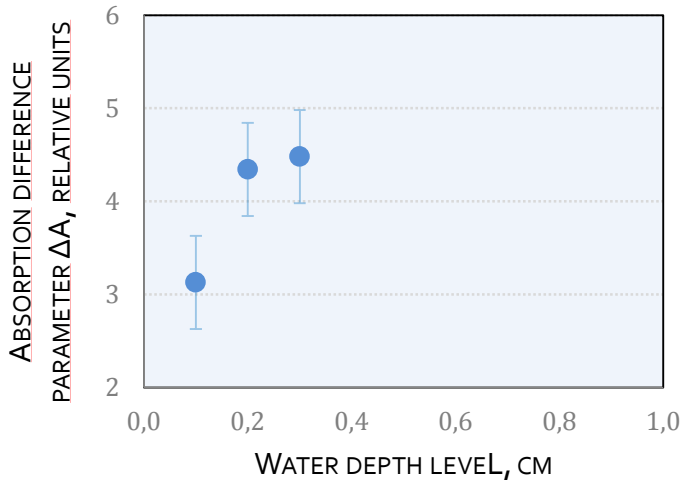

Fig. 50. Absorption difference parameter depending on the water depth level.

4.3 ESTIMATION OF WATER IN SKIN BY REFLECTANCE SPECTROSCOPY

The near-infrared spectral region was later explored even further by using a spectrometer and a camera with *InGaAs* detectors and spectral sensitivity in the spectral range of 900–1700 nm. The experimental setup was designed and it consisted of a near-infrared spectrometer (*Ocean Optics, NirQuest 512*) in the spectral range of 900–1700 nm, Y-type water free (WF) optical fiber probe, a halogen bulb light source, and a 3D printed nozzle as a spacer to separate skin from the detection and illumination fibers (Fig. 51). Optical fiber probe consisted of 6 illumination fibers in a circle around 1 detection fiber in the middle without any space between fiber ends. The distance between optical fiber ends to the skin surface of interest was kept constant of 5 mm by the nozzle (outer diameter 25 mm, inner diameter 4 mm). During measurements, room temperature was kept at 23°C. Room was dark to avoid any disturbances; however a dark spectrum was always subtracted from all measurements.

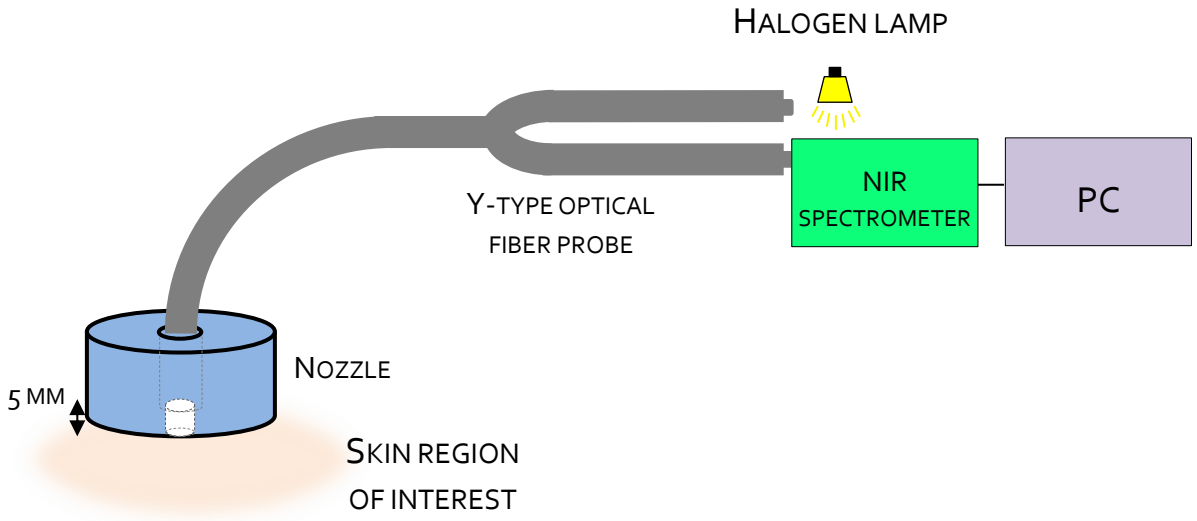

Fig. 51. Experimental setup of skin hydration measurements by near-infrared spectrometer, halogen lamp light source and fiber optics.

The acquired reflectance spectrum of skin was converted to absorbance values, and the spectrum of initial light reaching the sample I_0 was acquired by using *Avantes WS-2* reference tile for specular reflectance measurements in the spectral range of 350–1800 nm.

Results and discussion

Example skin absorption spectra of a female volunteer (26 years old, skin type II) at different body locations (foot and heel) and a comparison of visibly dry and normal skin is shown in Fig. 52. As was expected, the absorption spectrum of a visibly dry skin is lower

which could be explained with less water content in skin. When looking at the absorption spectrum of a heel which is also visibly dry and has a thicker skin, the absorption maximum at around 1420 nm is not as distinguishable as at other body locations which could be explained with the roughness of skin.

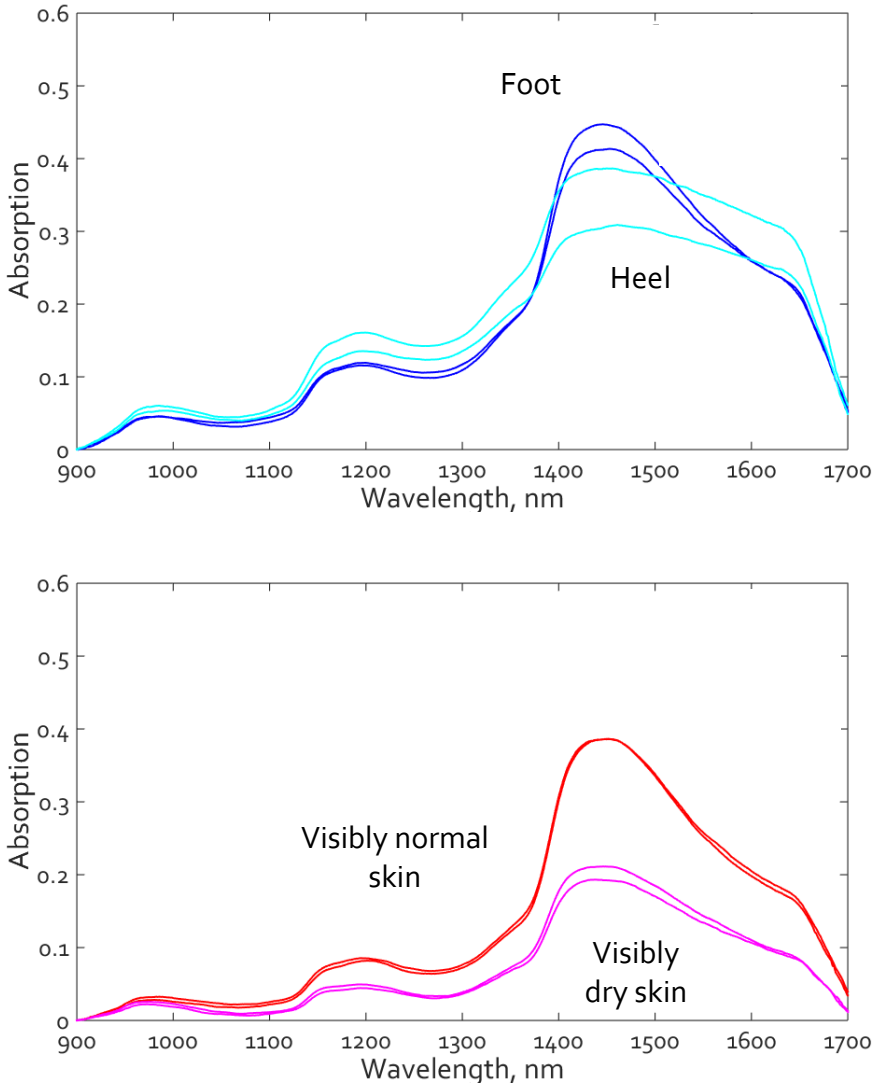

Fig. 52. Comparison of skin absorption spectra at different body sites (a) and of visibly dry and normal skin (b).

An experiment was done to see how the absorption spectrum of skin changes after application of a moisturizer (Fig. 53). Wavelengths of maximum (980 nm, 1200 nm, 1420 nm) and minimum (1050 nm, 13000 nm) water absorption values were chosen for observing skin absorption changes over time after application of a moisturizer on forearm skin of the same volunteer.

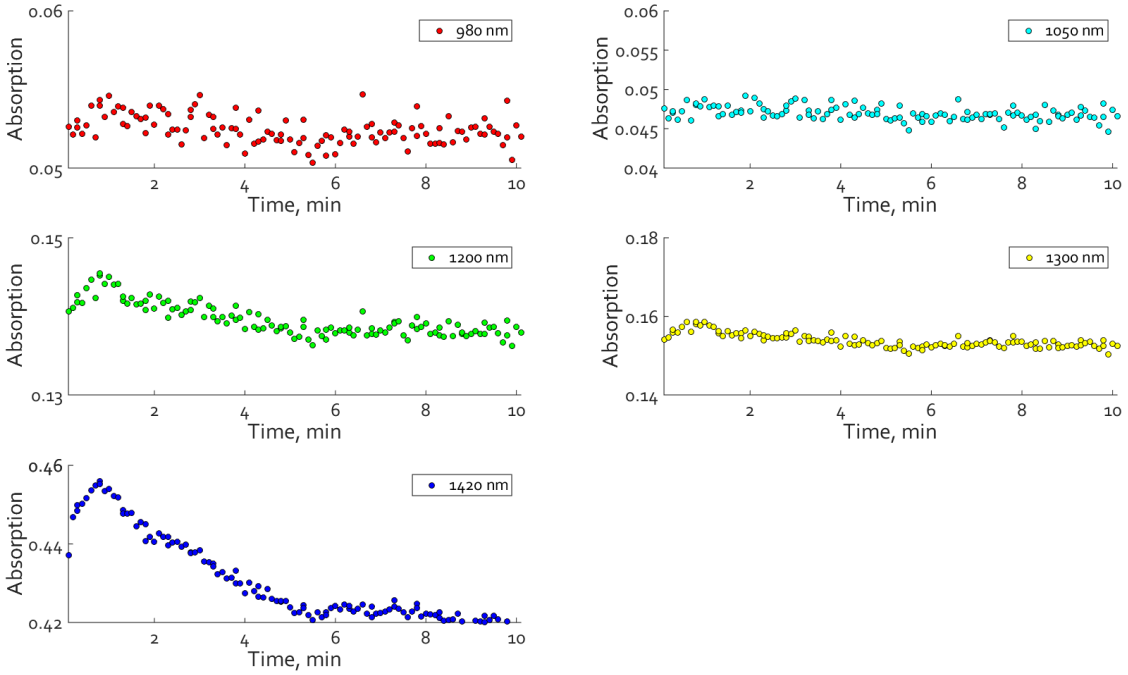

Fig. 53. Absorption changes over time after a moisturizer has been applied, observed at the wavelengths of local maximum (on the left) and local minimum (on the right) water absorption values.

As was expected, the best wavelength to observe skin absorption changes in this spectral range is 1420 nm as water absorption is the highest at this wavelength. Also, it is interesting to notice that absorption increases during the first 1 minute after application of a moisturizer, and then starts to slowly decrease up to minute 5 when absorption stays constant for the next 5 minutes. Similar behavior was observed for other volunteers. However, more statistical data are needed for further analysis.

4.4 ESTIMATION OF WATER IN SKIN BY NEAR-INFRARED IMAGING

Another type of experiment was performed in order to image water absorption changes in skin. Experimental setup consisted of a 320x256 pixel 8-bit near-infrared camera (*Xenics*, XS-1.7-320) sensitive in the spectral range of 900–1700 nm, near-infrared bandpass filters of central wavelengths 980±2 nm, 1100±2 nm, 1200±2 nm, 1300±2 nm, 1450±2 nm and 1600±2 nm (*Thorlabs*), transmission spectra shown in Fig. 54 [104], and a halogen lamp light source, directed at a 45° angle in order to eliminate the specular reflection off the skin surface coming directly into the camera (Fig. 55). These bandpass filters were chosen as wavelengths with maximum (980 nm, 1200 nm, 1450 nm) and minimum (1100 nm, 1300 nm) water absorption values.

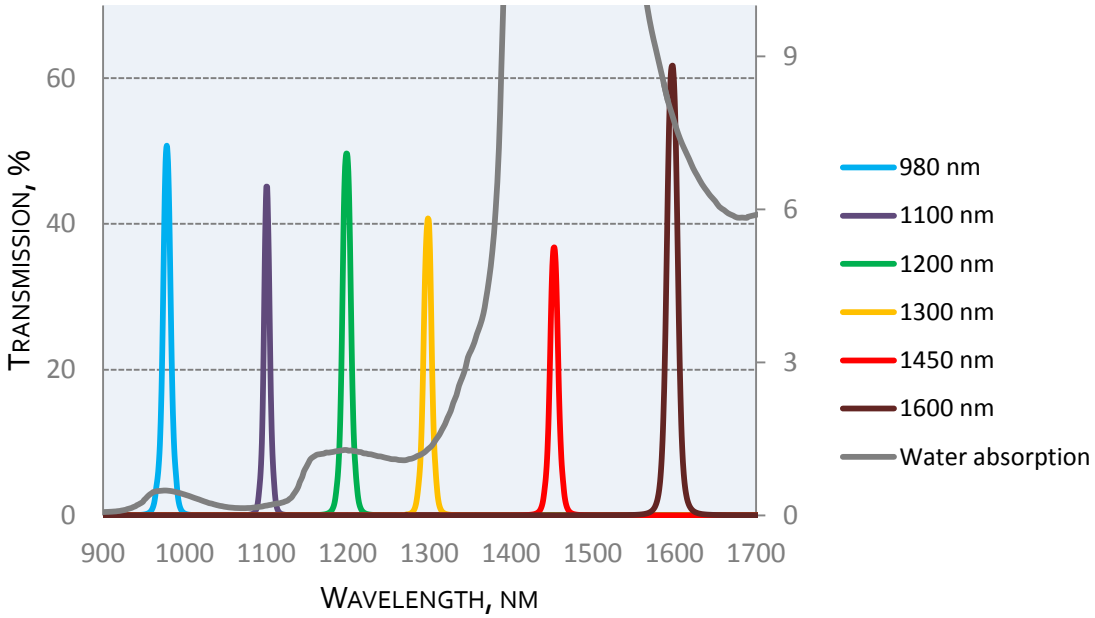

Fig. 54. Transmission spectra of bandpass filters [104].

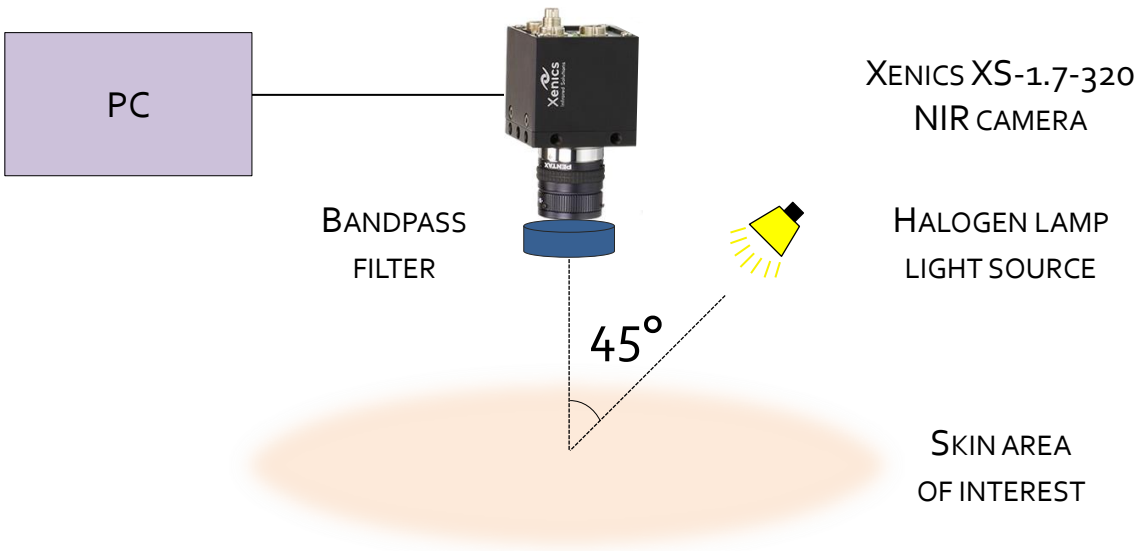

Fig. 55. Experimental setup for near-infrared imaging of skin.

Monochromatic 8-bit reflectance ($R(x, y)$) images were acquired by the camera, and a simple calculation was used to express absorption at each image pixel:

$$A(x, y) = \frac{1}{R(x, y)} \tag{21}$$

Results and discussion

Possibilities to detect water absorption differences between dry and moisturized skin were studied. However, when applying a thin layer of moisturizer (less than ~0,5 mm) on skin, in the experimental conditions it was hard to distinguish between dry and moisturized regions by the designed experimental setup. Only when putting a drop of water (at least 1 mm thick) directly on skin surface, it was possible to distinguish between normal skin and the drop of water on skin. In Fig. 56, an example of a blister on skin surface (2 mm in diameter, ~1 mm thick) is shown taken by using 6 bandpass filters (Fig. 56a), and a relative absorption parameter value was calculated as an average of a region of interest at normal skin and blister (Fig. 56b).

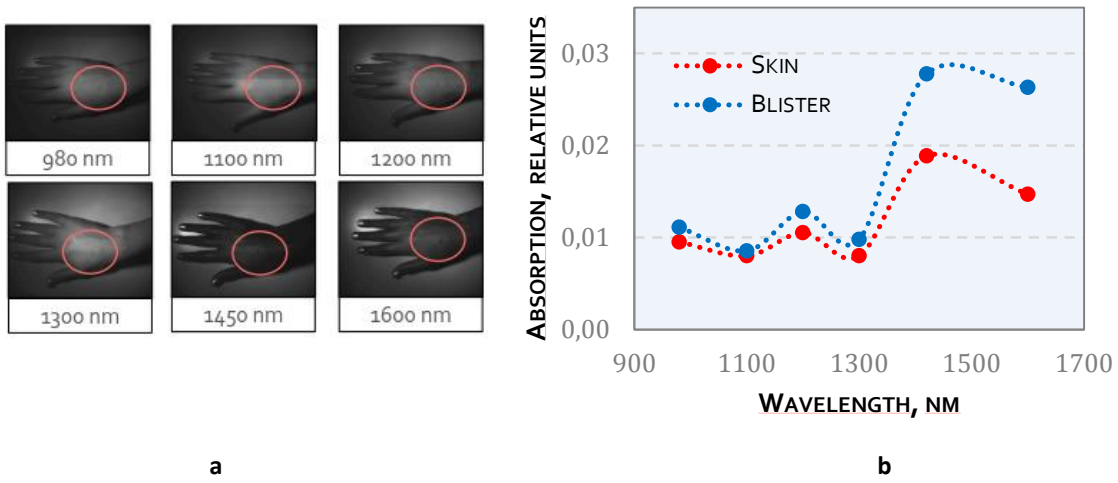

Fig. 56. a) Near-infrared images of a blister on skin by using different interference filters and b) relative absorption values of a blister and normal skin, calculated from each reflectance image.

The developed method shows potential for skin hydration mapping, however, a more sensitive imaging sensor should probably be used to see smaller skin hydration differences (for example, after application of a cream).

4.5 MONTE CARLO SIMULATIONS

In order to better understand what exactly may change in the acquired near-infrared diffuse reflectance spectra after application of a moisturizing cream, Monte Carlo simulations were performed. The program was written based on the open-source code for forward Monte Carlo for Multi-Layered media (MCML), developed by Lihong Wang and Steven L. Jacques [105–107], and modified as inverse Monte Carlo in order to acquire optical parameters of skin

when diffuse reflectance spectrum is known. A schematic of the written inverse Monte Carlo program is shown in Fig. 57.

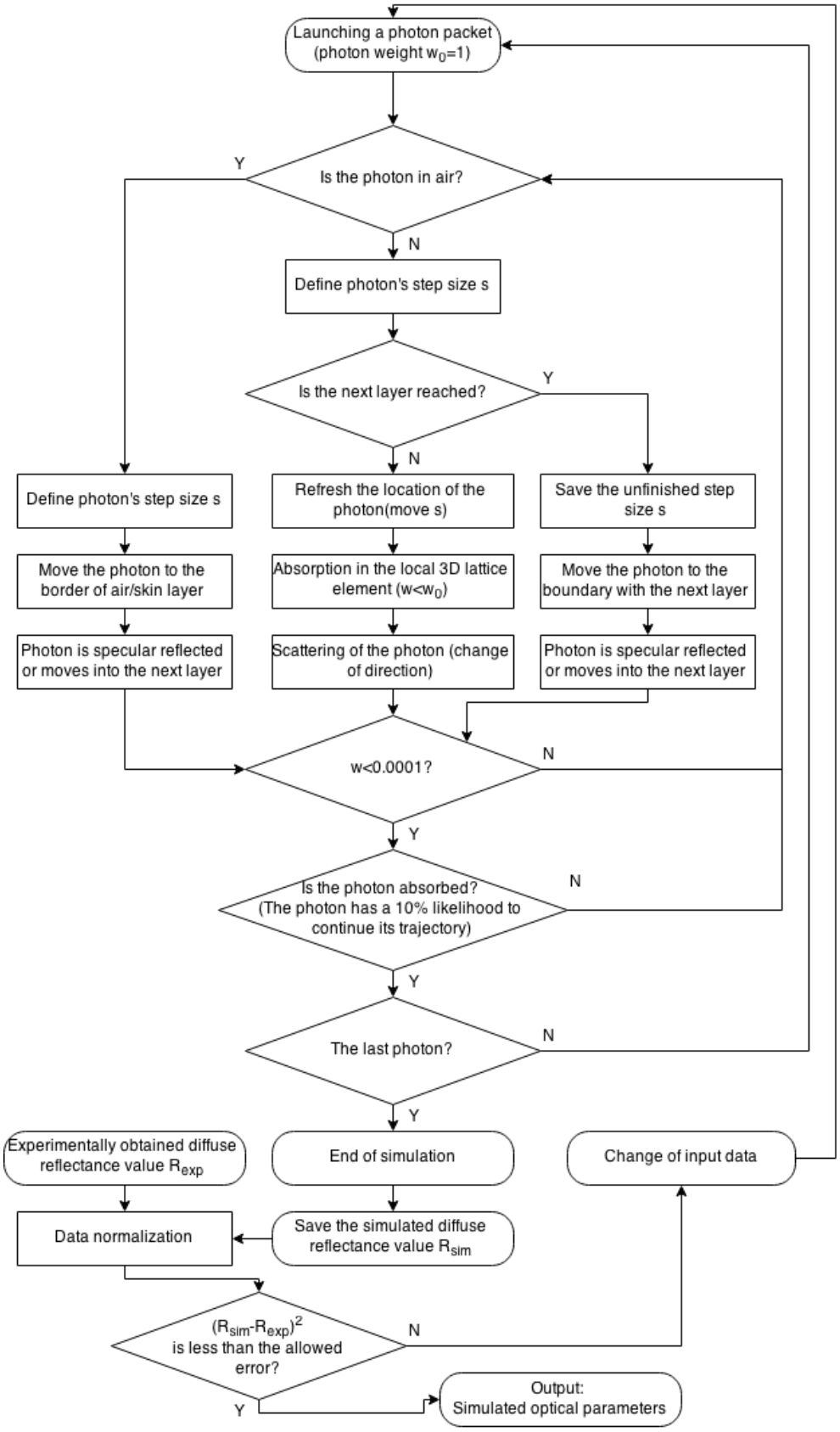

Fig. 57. A schematic of the inverse Monte Carlo program in order to calculate optical parameters of skin.

A one-layer skin model was chosen with the following parameters: anisotropy $g = 0.9$, layer thickness $d = 8$ mm, photon count 100 000, refraction coefficient $n = 1.33$. Wavelength-dependent absorption coefficient changed by equation $\mu_a(\lambda) = c_{H_2O} \cdot \mu_{H_2O}(\lambda)$, where μ_{H_2O} [%] is evenly distributed total water volume fraction in the skin layer and $\mu_{H_2O}(\lambda)$ are water absorption coefficient values $[cm^{-1}]$ (as in Fig. 12). Scattering coefficient μ_S $[cm^{-1}]$ values decrease almost exponentially from 18 cm^{-1} at 900 nm to 14 cm^{-1} at 1700 nm.

Two types of forward Monte Carlo simulations were performed: one where absorption coefficient is set constant for each wavelength, allowing the scattering coefficient to change, and the other one where scattering coefficient is set constant for each wavelength, allowing absorption coefficient to change. Diffuse reflectance spectra were then analyzed for different absorption coefficient (water volume fraction) values and for different scattering coefficient values.

Results and discussion

Monte Carlo simulations showed that reflected spectrum changes very little by changing water volume fraction values (related to absorption coefficient), while the scattering coefficient is constant (Fig. 58a). However, the reflected spectrum changes more visibly by changing the scattering coefficient (Fig. 58b) which suggests the importance of scattering.

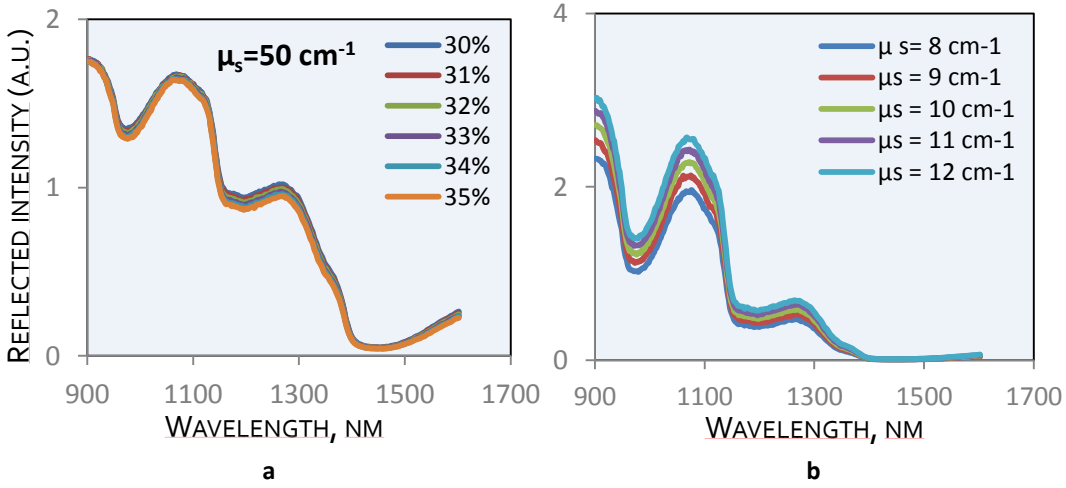

Fig. 58. Monte Carlo simulation results a) by changing water volume fraction (scattering coefficient is constant) and b) by changing scattering coefficient (absorption is constant).

4.6 CREAM PENETRATION STUDIES BY LASER-INDUCED SKIN AUTOFLUORESCENCE

The experimental setup for laser-induced skin autofluorescence studies was designed and experimentally validated. The setup consisted of a low-power light source, visible light spectrometer (*Avantes AvaspecULS2048,* spectral sensitivity 200–1100 nm), Y-type optical fiber probe for reflectance measurements from skin and optical cut-off filters located at the fiber end close to the spectrometer to eliminate light source irradiation from reaching the spectrometer. Different excitation sources were tested to find the best one for monitoring a treatment drug penetration in skin over time: 360 nm LEDs (without a filter), 405 nm laser, 437 nm laser and 532 nm laser.

A specific herbal drug (*Rinogels* by Silvanols) was tested. At first, it was put on a non-fluorescent plastic plate to test whether it has its own fluorescence by taking reflectance measurements. It was not possible to detect any fluorescence signal by using 360 nm LEDs; however, it might be due to the fact that for this light source there was no filter used to eliminate the laser illumination. It was also not possible to detect any fluorescence by 473 nm laser illumination, although a filter was used. By using 405 nm laser and 532 nm laser, drug fluorescence was noticed with fluorescence maximum at around 675 nm (Fig. 59). By analyzing excitation and emission spectra of fluorophores that are widely distributed in human skin [28], it is reasonable to suggest that the fluorophore in the drug could possibly be a combination of lipopigments, porphyrins and/or flavins, although no further analysis was done to test which fluorophore it was.

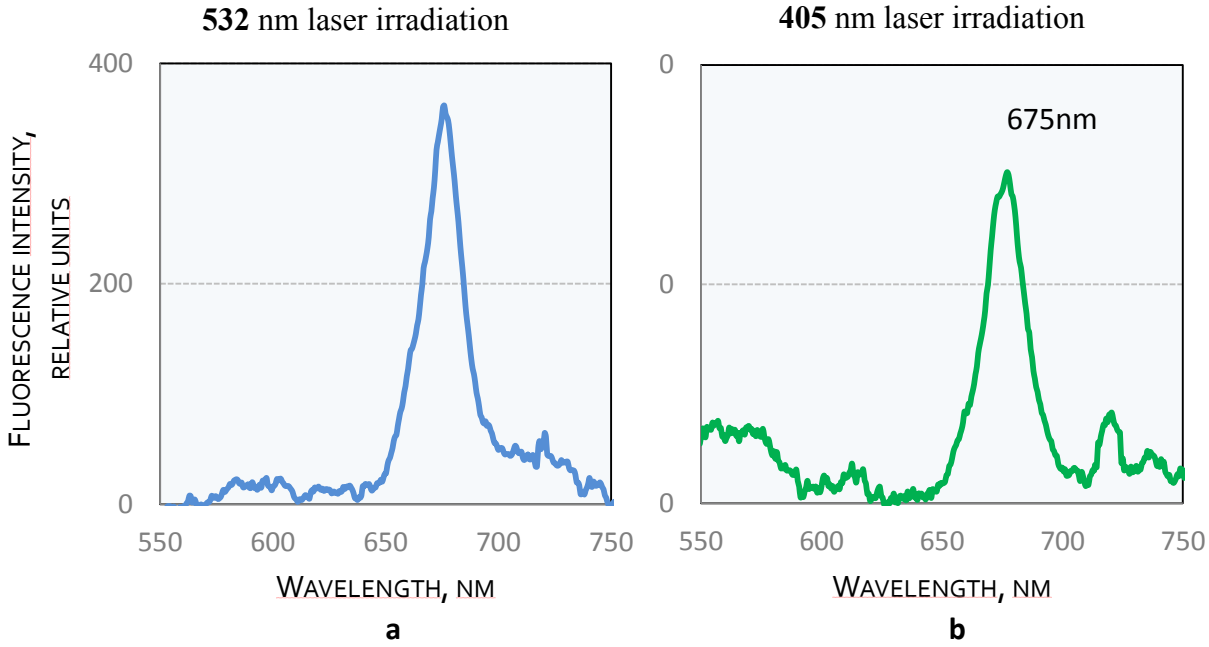

Fig. 59. Drug fluorescence spectra when irradiating with a 532 nm laser (a) and a 405 nm laser (b).

A parameter was proposed for comparison of skin autofluorescence spectrum changes over time after application of the drug:

$$p_{fl} = \frac{I_{drug}(675nm)}{I_{skin}(675nm)} \tag{22}$$

where $I_{drug}(675\ nm)$ is the normalized reflected intensity value at 675 nm of skin with the drug applied on it and $I_{skin}(675\ nm)$ is the normalized reflected intensity value at 675 nm of normal skin before the drug was applied. All spectra were normalized by the maximum reflected intensity value in the spectral range of 550–750 nm which was at 650 nm.

Results and discussion

A 532 nm laser irradiation was used to analyze cream penetration in skin by measuring skin autofluorescence changes. Measurements were taken at different times after the cream was applied on skin surface up to 13.5 hours. Fig. 60 shows comparison of skin autofluorescence spectra just after the application of the drug and 13.5 hours after, as well as the spectrum of normal skin (without any drug). Fig. 61 presents parameter p_{fl} changes over time after application of the drug.

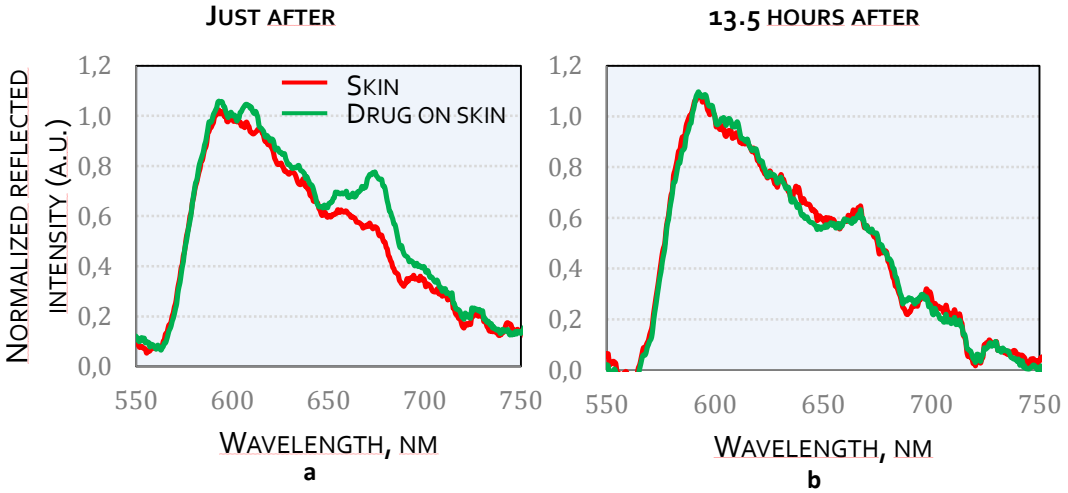

Fig. 60. Normalized skin autofluorescence spectra under 532 nm laser excitation a) just after application of the cream and b) 13.5 hours after application of the cream on skin surface.

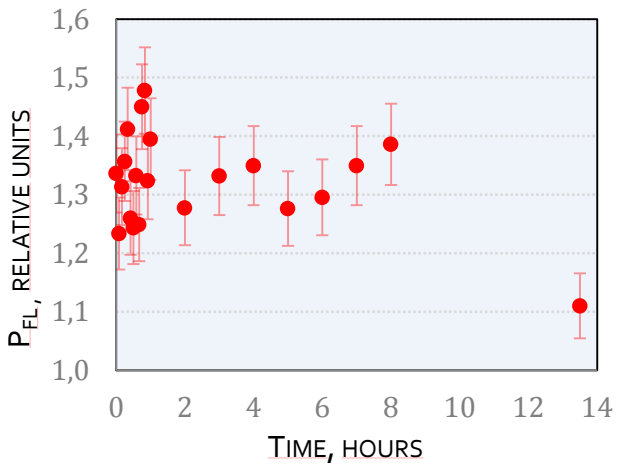

Fig. 61. Parameter p_{fl} changes over time after application of the drug on skin surface.

This study proposes a method for determination of the presence of a cream in tissue which can be useful to determine how long does a cream/drug stay in tissue after its application to skin surface. In this experimental study, it can be observed that after 13.5 hours the 675 nm fluorescence maximum that has been attributed to the fluorescence of the drug, is not as distinguished anymore and the measured skin autofluorescence spectrum is very similar to the skin autofluorescence spectrum taken before the drug was applied.

Even though this method seems promising, the obtained skin autofluorescence signal was quite noisy (Fig. 60) which can explain the p_{fl} parameter variations in Fig. 61. For further measurements, fluorescence spectrum approximation could be used beforehand to smoothen the signal before further analyzing the fluorescence intensity value at 675 nm. Also, this effect how a drug penetrates human tissue is probably related to tissue type, location, skin condition etc., thus future work should include more statistical data.

SUMMARY

This thesis summarizes the methodology improvements and experimental and clinical validation of optical methods in the visible and near-infrared spectral ranges for noninvasive assessment of skin parameters.

Novelty of this thesis:

1. Methodology for estimation of relative concentration distribution of skin bilirubin and hemoglobin was developed and experimentally tested by using hyperspectral imaging in the visible spectral range of 450–650 nm. A two-step algorithm was introduced to distinguish bilirubin and hemoglobin absorption in skin.
2. New algorithm for follow-up bilirubin and hemoglobin relative concentration changes during bruise development was proposed and clinically validated by means of self-developed experimental RGB imaging device.
3. Methodology for noninvasive determination of skin hydration and its changes in the spectral range of 900–1700 nm (including Monte Carlo simulations) was developed and experimentally validated.
4. Novel approach for estimation of facial skin erythema severity by using an RGB imaging device was introduced and clinically tested.
5. Methodology for follow-up of cream penetration in skin by laser-induced autofluorescence measurements was proposed and clinically validated.

1. Methodology improvements

The methodology for simultaneous estimation of skin bilirubin and hemoglobin in bruises by hyperspectral and RGB imaging:

- Image stabilization algorithms were applied to eliminate movement artefacts and to align the temporal measurements of the same bruise;
- A model for simultaneous bilirubin, hemoglobin and melanin absorption in skin was developed to determine bilirubin and hemoglobin relative concentrations at each pixel;

- A new two-step algorithm was proposed for a better estimation and distinguishing between hemoglobin and bilirubin relative concentrations in bruises;
- A new algorithm for distinguishing between bilirubin and hemoglobin absorption parameters by means of RGB imaging was developed.

The methodology for estimation of skin hydration changes over time after application of a moisturizer by near-infrared reflectance spectroscopy in the spectral range 900–1700 nm:

- Experimental setup comprising near-infrared spectrometer, Y-type optical fiber probe, halogen lamp light source and a plastic nozzle for placement was designed and assembled;
- The best wavelengths for detection of hydration changes were selected;
- Monte Carlo simulations were performed to understand how diffuse reflectance spectrum in the near-infrared spectral range is affected by changes in absorption and scattering; dominant role of scattering was shown.

The methodology for water distribution mapping in skin by near-infrared imaging:

- Experimental setup comprising near-infrared camera (detection in the spectral range 900–1700 nm), bandpass interference filters and a halogen lamp light source was designed and assembled;
- Imaging via interference filters was proposed to improve water detection sensitivity.

The methodology for estimation of facial skin erythema by RGB imaging:

- A new application for experimental multimodal skin imaging device was proposed;
- An original algorithm for erythema index assessment was proposed.

The methodology for estimation of drug penetration in skin by laser-induced skin autofluorescence:

- Experimental setup comprising a 532 nm laser, Y-type optical fiber probe, visible light spectrometer and an optical cut-off filter was designed and assembled;
- The optimum wavelength for fluorescence excitation was selected.

2. Experimental and clinical validation of the improved methods

2.1. Bilirubin and hemoglobin content changes in skin during bruise development:

- It is possible to monitor bilirubin and hemoglobin relative concentration changes in bruises over time by hyperspectral imaging, however, it is not very easy to distinguish between hemoglobin and bilirubin as bilirubin and hemoglobin both have absorption maximum at around 460 nm;
- Different algorithms were used to distinguish between both chromophores, and a two-step algorithm shows much better results than the simplified one in terms of distinguishing between bilirubin and hemoglobin absorption;
- It is possible to differentiate between bilirubin and hemoglobin absorption parameters by using RGB imaging; however, it is not as precise as hyperspectral imaging. RGB imaging can be used for simple mapping of bilirubin and hemoglobin in bruises. This simple method in its current state cannot be used for determination of the age of a bruise;

- Additionally, skin phantoms were developed to mimic skin tissue and the main chromophores of interest (hemoglobin, bilirubin and melanin) to see how absorption changes due to different concentration and depth of the absorbing substances. Phantom measurements are important for understanding how light interacts with tissue and how different chromophores change the total absorption spectrum acquired by a spectrometer or an imaging device;
- Additionally, a clinical study on parallel diffuse reflectance and fluorescence measurements by a hyperspectral imaging system was performed to test the potential of both modalities for diagnostics of atypical skin lesions that could be a very useful tool for early diagnostics of malignant lesions. Fluorescence modality shows a better distinguishability between benign and atypical nevi, compared to diffuse reflectance modality.

2.2. Erythema index measurements on facial skin of *rosacea* patients:

- Results show that point-measurement device is not as reliable as RGB imaging device, comparing to dermatologists' visual assessment;
- The new erythema index estimation algorithm could offer improved results as it shows better contrast between regions of increased redness and normal skin than other algorithms that were tested.

2.3. Penetration studies of moisturizing creams:

- Diffuse reflectance spectrum changes over the first minutes after a moisturizer was applied to the skin surface were obtained; results show an increase in absorption during the first minute after application of the moisturizing cream, and a decrease afterwards. The best wavelength for detecting the absorption changes in the spectral range of 900–1700 nm is 1420 nm (water absorption maximum);
- Monte Carlo simulations show that changes in scattering are affecting diffuse reflectance spectrum more than changes in absorption which explains the difficulties in measuring skin hydration just by differences in absorption at different spectral bands;
- Results show that by the designed experimental setup only a relatively large change in water content in skin can be observed (approximately 1 mm in thickness). This can be explained with very high water content in human skin (~65 %) in general, thus when there is a little increase in water content by adding a very thin layer of skin moisturizer, it is very difficult to detect this small of a change; a very sensitive imaging device is needed to identify this small of change;
- Skin autofluorescence spectrum when excited by a 532 nm laser is different when a treatment drug has been applied to skin surface, thus making it possible to monitor how long does it stay in the upper layers of skin.

Further work should include development of more advanced algorithms for calculation of relative chromophore concentration values when analyzing bruise development over time by hyperspectral/RGB imaging. Analytical models (e.g. diffusion model) could be included in order to estimate the age of a bruise. For experimental studies, a very important aspect is the measurement setup: hyperspectral imaging setup is very bulky, takes a relatively long time for one measurement which causes motion artefacts and it is not easy to move around. For future measurements more compact devices that are easy to move around should be used for an easier data acquisition. Thus RGB imaging has a great potential as RGB imaging devices can be made very compact and they are more accessible (possibly even smartphone cameras could be used for estimation of skin bilirubin and hemoglobin). The already developed methodology for RGB imaging of skin bilirubin and hemoglobin has to be improved but it is promising for further studies in this field.

Although near-infrared reflectance spectroscopy and imaging show potential for distinguishing changes in skin hydration in the spectral range up to 1.7 μm, further work should be done to develop a more standardized method for precise analysis of skin hydration change between different skin regions as diffuse reflected spectrum changes quite a lot even with small changes in pressure to skin surface. It seems that scattering plays the dominant role in how the shape of the diffuse reflected spectrum changes after application of a moisturizer; further work should include more phantom studies and more advanced Monte Carlo simulations to better understand what information can be acquired from near-infrared reflectance data.

Two clinical trials to validate the developed near-infrared reflectance spectroscopy technique and the laser-induced skin autofluorescence technique for drug penetration studies are planned in 2016.

THESIS STATEMENTS

1. The developed method of RGB imaging of bruises by a simple RGB imaging device is useful for acquiring relative concentration and distribution changes of skin bilirubin and hemoglobin over time.
2. The developed method of near-infrared imaging in the spectral range of 900–1700 nm ensures imaging of regions with increased skin hydration. Reflectance spectroscopy in this spectral range shows the potential to estimate skin hydration changes after application of moisturizing creams.
3. The developed method for erythema index estimation by RGB imaging shows a good correlation with doctors' visual assessment and provides more reliable and sensitive estimation of facial skin erythema, when compared to the existing methods.
4. Laser-induced autofluorescence technique was confirmed to be efficient for estimation of cream penetration in skin.

LIST OF PAPERS

I **I. Saknite** and J. Spigulis, "Determination of in vivo skin moisture level by near-infrared reflectance spectroscopy," *Proc. SPIE,* 9332, 93320Y (2015).

II **I. Saknite**, D. Jakovels, G. Krievina, and J. Spigulis, "Diffuse reflectance and fluorescence measurements of skin by multispectral imaging system," Proc. SPIE, 9129, 91293H (2014).

III A. Silapetere, J. Spigulis, and **I. Saknite**, "Development and Experimental Study of Phantoms for Mapping Skin Chromophores," Latv. J. Phys. Tech. Sci., 51(3) (2014).

IV **I. Saknite**, E. Kviesis, and J. Spigulis, "Water detection in skin by dual-band photodiodes," Proc. SPIE, 9032, 90320O (2013).

V **I. Saknite**, M. Lange, D. Jakovels, and J. Spigulis, "Determination of chromophore distribution in skin by spectral imaging," Proc. SPIE, 8474, 84740K (2012).

VI **I. Saknite**, D. Jakovels, and J. Spigulis, "Distant Determination of Bilirubin Distribution in Skin by Multi-Spectral Imaging," Latv. J. Phys. Tech. Sci., 48(2), 50–55 (2011).

VII D. Jakovels, J. Spigulis, and **I. Saknite**, "Multi-spectral mapping of in vivo skin hemoglobin and melanin," Proc. SPIE, 7715, 77152Z (2010).

VIII **I. Saknite**, A. Zavorins, D. Jakovels, J. Kisis, J. Spigulis, "Comparison of single–spot technique and RGB imaging for erythema index estimation," J. Physiol. Meas. (*submitted in September 2015; ongoing correspondence with Editorial board of the journal).*

IX **I. Saknite**, G. Tunens, J. Spigulis, "Study on near-infrared reflectance spectroscopy of skin for non-invasive determination of skin hydration," J. Biomed. Opt. (*submitted in November 2015).*

X **I. Saknite**, A. Zavorins, and J. Spigulis, "Skin Erythema Assessment by an RGB Imaging Device: a Clinical Study," OSA Technical Digest, JTu4A.16, http://dx.doi.org/10.1364/FIO.2015.JTu4A.16 (2015).

XI **I. Saknite**, A. Silapetere, and J. Spigulis, "Phantoms Used for Mapping of Skin Chromophores by Multi-spectral Imaging," OSA Technical Digest, BS3A.12, http://dx.doi.org/10.1364/BIOMED.2014.BS3A.12 (2014).

LIST OF CONFERENCE PRESENTATIONS

C1 OSA Frontiers in Optics and Laser Science, October 18–22, San Jose, CA, USA; poster presentation “Skin erythema assessment by an RGB imaging device: a clinical study” (2015).

C2 IONS Nanjing, July 10–12, Nanjing, China; oral presentation “Noninvasive estimation of skin bilirubin and hemoglobin in bruises by hyperspectral imaging” (2015).

C3 2nd International Conference on Photonics Solutions, July 6–8, Hua Hin, Thailand; oral presentation “Estimation of rosacea treatment effectiveness by RGB imaging device Skimager” (2015).

C4 Developments in Optics and Communications, April 8–10, Riga, Latvia; oral presentation “Estimation of rosacea treatment effectiveness by RGB imaging” (2015).

C5 Photonics West, February 7–12, San Francisco, USA; poster presentation “Determination of in vivo skin moisture level by near–infrared reflectance spectroscopy” (2015).

C6 Biomedical Optics, April 26–30, Miami, Florida, USA; poster presentation “Phantoms used for mapping of skin chromophores by multi–spectral imaging” (2014).

C7 Photonics Europe, April 14–17, Brussels, Belgium; poster presentation “Diffuse reflectance and fluorescence multispectral imaging system for assessment of skin” (2014).

C8 Developments in Optics and Communications, April 9–12, Riga, Latvia; oral presentation “Diffuse reflectance and fluorescence measurements of skin by multispectral imaging system” (2014).

C9 Advanced Laser Technologies, September 16–20, Budva, Montenegro; oral presentation “Novel multi–spectral imaging device for complex skin diagnostics” (2013).

C10 Biophotonics – Riga, August 26–31, Riga, Latvia; poster presentation “Water detection in skin by dual–band photodiodes” (2013).

C11 European Conferences on Biomedical Optics, May 12–16, Munich, Germany; oral presentation “Noninvasive imaging of bilirubin and water in skin by spectral imaging” (2013).

C12 Open Readings, March 20–23, Vilnius, Lithuania; oral presentation “Multi–spectral imaging device for skin diagnostics” (2013).

C13 Photonics West, February 2–7, San Francisco, USA; poster presentation „Determination of Chromophore Distribution by Spectral Imaging” (2013).

C14 Symposium on Biomedical Engineering and Medical Physics, October 11–12, Riga, Latvia; poster presentation „Spectral imaging used in determining the age of bruises depending on the bilirubin concentration" (2012).

C15 SPIE Optics & Photonics, August 12–16, San Diego, USA; oral presentation „Determination of chromophore distribution in skin by spectral imaging" (2012).

C16 Biophotonics in Dermatology and Cardiology, March 30–31, Riga, Latvia; poster presentation „In vitro measurements of bilirubin" (2012).

C17 Developments in Optics and Communications, April 12–14, Riga, Latvia; oral presentation „Distant determination of bilirubin distribution in skin by spectral imaging" (2012).

C18 Developments in Optics and Communications, April 24–26, Riga, Latvia; poster presentation "Determination of bilirubin distribution in skin by multi–spectral imaging" (2010).

ACKNOWLEDGEMENTS

I would like to thank professor Jānis Spīgulis for supervision, ideas and assistance during my PhD studies and especially for all the opportunities that have allowed me to develop myself professionally and work on different interesting and challenging topics.

I would like to thank my colleagues who have offered support, advice and helped with technical work throughout my PhD studies. First of all, to Dainis Jakovels for support, fruitful discussions, for being a great mentor and friend. To my colleagues who have given me support, help and advice: Marta Laņģe, Jānis Zaharans, Gita Krieviņa, Edgars Kviesis-Kipge, Inesa Feruļova, Ēriks Zaharans, Aleksejs Zavorins, Oskars Rubenis, Ilze Ļihačova, Aleksejs Ļihačovs, Ilona Kuzmina, Jacob Bauer, Uldis Rubīns, Dmitrijs Blizņuks, Kristīne Azarjana, Inga Šīrante.

I would like to thank Arita Silapētere for the development of skin phantoms and for being the first student who defended her bachelor thesis under my supervision, to Gatis Tunēns for the development of Monte Carlo simulation method, to Roberts Kadiķis for bruise hyperspectral image cube registration and to Juris Siņica-Siņavskis for help with the analysis of bruise hyperspectral data.

I would like to thank SPIE and OSA for Travel grants that allowed me to travel to the largest Optics conferences in the world.

I would like to thank my closest friends and family, especially my mother, for your great patience, support, advice, and always being there for me.

This work has been supported by the European Social Fund within the project "Innovative technologies for acquisition and processing of biomedical images", the European Regional Development Fund and the Latvian National research program.

BIBLIOGRAPHY

1. Haynes WM. “CRC Handbook of Chemistry and Physics, 95th Edition.” *CRC Press* (2015).

2. Hecht E. “Optics.” *Addison-Wesley* (2002).

3. Glenn Stark. “Light” [Online]. Encycl. Br. (2014). Available: http://www.britannica.com/EBchecked/topic/340440/light.

4. Kohen E, Santus R, Hirschberg JH. “Photobiology.” *Academic Press* (1995).

5. Niemz MH. “Laser-Tissue Interactions.” Third, Enl. *Springer* (2007).

6. Bashkatov a N, Genina E a, Kochubey VI, Tuchin V V. “Optical properties of human skin, subcutaneous and mucous tissues in the wavelength range from 400 to 2000 nm.” *J. Phys. D. Appl. Phys.* 38, 2543–2555 (2005).

7. “MedicaLook” [Online]. Available: http://www.medical-look.com/diseases_images/Skin-diseases1.jpg.

8. Tuchin V V. “Chapter 3: Light - Tissue Interactions.” In: *Biomedical Photonics Handbook. CRC Press LLC* (2003).

9. Jacques SL. “Origins of tissue optical properties in the UVA, visible and NIR regions.” *OSA TOPS Adv. Opt. Imaging Phot. Migr.* 2, 364–71 (1996).

10. Jacques SL, Prahl SA. “Introduction to Biomedical Optics” [Online]. Oregon Grad. Inst. Available: http://omlc.org/education/ece532/index.html.

11. Meglinski I V., Matcher SJ. “Computer simulation of the skin reflectance spectra.” *Comput. Methods Programs Biomed.* 70(2), 179–186 (2003).

12. Mobley J, Vo-Dinh T. “Chapter 2: Optical Properties of Tissue.” In: *Biomedical Photonics Handbook. CRC Press LLC*, 76 (2003).

13. McNaught AD, Wilkinson A, of Pure IU, Chemistry A. “Compendium of Chemical Terminology: IUPAC Recommendations.” *Blackwell Science* (1997).

14. Wallace MB, Wax A, Roberts DN, Graf RN. “NIH Public Access.” *Gastrointest Endosc Clin N Am*. 19(2), 233–242 (2009).

15. Dobusch A, Jordan H, Schmid W, Steiner A. “Brightness signal detection method for CCD matrix, uses stepped adjustment of amplification for each sensor element for bringing amplified signal into working range of A/D converter.” (2001).

16. Seeger K. “Semiconductor Physics: An Introduction.” *Springer Berlin Heidelberg* (2013).

17. Streetman BG, Banerjee S. “Instructor’s Manual, Solid State Electronic Devices, Fifth Edition.” *Prentice Hall* (2000).

18. Chen Y-W, Hsu W-C, Hsu R-T, Wu Y-H, Chen Y-J. “Low Dark Current InGaAs(P)/InP p–i–n Photodiodes.” *Jpn. J. Appl. Phys.* 42(Part 1, No. 7A), 4249–4252 (2003).

19. Rogalski A. “Infrared Detectors, Second Edition.” *CRC Press* (2010).

20. Andor. “NIR Spectroscopy with iDus InGaAs Detectors” [Online]. Available: http://www.lot-qd.de/files/downloads/andor/en/ingaas/Informationen_iDus_InGaAs.pdf.

21. Tran CD. “Principles, Instrumentation, and Applications of Infrared Multispectral Imaging, An Overview.” *Anal. Lett.* 38(5), 735–752 (2005).

22. Ocean Optics. “Ocean Optics Glossary” [Online]. Available: http://oceanoptics.com/glossary/.

23. B&WTek. “Spectrometer Knowledge” [Online]. (2015). Available: http://bwtek.com/spectrometer-part-3a-the-detector/.

24. Bearman G, Levenson R. “Chapter 8: Biological Imaging Spectroscopy.” In: *Biomedical Photonics Handbook. CRC Press LLC,* 26 (2003).

25. Li Q, He X, Wang Y, Liu H, Xu D, Guo F. “Review of spectral imaging technology in biomedical engineering: achievements and challenges.” *J. Biomed. Opt.* 18(10), 100901 (2013).

26. York T. “Fundamentals of Image Sensor Performance” [Online]. (2011). Available: http://www.cse.wustl.edu/~jain/cse567-11/ftp/imgsens/index.html#sec14.

27. “Digital Photography Preview - Sensors” [Online]. Available: http://www.dpreview.com/glossary.

28. Monici M. “Cell and tissue autofluorescence research and diagnostic applications.” *Biotechnol. Annu. Rev.* 11(SUPPL.), 227–256 (2005).

29. Lakowicz JR. “Principles of Fluorescence Spectroscopy.” *Springer* (2007).

30. Berezin M, Achilefu S. “Fluorescence lifetime measurements and biological imaging.” *Chem. Rev.* [Internet]. 110(5), 2641–2684 (2010). Available: http://pubs.acs.org/doi/pdf/10.1021/cr900343z.

31. Wagnières G a, Star WM, Wilson BC. “In vivo fluorescence spectroscopy and imaging for oncological applications.” *Photochem. Photobiol.* 68(5), 603–632 (1998).

32. Apinis P. “Cilvēks. Anatomija. Fizioloģija, Patoloģijas pamati.” Rīga (1998).

33. Kim O, McMurdy J, Lines C, Duffy S, Crawford G, Alber M. “Reflectance spectrometry of normal and bruised human skins: experiments and modeling.” *Physiol. Meas.* 33(2), 159–175 (2012).

34. Jones N, Ziegler OW. “Anatomy of the Skin” [Online]. Univ. Rochester Med. Cent. Heal. Encycl. Available: http://www.urmc.rochester.edu/encyclopedia/content.aspx?ContentTypeID=85&ContentID=P01336.

35. Sandby-Møller J, Poulsen T, Wulf HC. “Influence of epidermal thickness, pigmentation and redness on skin autofluorescence.” *Photochem. Photobiol.* 77(6), 616–620 (2003).

36. Koehler MJ, Vogel T, Elsner P, König K, Bückle R, Kaatz M. “In vivo measurement of the human epidermal thickness in different localizations by multiphoton laser tomography.” *Ski. Res. Technol.* 16(3), 259–264 (2010).

37. Xiao P. “Optothermal measurement of stratum corneum thickness and hydration-depth profile.” *Proc. SPIE*. 44(0), 276–286 (1997).

38. Wickett RR, Visscher MO. “Structure and function of the epidermal barrier.” *Am. J. Infect. Control*. 34(10), S98–S110 (2006).

39. Anderson R, Parrish J. “Optical properties of human skin.” *Sci. Photomed.* (1982).

40. Himes H, Roche F, Siervogel R. “Compressibility measurement of skinfolds of subcutaneous the.” *Am. J. Clin. Nutr.* 32(8), 1734–1740 (1979).

41. Burns T, others. “Rook’s textbook of dermatology.” (2004).

42. OMCL. “Optical Properties Spectra” [Online]. Oregon Med. Laser Cent. (2015). Available: http://omlc.org/spectra/.

43. Astner S, Anderson RR. “Skin Phototypes 2003.” *J. Invest. Dermatol.* 122(2) (2004).

44. Agar N, Young AR. “Melanogenesis: A photoprotective response to DNA damage?” *Mutat. Res. - Fundam. Mol. Mech. Mutagen.* 571(1-2 SPEC. ISS.), 121–132 (2005).

45. Randeberg LL. “Doctoral Thesis. Diagnostic applications of diffuse reflectance spectroscopy.” (2005).

46. Zijlstra WG, Buursma A, van Assendelft OW. “Visible and near infrared absorption spectra of human and animal haemoglobin: determination and application.” *VSP* (2000).

47. Denshaw-Burke M. “Methemoglobinemia” [Online]. (2014). Available: http://emedicine.medscape.com/article/204178-overview.

48. Umbreit J. “Methemoglobin-It’s not just blue: A concise Review.” *Am. J. Hematol.* 82, 134–144 (2007).

49. Koyuncu O, Turhanoglu S, Davarci I, Cevik C, Sessler DI, Turan A. “Correlation of carboxyhemoglobin levels and secondhand smoking related complications in pediatric tonsillectomy patients.” *Int. Anesthesiol. Clin.* 166, 2–6 (2014).

50. Coburn RF, Forster RE, Kane PB. “Considerations of the physiological variables that determine the blood carboxyhemoglobin concentration in man.” *J. Clin. Invest.* 44(11), 1899–1910 (1965).

51. Kikuchi G, Yoshida T, Noguchi M. “Heme oxygenase and heme degradation.” *Biochem. Biophys. Res. Commun.* 338(1), 558–567 (2005).

52. Constantin M, Choi AJS, Cloonan SM, Ryter SW. “Therapeutic potential of heme oxygenase-1/carbon monoxide in lung disease.” *Int. J. Hypertens.* 2012 (2012).

53. Silbernagl S, Lang F. “Color Atlas of Pathophysiology.” *Thieme* (2010).

54. Odell GB. “Neonatal jaundice” [Online]. (2010) Available: guidance.nice.org.uk/cg98.

55. Kumar P, Chawla D, Deorari A. “Light-emitting diode phototherapy for unconjugated hyperbilirubinaemia in neonates.” *Cochrane database Syst. Rev.* (12), CD007969 (2011).

56. Stokowski LA. “Fundamentals of phototherapy for neonatal jaundice.” *Adv. Neonatal Care*. 6(6), 303–312 (2006).

57. Alpay F, Sarici SU, Okutan V, Erdem G, Özcan O, Gökçay E. “High-dose intravenous immunoglobulin therapy in neonatal immune haemolytic jaundice.” *Acta Pædiatrica* [Internet]. 88(2), 216–219 (1999). Available: http://dx.doi.org/10.1111/j.1651-2227.1999.tb01085.x.

58. Chaplin M. “Water Structure and Science” [Online]. (2015). Available: http://www1.lsbu.ac.uk/water/water_vibrational_spectrum.html.

59. Buijs K, Choppin GR. “Near Infrared Studies of the Structure of Water. I. Pure Water.” *J. Chem. Phys.* 39(8) (1963).

60. Vaida V, Daniel JS, Kjaergaard HG, Goss LM, Tuck AF. “Atmospheric absorption of near infrared and visible solar radiation by the hydrogen bonded water dimer.” *Q. J. R. Meteorol. Soc.* [Internet]. 127(575), 1627–1643 (2001). Available: http://dx.doi.org/10.1002/qj.49712757509.

61. Hossenfelder S, Scherer S. “Backreaction webpage” [Online]. (2009). Available: http://backreaction.blogspot.com/2009/01/water-is-blue-because-water-is-blue.html.

62. Caspers PJ, Lucassen GW, Carter E a, Bruining H a, Puppels GJ. “In vivo confocal Raman microspectroscopy of the skin: noninvasive determination of molecular concentration profiles.” *J. Invest. Dermatol.* 116(3), 434–442 (2001).

63. Palmer KF, Williams D. “Optical properties of water in the near infrared.” *J. Opt. Soc. Am.* 64(8), 1107 (1974).

64. Randeberg LL, Hernandez-Palacios J. “Hyperspectral Imaging of Bruises in the SWIR Spectral Region.” *Proc. SPIE*. 8207, 82070N–82070N–10 (2012).

65. Randeberg LL, Roll EB, Nilsen LTN, Christensen T, Svaasand LO. “In vivo spectroscopy of jaundiced newborn skin reveals more than a bilirubin index.” *Acta Paediatr.* 94(1), 65–71 (2005).

66. Randeberg LL, Haugen OA, Svaasand LO. “Optical Diagnostics of Liver Pathology.” *Proc. SPIE.* 5141, 187–195 (2003).

67. Randeberg LL, Haugen O a., Haaverstad R, Svaasand LO. “A novel approach to age determination of traumatic injuries by reflectance spectroscopy.” *Lasers Surg. Med.* 38(4), 277–289 (2006).

68. Randeberg LL, Winnem AM, Blindheim S, Haugen O a., Svaasand LO. “Optical classification of bruises.” 5312, 54–64 (2004).

69. Randeberg LL, Winnem AM, Langlois NE, *et al.* “Skin changes following minor trauma.” *Lasers Surg. Med.* 39(5), 403–413 (2007).

70. Randeberg LL, Baarstad I, Løke T, Kaspersen P, Svaasand LO. “Hyperspectral Imaging of Bruised Skin.” *Proc. SPIE.* 6078, 60780O–60780O–11 (2006).

71. Stam B. “Doctoral Thesis. Three dimensional modeling of bruise evolution for improved age determination.” (2012).

72. Stamatas GN, Kollias N. “In vivo documentation of cutaneous inflammation using spectral imaging.” *J. Biomed. Opt.* [Internet]. 12(5), 051603 (2007). Available: http://www.ncbi.nlm.nih.gov/pubmed/17994872.

73. Stam B, Van Gemert MJC, Van Leeuwen TG, Aalders MCG. “3D finite compartment modeling of formation and healing of bruises may identify methods for age determination of bruises.” *Med. Biol. Eng. Comput.* 48(9), 911–921 (2010).

74. Yamanouchi I, Yamauchi Y, Igarashi I. “Transcutaneous Bilirubinometry: Preliminary Studies of Noninvasive Transcutaneous Bilirubin Meter in the Okayama National Hospital.” *Pediatrics* [Internet]. 65(2), 195–202 (1980). Available: http://pediatrics.aappublications.org/content/65/2/195.abstract.

75. “Manufacturer specifications of Colormate TLC Bilitest System, Ohmeda” [Online]. Medwow. Available: http://www.medwow.com/med/bilirubinometer/ohmeda-ge-healthcare/colormate-tlc-bilitest-system/20920.model-spec.

76. Jacques SL. “SpectRx develops portable optical spectrometer for monitoring hyperbilirubinemia in newborn infants” [Online]. Oregon Med. Laser Cent. (1997). Available: http://omlc.org/news/nov97/bilirubin11-97.html.

77. Robertson A. “Improved Transcutaneous Bilirubinometry: Comparison of SpectRx, BiliCheck and Minolta Jaundice Meter JM-102 for Estimating Total Serum Bilirubin in a Normal Newborn Population.” *J. Perinatol.* 22, 12–14 (2002).

78. Uwurukundo JMC, Baribwira C, Basinga P, Niyibizi P, Mutigima E. “Assessing the accuracy of the JM-102 transcutanous bilirubin measurement in dark skin jaundiced neonates. Case of University Teaching Hospital, Rwanda.” *Rwanda Med. J.* 69(June), 39–44 (2012).

79. Welch AJ, Van Gemert MJC. “Optical-thermal response of laser-irradiated tissue.” Opt. Response Laser-Irradiated Tissue. , 1–958 (2011).

80. Wang L V, Wu H. “Biomedical optics: principles and imaging.” *John Wiley & Sons* (2012).

81. Svaasand LO, Norvang LT, Fiskerstrand EJ, Stopps EKS, Berns MW, Nelson JS. “Tissue parameters determining the visual appearance of normal skin and port-wine stains.” *Lasers Med. Sci.* 10(1), 55–65 (1995).

82. Atkins P, de Paula J. “Physical Chemistry for the Life Sciences.” *OUP Oxford* (2011).

83. “User’s Manual for Nuance 2.10.” , 148 (2008).

84. Demos SG, Alfano RR. “Optical polarization imaging.” *Appl. Opt.* 36(1), 150–155 (1997).

85. Jakovels D, Spigulis J, Rogule L. “RGB Mapping of Hemoglobin Distribution in Skin.” In: *Proc. of SPIE-OSA Biomedical Optics*. , 80872B–80872B–6 (2011).

86. Wilkin J, Dahl M, Detmar M, *et al.* “Standard classification of rosacea: Report of the National Rosacea Society Expert Committee on the Classification and Staging of Rosacea.” *J Am Acad Dermatol*. 46(4), 584–7 (2002).

87. Tan J, Berg M. “Rosacea: Current state of epidemiology.” *J. Am. Acad. Dermatol.* [Internet]. 69(6 SUPPL.1), S27–S35 (2013). Available: http://dx.doi.org/10.1016/j.jaad.2013.04.043.

88. Hopkinson D, Tuchayi SM, Alinia H, Feldman SR. “Assessment of rosacea severity: A review of evaluation methods used in clinical trials.” *J. Am. Dermatology*. (2015).

89. Crawford GH, Pelle MT, James WD. “Rosacea: I. Etiology, pathogenesis, and subtype classification.” *J. Am. Acad. Dermatol.* 51(3), 327–341 (2004).

90. Tan J, Liu H, Leyden JJ, Leoni MJ. “Reliability of Clinician Erythema Assessment grading scale.” *J. Am. Acad. Dermatol.* 71(4), 760–763 (2014).

91. Diffey BL, Oliver RJ, Farr PM. “A portable instrument for quantifying erythema induced by ultraviolet radiation.” *Br. J. Dermatol.* 111, 663–672 (1984).

92. Kapsokalyvas D, Bruscino N, Alfieri D, *et al.* “Spectral morphological analysis of skin lesions with a polarization multispectral dermoscope.” *Opt. Express*. 21(4), 4826–40 (2013).

93. Jakovels D, Kuzmina I, Berzina A, Valeine L, Spigulis J. “Noncontact monitoring of vascular lesion phototherapy efficiency by RGB multispectral imaging.” *J. Biomed. Opt.* 18(12), 126019 (2013).

94. Clarys P, Alewaeters K, Lambrecht R, Barel a. O. “Skin color measurements: comparison between three instruments: the Chromameter(R), the DermaSpectrometer(R) and the Mexameter(R).” *Skin Res. Technol.* 6(17), 230–238 (2000).

95. Corporation AI. “1 / 2-Inch 3-Megapixel CMOS Digital.” , 1–46 (2006).

96. Demos SG, Alfano RR. “Optical polarization imaging.” *Appl. Opt.* 36(1), 150–155 (1997).

97. Spigulis J, Rubins U, Kviesis-Kipge E, Rubenis O. “SkImager: a concept device for in-vivo skin assessment by multimodal imaging.” *Proc. Est. Acad. Sci.* 63(3), 213 (2014).

98. Fluhr JW, Gloor M, Lazzerini S, Kleesz P, Grieshaber R, Berardesca E. “Comparative study of five instruments measuring stratum corneurn hydration (Comeometer CM 820.” *Ski. Res. Technol.* (9), 161–170 (1999).

99. Rigal Bazin, Sturelle, Descamps, Leveque L, Rigal Bazin, Sturelle, Descamps, Leveque L. “Near infrared spectroscopy: a new approach to the characterisation of dry skin.” *Ifscc*. 209(August), 197–209 (1993).

100. Martin K. “Direct measurement of moisture in skin by NIR spectroscopy.” *Journal-society Cosmet. Chem.* 261(October), 249–261 (1993).

101. Suh E-J, Woo Y-A, Kim H-J. “Determination of water content in skin by using a FT near infrared spectrometer.” *Arch. Pharm. Res.* 28(4), 458–462 (2005).

102. Iwasaki H, Miyazawa K, Nakauchi S. “Visualization of the human face skin moisturizing-ability by spectroscopic imaging using two near-infrared bands.” 6062, 1–8 (2006).

103. Arimoto H, Egawa M. “Water content distribution imaging of skin tissue using near-infrared camera and measurement depth analysis.” 8587, 85871T (2013).

104. Thorlabs. “NIR Bandpass Filter Specifications” [Online]. Available: http://www.thorlabs.de/newgrouppage9.cfm?objectgroup_id=1000.

105. Wang L, Jacques SL, Zheng L. “MCML—Monte Carlo modeling of light transport in multi-layered tissues.” *Comput. Methods Programs Biomed.* 47(2), 131–146 (1995).

106. Wang L, Jacques SL. “MCML - Monte Carlo for Multi-Layered media.” (1995).

107. Prahl SA, Keijzer M, Jacques SL, Welch AJ. “A Monte Carlo Model of Light Propagation in Tissue.” In: *SPIE Proceedings of Dosimetry of Laser Radiation in Medicine and Biology.* , 102–111 (1989).

APPENDICES

I. Saknite and J. Spigulis
"Determination of in vivo skin moisture level by near-infrared reflectance spectroscopy"
Proc. SPIE, 9332, 93320Y (2015)

Determination of in vivo skin moisture level by near-infrared reflectance spectroscopy

Inga Saknite*, Janis Spigulis
Biophotonics Laboratory, Institute of Atomic Physics and Spectroscopy, University of Latvia, Raina Blvd 19, Riga, LV-1586, Latvia

ABSTRACT

Near-infrared spectroscopy has a potential for noninvasive determination of skin moisture level due to high water absorption. In this study, diffuse reflectance spectra of in vivo skin were acquired in the spectral range of 900 nm to 1700 nm by using near-infrared spectrometer, optical fiber and halogen bulb light source. Absorption changes after applying skin moisturizers were analyzed over time at different body sites. Results show difference in absorption when comparing dry and normal skin. Comparison of absorption changes over time after applying moisturizer at different body sites is analyzed and discussed. Some patterns of how skin reacts to different skin moisturizers are shown, although no clear pattern can be seen due to signal noise.

Keywords: near-infrared, absorption, diffuse reflectance, skin, water, moisture, spectroscopy

INTRODUCTION

Near-infrared spectroscopy offers tools to distinguish between different water concentrations as water has distinct absorption peaks in the near-infrared spectral range. Thus, near-infrared spectroscopy is considered to have a potential to be informative for cosmetics and health industry to determine how dry the skin is, in other words, determine skin moisture level.

There is a huge variety of different moisturizers, lotions and other products that supposedly reduce skin dryness. However, it is not clear how much effect these products actually give in short and long term. Currently, commercially available devices (e.g. *Corneometer*, *Skicon*, *Nova*, etc.) for determination of skin moisture level are based on electrical properties of skin (conductance, capacitance). Studies show good correlation between results acquired by different commercially available devices [1]. However, these techniques are indirect as the given result is related not only to the level of skin moisture but also the surface state (contact impedance between the skin and the electrode can vary depending on skin roughness) and the thickness of stratum corneum (SC) that varies between different body parts [2].

*inga.saknite@lu.lv; phone 00 371 29162679

Skin moisture

Skin is the human body's largest organ that has many important functions to protect the body. One of them is the prevention of water loss. Skin consists of two main structural layers: epidermis and dermis. Epidermis consists of 5 sublayers (Figure 1), the outer of which, stratum corneum, is the main barrier that protects the body from dehydration, as well as from other molecules (e.g. irritants) entering into the skin. Stratum lucidum or the clear layer is only found in very thick epidermis (palms, soles), and is located between stratum corneum and stratum granulosum [3].

Skin has its own natural moisturizing mechanism that keeps it moist. Stratum granulosum (SG) is the second outer layer of epidermis, and it is where the most important transformations in the formation of SC barrier occur. At the SG, keratinocytes are transformed into corneocytes that are the building blocks of SC. In this process, natural body lipids are released, and they are the main barrier that protects wetter passing out through the SC. On most body sites, SC consists of 12 to 16 cell layers, but it can vary from 9 cell layers at eyelids to more than 50 cell layers at soles [3].

There are three main processes how skin moisturizers work in order to help skin when its natural barrier has been irritated. Humectants (glycerin, urea, lecithin, propylene glycol) attract water from dermis and bound it in the SC. Occlusive agents (zinc oxide, white petrolatum) provide a physical barrier to reduce water loss. Emmollients (petrolatum, lanolin, mineral oil) provide occlusivity and smooth flaky skin cells [4,5].

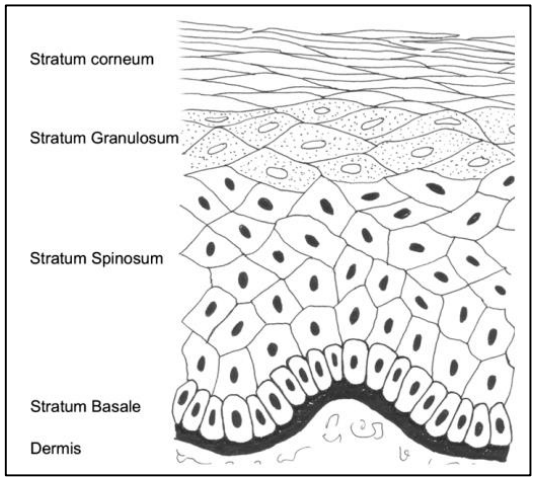

Figure 1. The five layers of epidermis.

Near-infrared reflectance spectroscopy

Near-infrared light penetrates deeper in tissue than visible light. In the spectral range of 900 nm to 1700 nm, light penetrates 1 mm up to 3 mm deep into the skin [6]. Thus, the diffuse reflected light brings information from different layers of skin. Besides, the penetration depth is dependent on water concentration in skin.

Previous studies on near-infrared reflectance spectroscopy as a technology for determination of in vivo skin moisture level can be found since 1990s. In 1993, Martin suggested a method to quantitate water on a relative basis to distinguish free, bulk and bound water, as well as additionally using scattering off the skin surface as a measure of skin smoothness [7]. In 2005, Suh et al presented work of doing *in vitro* skin moisture measurements on hairless mouse, as well as *in vivo* skin moisture measurements on human inner arm by FT NIR spectrometer. They used partial least squares regression to develop a calibration model by comparing near-infrared reflectance spectroscopy results to the conventional capacitance method [8]. In 2006, Iwasaki et al introduced a NIR spectral imaging system consisting of an indium gallium arsenide (*InGaAs)* NIR camera, halogen bulb light source and optical filters (1060 nm and 1450 nm) to differentiate skin where a moisturizer has been applied [9]. In 2011, Egawa et al suggested an imaging system for analysis of both water and oil content in facial skin by using a sensitive *InGaAs* NIR camera in the spectral range 1100 nm – 2200 nm which was also able to acquire images of skin at 1920

nm which is the strongest water band in this spectral range. They suggest that at 1920 nm it is possible to detect even small changes in water concentration in skin [10].

EXPERIMENTAL

In this study, a simple experimental setup was used to measure skin reflectance spectrum changes over time after applying two different moisturizers. Different body sites were measured with variety in thickness. The measurements were done in the spectral range of 900 nm – 1700 nm.

Experimental setup

Experimental setup consisted of a near-infrared spectrometer (*Ocean Optics*, *NirQuest 512*) in the spectral range of 900nm – 1700nm, Y-type water free (WF) optical fiber probe, a halogen bulb light source, and a 3D printed nozzle as a spacer to separate skin from the detection and illumination fibers (Figure 2). Optical fiber probe consisted of 6 illumination fibers in a circle around 1 detection fiber in the middle without any spaces. The distance between optical fiber ends to the skin surface of interest was kept constant of 5 mm by the nozzle (outer diameter 25 mm, inner diameter 4 mm).

During measurements, room temperature was kept at 23°C. Room was dark to avoid any disturbances.

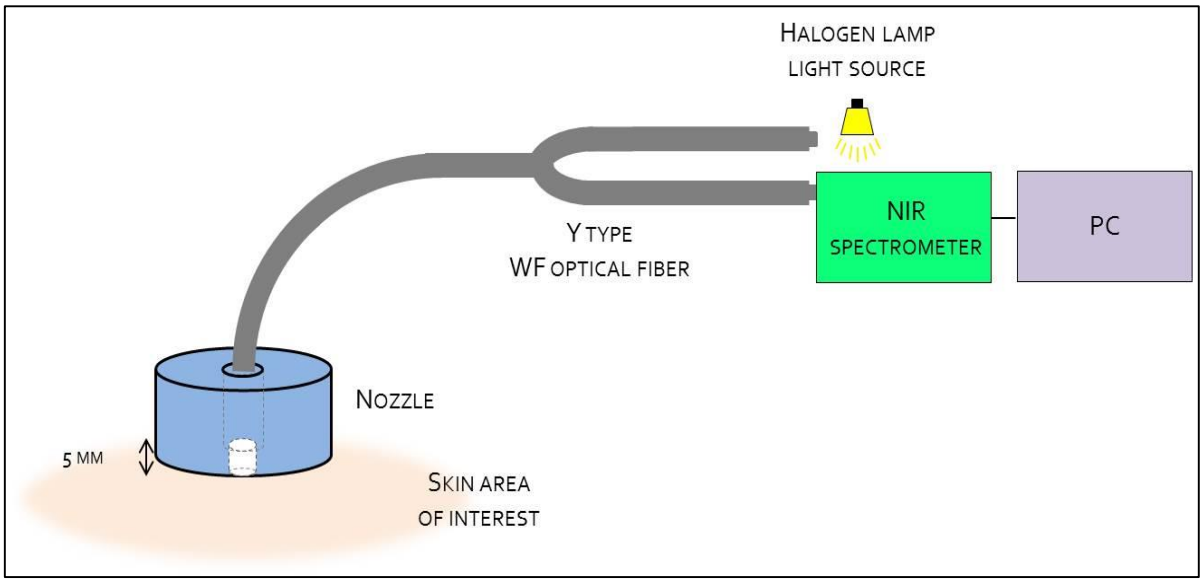

Figure 2. Experimental setup.

Data acquisition

During short time measurements (up to 15 minutes), the nozzle was kept fixed on the skin surface by using a tripod, and the arm (or some other body part) was kept as motionless as possible during the whole measurement. During longer time measurements (up to many hours), the nozzle wasn't kept constantly fixed on the skin surface. Instead, it was only put on skin surface when it was time to acquire data (e.g. once in every hour). In this case, the specific skin area was marked as precisely as possible with black markers around the nozzle in order to be able to put the nozzle exactly at the same place as the previous time.

Data analysis

Reflectance spectra were converted to absorbance values by using formula:

$$A = log_{10} \frac{I_0}{I} \quad (1)$$

where I_0 is the initial light from halogen bulb light source, measured as the reflected light from *Avantes WS-2* reference tile for specular reflection measurements in 350-1800 nm, and I is the diffuse reflected light.

For comparison of difference in absorption at particular wavelengths (e.g. 1300 nm and 1420 nm), an absorption difference parameter was introduced:

$$A_{1420-1300} = A_{1450} - A_{1300} = log_{10} \frac{I_{1300}}{I_{1450}} \quad (2)$$

where A_{1420} and A_{1300} are absorption values in relative units at the respective wavelengths.

During measurements, it was noticed that the spectrum is very sensitive to even small changes in with how much pressure the nozzle is applied to the skin surface. As an example, Figure 3 shows absorption spectrum changes due to different pressure (less, medium and more pressure). As it was quite clear that these changes are not due to changes in skin moisture level, all spectra acquired at the same measurement were normalized by subtracting the absorption value at 900 nm from each of the other wavelengths in the whole spectrum of one measurement.

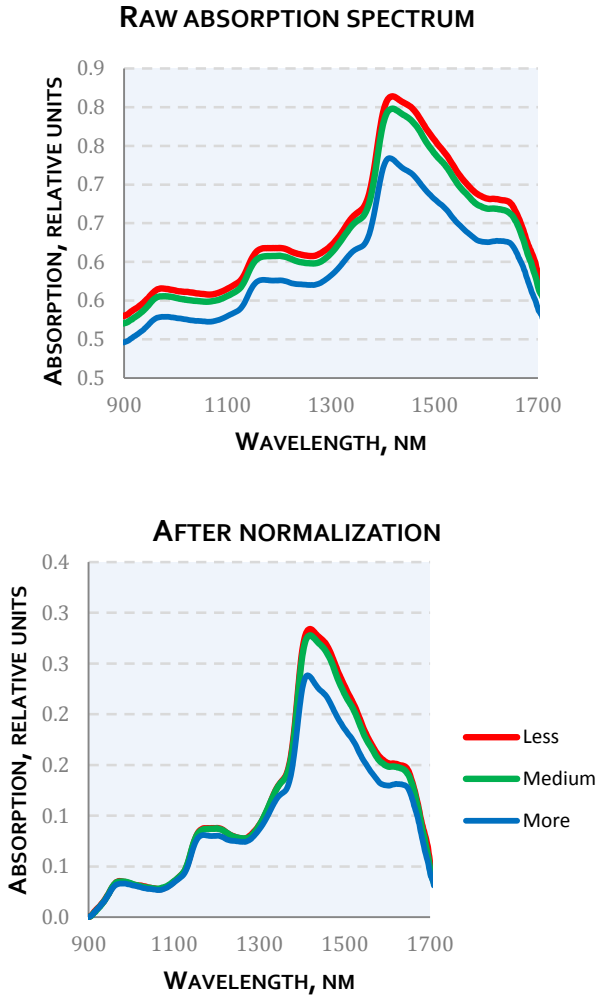

Figure 3. Left: an example of raw absorption spectra when applying different pressure on skin surface (less, medium and more) with the nozzle; Right: after normalizing spectra by subtracting absorption value at 900 nm for the whole spectrum.

Figure 3 shows that even after normalization absorption spectra differ just because of applied pressure difference. When the nozzle is pushed strongly to the skin surface, it appears that the absorption

decreases. That could mean that there actually is a temporary water loss in the upper skin layers due to pressure as some water is squeezed out of the upper layers of the skin. In future measurements, the nozzle was just put on skin surface without pushing it.

RESULTS

Absorption changes over time

Absorption peak values at 980 nm, 1050 nm, 1200 nm, 1300 nm, and 1420 nm were chosen for observing skin absorption changes over time after application of a moisturizer. Further, two examples are shown: moisturizer was applied on a wrist of two volunteers with healthy skin: in Figure 4, a female, 26 years old, skin type II; in Figure 5, a male, 29 years old, skin type III. As could be expected, the best changes can be seen at the wavelength of 1420 nm as it has the highest water absorption in the spectral range of 900 nm – 1700 nm. At shorter selected peak wavelengths (980 nm and 1050 nm) result is noisy.

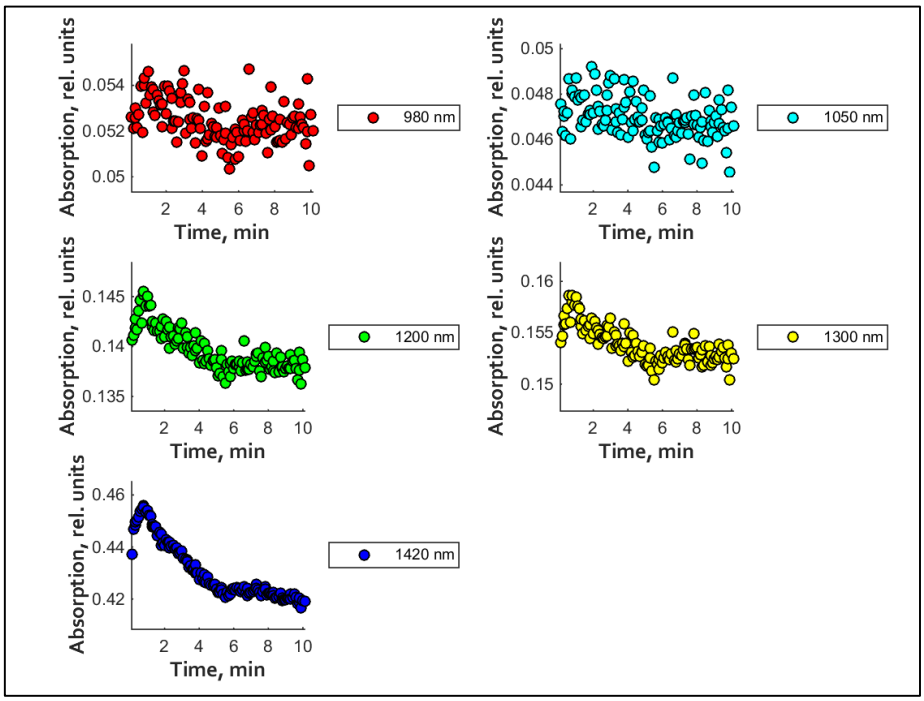

Figure 4. Absorption changes over time after application of a moisturizer on a wrist of a female, 26 years old, skin type II, healthy skin.

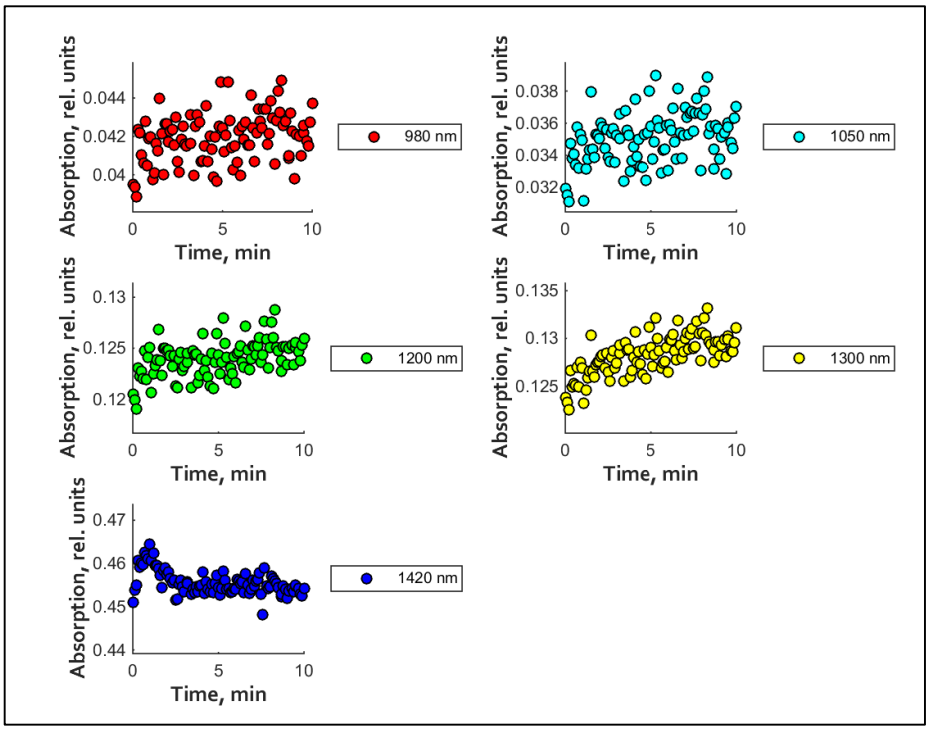

Figure 5. Absorption changes over time after application of a moisturizer on a wrist of a male, 29 years old, skin type III,
healthy skin.

Differences in absorption spectra of normal and dry skin

Difference in absorption spectra of dry and normal skin is shown in Figure 6. On the left image, difference in absorption of healthy skin on upper foot (both legs) and dry and rough skin on heel (sole) skin can be seen. On the right image, absorption of skin at two different body sites is shown: upper leg visibly looked healthy, however, lower leg visibly looked dry and rough. As it can clearly be seen in Figure 6, absorption values are lower for dry skin.

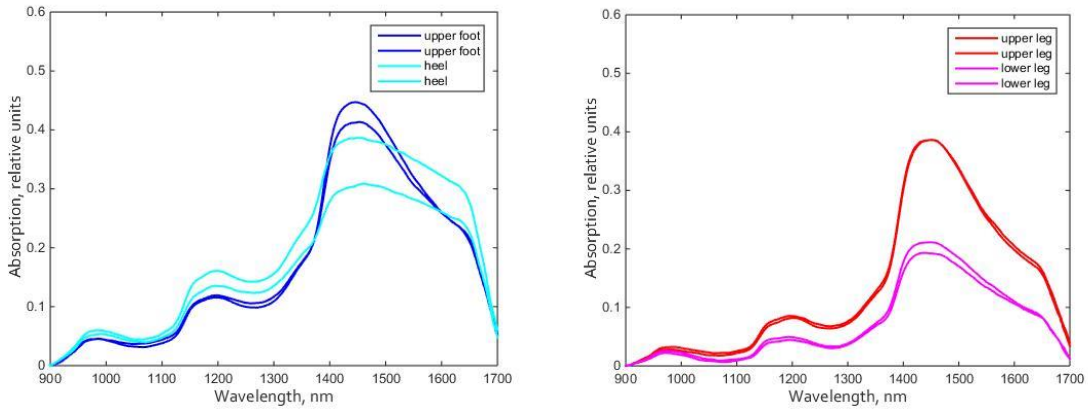

Figure 6. Comparison of absorption spectra for different body sites and dryness of skin. On the left: heel skin (dry, rough and thick) and upper foot skin. On the right: upper leg skin (healthy), compared to lower leg skin (visibly dry and rough).

Absorption changes over time at different body sites and 2 different moisturizers

Measurements of absorption changes over time of totally 8 hours were acquired after application of two different moisturizers: 1 and 2. Two different body sites of a female volunteer, 26 years old, skin type II, were measured: lower leg (both legs) and both soles. Lower leg was considered to be dry, and sole

skin was thicker and rougher. Absorption difference between 1420 nm and 1300 nm over time is shown in Figure 7. Moisturizer 1 was applied on left part, and moisturizer 2 was applied on right part of the body. At each time period of data acquisition (approximately 1, 2, 3, 4, 5 and 8 hours after moisturizer was applied on skin), 7 different measurements were done by putting the nozzle on skin each time separately. This was done to see how the data points scatter do to measurement error: it is not possible to put the nozzle back at exactly the same spot every time, even though markers were used.

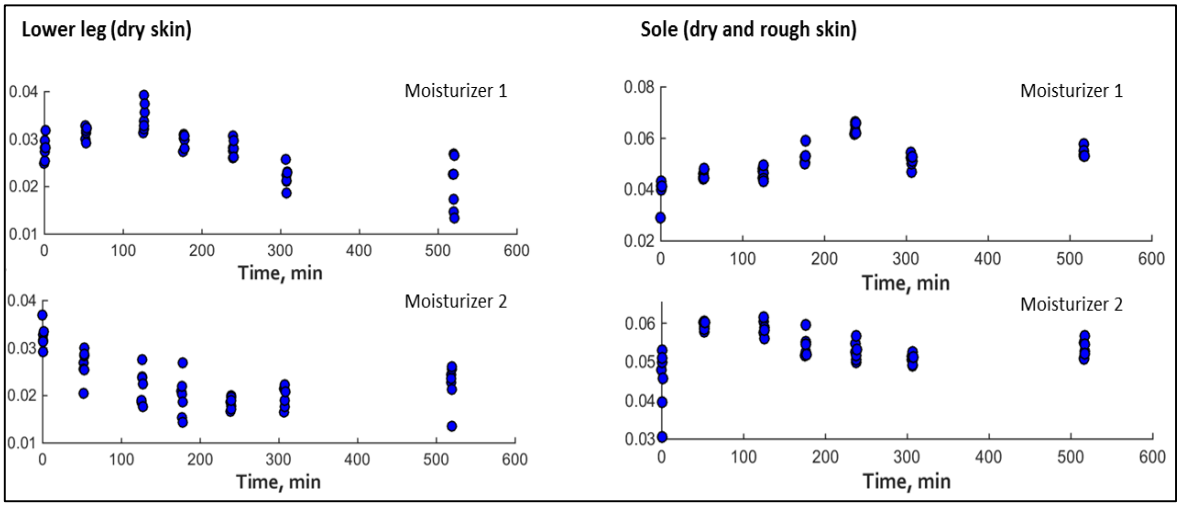

Figure 7. Absorption changes over time of 8 hours at two different body sites (lower leg and sole skin).

Conclusions and discussion

In this study, a simple near-infrared reflectance spectroscopy setup was used to analyze skin moisture changes over time and at different body sites. Difference in skin moisture levels (the dryness of skin) was seen visibly and also as a difference in absorption. The dryer and rougher the skin surface, the lower are absorption values, especially at the peak values of water absorption spectra (1200 nm, 1450 nm) that are the most sensitive to water concentration changes. Absorption spectrum of skin is similar to absorption spectra of water, as skin consists largely of water. Thus, a very sensitive detector is needed to see small changes in water concentration. This work shows possibilities to detect skin moisture level changes at the wavelength of 1420 nm. Although water absorption maximum is at 1450 nm, the wavelength of 1420 nm was chosen, because it was the peak value of the experimentally obtained absorption spectra of skin.

When analyzing results of changes in absorption over time, after a moisturizer has been applied, it can be seen that there is an increase in absorption during the first minute, and afterwards there is a slow decrease. This could be related to how the moisturizer slowly penetrates deeper in the tissue. The increased absorption at the beginning can be explained as an increase in water level because a moisturizer containing water and oil is applied. However, after some time the moisturizer has penetrated the tissue which could lead to a lower absorption.

As could be expected, absorption at peak wavelengths decreases for dry skin as there is less water in dry skin. This was shown in an example when comparing dry and healthy skin on legs of a volunteer.

Measurements of absorption changes at 1420 nm over 8 hours were analyzed at two different body sites. Both body sites had dry skin; however, on sole the skin is also much thicker and rougher. When comparing 1st moisturizer's effect on both body sites, we can see that in the case of the lower leg, absorption increases until 2 hours compared to around 4 hours in the case of sole skin. This could mean that more time is needed for the moisturizer to penetrate into rougher and thicker skin. When looking at the results of moisturizer 2, it is interesting to see that there seems to be a faster decrease in absorption than in the case of moisturizer 1. This could be related to different ingredients of both moisturizers, but in this study it wasn't analyzed any further.

For longer measurements (e.g. 8 hours) the nozzle cannot stay unmoved on the skin surface, and even with the use of markers on skin, it is almost impossible to put the nozzle back at exactly the same spot

every time. It was noted that there is quite a huge variation in data when comparing absorption spectra at the same time moment and the same measurement site, meaning, that the system is very sensitive to small differences in the measurement location, as well as pressure applied to skin with the nozzle. This experimental setup didn't allow use of near-infrared polarizers, so the reflection of skin can give its effect on results.

Acknowledgments

This work has been supported by the European Social Fund within project "Innovative biomedical image acquisition processing technologies (InBiT)" (No.2013/0009/1DP/1.1.1.2.0/13/APIA/VIAA/014).

REFERENCES

[1] Fluhr, J. W., Gloor, M., Lazzerini, S., Kleesz, P., Grieshaber, R. and Berardesca, E., "Comparative study of five instruments measuring stratum corneum hydration (Corneometer CM 820 and CM 825, Skicon 200, Nova DPM 9003, DermaLab). Part II. In vivo," Skin Research and Technology 5, 171-178 (1999).

[2] De Rigal, J., Losch, M. J., Bazin, R., Camus, C., Sturelle, C., Descamps, V. and Leveque, J. L., "Near-infrared spectroscopy: A new approach to the characterization of dry skin," J. Soc. Cosmet. Chem. 44, 197-209 (1993).

[3] Wickett, R. R., Visscher, M. O., "Structure and function of the epidermal barrier," American Journal of Infection Control 34(10), S98-S110 (2006).

[4] Dobos, K., "How Do Skin Moisturizers Work?" Chemists Corner, 3 April 2014, <http://chemistscorner.com/how-do-skin-moisturizers-work/> (5 January 2015).

[5] "emollients - topical", MedicineNet, 16 April 2014, <http://www.medicinenet.com/emollients-topical/article.htm > (5 January 2015).

[6] Bashkatov, A. N., Genina, E. A., Kochubey, V. I., Tuchin, V.V., "Optical properties of human skin, subcutaneous and mucous tissues in the wavelength range from 400 to 2000 nm," J. Phys. D: Appl. Phys. 38, 2543-2555 (2005).

[7] Martin, K. A., "Direct measurement of moisture in skin by NIR spectroscopy," J. Soc. Cosmet. Chem. 44, 249-261 (1993).

[8] Suh, E.-J., Woo, Y.-A. and Kim, H.-J., "Determination of Water Content in Skin by using a FT Near Infrared Spectrometer," Arch Pharm Res 28 (4), 458-462 (2005).

[9] Iwasaki, H., Miyazawa, K. and Nakauchi, S., "Visualization of the human face skin moisturizing-ability by spectroscopic imaging using two near-infrared bands," Proc. SPIE 6062, 606203-1 (2006).

[10] Egawa, M., Yanai, M., Kikuchi, K. and Masuda, Y., "Extended Range Near-Infrared Imaging of Water and Oil in Facial Skin," Applied Spectroscopy 65 (8), 924-930 (2011).

APPENDIX **II**

I. Saknite, D. Jakovels, G. Krievina, and J. Spigulis
"Diffuse reflectance and fluorescence measurements of skin by multispectral imaging system"
Proc. SPIE, 9129, 91293H (2014)

Diffuse reflectance and fluorescence multispectral imaging system for assessment of skin

Inga Saknite*, Dainis Jakovels, Janis Spigulis
Biophotonics Laboratory, University of Latvia, Raina Blvd 19, Riga, LV-1586, Latvia

ABSTRACT

The diffuse reflectance multispectral imaging technique has been used for distant mapping of *in vivo* skin chromophores (hemoglobin and melanin). The fluorescence multispectral imaging is not so common for skin applications due to complicity of data acquisition and processing, but could provide additional information about skin fluorophores. Both techniques are compatible, and could be combined into a multimodal solution.

The multispectral imaging system *Nuance* based on liquid crystal tunable filters was adapted for diffuse reflectance and fluorescence spectral imaging of *in vivo* skin. Uniform illumination was achieved by LED ring light. Combination of four LEDs (warm white, 770 nm, 830 nm and 890 nm) was used to support diffuse reflectance mode in spectral range 450-950 nm. 405 nm LEDs were used for excitation of skin autofluorescence. Multispectral imaging system was adapted for spectral working range of 450-950 nm with scanning step of 10 nm and spectral resolution of 15 nm. An average field of view was 50x35 mm in size with spatial resolution 0,05 mm (the pixel size). Due to spectrally different illumination intensity and system sensitivity, various exposure times (from 7…500 ms) were used for each image acquisition.

The proposed approach was tested for different skin lesions: benign nevus, hemangioma, basalioma and halo nevus. Spectral image cubes of different skin lesions were acquired and analyzed to test its diagnostic potential.

Keywords: Multispectral imaging, diffuse reflectance, autofluorescence, skin.

*inga.saknite@lu.lv; phone 00 371 29162679

INTRODUCTION

Multispectral imaging is a non-contact method that can be used for noninvasive mapping of skin chromophores, e.g. hemoglobin and melanin [1,2]. Fluorescence imaging gives information about skin fluorophores [3,4]. The characteristic absorption and emission spectra of skin fluorophores are shown in Figure 1. Diffuse reflectance and fluorescence multispectral imaging can be combined in a multimodal solution for analysis of skin lesions.

Multispectral imaging system based on liquid crystal tunable filters in combination with a light source of different LEDs in the visible and near-infrared spectral range can be adapted for acquisition of multispectral image cubes. These multispectral images can be later analyzed to acquire chromophore concentration maps and skin autofluorescence spectra.

Goal of this study was to test the developed system that combines diffuse reflectance and fluorescence multispectral imaging techniques by acquiring multispectral image cubes of different pigmented skin lesions. The drawback of this multimodal solution is time-consuming data acquisition and processing, as well as motion artefacts.

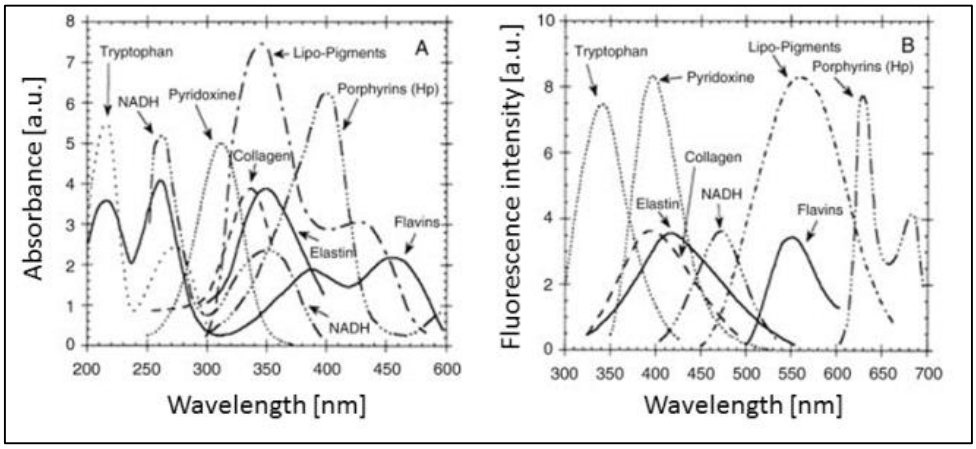

Figure 1. The characteristic absorption (to the left) and emission (to the right) spectra of skin fluorophores [3].

EXPERIMENTAL

Experimental setup

Multispectral imaging setup consisting of multispectral imaging system *CRi's Nuance*, light source of LED ring light, diffuser in front of the light source, as well as a computer with *Nuance* software was used for image acquisition in the spectral range of 450-950 nm.

Light source was developed as a ring light consisting of LEDs to cover the spectral range of 450-950 nm for diffuse reflectance mode: warm white, 770 nm, 830 nm and 890 nm. Spectra of used LEDs are show in Figure 2. Diffuser in front of the light source was used to achieve a uniform illumination of the skin area of interest.

Light source comprised an inner circle of violet (405 nm) illumination LEDs for skin autofluorescence imaging. No diffuser was used in front of ultraviolet LEDs.

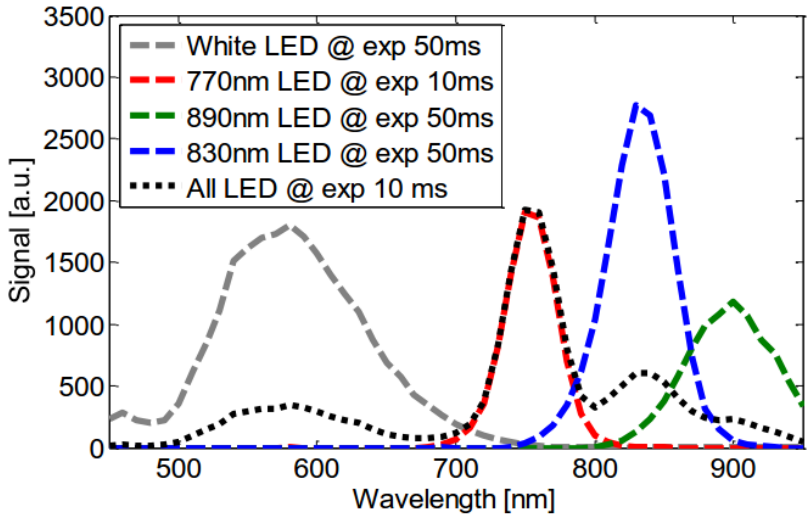

Figure 2. Spectra of illumination LEDs for diffuse reflectance mode at different exposure times.

Data acquisition and processing

For diffuse reflectance imaging mode, various exposure times (from 7…500 ms) were used for each wavelength in the spectral range of 450-950 nm due to spectrally different illumination intensity and system sensitivity. Images were acquired with a spectral step of 10 nm at wavelengths in the spectral range of 450-950 nm. Maximum pixel resolution was used.

For fluorescence mode, a constant exposure time of 200 ms was used to acquire images in the spectral range of 450-950 nm with a spectral step of 10 nm. Reduced pixel resolution was used by combining 4 pixels in 1 pixel.

As image acquisition process takes approximately 30-40 seconds for diffuse reflectance mode and 20-30 seconds for fluorescence mode, motion artefacts are unavoidable. Thus, image registration was performed for each image cube. Simple stickers were applied to the skin area around the lesion in order to improve the image registration performance. Image segmentation was used to distinguish the lesion from normal skin (Figure 3).

For diffuse reflectance imaging mode, optical density (OD) images were obtained:

$$OD = -log\frac{I}{I_0} \quad (1)$$

where I_0 are reference intensity values acquired by using a white reference reflector before the measurement of skin area of interest, and I are intensity values acquired of skin area of interest.

Average spectrum of segmented area of the lesion and segmented area of normal skin around the lesion was calculated by analyzing each image pixel of skin area of the lesion and skin area of normal skin for both modalities: diffuse reflectance and fluorescence imaging.

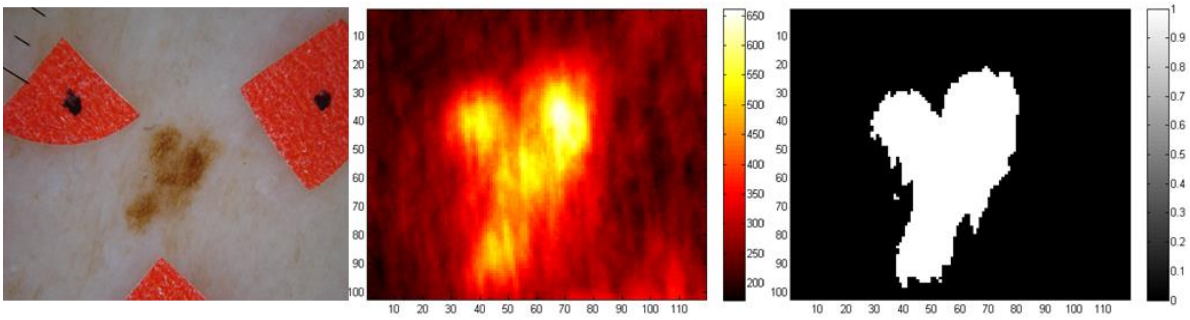

Figure 3. Example of diffuse reflectance data of a lesion: RGB image (to the left), optical density color map at 580 nm (in the middle), segmented lesion (to the right).

RESULTS

Pilot study was performed on 30 volunteers by acquiring diffuse reflectance and fluorescence images of 40 skin lesions: 23 benign nevi, 14 atypical nevi, and 3 other interesting lesions: hemangioma, basalioma and halo nevus. Dermatologist examined all volunteers to classify the lesions. In this study, 3 interesting lesions were further analyzed and compared to benign nevi (Figures 4-7). For diffuse reflectance imaging mode, a map of Optical density values at 580 nm is shown, as well as comparison of the average diffuse reflectance spectra of skin areas of interest (area of the lesion and area of normal skin around the lesion). For fluorescence imaging mode, a map of fluorescence intensity values at 580 nm is shown, as well as comparison of the average skin autofluorescence spectra of skin areas of interest. Also, an RGB image of the lesion and surrounding tissue is shown for each example.

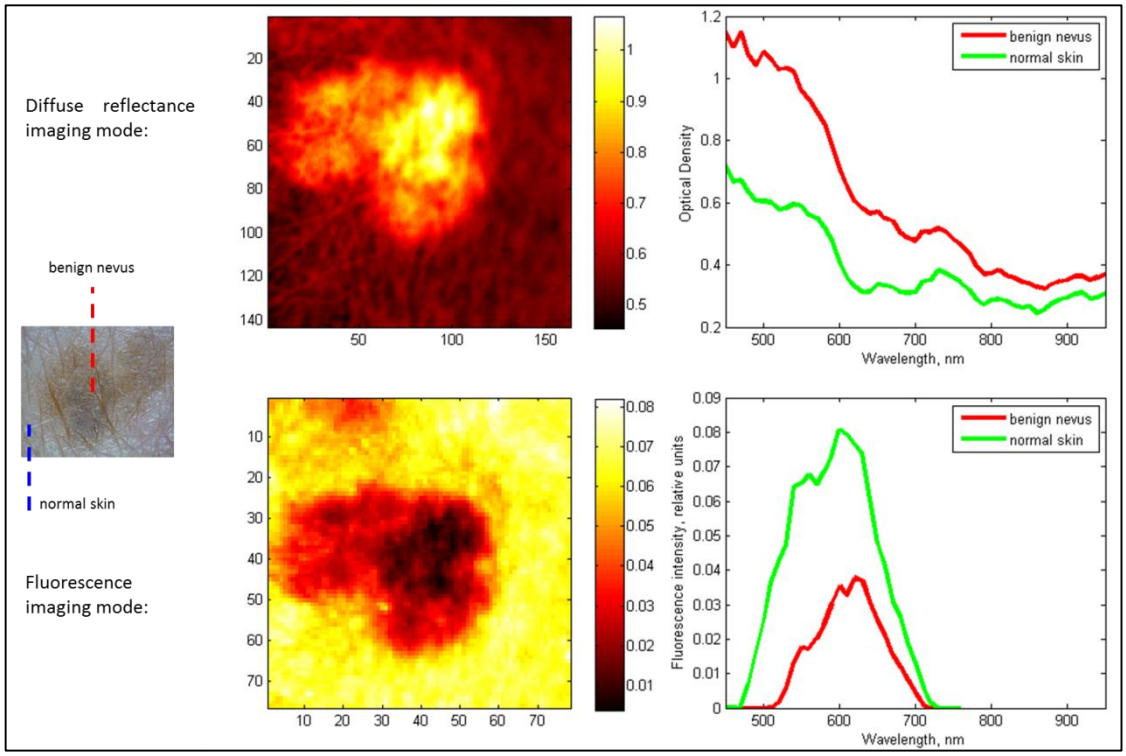

Figure 4. Diffuse reflectance and fluorescence imaging data analysis of **benign nevus**.

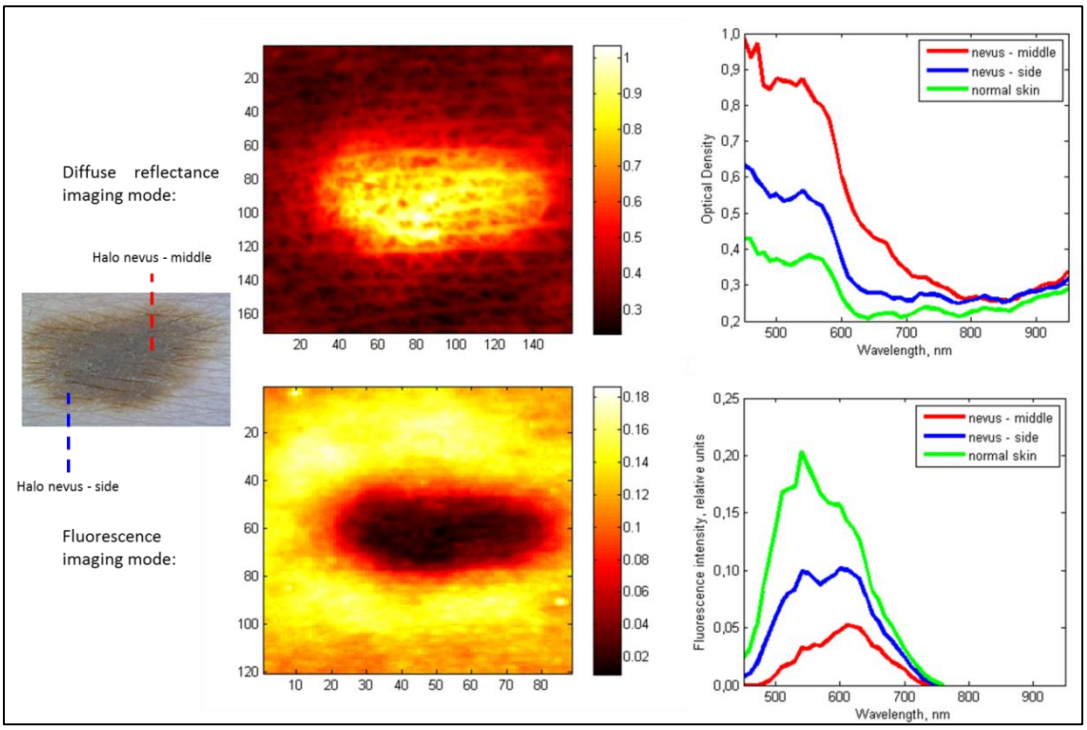

Figure 5. Diffuse reflectance and fluorescence imaging data analysis of **halo nevus**.

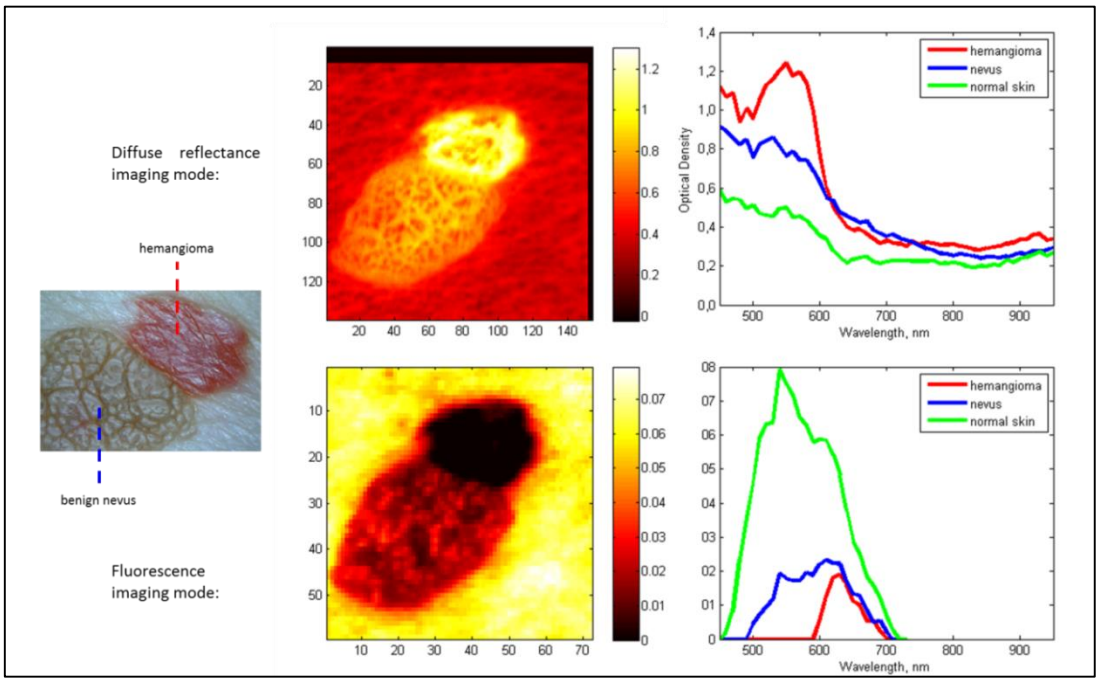

Figure 6. Diffuse reflectance and fluorescence imaging data analysis of **hemangioma** and **benign nevus**.

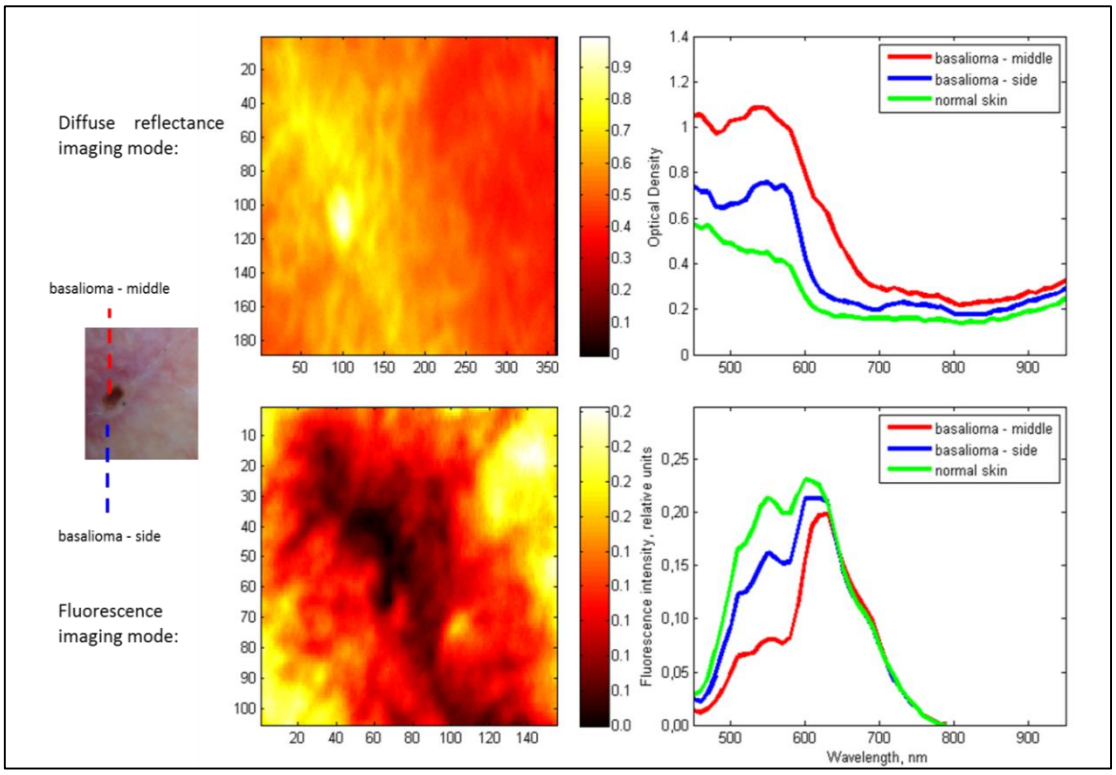

Figure 7. Diffuse reflectance and fluorescence imaging data analysis of **basalioma**.

DISCUSSION

Diffuse reflectance spectra of different skin lesions give information about the main chromophores that absorb light in the spectral range of 450-950 nm: hemoglobin and melanin. For benign nevi and halo nevus (Figures 4-6), reflectance spectra has the characteristics of melanin absorption spectrum – the average reflectance spectrum is *steeper* in the area of a pigmented lesion than in the area of normal skin, as there is an increased concentration of melanin in pigmented skin lesions like nevi. When looking at diffuse reflectance spectra of hemangioma and benign nevus (Figure 6), it is easy to see that the average spectrum of hemangioma shows the characteristic absorption maxima of hemoglobin at around 540 nm and 580 nm, comparing to the average reflectance spectrum of benign nevus and normal skin. Also, diffuse reflectance spectra of different parts of basilioma (Figure 7) show interesting results – both, the middle and side part of basilioma show an increased hemoglobin absorption, comparing to normal skin.

Characteristic absorption and emission data of skin fluorophores (Figure 1) suggest that when illuminating skin with 405 nm LEDs as was done in this study, main absorbing fluorophores would be Lipo-Pigments, Porphyrins and Flavins. Emission spectra of these fluorophores show that Lipo-Pigments emit light in the spectral range of 450-700 nm (with a maximum at 570 nm), Porphyrins emit light in the spectral range of 600-700 nm (with maxima at 630 nm and 670 nm), and Flavins emit light in the spectral range of 500-600 nm (with a maximum at 550 nm).

Results of this study show different skin autofluorescence spectra of different skin lesions that were analyzed. The average fluorescence spectra of the area of normal skin show similar patterns in all four analyzed cases: light is emitted in the spectral range of 450-700 nm that could be the autofluorescence of skin fluorophores Lipo-Pigments and Flavins. There is a decrease of detected fluorescence intensity in the regions of pigmented lesions, as expected. However, when looking at skin lesions with an increased hemoglobin concentration (hemangioma and basalioma, Figure 6-7), there is a significant decrease of fluorescence intensity in the spectral range of 500-600 nm, comparing the areas of pigmented lesion and normal skin. This is probably due to the increased hemoglobin absorption in this spectral range.

CONCLUSIONS

In this study, diffuse reflectance imaging and fluorescence imaging were combined in a multimodal solution and 4 different skin lesions were analyzed: benign nevus, halo nevus, hemangioma and basalioma. Diffuse reflectance and skin autofluorescence spectra of pigmented lesions and normal skin around the lesions were acquired and compared.

Results show differences in diffuse reflectance and fluorescence spectra due to different hemoglobin and melanin concentrations.

ACKNOWLEDGMENTS

This work has been supported by the European Social Fund within project "Innovative biomedical image acquisition processing technologies (InBiT)" (No.2013/0009/1DP/1.1.1.2.0/13/APIA/VIAA/014).

REFERENCES

[1] Välisuo, P., Kaartinen, I., Tuchin, V., Alander. J., "New closed-form approximation for skin chromophore mapping," J. Biomed. Opt. 16(4), 046012 (2011).

[2] Jacques, S. L., Samatham, R., Choudhury, N., "Rapid spectral analysis for spectral imaging," Biomed. Opt. Express 1(1), 157-164 (2010).

[3] Monici, M., "Cell and tissue autofluorescence research and diagnostic applications," Biotechnol. Annu. Rev. 11, 227-256 (2005).

[4] Alfono, R., Tata, D., Cordero, J., et al, "Laser induced fluorescence spectroscopy from native cancerous and normal tissue," IEEE J. Quant. Electron. 20(12), 1507-1511 (1984).

A. Silapetere, J. Spigulis, and I. Saknite
"Development and Experimental Study of Phantoms for Mapping Skin Chromophores"
Latv. J. Phys. Tech. Sci., 51(3) (2014)

DEVELOPMENT AND EXPERIMENTAL STUDY OF PHNTOMS FOR MAPPING OF SKIN CHROMOPHORES

A.Silapetere, I.Saknite, J.Spigulis

Biophotonics Laboratory
Institute of Atomic Physics and Spectroscopy, University of Latvia,
19 Raina Blvd., LV-1586, Riga, LATVIA
e-mail: arita.silapetere@gmail.com

Nowadays biomedical imaging is widely used to its numerous advantages: information about skin can be received in real time and noninvasively. Even though there are different spectral imaging techniques and methods already developed, only relative parameter values can be acquired by analysing multispectral images obtained. In multispectral imaging techniques, for determination of human skin parameters and physiological properties, it is important to better understand light interaction with tissue and to examine techniques used for measurements by calibration with skin phantoms. In this study, a skin phantom was created by using biological and chemical substances.

Keywords: skin phantom, multi-spectral imaging, skin chromophore mapping, bilirubin, melanin, haemoglobin.

1. INTRODUCTION

Since long time ago, light has been a useful tool for medical applications. Nowadays these applications include health care from neurosurgery to medical diagnostics. In this study, the field of interest is applications for human skin diagnostics. Optical methods are widely used in medicine due to numerous advantages: information about skin tissue can be obtained noninvasively and in real time, it can be a low cost technology and it doesn't affect patient's health in any known way [1]. Multi-dimensional pictures of skin are obtained by the wide range spectral imaging techniques and methods that have been developed, and only relative parameter values can be then calculated by using Beer-Lambert's law [2]. In order to better understand the physiological properties of skin and to calibrate the spectral imaging devices, there is a great need for a human tissue phantom. Human tissue phantoms or skin phantoms can be developed with known optical properties (absorbance and scattering). Optical

properties should be comparable to optical properties of tissue; they should be stable in time, so that they can be used as golden standards.

There has been research already done for the purpose to develop skin phantoms. In skin phantoms mostly water, agar, polyester, polyurethane, silicon, polydimethylsiloxane, fat and milk have been used as matrix materials. Phantoms containing hydrogel are appropriate for laboratory study for mimicking biological properties. Polymaterials and silicones are desirable for routine calibration as they are stable in time. As scattering media, titanium oxide powder, aluminium oxide powder, lipid based emulsion have been used. Wide ranges of materials are used as absorbers, for example, molecular dyes, inks, cells, haemoglobin cells, coffee, nigrosin [3-9].

In visible and near infrared spectroscopy it is crucial for phantoms to mimic layered structure and chemistry of the tissue. Biologically compatible structures are more suitable for these measurements than nonorganic polymers and silicones. Tissue engineering has developed to the point where biological structures can be created or grown in culture. Skin phantoms should have layered structure to modulate the unique structure of human skin. For molecular imaging techniques, more suitable skin phantoms are those that have molecular properties similar to human skin. Biological tissue simulating phantoms have the potential to become main calibration structures for molecular imaging systems [3].

In this study, a biologically compatible phantom was created. Fibrin matrix was chosen as the main medium for the skin phantom. Fibrin matrix allows an easy epidermal and dermal cell and chromophore (haemoglobin, bilirubin) inclusion that were used as absorbers. This allows accurate simulation of layered structure and the chemistry of skin.

Biological phantoms have a variety of applications, for example, different apparatus performance comparison, skin diagnostic equipment quality control and system testing [3].

When light interacts with human skin, some par of it is instantly reflected and some of it penetrates skin where it undergoes multiple scattering, some of it is being absorbed and diffuse reflected. By analysing diffuse reflected light, it is possible to get information about absorption in the tissue. With this technique, we consider scattering only as light transport and don't analyse it in more detail. (Fig.2.) [10]

Skin is a heterogeneous, multi-layered structure consisting of different absorbers. In so called therapeutic window that covers the spectral range from 600nm to 1300nm and shows the spectral range in which water absorption is very little, most tissue are weak absorbers, for example, tryptophan, NADH, collagen, elastin. In the spectral region of interest (450nm to 900nm) these tissue also have insignificant absorption properties. In this spectral range, absorbers with the most significant spectrum are haemoglobin, deoxyhaemoglobin, bilirubin and melanin. These are the chromophores within human skin that are responsible for the colour of skin and can give information about skin condition and human health as well [11].

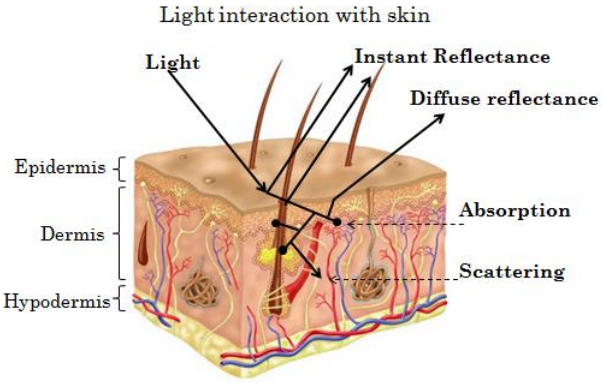

Fig.2. Light interaction with skin

Bilirubin is the breakdown product of heme degradation. Bilirubin is excreted in urine and bile; increased bilirubin concentration in these fluids may indicate health problems. Bilirubin concentration in skin is relatively low. Bilirubin concentration is increased in bruises - it is responsible for the yellow colour in bruises [12]. In Fig.3 absorption spectrum of bilirubin is shown.

When human skin is exposed to UV light, melanocytes produce melanin. Melanin serves as a photoprotectant; it minimizes damage done to human body and skin by UV radiation. It is responsible for skin tone - the higher melanin concentration in human skin, the darker is the skin tone. Melanin concentration is higher in birth marks and melanomas. In Fig.3.the absorption spectrum of melanin is shown [13].

Haemoglobin attached to red blood cells serves as an oxygen-transport in human body. Oxy-haemoglobin carries oxygen from lungs to other organs. It gives blood its red colour [14]. Oxy-haemoglobin and deoxy-haemoglobin structural differences result in differences in absorption spectrum in the spectral range from 500 nm to 600 nm In Fig.3 absorption spectrum of oxy-haemoglobin and deoxy-haemoglobin is illustrated.

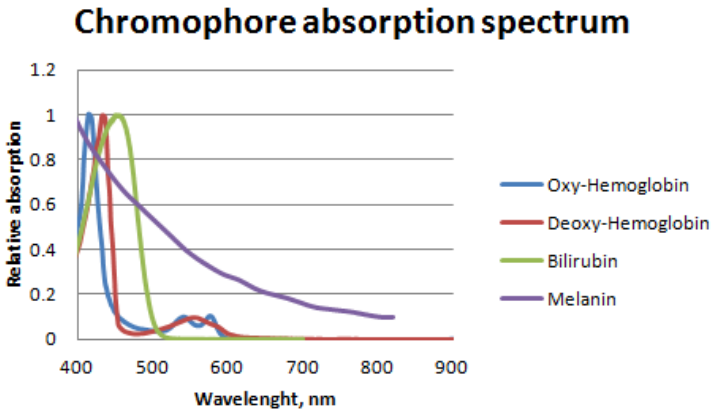

Fig.3. Chromophore absorption spectrum [15, 16].

2. EXPERIMENTAL

In this research, a phantom of skin was developed and its optical properties (absorption and scattering) were analysed. Different phantoms were examined and compared to find the most suitable. In this article, the most promising ones will be discussed. The main focus is on biologically equivalent substances. For mimicking skin medium and layered structure, fibrin matrix with epidermal and dermal cell inclusion was used. Synthesized bilirubin, red blood cells and nigrosin were used as absorbers. In order to analyse spectral properties of developed phantoms, a computer-aided multi-spectral imaging system *Nuance 2.4*(*Cambridge Research & Instrumentation, Inc*., USA) was used (Fig.1.). Data obtained are diffuse reflectance images of skin phantom in the visible and near infrared spectral range from 450 nm to 900 nm with step of 10 nm, thus making it an image sequence. A light source of three halogen lamps was used for illumination.

In front of the light source, there is a linear polarizer. The cross-polarization effect is used for reduction of instantly reflected light from the surface of the phantom. Linear polarizer in front of the light source is orthogonal to the built-in polarizer. The *Nuance 2.4* built-in polarizer is placed underneath the liquid crystal tuneable interface filter [17].

The spectral imaging device *Nuance 2.4* consists of tuneable interference filters that are used for spectral scanning. Light interaction with the medium differs depending on the wavelength of the light source [18]. For obtaining image sequence, different exposure times were used for each image at a particular wavelength; exposure time range was 1 to 6 milliseconds.

The computer program *Nuance 2.4* was set up with these parameters: 4x4 pixel binning and resolution of 0.15mm/pixel. Total resolution of the obtained image was 348x256 pixels. As a reference measurement, a thick piece of white paper was used. The surface area of examined phantoms is 1.886 cm^2. The distance between the sample and the camera was 17 cm. Time used for acquisition of one image sequence was approximately 20 seconds.

In the *Nuance 2.4* software, it is possible to obtain average spectrum of an area of the image that can be chosen by the user. For each image sequence, an average area spectrum was obtained and analysed using *Microsoft Office Excel 2007*. [19]

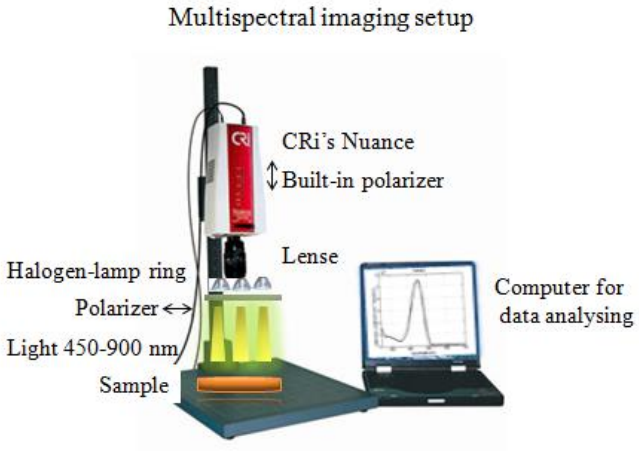

Fig.1. Experimental setup.

Fibrin matrix for skin phantoms can be prepared by mixing 0.47 ml blood plasma (47% of the solution), 0,4 ml 0,9% sodium chloride (40% of the solution), 0,8 µl tranexamic acid (0,8 mg/ml), 89,4µl calcium gluconate (8,94 mg/ml). To polymerize the solution, it was held for one hour in a cell incubator (temperature 37°C, CO_2concentration 5%). To make a complete phantom, the next step is to make the same solution, but adding dermal cells (180-270· 10^3 cells (fibroblast cell line – 7Dp3)). Afterwards, to polymerize the solution, it has to be held in the cell incubator for 10 minutes. The last step is to add

epidermal cells ($270 \cdot 10^3$ cells (keratinocyte cell line – 8Ep1)) and cell culture medium (Fetal bovine serum). To grow epidermal and dermal cells, the fibrin matrix with cellular inclusions are held in a cell incubator for at least two weeks [20].

To investigate absorption spectrum dependence on admixtures of absorbents, fibrin matrix without any cellular inclusions was made. In these experiments, to evaluate the determined chromophore phantom faster, fibrin matrix was used as medium for skin phantom as it takes only one day for it to be ready for measurements instead of two weeks that is the time needed to make a complete skin phantom with dermal and epidermal cells. Fibrin matrix can be used instead of full skin phantom because fibrin matrix and full skin phantom absorption is low comparing to that of synthesized bilirubin, nigrosin and haemoglobin. To examine calibration potential of the proposed skin phantom, 72 samples were made: each 24 contain the same absorbent in different concentrations. Synthesized bilirubin concentrations were 0,01 to 2,00 mg/ml, nigrosin concentrations were 1,5 to 312,8 μg/ml, red blood cell concentrations were 0,2 to 42,4 mg/ml. For further processing of the data, only 10 of 24 of the nigrosin samples could be used. 14 of the samples were oversaturated. Increasing the nigrosin concentration in the sample, the sample becomes dark purple, and most of the illumination light becomes absorbed instead of diffuse reflected.

For this study, a layered structure was made, that consisted of the bottom layer (volume: 0,3 ml, corresponding thickness: 0,16cm) of fibrin matrix, inclusion absorbent with variety of concentrations, and upper layer of fibrin matrix (volume:0,3 ml, corresponding thickness 0,16cm). In Fig.4 the visual appearance of samples is shown. The prepared sample maintains its optical properties up to one week. Afterwards, the biological structures break down and the spectrum of the sample changes.

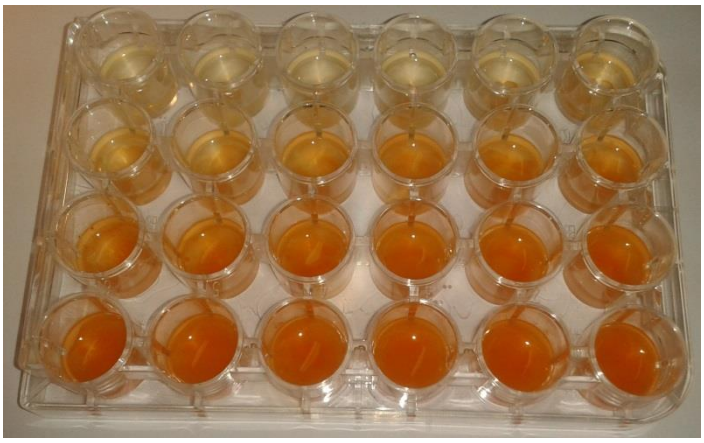

Fig.4. Sample of fibrin matrix with bilirubin inclusion of different concentrations.

3. RESULTS AND DISCUSSION

With the developed skin phantom, it was possible to imitate the spectrum of skin; it can be seen in Fig.5. In Fig.6, it is shown that absorber's concentration in the sample is high enough to imitate the determined chromophore absorption spectrum. Fig.7, Fig.8, Fig.9 illustrates relative intensity of the absorption spectrum dependence on concentration of the absorbent in the sample. We can see that intensity changes linearly to concentration of chromophore phantom in fibrin matrix. The data have been approximated.

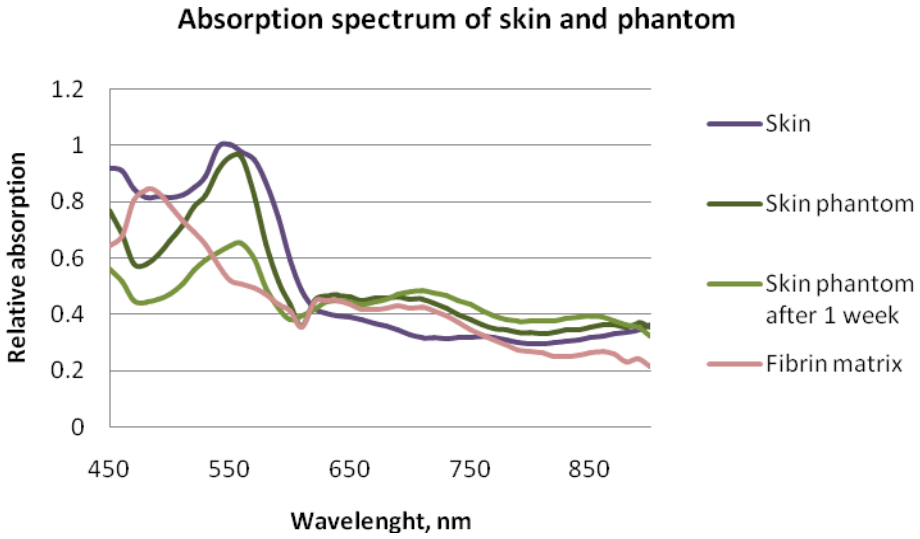

Fig.5. Absorption spectrum of human skin and skin phantom

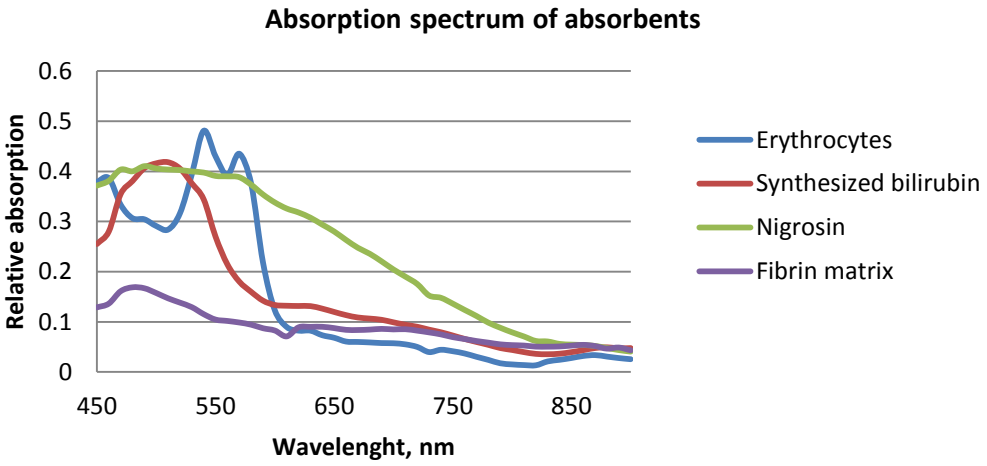

Fig.6. Absorption spectrum of absorbents.

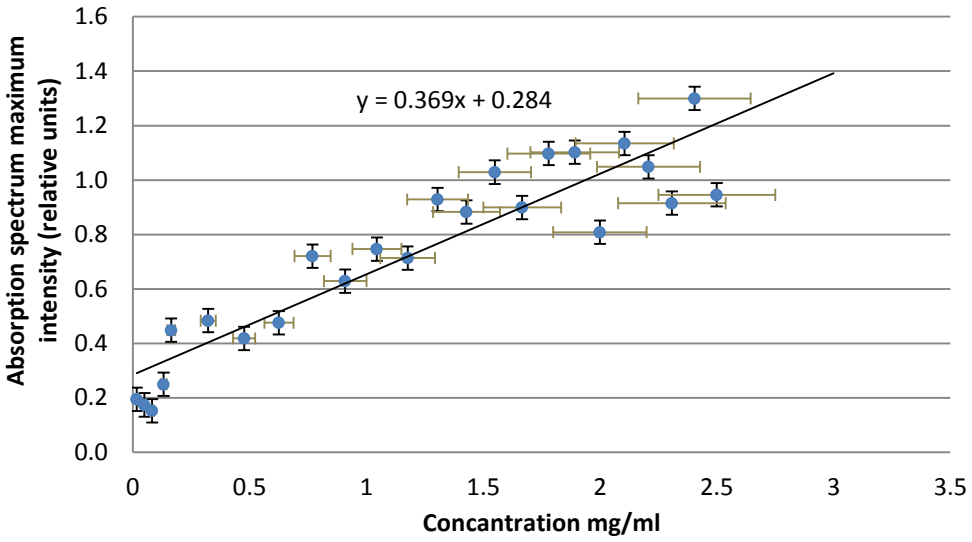

Fig.7. Absorption band intensity dependence on bilirubin concentration.

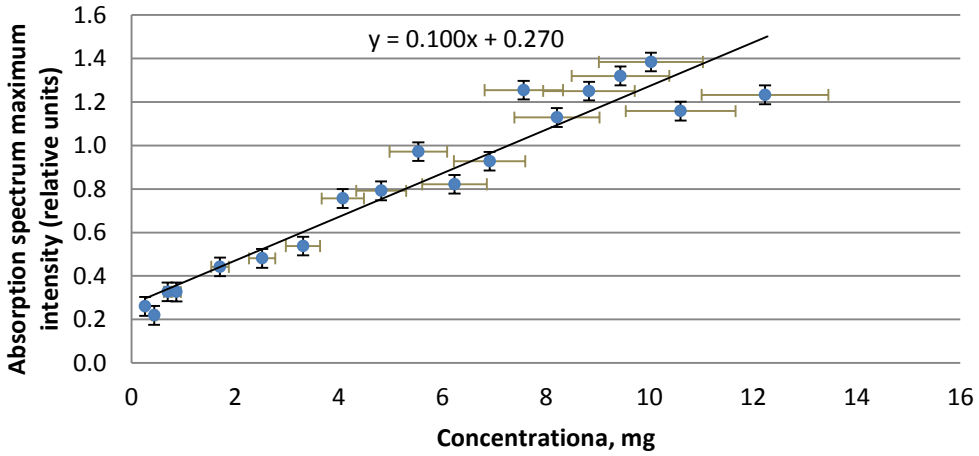

Fig.8. Absorption band intensity dependence on red blood cell concentration.

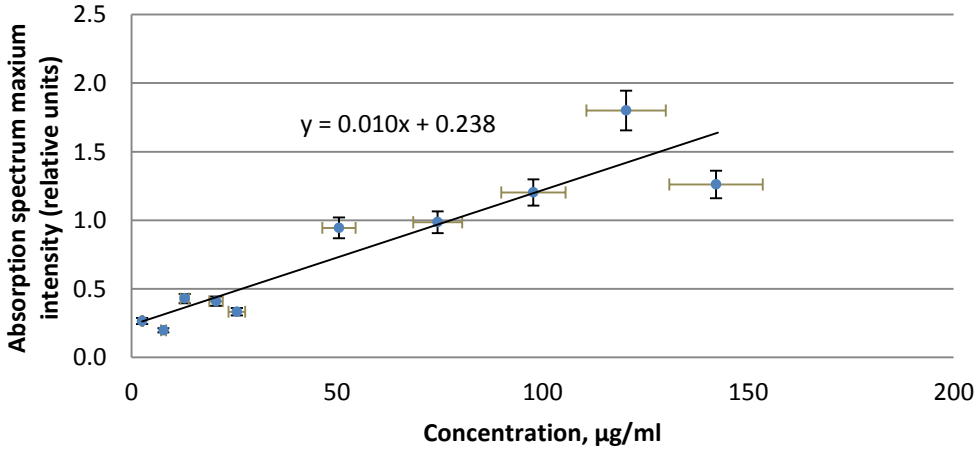

Fig.9. Absorption band intensity dependence on nigrosin concentration.

4. CONCLUSIONS

The results show that synthesized bilirubin, synthesized haemoglobin, and nigrosin can be used in biological phantoms as chemical substances that simulate skin chromophores. As a diffuse medium for mimicking diffuse nature of human skin, fibrin matrix combined with dermal and epidermal cells can be used in biological phantoms. Proposed skin phantom has a potential to be used for calibration of multi-spectral imaging devices.

Proposed skin phantom is good as a validation tool that is precisely characterized. However, it can't be used for interlaboratory comparison and standardization because of its instability in time.

5. REFERENCES

1. Xu, R., Xu, J., Qin, R., Huang, J. (2010) Developing multifunctional tissue simulating phantoms for quantitative biomedical optical imaging. *Proc.SPIE, 7567, 75670K*
2. Fujimoto, J. G., Farkas, G. L. (2009),Biomedical Optical Imaging, *DorotaJakubowski,FredericBevilacqua, Sean Merritt, Albert Cerussi, Bruce J. Tromberg (12) Quantitative Absorption and Scattering Spectra in Thick Tissues Using Broadband Diffuse Optical Spectroscopy, p.* 330-356
3. Pogue, B. W., Patterson, M. S. (2006) Review of tissue simulating phantoms for optical spectroscopy, imaging and dosimetry. *Journal of Biomedical Optics11(4),041102*
4. Ayers, F., Grant, A., Kuo, D., Cuccia, D. J., Durkin, A. J. (2008) Fabrication and characterization of silicone-based tissue phantoms with tunable optical properties in the visible and near infrared domain. *Proc. SPIE, 6870,687007*
5. Di Ninni, P. Martelli, F., Zaccanti, G. (2011) Toward a reference standard for tissue phantoms. *Proc. SPIE, 7906, 79060M*
6. Ankri, R.,Fixler, D., Taitelbaum, H. (2011)Reflected light intensity profile of two-layer tissues: phantom experiments, *Proc. SPIE, 16, 085001*
7. Pravdin, A. B., Utz, S.U.,Kochubey, V.I. (1995) Physical modeling of human skin optical properties using milk and erythrocytes mixtures, *Proc. SPIE, 2627, pp.221-226*
8. Bergmanna, T., Beera, S., Maedera, U., Burga, J.M.,Schluppb, P., Schmidtsb, T., Runkelb, F. and Fiebicha, M. (2011) Development of a skin phantom of the epidermis and evaluation by using fluorescence techniques. *Proc. SPIE 7906E..18B*
9. Saager, R.B.Kondru, C., Au, K., Sry, K., Ayers, F., Durkin, A.J. (2010) Multi-layer silicone phantoms for the evaluation of quantitative optical techniques in skin imaging. *Proc. SPIE 7567, 756706-1*
10. Vo-Dinh, T. (2003) Biomedical photonics Handbook, *Mobley, J., Vo-Dianh T., Tuchin, V.V., Norton, S.J. (1) Photonics and Tissue Optics*
11. Vo-Dinh, T. (2003) Biomedical photonics Handbook, *Mobley, J., Vo-Dinh, T. (2) Optical Properties of Tissue*
12. Sherwood, L. (2007) Human Physiology From Cells to Systems Sixth Edition *(16)The Digestive System*p.609
13. Saknīte, I. (2012) Ādas hromoforu sadalījuma noteikšana ādā ar multispektrālo attēlošanu: maģistradarbs, LU Fizikas un matemātikas fakultāte (Latvia)
14. Sherwood, L. (2007) Human Physiology From Cells to Systems Sixth Edition *(12) Body Defenses* p.443
15. Sherwood, L. (2007) Human Physiology From Cells to Systems Sixth Edition *(11) The Blood* p. 387
16. *Oregon Medical Laser Center*- website [25.04.2013.] http://omlc.ogi.edu/spectra/

17. Demos, S.G., Alfano, R.R. (1997) Optical polarization imaging. *Applied Optics*, Vol. 36, issue 1, p. 150 – 155.
18. *VariSpec Brochure*. Reacerch and Instrumentation, Inc. - website[18.02.2010.]. http://www.cri-inc.com/support/components.asp.
19. *Natural Phenomena Simulation Grup, University of Wterloo* – website [25.04.2013.] http://www.npsg.uwaterloo.ca/data/skin.php
20. Negri S, Federici G, Farinato S, Fila C. (2009) Human plasma as dermal scaffold for the generation of a completely autologous bioengineered skin. *Journal of Clinical Rehabilitative Tissue Engineering Research*, 13(47): 11-19

ĀDAS HROMOFORU *IN VITRO* KARTĒŠANAS MAKETU IZVEIDE UN EKSPERIMENTĀLA IZPĒTE

A.Silapētere, I. Saknīte, J. Spīgulis

KOPSAVILKUMS

Mūsdienās multispektrālās attēlošanas iekārtas izmanto ādas parametru un fizioloģisko procesu aprakstīšanai gan pētniecības, gan diagnostikas nolūkiem. Iekārtu darbības uzlabošanai ir nepieciešams labāk saprast gaismas mijiedarbību ar audiem, kā arī veikt šo iekārtu kalibrēšanu ar ādas maketu. Redzamā un tuvā infrasarkanā optiskā diapazona spektroskopijā ir svarīgi ādas maketi, kas simulē audu slāņaino struktūru un ķīmiskās īpašības, kā arī maketi, kas ir bioloģiski līdzvērtīgi. Šajā pētījumā tika izveidots ādas makets no bioloģiskām un ķīmiski sintezētām struktūrām.

Ādas maketa izveidei tika izmantota fibrīna matrica ar dermālo un epidermālo šūnu piejaukumu, lai imitētu ādas slāņaino struktūru. Fibrīna matrica tiek veidota no 0,47 ml plazmas, 0,4 ml fizioloģiskā šķīduma, 0,8 µl treneksāmskābes un 89,4 µl kalcija glukanāta. Izveidoto matricu ievieto šūnu inkubatorā, lai tā polimerizētos. Nākošais slānis tiek veidots ar dermālo šūnu piejaukumu (180-270· 10^3 šūnas), un pēdējais fibrīna matriksa slānis tiek veidots ar epidermālo šūnu piejaukumu (270· 10^3 šūnas) un šūnu augšanu veicinošu serumu (FBS). Šūnu kultivēšanai nepieciešamas vismaz divas nedēļas. Šajā slāņainajā struktūrā ir iespējams pievienot ādas hromoforu simulējošus iekļāvumus. Optiskajā diapazonā no 450-900 nm ādas hromoforas, kurām ir visizteiktākais spektrs, ir bilirubīns, melanīns un hemoglobīns. Lai simulētu ādas hromoforu spektrālās īpašības, tika izmantots sintezēts bilirubīns, eritrocītu masa un nigrozīns.

Lai izpētītu šī maketa iekārtu kalibrēšanas potenciālu, tika izveidoti 76 paraugi, kur katros 24 paraugos bija pievienots viens no absorbentiem ar dažādām koncentrācijām. Pilna ādas maketa audzēšanai nepieciešamas divas nedēļas, lai ātrāk tiktu iegūti pirmie rezultāti tika veidoti maketi bez dermālo un epidermālo šūnu piejaukuma. Fibrīna matricas un ādas imitējošā maketa absorbcijas spējas ir mazas salīdzinājumā ar hromoforu absorbcijas spējām. Lai novērtētu maketu, kas paredzēti konkrētu hromoforu spektrālo īpašību imitēšanai, iespējams veikt eksperimentus ar fibrīna matricu, kuras izveidošanai ir nepieciešama viena diena. Sintezētā bilirubīna koncentrācijas tika mainītas robežās no 0,01-2,00 mg/ml, melanīna optisko īpašību simulējošās vielas nigrozīna koncentrācija tika mainīta no 1,5 – 312,8 µg/ml, eritrocītu masas koncentrācija mainījās no 0,2 – 42,4 mg/ml.

Mērījumi tika veikti, izmantojot multispektrālās attēlošanas iekārtu *Cri Nuance 2.4.* (*Cambridge Reaserch & Instrumentation, Inc.,* Amerikas Savienotās Valstis). Absorbcijas spektrs tika apstrādāts, izmantojot *Microsoft Office Excel 2007*.

Iegūtajos rezultātos ir iespējams redzēt, ka piedāvātais ādas makets spēj simulēt ādas optiskās īpašības. Izmantotie absorbenti – sintezētais bilirubīns, nigrozīns un eritrocītu masa - spēj simulēt ādas hromoforu spektrālās īpašības. Palielinot absorbentu koncentrāciju paraugā, palielinās absorbcijas spektra maksimālā intensitāte. Izveidotais ādas makets varētu būt izmantojams iekārtu kalibrēšanai, taču šis makets nav piemērots starplaboratoriju iekārtu salīdzināšanai, jo tas nav stabils laikā.

I. Saknite, E. Kviesis, and J. Spigulis
"Water detection in skin by dual-band photodiodes"
Proc. SPIE, 9032, 90320O (2013)

Water detection in skin by dual-band photodiodes

Inga Saknite[1], Edgars Kviesis[1], Janis Spigulis[1]

[1]Biophotonics Laboratory, Institute of Atomic Physics and Spectroscopy, University of Latvia, Raina Blvd 19, Riga, LV-1586, Latvia

ABSTRACT

Purpose of this study was to develop a simple model for possibilities to detect water in skin by diffuse reflectance spectra. The model is based on comparison of diffuse reflectance spectra when illuminating water sample with LEDs of different wavelengths (1200 nm, and 1450 nm). The illumination LEDs were chosen due to water absorption differences in near-infrared spectral range. For detection, dual-band photodiode *DSD2* by *Thorlabs* was used. Due to differences of water absorption at different wavelengths in the near-infrared spectral region, this correlation could be used for mapping of water content in skin or, in other words, determine relative moisture level in skin. Simple experimental setup of illuminating LEDs, detecting photodiode, oscilloscope for measuring the signal received by photodiode, and a sample of water in a Petri plate, was used. The signal of the oscilloscope was interpreted as a parameter that describes intensity of light that is initially illuminated by the LEDs and that travels through the water sample. This study shows the basic principles used and first results, as well as gives insight of further work that will be carried out.

Spectral imaging, diffuse reflectance, water, dual-band photodiode, moisture level.

1. INTRODUCTION

The concept of a non-invasive skin assessment has an important role in every-day work for medical doctors, dermatologists, and other experts. Although many studies have already been carried out in the field of noninvasive spectral imaging, there are still developments to be done for a better understanding of light interaction with tissue and interpretation of the acquired data. Hemoglobin and bilirubin are chromophores that can give information on skin condition in different skin lesions, for example, mapping of these chromophores show different relative chromophore concentrations for melanomas and normal skin[1,2]. Also, research has been done to map chromophores, bilirubin and haemoglobin, to see changes in bruise development over time that has a potential for determination of the age of a bruise[3]. These measurements can be done by multispectral imaging techniques, as well as simple RGB imaging techniques by comparing diffuse reflectance spectra at different spectral bands, knowing which bands give information about different chromophore absorption.

The same principle as in RGB imaging could also be used for detection of different water concentrations in skin, however, with the difference of spectral bands used for both illumination and detection. Water absorption is very low in the visible spectral range – that is why visible spectral range can be used for different medical applications, and it is often called "medical window". Water absorption increases in the near-infrared spectral range with the first relatively noticeable absorption peak being at ~980 nm. As non-expensive silicon detectors have some (although little) spectral sensitivity also at ~980 nm, the first idea would be to try to use spectral bands of 980 nm and, for example, 650 nm for determination of water content in a sample (or skin). However, because of the low sensitivity of silicon-based detectors

at this near-infrared spectral range and also the relatively small water absorption peak, the results are not promising[3]. The next try that was carried out in this study, is to use more expensive *InGaAs* detectors that have good spectral sensitivity in the near-infrared spectral range that is of interest. A much more noticeable water absorption peak in the near-infrared range, comparing to 980 nm peak, is at 1450 nm, so that could be used for this study.

2. EXPERIMENTAL

2.1.Experimental setup

A basic setup was used for measurements. It consists of two illumination LEDs of wavelengths 1200 nm(*Thorlabs*, 2.5mW T-1 3/4) and 1450 nm (*Thorlabs*, 2.0mW T-1 3/4), photodiode for detection (*Thorlabs* Dual Sandwich Detector *DSD2*), oscilloscope (*Tektronix MSO4054B*) for signal acquisition from the photodiode, as well as a sample of water in a Petri plate. Under the Petri plate, there is a white sheet of paper. The illumination LEDs were operated by a power source (I = 20 mA), each of them separately. The photodiode was operated by a power source (I = 10 mA). Distance between the diodes (both, illumination and photodiode) and the bottom of the Petri plate with water sample was kept constant for the whole measurements, and it was 1 cm. The illumination diode and the photodiode were next to each other. Experimental setup is shown in Figure 1.

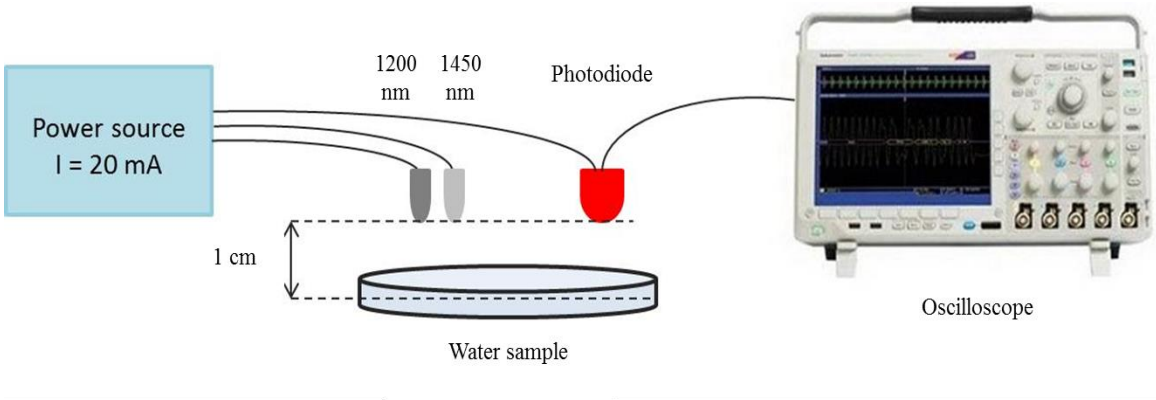

Figure 1. Experimental setup for the measurements

2.2.Working principle

Water is a diffuse medium, so with this experimental setup, it is assumed that some part of the incident light, illuminated by the LED (1200 nm or 1450 nm), is then received at the photodiode after the process of diffuse reflectance in the water sample. Some part of the incident light is also instantly reflected from the water sample surface. However, the photodiode should not be able to receive the instantly reflected radiation, because the active area of it is very small (with diameter of 1,5 mm), as well as it is sensitive only to photons that go directly in its active area (in an angle perpendicular or almost perpendicular to the surface of the water sample). Also, the viewing angle of the illumination diode is very narrow (15 degrees). A schematic representation of light interaction with water sample is shown in Figure 2.

If all the assumptions are done correctly, the photodiode should receive radiation that is a fraction of the incident light and that carries information about absorption of water. This process could be physically described by Beer-Lambert-Bouguer law (equation 1). From this equation, an absorption parameter *A* can be derived (equation 2), and it is dependent on concentration *c* of the absorbing substance (in this case – water), the molar extinction coefficient ε_λ of the absorbing substance, as well as the length *l* that incident rays travel in the absorbing substance.

$$I = I_0 e^{-\varepsilon_\lambda \cdot c \cdot l} \quad (1)$$

$$A = ln\frac{I_0}{I} = \varepsilon_\lambda \cdot c \cdot l \quad (2)$$

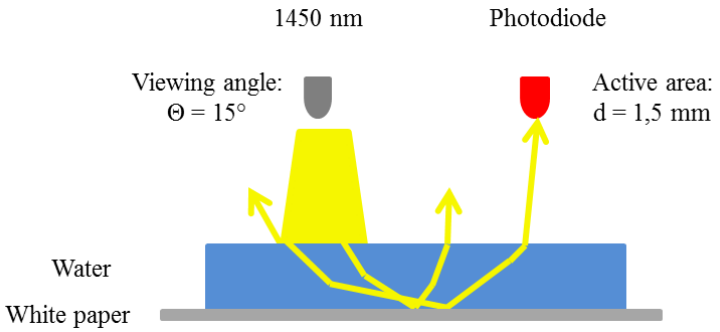

Figure 2. A schematic representation of light interaction with water sample.

Comparison of spectral sensitivity of the photodiode, as well as normalized spectra of both illumination diodes (1200 nm and 1450 nm), and absorption spectrum of water, all in relative units, in the spectral range 400 nm to 1800 nm is shown in Figure 3. As it can be seen, spectral sensitivity of the photodiode at wavelengths 1200 nm and 1450 nm could be considered almost equivalent, thus it is expected that this relatively small difference doesn't affect the results.

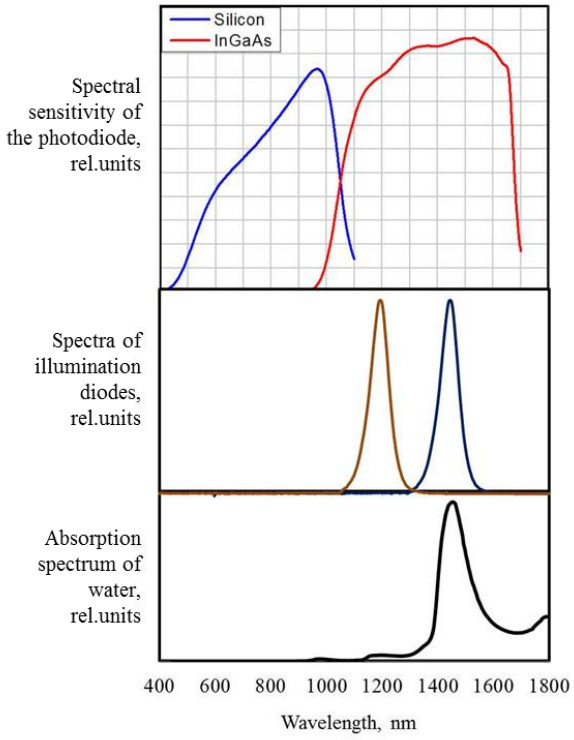

Figure 3. Comparison of spectral sensitivity of the photodiode (top), spectra of illumination diodes (middle), and absorption spectrum of water (bottom)[4].

2.3.Measurements

Measurements were done separately for each of the illumination LED. When LED was switched on, the oscilloscope signal was registered. The RMS (root mean square) value was registered.

The measurements were done in dark in order to lower the noise level. However, the dark level was also registered before the LED was switched on.

At first, a reference value was registered by using the above described experimental setup with an empty Petri plate (without water in it) in order to register incident light. Afterwards, water was filled in the Petri plate with a depth level of 1 mm. After that, measurements were done after adding 1 mm of water level each time.

The registered signal by oscilloscope is a value in millivolts (mV). As it is linearly dependent on photons reaching the photodiode, this registered value is assumed to be equivalent to the absorption parameter *A* that can be derived from the Beer-Lambert-Bouguer's law (equation 2). The reference value has to be subtracted, thus giving the relative absorption parameter:

$$\Delta A = A_n - A_{ref} \quad (3)$$

For comparison of absorption parameter when illuminating the sample with both different LEDs (1200 nm and 1450 nm), a relative difference parameter is introduced:

$$\Delta D = \frac{\Delta A_{1450}}{\Delta A_{1200}} \quad (4)$$

3. RESULTS AND CONCLUSIONS

First results show that the absorption parameter ΔA is larger when illuminating the same sample with LED of wavelength 1450 nm than when illuminating it with LED of 1200 nm, as it was expected (Table 1). At 1450 nm water absorption is much larger than at 1200 nm (Figure 3). The error of the measurement is the standard deviation of RMS signal, registered by the oscilloscope.

LED wavelength, nm	Reference Aref, mV	Absorption parameter A_n (water level: 0,1 cm), mV	Relative absorption parameter ΔA, mV
1450	39,4 ± 0,5	9,2 ± 0,5	30,2 ± 0,5
1200	51,5 ± 0,5	44,7 ± 0,5	6,8 ± 0,5

Table 1. Comparison of relative absorption parameter when illuminating with each of LEDs.

In Figure 4, the correlation between relative absorption parameter ΔA and the water depth level in the Petri plate, is shown when illuminating the sample with LED of wavelength 1200 nm. In Figure 5, the same correlation is shown when illuminating the sample with LED of wavelength 1450 nm. It is possible to see that the relative absorption parameter ΔA increases with an increased water depth level (water concentration) that was expected. However, when illuminating with LED of 1450 nm, this correlation is not that good – after water level of 0,3 cm, the relative absorption parameter doesn't change almost at all with an even more increased water depth level.

In Figure 6, the difference parameter ΔD depending on the water depth level is shown. It describes difference in absorbance when comparing the results of illuminating the sample with each of the LEDs.

These first results show that this simple technique could possibly be used for determination of relative water concentrations in skin. However, for now these measurements have only been done *in vitro* due to the low sensitivity of the photodiode signal, as well as to test the illumination and detection diodes for this model. Future work includes the need to increase the sensitivity of the photodiode signal, more experiments regarding different experimental setups (different distances and angles of illumination and detection diodes, as well as distance to the sample).

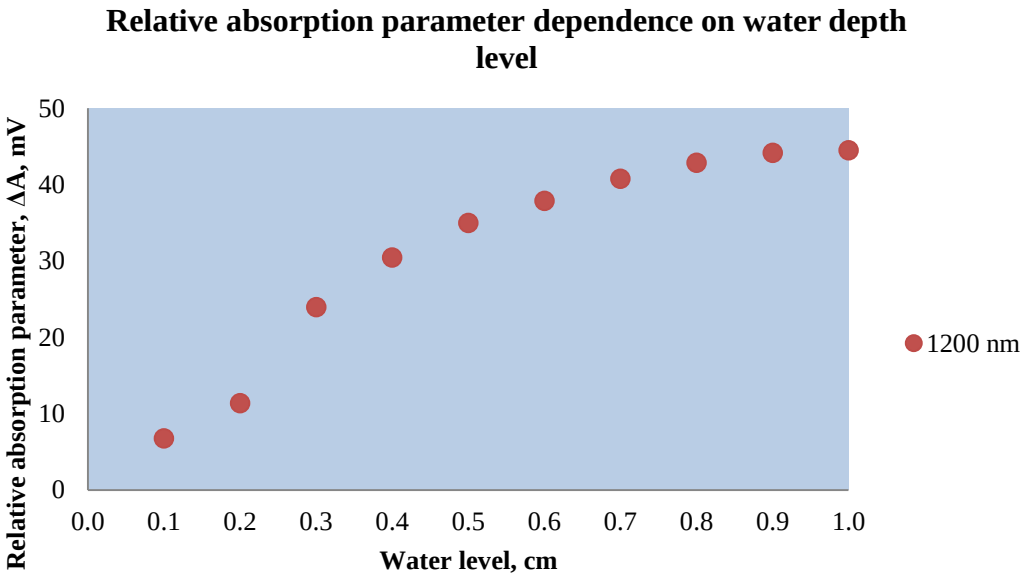

Figure 4. Relative absorption parameter depending on water depth level when illuminating with LED of 1200 nm.

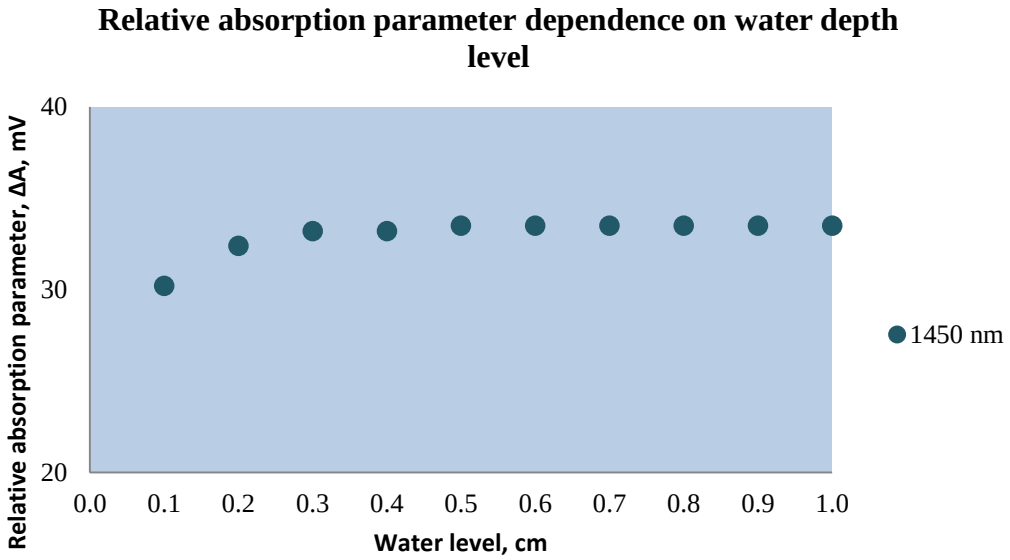

Figure 5. Relative absorption parameter depending on water depth level when illuminating with LED of 1450 nm.

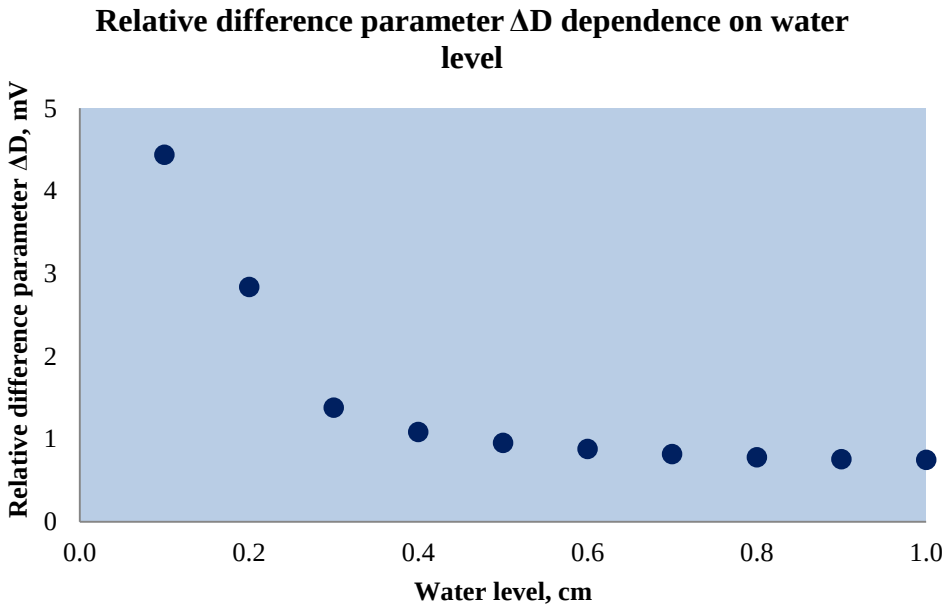

Figure 6. Relative difference parameter dependence on water depth level.

4. ACKNOWLEDGEMENTS

This study was supported by the European Regional Development Fund, grant #2010/0271/2DP/2.1.1.1.0/10/APIA/VIAA/030.

5. REFERENCES

[1] Kuzmina, I., Diebele, I., Jakovels, D., Spigulis, J., Valeine, L., Kapostinsh, J., Berzina, A., "Towards noncontact skin melanoma selection by multispectral imaging analysis," J.Biomed.Opt. 16(6), 060502-1 (2011).

[2] Diebele, I., Kuzmina, I., Lihachev, A., Kapostinsh, J., Derjabo, A., Valeine, L., Spigulis, J., "Clinical evaluation of melanomas and common nevi by spectral imaging," Biomedical Optics Express 3(3), 467-472 (2012).

[3] Saknite, I., Lange, M., Jakovels, D., Spigulis, J., "Determination of chromophore distribution in skin by spectral imaging," Proc. SPIE 8474, 84740K (2012).

[4] Oregon Medical Laser center, Optical spectra, http://omlc.ogi.edu/spectra/ (20 August 2013).

I. Saknite, M. Lange, D. Jakovels, and J. Spigulis
"Determination of chromophore distribution in skin by spectral imaging," Proc. SPIE
8474, 84740K (2012)

Determination of Chromophore Distribution in Skin by Spectral Imaging

Inga Saknite*[1], Marta Lange[2], Dainis Jakovels[1], Janis Spigulis[1]

[1]Biophotonics Laboratory, Institute of Atomic Physics and Spectroscopy,
University of Latvia, Raina Blvd. 19, LV-1586, Riga, Latvia
[2]Institute of Biomedical Engineering and Nanotechnologies, Riga Technical University,
Ezermala Str. 6k, LV-1006, Riga, Latvia

ABSTRACT

Possibilities to determine chromophore distribution in skin by spectral imaging were explored. Simple RGB sensor devices were used for image acquisition. Totally 200 images of 40 different bruises of 20 people were obtained in order to map chromophores bilirubin and haemoglobin. Possibilities to detect water *in vitro* and *in vivo* were estimated by using silicon photodetectors and narrow band LEDs. The results show that it is possible to obtain bilirubin and haemoglobin distribution maps and observe changes of chromophore parameter values over time by using a simple RGB imaging device. Water *in vitro* was detected by using differences in absorption at 450 nm and 950 nm, and 650 nm and 950 nm.

Keywords: RGB imaging, spectral imaging, skin chromophore, diffuse reflectance, bilirubin, haemoglobin, water

1. INTRODUCTION

Determination of chromophore concentration distribution in skin can be very useful and important in forensic science, for example, bilirubin and hemoglobin concentration and distribution in bruises can give information about the age of a bruise, as well as medical diagnostics, especially dermatology, as it can give information on the healing process of a bruise in a non-invasive way [1,2].
Aim of the present study was to develop and test a simple method for mapping skin chromophores - bilirubin, hemoglobin and water - by using RGB imaging. The technique is based on analysis of spectrum of each chromophore, focusing on the peak absorption values of the spectrum in the visible and near infrared spectral ranges. The technique involves spectral analysis of diffusely reflected light from skin and image analysis in *Matlab* by using the acquired image data.
Simple digital cameras were applied for image acquisition. They detect three – red (R), green (G) and blue (B) – components in case of a color camera or just one component in case of a monochromatic camera. Each camera has a known spectral sensitivity, and by using this information and selecting suitable LEDs for illumination of skin area, it is possible to acquire data of chromophore absorption in this skin area. A color digital camera was used for measurements of bruises in order to determine bilirubin and hemoglobin concentrations in visible spectrum, and a monochromatic camera was used for *in vitro* detection of water in visible and near infrared (NIR) spectrum [3].

2. EXPERIMENTAL

2.1. Bilirubin and hemoglobin distribution in bruises

Bilirubin and hemoglobin are two main skin chromophores that absorb light and have distinct absorption peaks in the visible spectrum and whose concentration and distribution in skin changes rapidly in bruises right after the injury. Previous studies show that right after the injury there is a rapid increase in hemoglobin level in the skin area because of the breaking of small capillaries, and afterwards bilirubin is produced as a breakdown product of hemoglobin, thus decreasing the level of hemoglobin concentration. Different studies show different amount of days after the injury when the bilirubin concentration has its maximum value. However, there is a tendency that shows how different parameters of a bruise, such as its color, size of its area and changes of bilirubin and hemoglobin relative concentrations, can be used in order to determine the age of a bruise [4,5].

2.1.1. Data acquisition

RGB imaging device consists of a color camera *iDS UI-1246LE-C-GL* (IDS Imaging Development Systems, Germany, 1.3 megapixels resolution) that is connected to PC via USB, eight RGB LEDs in a form of a ring, a switch that allows to use R, G or B channel separately, light diffuser in front of LEDs to provide uniform illumination, and two linear polarizers – one in front of the camera, and the other one, placed orthogonally to the first one, right in front of the light sources, thus reducing the instantaneous reflectance of the skin [6]. A spacer was used to keep a constant (3 cm) distance between the ring LEDs and skin area of interest. Obtained image of the skin area was 22x14 mm. All three R, G and B channels were switched on while acquiring the image.

Figure 1 shows the spectral sensitivity of the color camera. The camera acquires three images, each of them from a different spectral range. As it is shown in Figure 1, B channel has its sensitivity peak at approximately 440 … 460 nm, G channel – at approximately 530 … 550 nm and R channel – at approximately 610 … 650 nm. Figure1 also shows relative spectra of each of the RGB diodes separately (continuous line) and all diodes working simultaneously (dotted line). As it can be seen in Figure 1, spectra of RGB diodes have very similar peaks to the ones of channels of RGB camera, thus giving a better spectral response of the RGB imaging device [3].

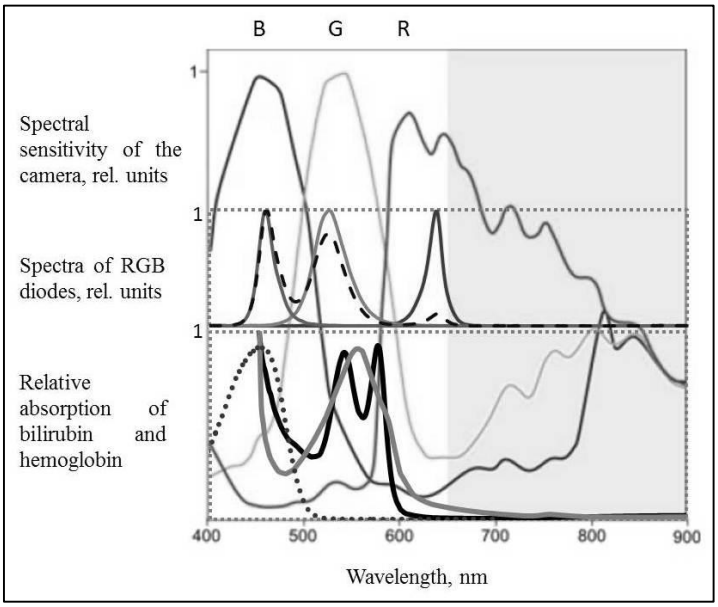

Figure 1. Comparison of spectral sensitivity of the RGB camera (on the top), spectra of RGB diodes (in the middle) and relative absorption of bilirubin (dotted line) and hemoglobin (continuous line) (on the bottom).

Relative absorption of chromophores bilirubin and hemoglobin are also shown in Figure 1 [7]. It can be seen that spectral response of B channel can give information about both bilirubin and hemoglobin

absorption, R channel - about hemoglobin absorption, and there is very little absorption of any of both chromophores in the R channel, thus it can be used as a reference channel.

2.1.2. Image analysis

The RGB imaging device acquires a three dimensional image of the skin area – an image of the same skin area acquired at the same time but from all three different channels. The three dimensional image was separated in three images of each channel and analyzed further in *Matlab*.

A simple model was used to acquire relative bilirubin and hemoglobin concentration and distribution maps. Each of the acquired diffuse reflectance images of each channel R, G and B was transformed to a value proportional to optical density (OD) and thus representing relative absorption of a chromophore. Relative haemoglobin absorption was estimated as:

$$Hb = \frac{R}{G} \quad (1)$$

Comparison of diffuse reflectance images of channels B and R gives information about both bilirubin and haemoglobin absorption (Figure 1), thus relative absorption value of both haemoglobin and bilirubin was estimated as:

$$BilHb = \frac{R}{B} \quad (2)$$

By using formulas (1) and (2), relative bilirubin absorption was estimated as:

$$Bil = BilHb - Hb = \frac{R}{B} - \frac{R}{G} \quad (3)$$

By using formulas (1), (2) and (3), relative bilirubin and haemoglobin concentration values for each image pixel were calculated, thus creating relative chromophore concentration distribution maps. An example of relative bilirubin and haemoglobin concentration distribution maps of a particular bruise, 24 hours after it was obtained, in comparison with its RGB image is shown in Figure 2.

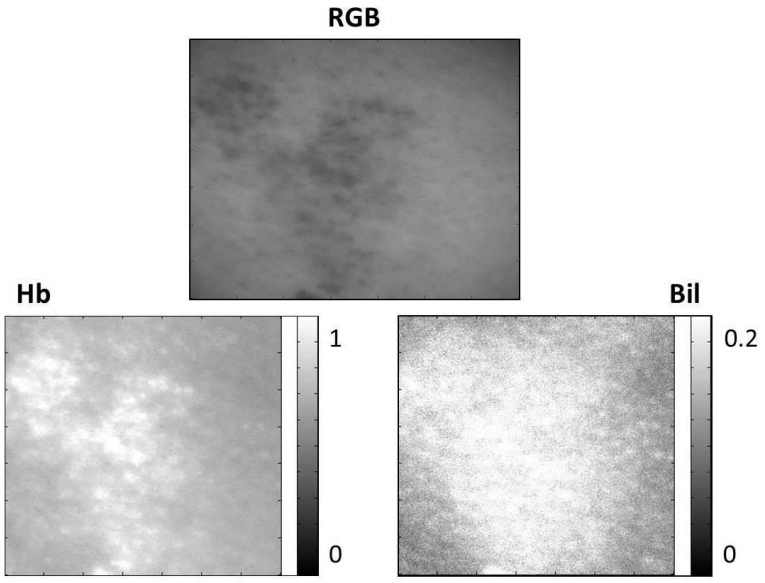

Figure 2. An example of relative bilirubin and haemoglobin concentration distribution maps (Hb and Bil) of a bruise, 24 hours after it was obtained, and an RGB image of the bruise (RGB).

In order to compare relative bilirubin and haemoglobin concentration changes in a bruise over time, bilirubin and haemoglobin parameter value was calculated for each image of a bruise over time by using

relative bilirubin and haemoglobin concentration distribution maps. A threshold value for haemoglobin ($T_{Hb} = 0.75$) and bilirubin ($T_{Bil} = 0{,}15$) was used to calculate bilirubin and haemoglobin parameter values – pixel count above the threshold value divided by total pixel count in an image.

2.2. Water detection *in vitro* and *in vivo*

Most of human body, including skin, consists of water. Liquid water has very low absorption in the visible spectrum, but it increases rapidly in the near-infrared and infrared spectrum. Comparison of water absorption in the visible and near-infrared spectrum could be used to non-invasively determine relative water concentration in tissue, for example, in blotches and blisters or other skin defects that have increased water concentration.
Previous studies show comparison of water absorption peaks from 900 to 1600 nm [8] or other wavelength above 1000 nm. However, this spectral range is available only by means of more sophisticated and expensive spectral detectors.
In this study, silicon-based photodetectors were used in order to compare water absorption around 450 nm and 650 nm with water absorption around 940 nm. *In vitro* and *in vivo* measurements were taken to check if it is possible to detect water in skin by using a simple and cheap water detection device.

2.2.1. Data acquisition

Water detection device consists of a monochromatic camera *iDS UI-1241LE-M* (IDS Imaging Development Systems, Germany, 1.3 megapixels resolution) that is connected to PC via USB, twelve LEDs of three different wavelengths (four LEDs of each wavelength) – 450 nm (B), 650 nm (R) and 940 nm (IR) – in a form of a ring, an FTDI chip FT245RQ (Future Technology Devices International Ltd.) to switch LEDs by a program in *Matlab*, light diffuser in front of LEDs to provide uniform illumination. A spacer was used to keep a constant (10 cm) distance between the ring LEDs and surface area of interest. Images were obtained separately by switching blue (B), red (R) or IR diodes. At first, a surface without any water was acquired as a reference for each of the channels - $B_{ref}, R_{ref}, IR_{ref}$.

Figure 3 shows the spectral sensitivity of the monochromatic camera, normalized spectra of each of the LEDs separately (continuous line) and all diodes working simultaneously (dotted line), as well as water absorption spectrum in the visible and near-infrared spectral range [7].

2.2.2. Image analysis

A simple model was used to acquire relative water concentration and distribution maps. Each of the acquired diffuse reflectance images of each channel B, R and IR was transformed to a value proportional to optical density (OD) and thus representing relative absorption of water:

$$OD_B = \frac{B_{ref}}{B} \tag{4}$$

Relative water absorption was estimated in two ways by comparing B and IR channels, as well as by comparing R and IR channels. Water parameter value that describes water absorption was estimated as:

$$W_B = OD_{IR} - OD_B \tag{5}$$

$$W_R = OD_{IR} - OD_R \tag{6}$$

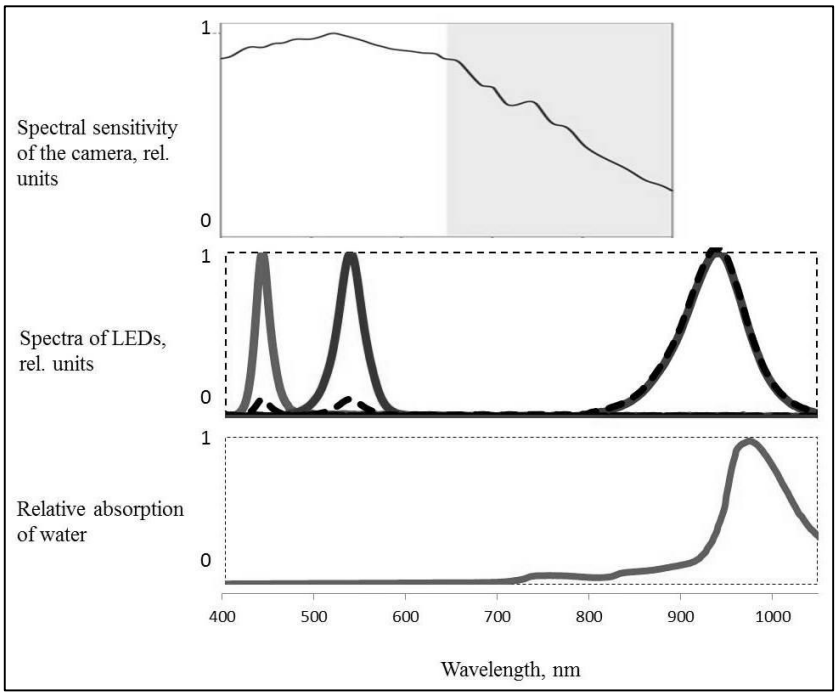

Figure 3. Comparison of spectral sensitivity of the monochromatic camera (on the top), spectra of LEDs (in the middle) and relative absorption water (on the bottom).

3. RESULTS

Totally 200 images of 40 different bruises of 20 persons were obtained in order to map chromophores bilirubin and haemoglobin and to analyze relative bilirubin and haemoglobin parameter value changes over time in the same bruise. Results show that it is possible to observe bilirubin and haemoglobin parameter changes over time by simple RGB camera. An example of parameter changes over time for one bruise is shown in Figure 4.

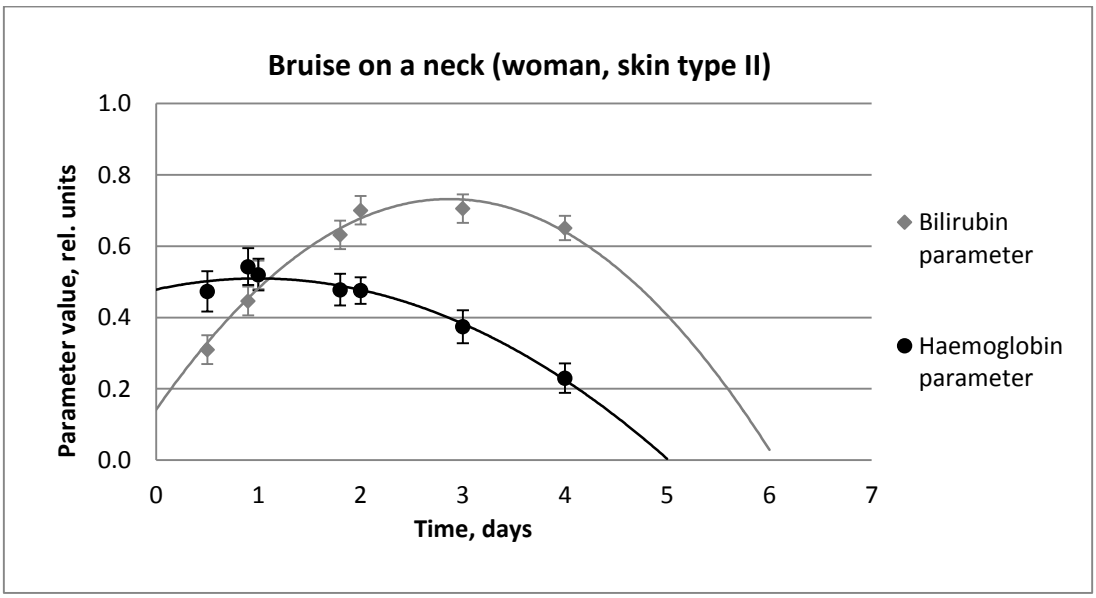

Figure 4. An example of parameter changes over time for a bruise on a woman's neck (skin type II).

In order to compare bruises of different origin, the day of maximum bilirubin and haemoglobin parameter value was estimated for each bruise. Figure 5 shows diagram of comparison of bruises obtained differently. Figure 6 shows comparison of bruises in different parts of body. Figure 7 shows histogram of days of maximum bilirubin parameter value in all bruises.

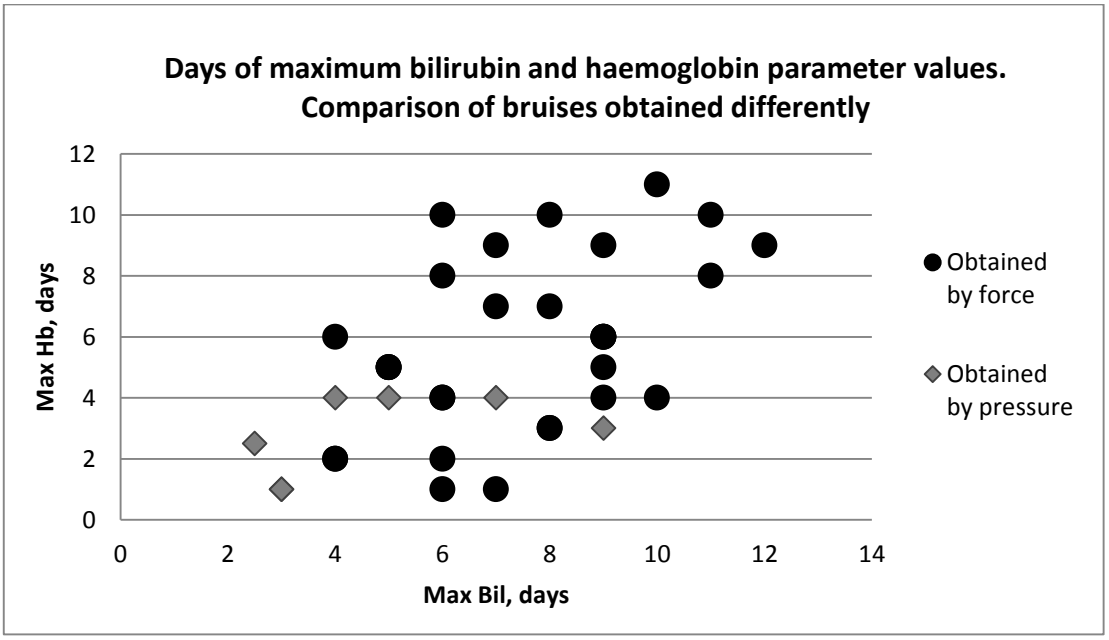

Figure 5. Comparison of bruises obtained differently (by force and by pressure) by comparing days of maximum bilirubin and haemoglobin parameter values.

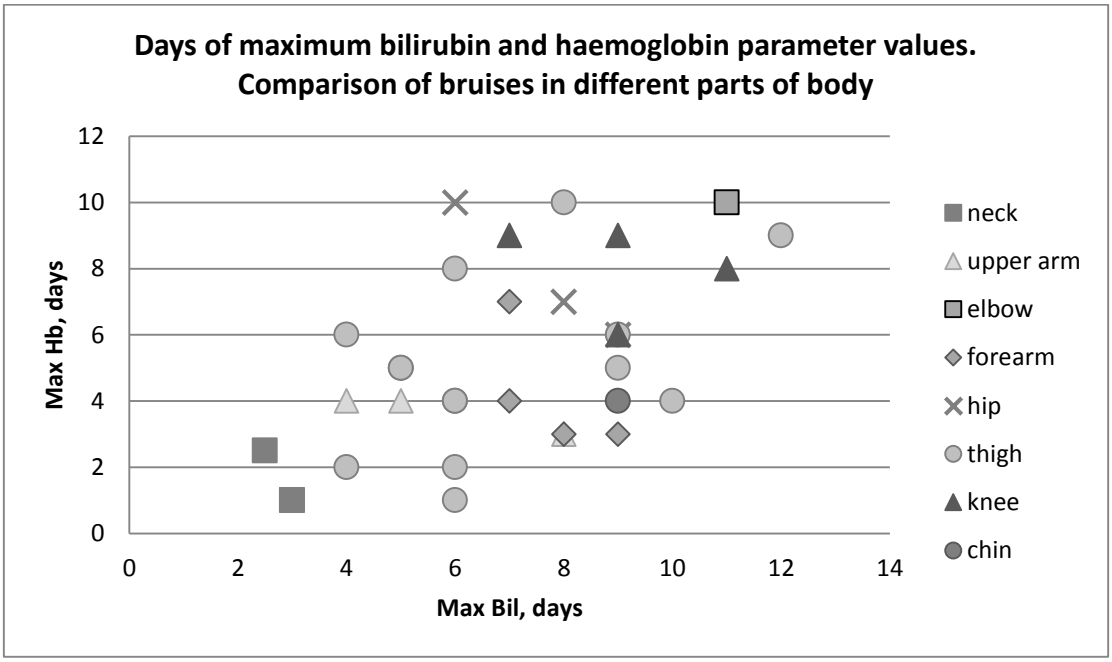

Figure 6. Comparison of bruises in different parts of body by comparing days of maximum bilirubin and haemoglobin parameter values.

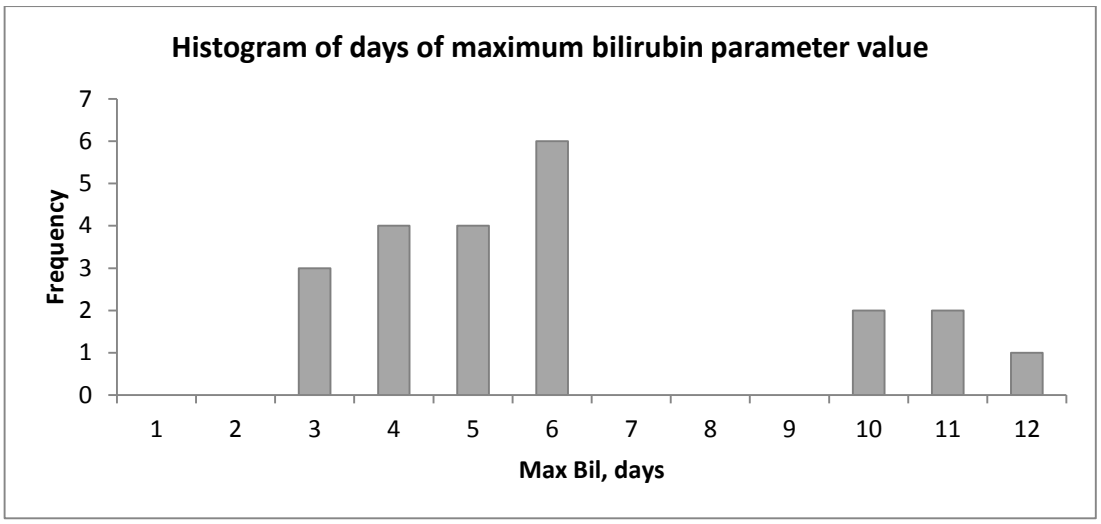

Figure 7. Histogram of days of maximum bilirubin parameter value.

Results of water detection device show that it is possible to detect small drops of water on a surface, such as white flat plastic, by comparing water absorption both at 450 nm and 940 nm, as well as 650 nm and 940 nm. However, it was not possible to observe different water concentrations, and it was not possible to detect water in skin tissue, for example, in blisters.

4. CONCLUSIONS

In this study, 40 different bruises were compared and observed over time in order to analyze chromophore bilirubin and haemoglobin relative concentration values over time. A simple RGB camera was used for image acquisition. Results show that it is possible to observe chromophore bilirubin and haemoglobin relative concentration changes over time by this simple device and method. However, this relatively small statistical data of 40 bruises does not show much correlation that could be used, for example, for medical or forensic applications. Maximum bilirubin and haemoglobin parameter values are very different for different bruises. Also, the skin type, location of the bruise, as well as how the bruise was obtained, could be the reason for such differences. For further studies these factors, as well as surface area changes of a bruise over time, should be taken into account.
Results show, that it is possible to detect small water drops *in vitro* by a simple device by comparing water absorption in the spectral range of visible and near-infrared light. However, it was not possible to detect water *in vivo*. These results show that cheap silicon-based photodetectors can be used to detect water absorption changes at 450 nm and 650 nm with water absorption at 940 nm, however, the device should be improved in order to be able to detect water *in vivo*.

5. ACKNOWLEDGEMENTS

This work was supported by projects of European Social Fund “Support for doctoral studies at University of Latvia” (# 1DP/1.1.2.1.2./09/IPIA/VIAA/004) and European Regional Development Fund “Novel optical technologies for complex non-contact skin diagnosis” (# 2010/0271/2DP/2.1.1.1.0/10/APIA/VIAA/030)

REFERENCES

[1] Stam, B., van Gemert, M.J., van Leeuwen, T.G., Teeuw, A.H., van der Wal, A.C., Aalders, M.C., "Can color inhomogeneity of bruises be used to establish their age?", J. Biophotonics, vol. 4(10), 759–67 (2011).
[2] Saknite, I., Jakovels, D., Spigulis, J., „Distant determination of bilirubin distribution in skin by multi-spectral imaging", Latv.j.Phys.Techn.Sci., vol.48 nr. 2, 50-55 (2011).
[3] Jakovels, D., Spigulis, J., Rogule, L., „RGB Mapping of Hemoglobin Distribution in Skin", Proceedings of SPIE, vol. 8087, 80872B (2011).
[4] Randeberg, L.L., [Diagnostic applications of diffuse reflectance spectroscopy. Doctoral thesis], Norwegian University of Science and Technology, Trondheim, 62 (2005).
[5] Häggblad, E., [In Vivo Diffuse Reflectance Spectroscopy of Human Tissue. Doctoral thesis.], Linköping University, Linköping, 151 (2008).
[6] Demos, S.G., Alfano, R.R., „Optical polarization imaging", App.Opt., 36(1), 150-155 (1997).
[7] http://omlc.ogi.edu/spectra/
[8] Nachabe, R., Hendriks, B.H.W., Desjardins, A.E., van der Voort, M., van der Mark, M.B., Sterenborg, H.J.C.M., ''Estimation of lipid and water concentrations in scattering media with diffuse optical spectroscopy from 900 to 1600 nm'', Journal of Biomedical Optics, vol. 15(3), 037015 (2010).

I. Saknite, D. Jakovels, and J. Spigulis
"Distant Determination of Bilirubin Distribution in Skin by Multi-Spectral Imaging"
Latv. J. Phys. Tech. Sci., 48(2), 50–55 (2011)

DISTANT DETERMINATION OF BILIRUBIN DISTRIBUTION IN SKIN BY MULTI-SPECTRAL IMAGING

I. Saknite, D. Jakovels, J. Spigulis

Bio-Optics and Fibre Optics Laboratory, Institute of Atomic Physics and Spectroscopy, University of Latvia,

19 Raina Blvd., LV-1586, Riga, LATVIA
e-mail: inga.saknite@gmail.com

Multi-spectral imaging technique was used for mapping the bilirubin distribution in bruised skin. Temporal changes of the bilirubin content in skin photo-types II and III have been observed. The obtained results confirm the clinical potential of this technique for skin bilirubin diagnostics.

Keywords: multi-spectral imaging, mapping of skin chromophore distribution, bilirubin.

1. Introduction

Determination of the bilirubin content and distribution in skin is crucial for diagnostics of infant bilirubinemia, follow-up of wound healing after surgeries, estimation of the age of bruises in forensic medicine, etc. The skin colour in these cases is mostly affected by haemoglobin and its breakdown product bilirubin.

Visual assessment is not accurate enough to determine the age of a bruise [1]. The diffuse reflectance spectroscopy has been successfully used to analyse the temporal changes of bilirubin content in bruises [2, 3, 4], being able to determine the age of a bruise with an accuracy of one day [5]. The multi-spectral imaging combines spectroscopic and imaging techniques, therefore is useful for distant mapping of skin chromophores (haemoglobin and melanin) [6]. At the present work, this technology is further developed to use it for mapping of skin bilirubin distribution.

2. Experimental

The main area of the study was bruises on human skin, which were tested at different times after they had been received in order to analyze changes in the bilirubin concentration over time. A computer-aided multi-spectral imaging system *Nuance 2.4* (*Cambridge Research & Instrumentation, Inc., USA*) with white LED illumination was used to obtain image cubes of human skin in the spectral range of 450–750 nm (Fig. 1). Light propagation in skin was approximated by Beer-Lambert's law [7]. The measured absorption spectrum was expressed as a superposition of absorption spectra of four chromophores (oxyhaemoglobin, deoxyhaemoglobin, melanin and bilirubin). Relative chromophore concentration values were obtained solving the least-squares problem, and the corresponding parameter distribution maps were constructed.

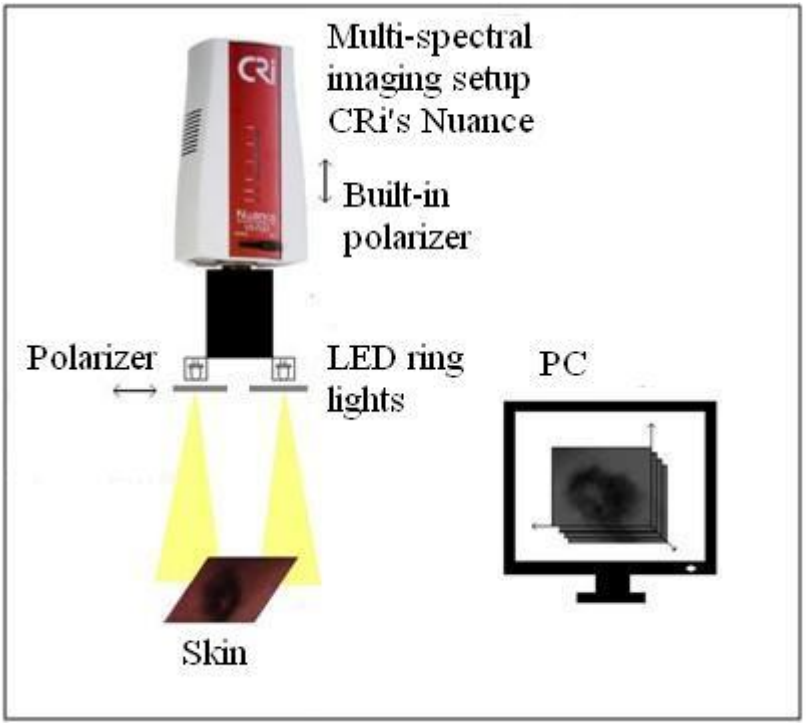

Fig. 1. The experimental setup

As the light source, a 24 warm-white LED ring was used. The normalized LED spectrum in comparison with the spectra of four chromophores is shown in Fig. 2 [7].

The cross-polarization technique was applied in order to reduce the specular reflection, so a linear polarizer was placed in front of the light source orthogonally to the built-in polarizer [8].

The liquid crystal tuneable interference filter was used for spectral scanning. The light's penetrability in skin differs for different wavelengths [9]. Thus, various exposure times (1 … 6 miliseconds) were taken for obtaining monochromatic images at different wavelengths.

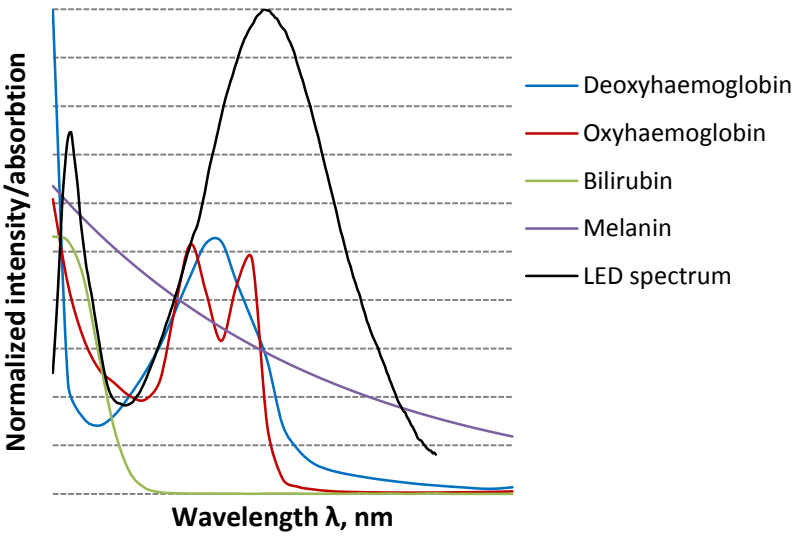

Fig. 2. LED emission spectrum in comparison with the absorption spectra of chromophores

The skin area under study was ~50x35 mm. 4x4 pixel binning was used to speed up the image processing, but the resolution was decreased to 0.15 mm/pixel (348x256 pixel image).

A white paper sheet was used for reference measurements. Because the paper is not an ideal reflector, a correction was made for each acquired image. The correction was made comparing the paper sheet with the standard white reference tile (*Avantis* [10]).

The total time to take an image cube of the spectral range of 450–750 nm with a spectral resolution of 10 nm was approx. 15 seconds.

The image processing was performed in *Matlab*. A built-in function *LSQR* was applied to solve the relevant linear equation system by the least squares method. In order to increase the speed of the algorithm, the image resolution was reduced 5 times, so for the bilirubin concentration maps it was 0.75 mm/px (70x51 pixel images), and the maps were generated in about 6 seconds.

The Beer-Lambert law was employed to describe the light interaction with tissue. The optical density (OD) values were derived from the law as follows:

$$OD_\lambda = lg\frac{I_0(\lambda)}{I(\lambda)} \quad (1)$$

where I_0 is the reflection intensity from the white reference (the initial radiation), I is the intensity of light reflected back from the skin. The predicted OD spectrum is expressed as the superposition of spectra of four chromophores:

$$OD_\lambda = \varepsilon_{OH}(\lambda)\cdot C_{OH} + \varepsilon_{DOH}(\lambda)\cdot C_{DOH} + \varepsilon_{Mel}(\lambda)\cdot C_{Mel} + \varepsilon_{Bil}(\lambda)\cdot C_{Bil} \quad (2),$$

where ε is the molar extinction coefficient (the tabular values for each chromophore are shown in Fig. 2 [11]), and C is the relative concentration for each chromophore. As these concentration values are dependent on the optical path length of the radiation in tissue, a correction coefficient was applied (taken from [12]).

The relative concentration values for each pixel of each chromophore were obtained solving the problem by the least squares method in *Matlab,* and the distribution maps for relative bilirubin concentration were constructed.

20 bruises were observed in time, and the total number of 51 image cubes were obtained and analyzed. Eight volunteers participated in the experiment: 7 female and 1 male in the age range from 20 to 32 years, 7 individuals with the skin type II and 1 with skin type III (Fitzpatrick's scale).

The maps of relative bilirubin concentration were analyzed in time, and its average values of a particular square of the bruise region were observed as a function of time.

3. Results and Discussion

The maps of bilirubin concentration show that it increases in time for most of the bruises observed in the experiment. The maps showing the bilirubin relative concentration changes in time are shown in Fig. 3. To analyse quantitative concentration changes in time, a region of a particular square of all maps was chosen and the average relative concentration value was calculated. The relative bilirubin concentration changes as a function of time are displayed in Fig. 4.

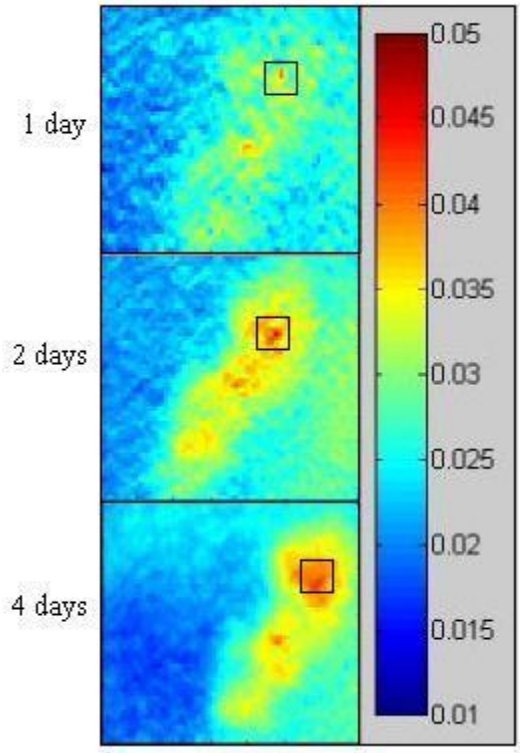

Fig. 3. Maps of relative bilirubin concentration changes over time (female, 21 years old, II skin type).

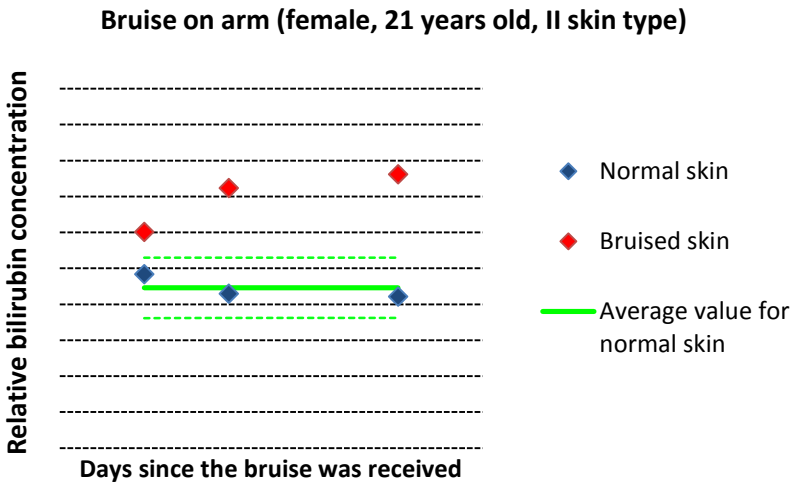

Fig. 4. Relative bilirubin concentration changes as a function of time

When comparing all obtained average values of relative concentration of bilirubin in bruises and normal skin, a difference can be seen. These values for skin type III appear to be greater than in skin type II, both in normal and bruised skin (Fig. 5).

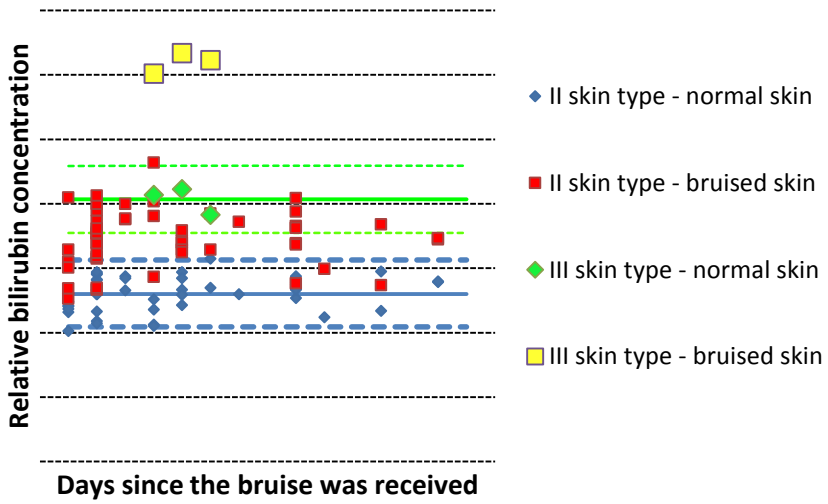

Fig. 5. Comparison of relative bilirubin concentration for two types of skin

4. Conclusions

A simplified model with a relevant algorithm was used to obtain relative bilirubin concentration maps. The results show that it is possible to observe temporal changes in the bilirubin concentration in bruised skin. As expected [5], this concentration increases in time during the first days after the bruise has been received. A difference in relative bilirubin concentrations between skin types II and III was observed, which can be assigned to the influence of melanin on the skin parameters and is to be studied further.

References

1. Pilling, M.L., Vanezis, P., Perrett, D., & Johnston, A. (2010). Visual assessment of the timing of bruising by forensic experts. *J Forensic Leg Med*, 17 (3), 143 – 149.
2. Ruvolo Jr., E.C., Bargo, P.R., Dietz, T., Scamuffa, R., Shoemaker, K., DiBernardo, B., & Kollias, N. (2010). Use of spectral imaging for documentation of skin parameters in face lift procedure. *Proc. SPIE, 7548,* 75480A.
3. Duckworth, M.G., Caspall, J.J., Mappus, R.L., Kong, L., Yi, D., & Springle, S.H. (2008). Bruise chromophore concentrations over time. *Proc. SPIE, 6915,* 69152S.
4. Springle, S., Yi, D., Caspall, J., Linden, M., Kong, L., & Duckworth, M.G. (2007). Multispectral image analysis of bruise age. *Proc. SPIE, 6514,* 65142T.
5. Randeberg, L.L., Haugen, O.A., Haaverstad, R., & Svaasand, L.O. (2006). A novel approach to age determination of traumatic injuries by reflectance spectroscopy. *Las. Surg. Medic., 38,* 277 – 289.
6. Jakovels, D., Spigulis, J., & Saknite, I. (2010). Multi-spectral mapping of *in vivo* skin haemoglobin and melanin. *Proc. SPIE, 7715,* 77152Z.
7. Saknīte, I. (2010). Bilirubīna un melanīna sadalījuma noteikšana ādā ar multispektrālās attēlošanas metodi: bakalaura darbs. LU Fizikas un matemātikas fakultāte (in Latvian).
8. Demos, S.G., Alfano, R.R. (1997). Optical polarization imaging. *Appl. Opt., 36* (1), 150 – 155.
9. *VariSpec Brochure.* Research and Instrumentation, Inc. [18.05.2010.]. http://www.cri-inc.com/support/components.asp.
10. *Avantes* website – [17.05.2010.]. http://www.avantes.com/Colorimetry/White-Reference-Tile/Detailed-product-flyer.html.
11. *Oregon Medical Laser Center* website – [12.05.2010.]. http://omlc.ogi.edu/spectra/.
12. Priedītis, K. (2004). Fotopletizmogrāfiskā signāla datorapstrāde un analīze : maģistra darbs. LU Fizikas un matemātikas fakultāte (in Latvian).

Darba mērķis bija izveidot iespējami vienkāršu metodi ādas hromoforas bilirubīna *in vivo* kartēšanai no attāluma. Ar neinvazīvu optisko metodi – multispektrālo attēlošanu – tika novērota 20 zilumu attīstība laikā, kopā uzņemot 51 attēlu masīvu. Gaismas mijiedarbības ar ādu aprakstam tika izmantota difūzi atstarotās gaismas teorija, un ar *Nuance 2.4* multispektrālās attēlošanas sistēmu komplektā ar datoru tika iegūtas ādas attēlu optiskā blīvuma (OD) vērtības, kas iegūtas kā sākotnējā starojuma intensitātes un no ādas virsmas atpakaļ atstarotās gaismas intensitātes attiecība. Izmantojot Bēra-Lamberta likumu, OD spektrs tika izteikts kā četru ādā esošu hromoforu – oksihemoglobīna, deoksihemoglobīna, melanīna un bilirubīna - atsevišķo spektru superpozīcija. Ar mazāko kvadrātu metodi programmā *Matlab* tika aprēķinātas relatīvās bilirubīna koncentrācijas vērtības, iegūstot koncentrāciju sadalījuma kartes.

Pierādīts, ka ar multispektrālo attēlošanu iespējams neinvazīvi veikt ādas hromoforas bilirubīna kartēšanu un novērot bilirubīna koncentrācijas izmaiņas laikā. Pirmajās dienās pēc ziluma iegūšanas bilirubīna koncentrācija laikā pieaug, kas atbilst literatūrā pieejamajai informācijai par bilirubīna veidošanos zilumos.

D. Jakovels, J. Spigulis, and I. Saknite
"Multi-spectral mapping of in vivo skin hemoglobin and melanin"
Proc. SPIE, 7715, 77152Z (2010)

Multi-spectral mapping of in-vivo skin hemoglobin and melanin

Dainis Jakovels, Janis Spigulis, and Inga Saknite
Bio-optics and Fiber Optics Laboratory, Institute of Atomic Physics and Spectroscopy,
University of Latvia, Raina Blvd 19, LV – 1586, Latvia

ABSTRACT

The multi-spectral imaging technique has been used for distant mapping of *in-vivo* skin chromophores by analyzing spectral data at each reflected image pixel and constructing 2-D maps of the relative concentrations of oxy-/deoxy-hemoglobin and melanin. Instead of using a broad visible-NIR spectral range, this study focuses on narrowed spectral band 500–700 nm, so speeding-up the signal processing procedure. Regression analysis confirmed that superposition of three Gaussians is optimal analytic approximation for the oxy-hemoglobin absorption tabular spectrum in this spectral band, while superposition of two Gaussians fits well for deoxy-hemoglobin absorption and exponential function - for melanin absorption. The proposed approach was clinically tested for three types of *in-vivo* skin provocations – ultraviolet irradiance, chemical reaction with vinegar essence and finger arterial occlusion. Spectral range 500–700 nm provided better sensitivity to oxy-hemoglobin changes and higher response stability to melanin than two reduced ranges 500–600 nm and 530–620 nm.

Keywords: multi-spectral imaging, hemoglobin, melanin, skin chromophore mapping

1. INTRODUCTION

The mapping of *in-vivo* skin chromophores is based on multi-spectral imaging that combines spectral analysis of diffusely reflected light and image analysis, resulting in 2-D maps of the relative concentrations of chromophores, e.g. oxy-/deoxy-hemoglobin and melanin [1, 2]. Such mapping ensures reliable non-invasive evaluation of skin condition [3, 4, 5]. The least-squares regression analysis of a broad visible-NIR spectral range was successfully used to estimate the chromophore content in skin [2, 6]. A drawback of this technique is time-consuming (proportional to the quantity of spectral information) data acquisition and processing; narrowing of the working spectral range can speed-up the procedure. However, there is a risk to loose specificity and sensitivity to the main skin chromophores, therefore optimal spectral range for skin chromophore mapping should be found [7]. For instance, potential of the reduced spectral range 525–645 nm for imaging of skin hemoglobin oxygen saturation has been demonstrated recently [8]. The third main skin chromophore – melanin – could not be mapped since the measurements were taken for palm skin.

The present study continues examination [9] of specific spectral intervals from the point of applicability for simultaneous distant mapping of three main *in-vivo* skin chromophores - oxy-hemoglobin, deoxy-hemoglobin and melanin.

2. EXPERIMENTAL

2.1. Data acquisition

The multi-spectral imaging system *Nuance 2.4* (Cambridge Research & Instrumentation, Inc., USA) in connection with PC was used for spectral imaging of in-vivo skin (Figure 1a). 24 white *warm* LED ring source was created to achieve uniform illumination at optimal working distance 15…20 cm. Linear polarizer was placed in front of the light source and orientated orthogonally to the built-in polarizer of *Nuance*, so reducing the specular reflectance of skin [10].

Skin area under the study was 50x35 mm. 4x4 pixel binning was used to increase detector matrix sensitivity that speeded up image cube acquisition process but reduced spatial resolution to 0.15x0.15 mm (the pixel size). As the least-squares regression analysis applied in imaging is a time consuming process, the appropriate spatial resolution for data processing was found to be 0.75x0.75 mm.

Due to spectrally different illumination intensity and system sensitivity, various exposure times (3…50 ms) were used for each image acquisition. The total 21 image cube (spectral range 500 – 700 nm, step 10 nm) acquisition process took less then 10 s, with spectral resolution 10 nm (bandwidth of the *Nuance* liquid crystal tunable filter).

The white reference measurements were taken from sticky white office paper sheet (spectral reflectance 0.90 ± 0.04 within the 500-700 nm band) that was attached to the forearm skin.

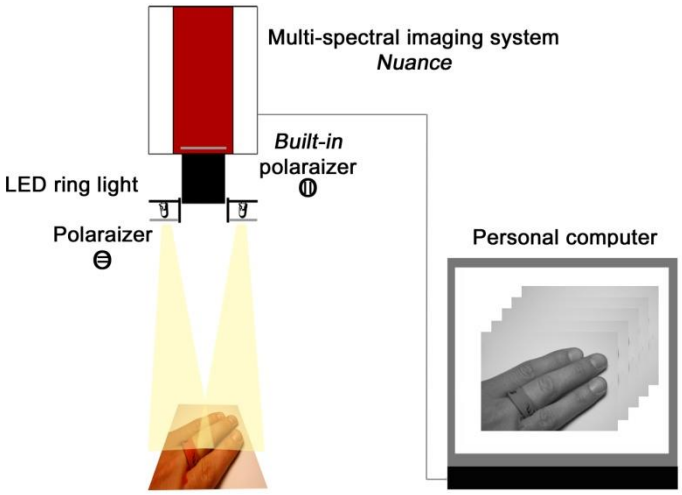

Figure 1. The experimental setup.

2.2. Data processing

Data processing was performed in *MatLab*. The back reflected light intensity (I) values at each pixel were transformed to the optical density (OD) as follows:

$$OD(\lambda) = -log\left(\frac{I(\lambda)}{I_0(\lambda)}\right) (1),$$

where I_0 – reflection intensity from the white reference. Optical density of the superficial skin layer has been predicted in frame of three chromophore absorbtion model:

$$OD_{predicted}(\lambda) = a_{OH} \cdot \varepsilon_{OH}(\lambda) + a_{DOH} \cdot \varepsilon_{DOH}(\lambda) + a_{Mel} \cdot \varepsilon_{Mel}(\lambda) + a_{Offset}(2),$$

where ε_{OH}, ε_{DOH} and ε_{Mel} correspond to molar absorption spectra for oxy-hemoglobin (OH), deoxy-hemoglobin (DOH) and melanin (Mel), a_{OH}, a_{DOH} and a_{Mel} represent the relative chromophore concentration values, a_{Offset} – the difference between the predicted and measured spectra.

The predicted OD spectrum at each image pixel was compared to the measured OD spectrum by solving the nonlinear least-squares problem using the Trust-Region algorithm [11], with subsequent extraction of the corresponding relative concentrations of the skin chromophores [2]. The reference absorption spectra of the three chromophores were taken from the literature data [12, 13].

Analysis of the reference spectra allowed proposing handy analytic expressions that approximated well the tabular data within the spectral interval 500-700 nm. Superposition of three Gaussians proved to be optimal for approximation of the OH spectrum, while superposition of two Gaussians suited well for approximation of the DOH spectrum [9]. The values of multiple determination coefficients R^2 were obtained as R^2_{OH} = 0.9988 for oxy-hemoglobin and R^2_{DOH} = 0.9973 for deoxy-hemoglobin.

The relative values of the respective skin chromphore concentrations a_{OH}, a_{DOH}, a_{Mel} have been determined in *MatLab* at each image pixel, and the chromophore maps representing the planar distribution of the particular chromophore have been constructed.

Multiple determination coefficient R^2 value represents goodness of predicted and measured spectra fit and can be used as qualitative parameter to find poor correlation regions/points. Therefore binary threshold mask can be created from R^2 map and applied to parameter maps (Figure 2).

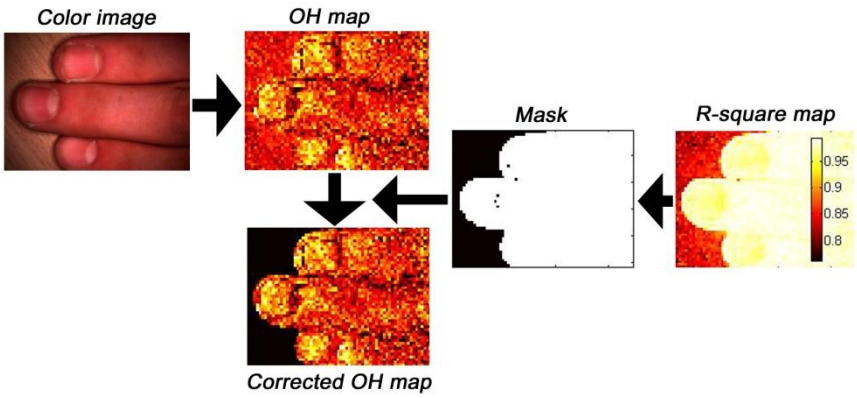

Figure 2. Oxy-hemoglobin map correction using R^2 mask (threshold R^2 = 0.97).

2.2. Skin provocations

Three different provocations were applied in order to examine the proposed method.

UV provocation was made by electrodeless high-frequency discharge Mercury lamp with specific UV-C peak at 253.7 nm to two volunteers (skin types 2 and 3). Four different doses (0.5, 1.0, 1.5 and 2.0 minutes provocation time) were applied to forearm skin through a mask with ø5 mm apertures to achieve different skin responses for local irritation. All provoked areas were placed to fit 50x35 mm rectangle – one image. Erythema appeared visible at all provocation areas in 2 hours, and skin color changed from dark red to dark brown in the next days. Three measurement series (2, 4 and 8 h after provocation) were taken during the first day to observe erythema development. Next days three additional measurement series (1, 2 and 4 days after provocation) were repeated to notice melanin changes.

Vinegar essence was used for chemical skin provocation. It was found that different skin areas have strictly various reaction intensity and speed to stimulus. Thus "cross" was sketched on forearm using vinegar essence ink. Skin tingling started in a minute right after it provoked area was flushed and washed using soaps. Skin erythema appeared in few minutes. Measurements were taken 20, 40 ad 60 minutes after the provocation.

A resin cuff for arterial occlusion (3 min.) was used to reduce skin blood oxygenation in a finger [14]. Measurements were taken every minute before, during full occlusion and after removal of the cuff.

After appropriate signal processing, the maps of relative chromophore concentrations were created to follow-up the provoked skin responses.

3. RESULTS AND DISCUSSION

3.1. Comparison of spectral ranges

The spectral range 500–700 nm clearly showed better sensitivity to the OH content changes and higher stability to melanin if compared to the narrower bands 500–600 nm and 530–620 nm. Sensitivity to the OH content changes was evaluated as contrast between provoked area and normal skin, and for the range 500-700 nm it was for ~20 % higher than that for both reduced spectral ranges. Stability to melanin was verified by analyzing the chemical and mechanical provocations where its concentration increase was not expected; hemoglobin changes in these tests could influence results causing melanin artifacts. False-increased melanin content at the chemical provocation areas was obtained using the narrower spectral ranges 500-600 nm (up to 20%) and 530-620 nm (up to 30%). Consequently, the spectral interval 500–700 nm was chosen as the best option for simultaneous mapping of the three skin chromophores. However, still slight interaction between melanin and DOH can appear, especially during strong erythema.

3.2. UV-provocation responses

Weak visible skin erythema appeared within 2 hours at all UV-provoked areas where and became stronger in next hours proportionally to applied UV doses. Increased concentration of OH (up to 250 % for skin type 3 and 200% for skin type 2 compared to normal skin) and DOH (up to 50 %) were obtained reaching maximum 8 h after provocation. More stabile erythema was observed for higher provocation doses (1.5 and 2.0 min.). Slightly different melanin

concentrations at both skin types were observed - for type 3 it was ~1.5 times higher if compared to type 2. Noticeably increased melanin concentration appeared on the second day for skin type 3 and on the fourth day for skin type 2, but it was still quite weak compared to background skin melanin concentration variations. Melanin and DOH interaction was noticed during intensive erythema.

The extracted chromophore maps are presented at Figure 3. Different background (normal skin) chromophore map color can be explained as artifact caused acquiring reference image, but changes in skin condition in time are not excluded as well.

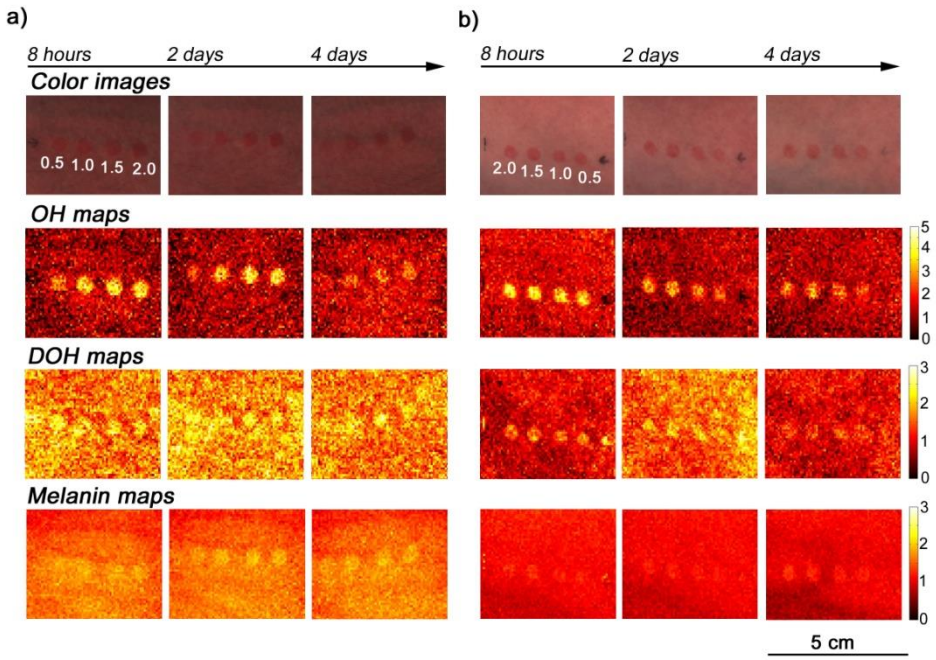

Figure 3. Skin chromophore distribution maps 8 hours, 2 days and 4 days after UV provocation: a) skin type 3, b) skin type 2.

3.3. Chemical provocation responses

Visible skin erythema appeared within several minutes after the provocation with vinegar essence. Increased OH concentration at the irritated area has been obtained, with maximum 20 minutes after provocation (+300% comparing to normal skin) and linear decrease within an hour, as shown in Figure 4. Slight increase of DOH concentration was obtained, as well.

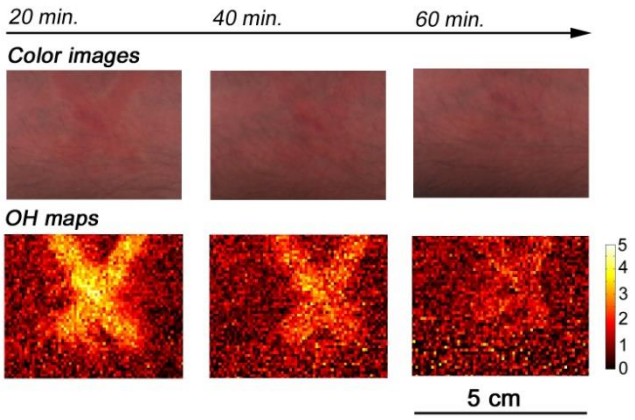

Figure 4. Color images and oxy-hemoglobin distribution maps 20, 40 and 60 minutes after chemical provocation.

3.4. Responses during and after the finger occlusion

Strong (down to 10 %) and fast OH concentration decrease was observed during the middle finger occlusion that lasted 3 minutes. A half minute after the cuff release it increased twice comparing to the level before provocation. Thus the expected OH (oxygenation) decrease and overshoot was observed [14].

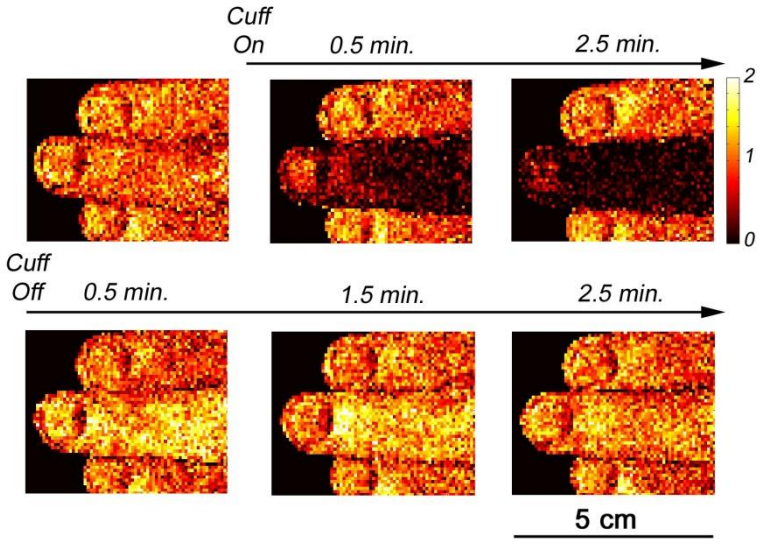

Figure 5. Oxy-hemoglobin concentration maps before, during and after the finger occlusion.

4. CONCLUSIONS

In frame of the simplified 3-chromophore model, the spectral range 500-700 nm is considered to be optimal for simultaneous mapping of OH, DOH and melanin; narrowing of this range (500-600 nm, 530-620 nm) has lead to unacceptable results. But still interaction between melanin and DOH can appear, especially during strong erythema.

Tabulated molar absorption spectral data for this region can be well approximated by superposition of three Gaussians for OH, superposition of two Gaussians for DOH and exponential function for melanin. Such analytical approximations considerably reduced the signal processing time.

Efficiency of the proposed model and methodology was confirmed by the repeated test measurements. Three different provocations (UV, chemical and arterial occlusion) resulted in notable changes of the skin chromophore content and were well reflected in the obtained maps of the three main chromophores. The results correlated well with previous study [9].

The accuracy of chromophore mapping can be further improved taking into account more specific aspects like different light penetration depths at various wavelengths [15] and the scattering effects in skin [16]. Experimental comparison with other skin mapping methods [17] would be performed. There is still potential to speed-up the mapping procedure by modifying the data processing algorithms.

5. ACKNOWLEDGMENTS

This work was partially funded by two projects of European Social fund - "Biophotonics research group" (No.2009.0211/1DP/1.1.1.1.2.0/09/APIA/VIAA/077) and "Support for doctoral studies at University of Latvia" (Nr.1DP/1.1.2.1.2./09/IPIA/VIAA/004).

REFERENCES

[1] Stamatas, G. N., Kollias, N., "In vivo documentation of cutaneous inflammation using spectral imaging," J Biomed Opt 12(5), 051603 (2007).

[2] Ilias, M. A., Haggblad, E., Anderson, C., "Visible, hyperspectral imaging evaluating the cutaneous response to ultraviolet radiation," Proc. SPIE 6441, 644103 (2007).

[3] Randeberg, L. L., Winnem, A. M., Langlois, N. E., "Skin changes following minor trauma," Laser Surg Med, 39(5), 403-413 (2007).

[4] Balas, C., Themelis, G., Papadakis, A., "A Novel-Spectral Imaging System: Application on in-vivo Detection and Grading of Cervical Precancers and of Pigmented Skin Lesions," In Proc. of "Computer Vision Beyond the Visible Spectrum" CVBVS'01 Workshop, Hawaii, USA, Dec. (2001).

[5] Vogel, A., Chernomordik, V. V., Demos, S. G., "Using noninvasive multispectral imaging to quantitatively assess tissue vasculature," J Biomed Opt 12(5), 051604 (2007).

[6] Zonios, G., Bykowski, J., Kollias, N., "Skin, melanin, haemoglobin, and light scattering properties can be quantitatively assessed in vivo using diffuse reflectance spectroscopy," J Invest Dermatol 117(6), p. 1452-7 (2001).

[7] Eames, M. E., Wang, J., Pogue, B. W., "Wavelength band optimization in spectral near-infrared optical tomography improves accuracy while reducing data acquisition and computational burden," J Biomed Opt 13(5), 054037 (2008).

[8] Zuzak, K. J., Gladwin, M. T., Cannon III, R. O., "Imaging haemoglobin oxygen saturation in sickle cell disease patients using noninvasive visible reflectance hyperspectral techniques: effects of nitric oxide," Am J Physiol Heart Circ Physiol 285, H1183-1189, (2003).

[9] Jakovels, D., Spigulis, J., "2-D mapping of skin chromophores in the spectral range 500-700 nm," J Biophoton 3, 125-129 (2010).

[10] Demos, S. G. and Alfano, R. R., "Optical polarization imaging", App Opt 36(1), 150-155 (1997).

[11] Byrd, R. H., Schnabel, R. B., Schultz, G. A., "A trust region algorithm for nonlinearly constrained optimization," SIAM J. Numer. Anal. 24, 1152-1170 (1987).

[12] Prahl, S., "Tabulated Molar Extinction Coefficient for Hemoglobin in Water," http://omlc.ogi.edu/spectra/hemoglobin/summary.html, Last access: March, 2010.

[13] Jacques, S. L., "Extinction coefficient of melanin," http://omlc.ogi.edu/spectra/melanin/eumelanin.html, Last access: March, 2010.

[14] Clark, D. J., Essex, T. J. H., Cater, B., "Skin oxygen saturation imager," Adv Exp Med Biol 428, 573-577 (1997).

[15] Arridge, S. R., Hiroaka, M. and Schweiger, M., "Statistical basis for the determination of optical pathlength in tissue," Phys Med Biol 40(9), 1539-1558 (1995).

[16] Kiseleva, I. A., Sinichkin, Y. P., "The apparent optical density of the scattering medium: influence of scattering," Proc. SPIE 4707, 223-227 (2002).

[17] Dolotov, L. E., Kiseleva, I. A., Sinichkin, Y. P., "Digital imaging of human skin," Proc. SPIE 5067, 139-147 (2003).

I. Saknite, A. Zavorins, D. Jakovels, J. Kisis, J. Spigulis
"Comparison of single-spot technique and RGB imaging for erythema index estimation"
J. Physiol. Meas. (*submitted April 21, 2015, under review*)

Comparison of single-spot technique and RGB imaging for erythema index estimation

I Saknite[1], **A Zavorins**[2], **D Jakovels**[1], **J Spigulis**[1], **J Kisis**[2]
[1] University of Latvia, Institute of Atomic Physics and Spectroscopy, Biophotonics Laboratory, Raina Blvd 19, Riga LV-1586, Latvia
[2] Riga Stradins University, Department of Infectology and Dermatology, Linezera Street 3, Riga LV-1006, Latvia
E-mail: inga.saknite@lu.lv

Abstract. Commercially available point measurement device *Mexameter* and an experimental RGB imaging prototype device were used for erythema index estimation of 50 rosacea patients by analysing the level of skin redness on forehead, both cheeks and both sides of a nose. Results are compared with Clinician's Erythema Assessment (CEA) values given by two dermatologists. *Mexameter* uses 568 nm and 660 nm LEDs for illumination and single photodetector for the reflected light intensity measurement, while the used prototype device acquired RGB images at 460 nm, 530 nm, and 665 nm LED illumination. Several erythema index estimation algorithms were used for comparison to determine which gives the best contrast between increased erythema and normal skin. The erythema index estimations and CEA values correlated much better to the RGB imaging data than to those obtained by the conventional *Mexameter* technique that is widely used by dermatologists and in clinical trials. In result, new erythema index estimation approach is proposed that represents erythema index of skin area 30 millimetres in diameter with higher accuracy than other available methods.

1. Introduction

Rosacea is a chronic inflammatory skin disease that involves flushing, transient or persistent erythema, visible blood vessels (*telangiectasias*), as well as papules and pustules on central convexities of the facial skin (cheeks, chin, nose, and central forehead) (Wilkin *et al*. 2002). These are considered the primary features of *rosacea*. It is one of the most common conditions that dermatologists treat with a prevalence of 2-22% in Europe (Tan & Berg 2013). Pathophysiology of *rosacea* is not fully understood and involves dysregulation of several systems, including innate immunity and neurovascular mechanisms, and the cause of *rosacea* is still being discussed (Hopkinson *et al*. 2015; Crawford *et al*. 2004). Its severity is usually determined clinically by visual assessment of primary features of *rosacea*, including erythema. Different scales are used for erythema assessment in clinical trials, and up until now there has been no validated scale for erythema estimation. Recently, a relatively reliable Clinician's Erythema Assessment (CEA) grading scale has been introduced that ranges from 0 (clear skin, no erythema) to 4 (severe erythema) (Tan *et al*. 2014). The accuracy of the measurements is of great importance as it is often used as the golden standard for evaluation of *rosacea* treatment cream performance (Tan *et al*. 2014; Fowler *et al*. 2013). Unfortunately, it is impossible to avoid evaluator bias (Tan *et al*. 2014). More objective erythema estimation can be done by spectroscopic devices (e.g., *Mexameter*®, *Chromameter*®, *DermaSpectrometer*®), computer analysis of a digital photograph, lesion counts of papules and pustules, assessment of secondary signs and symptoms (burning, stinging, itching), and other (Hopkinson *et al*. 2015). However, the most available and commonly used devices by dermatologists (e.g. *Mexameter*®) estimate only a small region of skin (around 5 mm in diameter) by a single photodetector that does not allow a simple and reliable estimation of skin erythema of a

larger region of skin. It is very important to develop a simple and reliable method for skin erythema estimation of a larger area of skin, as local factors such as *telangiectasia* may influence the result substantially, and RGB imaging is a promising tool to achieve that.

Spectroscopic techniques for erythema assessment are mainly based on comparison of diffuse reflected intensities at different spectral bands - mostly green and red, due to high hemoglobin absorption in the green spectral region and very low absorption in the red. Erythema index can then be calculated as:

$$EI_{RG} = log\frac{I(R)}{I(G)} \approx \frac{I(R)}{I(G)} \tag{1}$$

where $I(R)$ is reflected intensity of the red light and $I(G)$ is the reflected intensity of the green light (Diffey *et al*. 1984). For RGB imaging purposes, logarithm in the formula is often neglected, as only relative values are further used. The approximately equal sign in (1) is used to show that the important parameter here is the relation between the two signals that describe absorption of hemoglobin. In this study, only the relation (not the logarithm of the relation) was further used, as only relative parameter values are observed. Although there is even higher hemoglobin absorption in the blue spectral range, it is not commonly used due to lower mean penetration depth in skin (less than 300 μm compared to approximately 500-700 μm for the green light) (Bashkatov *et al*. 2005).

Several studies use the spectral imaging for erythema index estimation. Polarization multispectral dermoscope has been developed for *in vivo* imaging of skin lesions by using linearly polarized illumination at wavelengths of 470 nm, 530 nm and 625 nm. Blood contrast parameter was calculated as the difference in green and red polarized light illumination images:

$$EI_{BC} = \frac{Green90 - Red90}{Green90 + Red90} = \frac{I(G) - I(R)}{I(G) + I(R)} \tag{2}$$

where $Green90$ and $Red90$ are images at polarized green and red, respectively, illumination (Kapsokalyvas *et al*. 2013).

Noncontact monitoring of vascular lesion phototherapy efficiency has been demonstrated by an experimental RGB imaging system, and melanin-corrected erythema index was calculated as

$$EI_{BRG} = OD(G) - \frac{OD(B) + OD(R)}{2} \approx \frac{\sqrt{I(B) \cdot I(R)}}{I(G)} \tag{3}$$

where $OD(R)$, $OD(G)$ and $OD(B)$ are optical density values representing absorption at the red, green and blue spectral channels and are expressed as:

$$\mathrm{OD}(\lambda) = log\frac{I_0(\lambda)}{I(\lambda)} \tag{4}$$

where I_0 is the intensity of light reflected from a white reference and I is the reflected light intensity from skin surface. $I(R)$, $I(G)$ and $I(B)$ are the reflected intensity values as detected in the red, green and blue spectral channels of image sensor. A new parameter representing the contrast of erythema index (CEI) has been introduced as a measure of erythema index deviation throughout the image area:

$$CEI = \frac{EI_{std}}{EI_{mean}} \tag{5}$$

where EI_{std} is the standard deviation of erythema index and EI_{mean} is the mean value of EI at the region of interest (Jakovels *et al*. 2013).

Most devices for erythema estimation use point measurement systems, acquiring reflected intensity value from a small skin spot of some millimeters in diameter. In particular, *Mexameter*® is a commercially available device that comprises 16 circularly arranged LEDs emitting at wavelengths 568 nm, 660 nm and 880 nm, and a photodetector that measures intensity of the light reflected by skin area of 5 mm in diameter (Matias *et al*. 2015; Clarys *et al*. 2000). Erythema index is calculated from reflected light intensities at 568 nm and 660 nm, based on (1).

2. Materials and methods

This study analyzed three data sets: visual assessment by two dermatologists (CEA, scale from 1 to 4), *Mexameter® MX18* measured erythema index value (EI_M, scale from 1 to 1000), and four erythema index values based on the RGB imaging device measurements and calculated by using four different erythema index estimation algorithms - $EI_{RG}, EI_{BC}, EI_{BRG}$ and a newly proposed erythema index estimation EI_{BG} that will be explained shortly.

2.1. Data acquisition by SkImager

The experimental RGB imaging prototype with provisional brand name *SkImager* is a handheld wireless, battery-powered device that comprises a 3 Mpix CMOS sensor color camera (*Micron* MT9T031, quantum efficiency shown in figure 1a (A.I. Corporation 2006) surrounded by a ring-shaped LED illuminator emitting white, blue (460nm), green (530nm) and red (665nm) spectral bands (figure 1b), linear polarizers in front of the LEDs and the camera, oriented orthogonally to each other (in order to suppress the specular reflection (Demos & Alfano 1997)), an on-chip microcomputer, a touchscreen and an SD memory card (Spigulis *et al*. 2014). The distance between skin surface and the detector is kept constant at 50 mm and the device touches skin surface so that outside light does not reach the detector. Skin area of 30 mm in diameter can be evaluated. Illumination LEDs are evenly distributed in a circle (four LEDs of each type: white, red, green, blue), and each type of LEDs is sequentially switched on for approximately 1 second while an RGB image is taken, thus the total measurement time is approximately 5 seconds. Absorption spectra of skin chromophores oxyhemoglobin, deoxyhemoglobin and melanin are shown in figure 1c (O.M.L.C. 2015).

2.2. Data processing

SkImager acquires three spectral images (red, green, and blue) at each illumination (white, red, green, and blue). Each spectral image represents three roughly separated spectral regions: 600-700 nm (red), 500-600 nm (green), and 400-500 nm (blue) (figure 1a) (A.I. Corporation 2006). Only one spectral image for each illumination was further used (red spectral image for red illumination, green spectral image for green illumination, and blue spectral image for blue illumination), as there is a much lower signal in the other spectral bands that do not provide much information about absorption in the particular wavelength range. Thus three separate images for each measurement are further used, and each pixel has a reflected intensity value at red, green and blue illumination: $I_i(R)$, $I_i(G)$ and $I_i(B)$, respectively.

For erythema severity estimation, a new erythema index parameter was introduced. Hemoglobin absorption can be related to difference between the red and the green spectral images (Diffey *et al*. 1984); however, melanin absorption in the upper skin layers should also be considered (Jakovels *et al*. 2013; Jakovels *et al*. 2011). The melanin-corrected erythema index EI_{BRG} (3) considers that all three spectral images are used. A new empirical erythema index estimation method with using only two adjacent spectral band images is introduced. Erythema index can be estimated as absorption in green spectral band, melanin absorption can be estimated as difference in absorption between blue and green spectral bands, and thus melanin-corrected erythema index can then be estimated as:

$$\mathrm{EI_{BG}} = \mathrm{OD(G)} - [\mathrm{OD(B)} - \mathrm{OD(G)}] \tag{6}$$

By using (4), the previous equation (6) can then be expressed by using reflected light intensities as:

$$\mathrm{EI_{BG}} = \log\left[\frac{[I_0(G)]^2}{I_0(B)} \cdot \frac{I(B)}{[I(G)]^2}\right] \approx \frac{I(B)}{[I(G)]^2} \tag{7}$$

as the first multiplier in the formula is a constant for all measurements. Further a multiplier of 100 is used for better data representation:

$$\mathrm{EI_{BG}} = 100 \cdot \frac{I(B)}{[I(G)]^2} \tag{8}$$

Erythema index for each measurement is calculated as the mean erythema index value of all pixels of the skin area of interest.

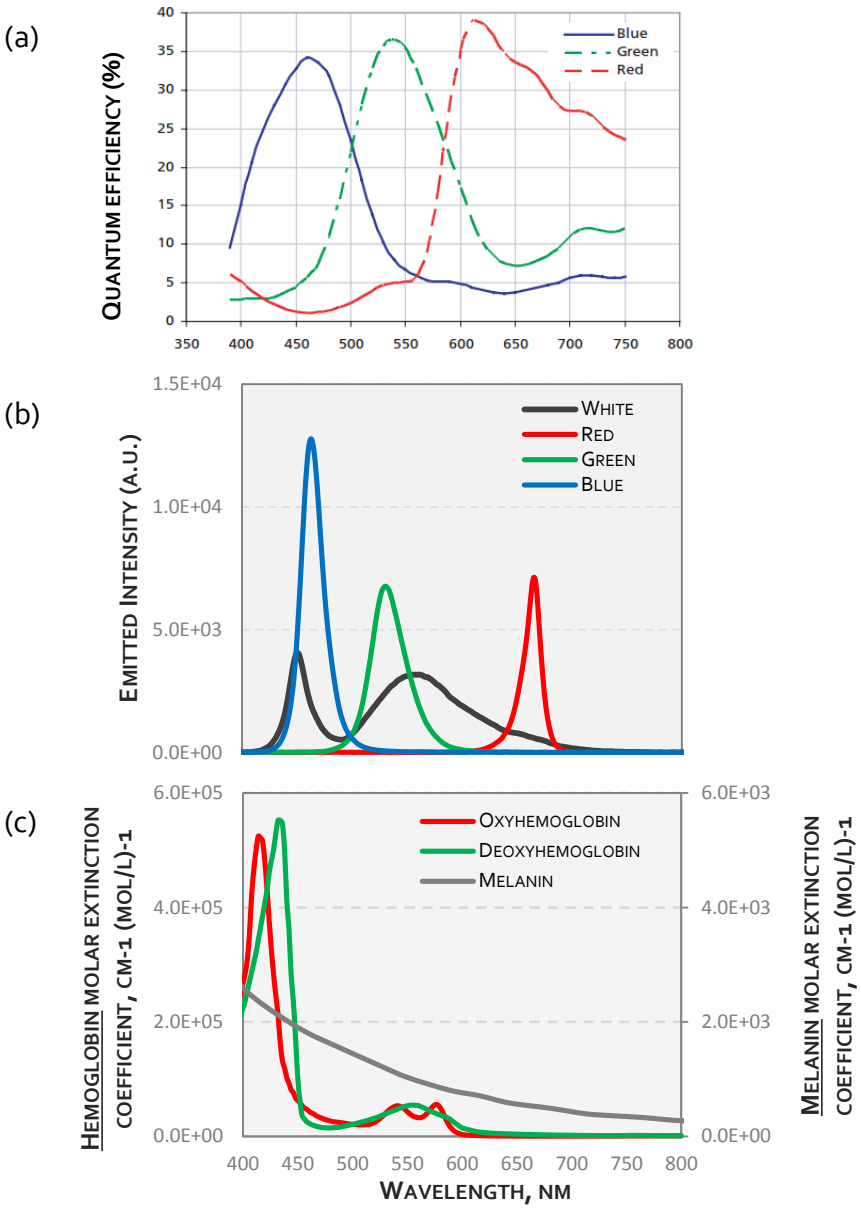

Figure 2. (a) Quantum efficiency of the CMOS sensor used in *SkImager* (A.I. Corporation 2006), (b) Spectra of *SkImager* LEDs and (c) Skin chromophore absorption spectra (O.M.L.C. 2015).

2.3. Participants

Five parts of facial skin were measured for each patient (central forehead, right cheek, left cheek, right part of nose and left part of nose). For each facial part three data sets were obtained: adopted CEA, *Mexameter* erythema index values (EI_M), and *SkImager* erythema index values ($EI_{RG}, EI_{BC}, EI_{BRG}, EI_{BG}$). Before each measurement, patient was asked to sit still and relax for at least 15 minutes in order to avoid other factors affecting their skin color (such as cold outside temperature, fast walking, etc.). Two dermatologists independently graded persistent erythema on each of the five facial regions on a 4-point scale (1 – mild, 2 – moderate, 3 – severe, 4 – very severe erythema), and for all 50 patients their opinions matched. 50 female *rosacea* patients (ages 25 to 60) with dermatologists' estimated CEA index of mostly 2 and 3 participated in the study. The study protocol was approved by the local ethics committee, and each patient gave a written informed consent before the trial. In order to distinguish erythema caused by rosacea and erythema potentially caused by another etiology, a primary screening procedure was done (Elewski *et al*. 2011) by a dermatologist. Only patients with *erythematotelangiectatic rosacea* (Two *et al*. 2015) subtype were enrolled in this study. Differential diagnoses to be ruled out included seborrheic dermatitis, allergic and irritant contact dermatitis and connective tissue diseases such as systemic lupus erythematosus.

3. Results

The obtained results are presented in two parts: comparison between different erythema index estimation algorithms, as well as the newly proposed algorithm, and comparison of results of all three data sets (CEA, *Mexameter* and *SkImager*) for 500 measurements (50 patients, two temporal measurements 1 month apart, 5 facial regions).

3.1. Comparison of different erythema index estimation algorithms

It was expected that visibly seen blood vessels (and other regions with an increased redness) would result in increased erythema index values, compared to normal skin. Erythema index values of 30 patients were analysed to test which erythema index calculation gives the best contrast between areas of increased redness and normal skin., as well as which erythema index calculation gives the best contrast between areas of pigmentation and normal skin. This was done by taking a white LED illumination image of a region of facial skin (forehead, noise or cheek) of any of the patients which shows a region of normal skin, a region of increased redness (i.e. visibly seen blood vessels) and a region of pigmentation. Example of one of the data used is shown in figure 2. In the upper row, white LED illumination RGB image, blue LED illumination blue spectral channel, green LED illumination green spectral channel and red LED illumination red spectral channel images are shown; in the lower row normalized erythema index maps are shown, representing each of the four used calculations for erythema index estimation.

In the White LED illumination image three small regions of interest of at least 10 pixels each were chosen: one representing a region of normal skin (black ROI line in figure 2 white image), one representing a region of increased redness (red ROI line in figure 2 white image) and one representing pigmentation (blue ROI line in figure 2 white image). The average erythema index value of each of the three regions, as well as the standard deviation was then calculated, and it was done for all four erythema index calculations for comparison. To estimate the contrast between increased erythema and normal skin, the average erythema index value of a region of increased redness was divided by erythema index value of a region of normal skin. Similarly, the contrast of pigmentation and normal skin was calculated by dividing the average erythema index value of pigmentation with the average erythema index value of normal skin. An example of the calculated contrast parameters of one patient is shown in table 1.

Out of all the analysed 30 patient data, for each patient the maximum contrast of blood vessels and normal skin and contrast of pigmentation and normal skin value was estimated to determine which erythema index calculation gives the best contrast. In case of contrast of blood vessels and normal skin, it is better to have a higher contrast value as it increases the scale of the level of redness that can be distinguished. In case of contrast of pigmentation and normal skin the lowest contrast value is the best as it means that the absorption of melanin has been subtracted more.

The best contrast between an increased erythema (blood vessels) and normal skin was achieved by using the EI_{BG} estimation algorithm (the highest contrast value for 29 out of 30 patients) (table 2). For 1 of 30 the highest contrast value was shown by the EI_{BC} algorithm. In case of contrast between pigmentation and normal skin the lowest contrast value was achieved using the EI_{BRG} estimation algorithm (the lowest contrast value for 27 out of 30 patients). For 3 out of 30 patients the lowest contrast value was shown by the EI_{BC} algorithm.

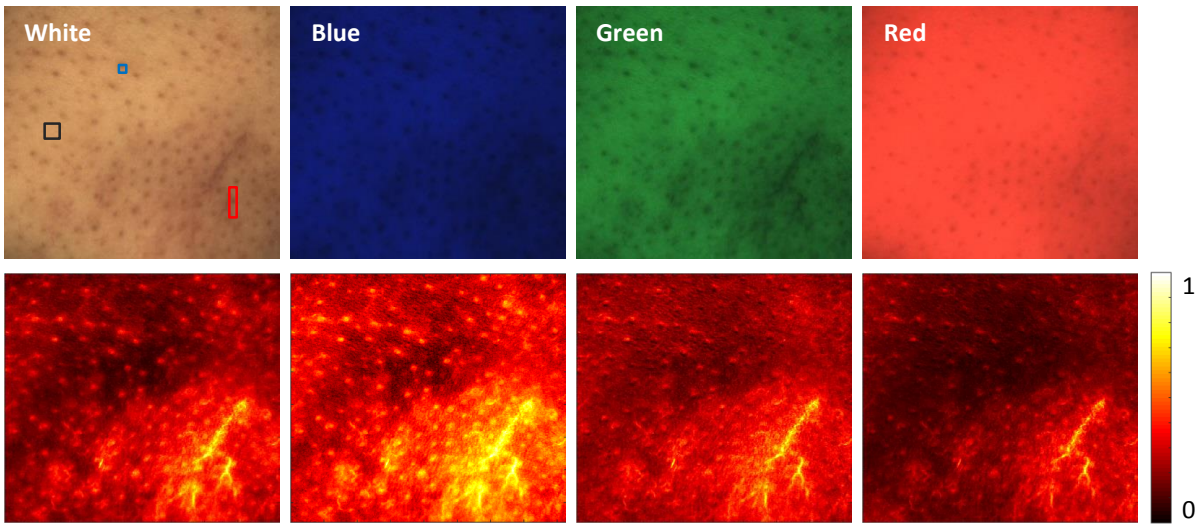

$$EI_{RG} = \frac{I(R)}{I(G)} \qquad EI_{BC} = \frac{I(G) - I(R)}{I(G) + I(R)} \qquad EI_{BRG} = \frac{\sqrt{I(B) \cdot I(R)}}{I(G)} \qquad \mathrm{EI_{BG}} = 100 \cdot \frac{I(B)}{[I(G)]^2}$$

Figure 3. Example of white and spectral images of a nose (on top) and normalized different erythema index distribution maps (bottom).

Table 1. Example of the calculated contrast parameters of one patient data.

	Normal skin	**Blood vessels**	**Pigmentation**	**Contrast of Blood vessels and Normal skin**	**Contrast of Pigmentation and Normal skin**
$\boldsymbol{EI_{RG}}$	0,11 ± 0,01	0,91 ± 0,05	0,61 ± 0,12	8,64 ± 0,43	5,81 ± 0,70
$\boldsymbol{EI_{BC}}$	0,18 ± 0,02	0,95 ± 0,03	0,75 ± 0,10	5,15 ± 0,16	4,04 ± 0,41
$\boldsymbol{EI_{BRG}}$	0,17 ± 0,02	0,90 ± 0,05	0,58 ± 0,13	5,40 ± 0,31	3,44 ± 0,45
$\boldsymbol{EI_{BG}}$	0,09 ± 0,01	0,89 ± 0,06	0,48 ± 0,13	10,29 ± 0,67	5,53 ± 0,72

By analysing results of 30 patient data, the erythema index ranges were estimated for normal skin, increased erythema and pigmentation. For EI_{BG} estimation algorithm, erythema index values for normal skin ranged from $0{,}09 - 1{,}27$ with an average of 0,77; for skin area of increased erythema (e.g. blood vessels) the values ranged from $0{,}86 - 3{,}69$ with an average of 1,76; for skin area of pigmentation (increased melanin content) the values ranged from $0{,}48 - 3{,}24$ with an average of 1,28. Some ranges overlap which can be explained by the fact that skin colour of the patients, mostly in terms of redness, varied greatly, and what for some was reduced redness, for others was increased redness, compared to the whole facial skin.

Table 2. Contrast parameter comparison for all 30 patient data.

Contrast of Blood vessels and Normal skin				Contrast of Pigmentation and Normal skin			
EI_{RG}	EI_{BC}	EI_{BRG}	EI_{BG}	EI_{RG}	EI_{BC}	EI_{BRG}	EI_{BG}
8,64	5,15	5,40	10,29	5,81	4,04	3,44	5,53
1,56	1,93	1,35	1,82	1,72	2,10	1,18	1,69
1,91	1,68	1,53	2,43	1,17	1,18	1,04	1,26
1,76	1,55	1,64	3,29	1,26	1,24	1,33	2,10
1,86	1,36	1,54	2,32	1,47	1,24	1,20	2,55
1,66	1,62	1,39	1,94	1,41	1,43	1,31	1,99
1,89	1,57	1,49	2,31	1,31	1,27	1,06	1,51
1,60	1,57	1,30	2,01	1,48	1,49	1,27	2,20
1,57	1,65	1,29	1,66	1,30	1,39	1,10	1,37
1,88	1,51	1,55	2,59	1,54	1,37	1,29	1,90
1,94	1,80	1,48	2,99	1,13	1,17	1,07	1,15
1,62	1,46	1,34	2,02	1,77	1,53	1,42	2,51
1,48	1,49	1,19	1,73	1,37	1,39	1,18	1,70
1,88	1,85	1,59	2,99	1,43	1,51	1,21	1,64
2,17	1,73	1,63	3,79	1,34	1,31	1,13	1,68
1,24	1,19	1,18	1,42	1,07	1,06	1,04	1,19
1,49	1,29	1,28	1,63	1,16	1,11	1,08	1,26
1,79	1,51	1,49	2,59	1,25	1,21	1,08	1,29
2,01	1,62	1,62	2,70	1,31	1,27	1,14	1,43
2,33	1,69	1,92	4,56	1,54	1,39	1,42	2,56
1,78	1,64	1,57	2,82	1,32	1,32	1,20	2,06
1,55	1,41	1,39	2,24	1,36	1,30	1,24	1,96
1,05	1,06	1,02	1,17	1,11	1,12	1,00	1,31
1,86	1,58	1,45	2,27	1,45	1,37	1,22	1,56
1,75	1,47	1,52	2,43	1,19	1,16	1,00	1,14
1,29	1,22	1,23	1,56	1,00	1,00	1,03	1,26
1,44	1,29	1,29	1,98	1,14	1,11	1,10	1,37
1,50	1,51	1,31	1,74	1,15	1,18	1,02	1,07
1,26	1,23	1,17	1,68	1,09	1,09	1,08	1,21
1,31	1,33	1,14	1,34	1,34	1,36	1,17	1,39

3.2. Comparison of CEA, Mexameter and SkImager results

For 500 total measurements three data sets were analysed: CEA, *Mexameter* and *SkImager* erythema estimation values. All 500 measurements were divided in four groups, depending on the corresponding CEA value of each measurement, and boxplots, created with *Matlab*, show the correlation of CEA and EI_M values, acquired by *Mexameter* (figure 2). The box in the plot represents all data of 25th to 75th percentiles; the lines include 99,3% of all the data, and the red crosses represent outliners. The blue dots in the box represent the medians, and linear fitting of medians and CEA values was done to acquire the coefficient of determination R^2.

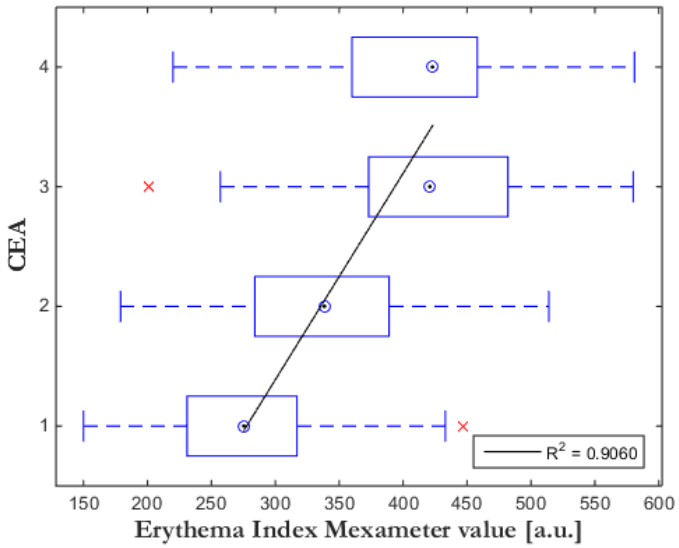

Figure 4. A boxplot of all *Mexameter* estimated erythema index $\boldsymbol{EI_M}$ values for each corresponding CEA value and linear regression correlation between CEA value and the median value of $\boldsymbol{EI_M}$ for each corresponding CEA value.

Similarly, boxplots of two of the erythema index estimation algorithms EI_{BRG} and EI_{BG} are shown in figure 4. The correlation graphs clearly show a much better linear correlation (R^2~0,99) between CEA and the median EI_{BRG} and EI_{BG} values. Correlation between CEA and the other two erythema index estimation algorithms (EI_{BC} and EI_{RG}) was also calculated, and the coefficients of determination are $R^2 = 0{,}9940$ and $R^2 = 0{,}9989$, respectively. It seems that there is not much difference when comparing all four different erythema index estimation algorithms in terms of how well they correlate with dermatologists' estimated CEA, however they show a much better correlation when comparing with erythema index estimations acquired by *Mexameter*.

Linear fitting was also done on all data points (not just medians) to see how well all the CEA and EI values correlate. As expected, the coefficients of determination are not very high. The lowest coefficient value is for EI_M ($R^2 = 0{,}3032$). The other four erythema index estimation algorithms show similar coefficient values: $R^2 = 0{,}4458$ (EI_{RG}), $R^2 = 0{,}4386$ (EI_{BC}), $R^2 = 0{,}4486$ (EI_{BRG}) and $R^2 = 0{,}4361$ (EI_{BG}).

A two-sample t-test was performed to test whether there is a significant ($p < 0{,}05$) difference between two consecutive CEA groups (1 and 2, 2 and 3, 3 and 4) for all EI estimation algorithms. Results show that there is a significant difference ($p < 0{,}05$) between the groups for all EI estimation algorithms except EI_M results, acquired by *Mexameter* – there was not a significant difference between CEA groups 3 and 4 for EI_M.

4. Conclusions and discussion

In this study, for the first time in authors' knowledge, different in literature available erythema index estimations are compared in terms of how well they distinguish skin region of increased redness and normal skin. Commonly used method of visual assessment of facial erythema by an experienced dermatologist (CEA) is compared to commonly used single-spot optical measurement device (*Mexameter*). In addition, an RGB imaging technique is proposed and clinically validated for a more accurate and reliable estimation of skin erythema; also a new erythema index estimation algorithm is proposed using only blue and green spectral images.

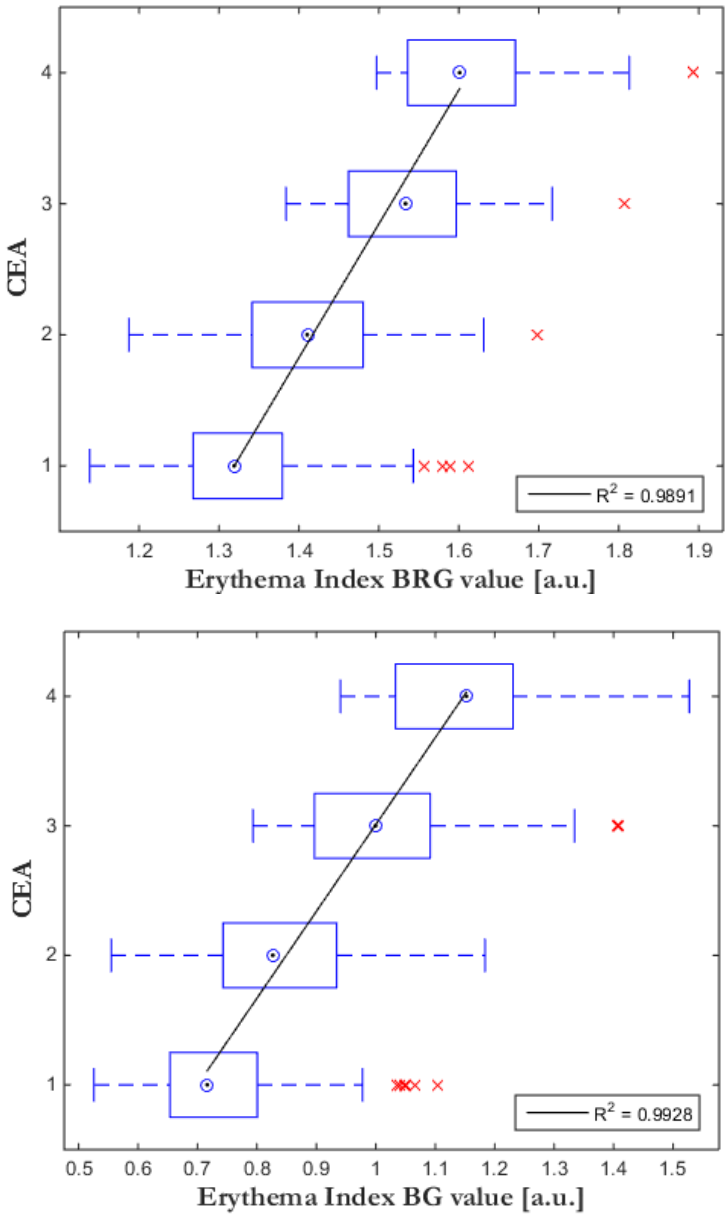

Figure 5. Boxplots and correlation graphs between CEA and ***EI*** for all four ***EI*** estimation algorithms.

This study shows a comparison between four different in literature available erythema index estimation algorithms and proposes a new algorithm using only blue and green spectral images (EI_{BG}). The new erythema index estimation algorithm shows the best contrast between skin area with increased redness and normal skin, compared to other erythema index estimation algorithms, and it was validated by data of 30 patients. This is important when very small changes in skin erythema have to be distinguished, for example, in clinical studies for determination of *rosacea* treatment cream effectiveness. Sometimes the effect of a treatment cream can be very small, thus very precise and accurate erythema index estimation algorithms can be of great importance.

It is also important to minimize the effect of melanin absorption when estimating erythema index, as melanin also affects the total skin absorption in all three spectral ranges. The lowest contrast between pigmentation (increased melanin content) and normal skin regions was achieved by using a previously developed erythema index estimation EI_{BRG}. In case of high skin pigmentation, it would be more useful to use this erythema index estimation algorithm as it is less affected by melanin absorption in skin.

One of the main goals of this study was to see how well the visual assessment of a dermatologist correlates with the result obtained by an optical device. Often in clinical studies only dermatologist's visual assessment is taken into account; however, it can be very subjective, even in case of a very experienced specialist. Unfortunately, there is currently no noninvasive golden standard technique that can give the real erythema index value, so there was no technique or data to compare all the results to. However, the idea was to at least get the sense of how well the currently used estimations (both visual and optical) correlate to each other. Thus the output data of two optical devices used for erythema index estimation, a single-spot measurement device *Mexameter* and an RGB imaging device *SkImager*, were compared to dermatologists' assessment (CEA values). Out of 500 measurements in total, it can be concluded that the results differ greatly when comparing dermatologists' visual assessment and the results of optical devices which is probably due to different subjective factors that affect dermatologists' opinion. It was also clearly noted that results of RGB imaging device correlate better with CEA values than results obtained by single-spot technique *Mexameter*. This can easily be explained by the fact that *Mexameter* uses a spot measurement of only 5mm in diameter while RGB imaging device *SkImager* acquires spectral data of a larger area of skin of up to 30 mm in diameter and then an average erythema index value can be calculated or erythema index distribution map obtained and further analysed.

In conclusion, this study shows that single-spot measurements might not be very reliable when compared to the RGB imaging even though they are often used in clinical studies. RGB imaging shows a much better correlation with dermatologists' estimation and shows more reliable results. A new erythema index estimation algorithm was proposed, and it demonstrates a better contrast between blood vessel and normal skin regions than other algorithms.

Acknowledgements

This work has been supported by Latvian National Research Programme "Cyber-physical systems, ontologies and Biophotonics for safe & smart city and society" (SOPHIS) under grant agreement #10-4/VPP-4/11.

References

Bashkatov, a N., Genina, E. a, Kochubey, V.I. & Tuchin, V. V, 2005. Optical properties of human skin, subcutaneous and mucous tissues in the wavelength range from 400 to 2000 nm. *Journal of Physics D: Applied Physics*, **38**, pp.2543–2555.

Centre, O.M.L., 2015. Optical Properties Spectra. Available at: http://omlc.org/spectra/ [Accessed January 1, 2015].

Clarys, P., Alewaeters, K., Lambrecht, R. & Barel, a. O., 2000. Skin color measurements: comparison between three instruments: the Chromameter(R), the DermaSpectrometer(R) and the Mexameter(R). *Skin research and technology : official journal of International Society for Bioengineering and the Skin (ISBS) [and] International Society for Digital Imaging of Skin (ISDIS) [and] International Society for Skin Imaging (ISSI)*, **6**(17), pp.230–238.

Corporation, A.I., 2006. 1 / 2-Inch 3-Megapixel CMOS Digital. , pp.1–46.

Crawford, G.H., Pelle, M.T. & James, W.D., 2004. Rosacea: I. Etiology, pathogenesis, and subtype classification. *Journal of the American Academy of Dermatology*, **51**(3), pp.327–341.

Demos, S.G. & Alfano, R.R., 1997. Optical polarization imaging. *Applied Optics*, **36**(1), pp.150–155.

Diffey, B.L., Oliver, R.J. & Farr, P.M., 1984. A portable instrument for quantifying erythema induced by ultraviolet radiation. *The British journal of dermatology*, **111**, pp.663–672.

Elewski, B.E., Draelos, Z., Dreno, B., Jansen, T., Layton, A. & Picardo, M., 2011. Rosacea - global diversity and optimized outcome: proposed international consensus from the Rosacea International Expert Group. *Journal of the European Academy of Dermatology and Venereology : JEADV*, **25**(2), pp.188–200.

Fowler, J.J., Jackson, M., Moore, A., Jarratt, M., Jones, T., Meadows, K., Steinhoff, M., Rudisill, D. & Leoni, M., 2013. Efficacy and safety of once-daily topical brimonidine tartrate gel 0.5% for the treatment of moderate to severe facial erythema of rosacea: results of two randomized, double-blind, and vehicle-controlled pivotal studies. *Journal of drugs in dermatology : JDD*, **12**(6), pp.650–656.

Hopkinson, D., Tuchayi, S.M., Alinia, H. & Feldman, S.R., 2015. Assessment of rosacea severity: A review of evaluation methods used in clinical trials. *Journal of American Dermatology*.

Jakovels, D., Kuzmina, I., Berzina, A., Valeine, L. & Spigulis, J., 2013. Noncontact monitoring of vascular lesion phototherapy efficiency by RGB multispectral imaging. *Journal of biomedical optics*, **18**(12), p.126019.

Jakovels, D., Spigulis, J. & Rogule, L., 2011. RGB Mapping of Hemoglobin Distribution in Skin. In *Proc. of SPIE-OSA Biomedical Optics*. p. 80872B–80872B–6.

Kapsokalyvas, D., Bruscino, N., Alfieri, D., de Giorgi, V., Cannarozzo, G., Cicchi, R., Massi, D., Pimpinelli, N. & Pavone, F.S., 2013. Spectral morphological analysis of skin lesions with a polarization multispectral dermoscope. *Optics express*, **21**(4), pp.4826–40.

Matias, A.R., Ferreira, M., Costa, P. & Neto, P., 2015. Skin colour, skin redness and melanin biometric measurements: comparison study between Antera 3D, Mexameter and Colorimeter. *Skin research and technology : official journal of International Society for Bioengineering and the Skin (ISBS) [and] International Society for Digital Imaging of Skin (ISDIS) [and] International Society for Skin Imaging (ISSI)*.

Spigulis, J., Rubins, U., Kviesis-Kipge, E. & Rubenis, O., 2014. SkImager: a concept device for in-vivo skin assessment by multimodal imaging. *Proceedings of the Estonian Academy of Sciences*, **63**(3), p.213.

Tan, J. & Berg, M., 2013. Rosacea: Current state of epidemiology. *Journal of the American Academy of Dermatology*, **69**(6 SUPPL.1), pp.S27–S35. Available at: http://dx.doi.org/10.1016/j.jaad.2013.04.043.

Tan, J., Liu, H., Leyden, J.J. & Leoni, M.J., 2014. Reliability of Clinician Erythema Assessment grading scale. *Journal of the American Academy of Dermatology*, **71**(4), pp.760–763.

Two, A.M., Wu, W., Gallo, R.L. & Hata, T.R., 2015. Rosacea: part I. Introduction, categorization, histology, pathogenesis, and risk factors. *Journal of the American Academy of Dermatology*, **72**(5), pp.749–760.

Wilkin, J., Dahl, M., Detmar, M., Drake, L., Feinstein, A., Odom, R. & Powell, F., 2002. Standard classification of rosacea: Report of the National Rosacea Society Expert Committee on the Classification and Staging of Rosacea. *J Am Acad Dermatol*, **46**(4), pp.584–7.